Iris Hehn, Dipl.-Ing.

Influence of Embedded Dipolar Groups on the Electronic and Structural Properties of Self-Assembled Monolayers

DISSERTATION

zur Erlangung des akademischen Grades

Doktorin der technischen Wissenschaften

eingereicht an der

Technischen Universität Graz

Betreuer

Ao. Univ.-Prof. Dipl.-Ing. Dr.techn. Egbert Zojer

Institut für Festkörperphysik

Graz, Mai 2016

EIDESSTATTLICHE ERKLÄRUNG

Ich erkläre an Eides statt, dass ich die vorliegende Arbeit selbstständig verfasst, andere als die angegebenen Quellen/Hilfsmittel nicht benutzt, und die den benutzten Quellen wörtlich und inhaltlich entnommenen Stellen als solche kenntlich gemacht habe. Das in TUGRAZonline hochgeladene Textdokument ist mit der vorliegenden Dissertation identisch.

Datum

Unterschrift

Acknowledgements

I would like to sincerely thank the following institutions and people, without whom the completion of this thesis would not have been possible:

The Austrian Science Fund (FWF): for providing the financial support of the project

ZID (TU Graz): for providing the computational resources of icluster and dcluster and computer support

Vienna scientific cluster: for computational resources on the vsc3 cluster and the administration team for keeping the cluster running smoothly

Egbert Zojer: for the excellent scientific supervision of this thesis; for his help and support in solving any problems encountered during calculation, data evaluation, interpretation and presentation; and finally for inspiring a motivating, friendly and open atmosphere in our group

Michael Zharnikov and **Swen Schuster**: for collaboration on the embedded ester project; for providing excellent experimental data, and being available for and interested in long discussions about data evaluation, interpretation and comparison between experiment and calculations

Claudio Zannoni: for providing me the opportunity to spend a month in his group in Bologna to improve my understanding of molecular dynamics simulations

Otello Roscioni: for his immense help in running MD simulations; for his excellent work on developing the combined MD+embedding algorithm and for always having an open ear for any problems concerning molecular dynamics

All members of Claudio Zannoni's group in Bologna: for the warm and welcoming atmosphere in the office and for keeping me busy outside of work in Bologna

David Egger and **Manuel Vieider**: for introducing me to the intricacies of running DFT and MD calculations and for being extremely patient in answering all my endless questions

Thomas Taucher: for collaboration on the XPS project and in writing the paper; for helping me with any computer- and python- related problems in the most patient way

Oliver Hofmann: for his valuable input in writing the XPS paper and for long and fruitful discussions about calculation results and how best to present them

All members of our extended group (including some former members):
Anton, Anu, Berni, David, Egbert, Elsi, Georgii, Gernot, Giulia, Hermann, Jimmy, Karin, Lisi, Manuel, Markus, Natalia, Oliver, Philipp, Shashank, Simon, Thomas, Veronika:
for scientific discussions; for their help and support; for the great atmosphere in our group and, most importantly, for all the interesting, motivating and fun coffee and lunch breaks

All my other colleagues and friends: for their support and motivation especially when things didn't work according to plan

My family: for their unwavering support throughout all these years

Abstract

Using self-assembled monolayers (SAMs) to intentionally tune specific substrate properties has been the focus of a very wide and active field of scientific research. For the application in organic electronics, modifying electronic properties of metal substrates by adsorbing SAMs is of special interest. The most widely used approach to achieve this is substituting the terminal moiety of a SAM with a functional group. However, an alternative method is introducing dipolar groups into the molecular backbone instead of changing the terminal unit. This offers the distinct advantage of tuning electronic properties of the SAM without altering the interface to the next layer. This is of significant interest for multilayer devices like solar cells or transistors, which are the two major areas of application for SAMs in the field of organic electronics.

Therefore, the main goal of this thesis is to study the impact of embedded dipolar groups on the structural and electronic properties of SAMs. The effects are investigated for both aliphatic and aromatic molecules using computational methods. Specifically, molecular dynamics (MD) simulations are performed to capture structural properties on larger spatial scales including molecular packing structures and order-disorder effects. They are complemented by quantum mechanical calculations employing density functional theory (DFT) to gain insight into specific electronic system properties like work functions and atomic core level energies. The effect of mixing molecules with different dipolar orientations in a SAM is investigated, considering homogeneous and inhomogeneous mixtures of varying concentrations. Additionally, the impact of depolarization on molecular dipoles and molecular geometries inside a SAM is addressed using molecular dynamics and a customized electrostatic embedding procedure.

Kurzfassung

Die Verwendung von selbstassemblierten Monolagen (SAMs) um spezifische Substrateigenschaften zu modifizieren steht seit langem im Fokus wissenschaftlicher Forschung. Für die Anwendung im Bereich organischer Elektronik ist die Modifikation elektronischer Eigenschaften metallischer Substrate von besonderem Interesse. Der am weitesten verbreitete Ansatz dafür ist die SAM-Endeinheit durch eine funktionale chemische Gruppe zu substituieren. Eine alternative Methode ist das Einbringen dipolarer Gruppen in der Mitte des Moleküls, was den Vorteil hat, dass die elektronischen Eigenschaften der Monolage gezielt modifiziert werden können ohne die Grenzfläche zur nächsten angrenzenden Schicht zu verändern. Dies ist von speziellem Interesse für die Verwendung von SAMs in vielschichtigen Bauelementen, wie etwa Solarzellen oder Transistoren, die auch gleichzeitig die zwei Hauptanwendungsgebiete von SAMs im Bereich der organischen Elektronik darstellen.

Auf diesen Überlegungen basierend liegt das Hauptziel dieser Arbeit in der Untersuchung von eingebetteten dipolaren Gruppen und deren Auswirkungen auf die strukturellen und elektronischen Eigenschaften von SAMs. Es werden die Effekte sowohl für aliphatische als auch aromatische Moleküle mithilfe von Computersimulationen untersucht. Im Speziellen werden Molekulardynamiksimulationen durchgeführt, um strukturelle Eigenschaften in größeren Längenskalen, wie etwa molekulare Packungen in der Monolage, oder Unordnungseffekte zu studieren. Komplementiert werden diese Ergebnisse durch quantenmechanische Rechnungen basierend auf der Dichtefunktionaltheorie, die Einblicke in spezifische elektronische Eigenschaften des untersuchten Systems, wie etwa Austrittsarbeiten oder Bindungsenergien ermöglichen. Die Veränderungen, die sich durch das Mischen von Molekülen mit unterschiedlichen Orientierungen der Dipolmomente in einer SAM ergeben werden für homogene sowie inhomogene Mischungen verschiedener Konzentrationen studiert. Zusätzlich wird der Einfluss von Depolarisationseffekten auf molekulare Geometrien und Dipole mithilfe von Molekulardynamiksimulationen und elektrostatischer Einbettungsmethoden untersucht.

Contents

Preface

This thesis is divided into two Parts. Part I gives fundamental information about the systems studied in this work as well as the methods employed to investigate them. The results obtained during this PhD thesis are presented in Part II.

Chapter 1 introduces the reader to the topic of self-assembled monolayers (SAMs) and gives an introduction into the systems studied in this thesis. The characteristics making them interesting to investigate are discussed.

The basics of the applied computational methods molecular dynamics (MD) and density functional theory (DFT) are summarized in Chapters 2 and 3. In addition to a general introduction to the theoretical concepts, specific computational details relevant for this thesis are provided for both methods in the respective Chapters.

Chapter 4 treats the highly important aspect of geometry optimization. Before quantum-mechanical properties of a system can be calculated, the exact molecular conformation and arrangement on the substrate needs to be known. It is obtained by employing geometry optimization techniques on a reasonable starting guess for the initial geometry. This was an especially tricky and important part for the systems described in this thesis. A customized procedure combining MD and DFT methods was developed to treat this aspect. Details explaining the method and reasons why this approach was chosen are given in Chapter 4.

In Chapter 5 the method of calculating core level energies within the DFT framework using the initial state approach is introduced and explained. A postprocessing step to account for screening effects of the metal substrate is devised. Further, XP spectra are calculated from individual atomic core level energies including exponential damping effects. This methodological approach is then applied to two test systems to illustrate the occurrence of chemical and electrostatic shifts in XP spectra. The respective origins of shifts are clarified by artificially reducing the coverage in the systems, which eliminates collective electrostatic effects and the resulting electrostatic shifts, leaving only chemical influences. With this computational approach the impact of chemical and electrostatic shifts can be analyzed separately.

In Chapter 6 the computational method introduced and tested in Chapter 5 is applied to further investigate SAMs of alkyl thiolates with embedded dipolar ester groups on Au(111) substrates. The ester groups effectively separate the molecules into two electrostatically different segments. The chemical structure of these two

segments is the same. SAMs of molecules with varying chain lengths below and above the ester group are investigated. Specifically, the impact of the molecular conformation on the dipole moment is studied. The precise orientation of dipoles and their collective interaction strongly affect the system's work function and atomic binding energies. Both quantities are calculated for different systems and compared to experimental data. The bond dipole contribution to the overall electrostatic situation and its interaction with the ester dipole is also investigated.

Chapters 5 and 6 focus on determining and quantifying the impact of dipolar groups on the electronic properties of SAMs containing molecules with only one dipole orientation. This of course, raises the question of how the behavior of the film is modified in case of mixed SAMs, containing molecules of different dipolar orientations. This topic of mixed dipolar SAMs is addressed in Chapter 7. SAMs of aromatic molecules, specifically pyrimidine-substituted terphenyls are chosen as an ideal test system for this investigation. Replacing the middle phenylene ring of a terphenyl molecule by a pyrimidine unit introduces a significant, additional dipole moment into the molecule, without changing the terminal moiety. Furthermore, the pyrimidine segment can be inserted in two different orientations, aligning the dipole in both cases along the molecular axis, but once pointing towards the substrate and once away from it. With this trio of molecules the electrostatic effects in mixed monolayers of molecules with different dipolar orientations are studied. These systems offer the possibility to test mixtures of oppositely oriented dipoles as well as effectively diluting the dipole density in a densely packed SAM, by mixing dipolar molecules with pure terphenyls. The impact of the mixing ratio is investigated for these different types of systems and calculated results are compared to experimental data. Additionally, the possibility of phase separation into domains of similar dipole orientation within a mixed SAM is discussed.

Whereas in the previous chapters density functional theory is the main computational method used to investigate self-assembled monolayers, Chapter 8 focuses on molecular dynamics as an approach to study SAMs. More specifically, in this chapter molecular dynamics simulations, combined with an electrostatic embedding scheme are employed to study the effects of depolarization on the molecular dipoles and the structural properties of SAMs. Standard MD simulations using additive force fields neglect to treat polarization phenomena, as electrostatic interactions are modeled by fixed atomic partial charges and Coulomb potentials. The approach presented in Chapter 8 bases on combining MD simulations with an electrostatic embedding approach. This enables the calculation of more realistic atomic charges by taking into account the influence of the electrostatic field generated by the surrounding molecules. Molecular dynamics is chosen as the principle method as it allows the use of far larger unit cells than density functional theory and thus order-disorder effects can be investigated. Tests of the individual steps of the iterative procedure as well as final results, obtained for four different SAMs are presented.

Part I.

Introduction and Fundamentals

1. Introduction

1.1. Self-assembled monolayers

Self-assembled monolayers (SAMs) are ordered two-dimensional arrays of molecules adsorbed onto a substrate. The molecules that build a SAM generally consist of three parts[1,2]: (1) the docking group, with which the molecule binds to the substrate, (2) a molecular backbone and (3) an end or terminal group with some functionalization. Most SAMs are strongly chemisorbed to the substrate. A common pairing is a thiol docking group adsorbed onto a gold substrate.[3–12] In this case the hydrogen splits off from the thiol group and the sulfur atom binds covalently to the gold substrate,[1] which is called dissociative adsorption. The most common molecular backbones are either alkyl chains of varying lengths[1,13–18] or a chain of conjugated carbon rings.[1,19–23] Recently, scientific interest has been focused on functionalizing the backbone by introducing embedded dipolar groups[24], e.g. ester groups into alkyl thiols[25] or pyrimidine units into terphenyls.[21,26] The terminal group offers another possibility to functionalize the SAM in multiple forms.[1,13,27,28] This group is especially important as it constitutes the surface of the SAM and therefore, directly interacts with its surroundings.[29–33] It can also form the interface to a following layer, if the SAM is used in a multilayer application. In such cases it gravely impacts the interaction with the following layer, both chemically and structurally. By choosing appropriate terminal groups the SAM can be used, for example to create hydrophobic/hydrophilic surfaces.[34–37] Material protection in general is a widespread application of SAMs, e.g. as a thin coating to enhance chemical resistance of materials[38,39], for corrosion protection.[40] SAMs can also be used in biological or medical applications[41–46] or as sensors.[47,48] The increasing development of nanotechnology offers a further field for employing SAMs, where they can be used for patterning, stabilization and functionalization of nanoscale structures.[1,49–52] The field of organic electronics, on the other hand, offers a completely different range of applications for SAMs, where not only their structural characteristics but also their electronic properties are important. In this context it should be noted that the molecular structure, the packing structure of the SAM and its resulting electronic properties are of course related. In the field of organic electronics SAMs are mostly studied for application in organic solar cells[53–57] or transistors, where they can either be used as the active semiconducting layer,[58–60] or as a means to modify and stabilize interfaces.[27,61–66] For these applications the interaction of a SAM with a metal substrate and the way it can alter its electronic properties, like most essentially the work function and energy level alignment, are crucial.[67–71] The adsorption of SAMs onto metal contacts allows the precise tuning of the energy level alignment in devices. Contact work functions

can be adjusted[14,24,72–74], for example to fit to the charge transport levels of adjoining semiconducting layers. Therefore, investigating the exact electronic characteristics of self-assembled monolayers on metal substrates and how to purposefully influence them is a major field of research in surface science.

1.1.1. Production techniques for SAMs

In principle SAMs can be produced in two ways, either by adsorption from solution or by deposition of molecules from the gas phase.[1,4,5,75] The first approach is most commonly persued by leaving the cleaned substrate in the solution for a certain amount of time, thus giving the molecules time to adsorb onto the substrate and order themselves. This is the most common way to produce SAMs.

For deposition from the gas phase[1,3,76–82] the a vacuum chamber is required. The molecules are converted to gas phase by evaporation from a Knudsen cell and directly adsorb onto the substrate without interaction with a solvent. This technique also offers the possibility to adsorb at different substrate temperatures or anneal the film after deposition, when a heated sample holder is used.

A related, solution based technique for building ordered thin films is the Langmuir-Blodgett method.[9,83–86] In this approach molecules with a hydrophilic head and a hydrophobic tail are distributed on a water surface, where they float as a dense film, with the hydrophobic tail pointing away from the water surface. When the substrate is vertically pulled out of the bath, the molecules stick to it with their hydrophilic heads, creating a well ordered SAM. The process can be repeated several times to create multilayers. Langmuir-Blodgett films differ from SAMs however in the aspect that they do not really self-assemble. The are already transferred to the substrate in an ordered arrangement.

1.1.2. Measurement techniques applied to investigate SAMs

A number of different measurement techniques are available to study and characterize SAMs[76,87–89]. As already mentioned above, when studying SAMs one is interested, on the one hand, in structural properties like the molecular geometry and the lateral arrangement of the molecules on the substrate and, on the other hand, in electronic properties like the work function of the system, core level binding energies or electronic transport levels.

A quantity of foremost interest is the molecular packing structure of the molecules on the substrate determined by the surface unit cell. This information can be gathered with low-energy electron diffraction (LEED)[11,89] measurements. This technique is based on diffracting electrons from the two dimensional substrate-SAM system. The difference to standard X-ray diffraction is that LEED is extremely surface sensitive due to the low kinetic energy of the electrons used. This makes LEED the method of choice to study the packing structure of thin films and SAMs. Even more detailed structural data can be obtained by using scanning tunneling microscopy

(STM).[90,91] Compared to LEED, STM measurements give more local information about the molecular alignment and packing structure. Different domains and local defects in the molecular arrangement can be revealed.

Optical spectroscopy is another powerful tool used to monitor electronic and structural properties of thin films. As light has a relatively large mean free path, the overall signal contains contributions of the thin film as well as the underlying bulk. To distinguish the optical responses of the two phases, differential methods are applied. The techniques used for this purpose are differential reflectance spectroscopy (DRS)[92,93] and reflectance difference spectroscopy (RDS).[94]

Other techniques employed to investigate thin films are based on the photoelectric effect. Photoelectrons can be emitted if the energy of the incident photon is larger than the ionization potential of the sample. This energy barrier depends on the energy level alignment in the film. Photoelectron emission microscopy (PEEM)[95,96] is a powerful technique based on the photoelectric effect, which allows to probe film structures with lateral resolution. Another surface microscopy technique is low energy electron microscopy (LEEM),[97,98] which is based on the elastic backscattering of low energy electrons in thin films. Numerous surface and thin film properties like molecule adsorption and film growth, as well as phase transitions and surface reactions can be monitored with LEEM.[97,98]

For flat lying molecules adsorbed onto a surface, the adsorption distance is often of paramount interest. This quantity can be determined by X-ray standing wave (XSW)[99,100] measurements. Used measurement techniques to determine tilt angles are infrared reflection spectroscopy (IRS)[76,101,102] and near-edge X-ray absorption fine structure spectroscopy (NEXAFS).[103,104]

One of the most relevant electronic properties of a SAM is its work function, e.g. the work function modification the SAM introduces compared to the pristine substrate. The work function of a system can be measured either by using the secondary electron cutoff in ultraviolet photoelectron spectroscopy (UPS)[14,17,105,106] or with Kelvin probe measurements[107–109]. Another, widely applied experimental method to study SAMs is X-ray photoelectron spectroscopy (XPS).[76,110] In XPS the kinetic energy of the ejected photoelectrons is measured, from which their original atomic binding energies can be determined, as the energy of the incident X-ray beam is known precisely. Based on this approach XPS is inherently element specific, meaning each element produces a characteristic, so-called fingerprint spectrum with distinct peaks at specific energies. As atomic binding energies are very sensitive to their close chemical environment, XPS is an ideal technique to investigate which chemical compounds are present in a sample. Additionally, XPS is also sensitive to the electrostatic surroundings of each contributing atom. This has become of increasing scientific interest recently.[25,26] Electrostatic influences versus chemical influences on XP spectra are also investigated in this thesis. The according methodological approach and the obtained results are presented and discussed in Chapter 5.

Experimental studies yield essential insights into SAM structures and electronic

situations. They are vital for theoretical studies for benchmarking and testing new methods to make sure the employed computational approach provides reasonable and trustworthy results for the system of interest. Additionally, experimental data is sometimes needed as input for calculations. A typical example is using the experimentally determined surface unit cell of a SAM as a starting point for quantum mechanical geometry optimization.

On the other hand, theoretical methods are able to provide additional insight into system quantities which is not accessible via experiments. A good example is the exact molecular structure of a SAM. From experiments one can determine tilt, twist and azimuth angles. However, in simulations the precise position of each atom is known. Another example are measured XP spectra providing averaged information about atomic binding energies. DFT calculations on the other hand provide insight into the atomic core level energies of each individual atom in the unit cell (details see Chapter 5). Another asset of computational methods is the simulation of artificial test systems in "Gedankenexperiments", where effects can be studied individually and other spurious influences can be suppressed by cleverly defining the test system.

Thus, experiment and calculation are able to provide complementary information and benefit from each other. Combining both experimental and theoretical methods in the study of SAMs is surely the best strategy to obtain detailed, realistic and trustworthy information about the system.

1.1.3. Work function and collective electrostatic effects

In general the work function Φ of a metal is defined as the minimum energy (at T = 0 K) needed to remove an electron from a metal that contains N electrons and place it above the surface.[111] The initial state of this transition is a metal containing N electrons in its ground state described by the energy $E(N)$. In the final state of the transition the metal, now containing N-1 electrons, relaxes into its new ground state energy $E(N-1)$, while the one, removed electron now has an electrostatic energy described by the vacuum level E_{vac}. In this definition, the work function is described as the energy difference between the final and initial state of this transition:[111]

$$\Phi = [E_{vac} + E(N-1)] - E(N) \tag{1.1}$$

The energy difference between $E(N-1)$ and $E(N)$ can be expressed by the chemical potential μ, or the Fermi energy E_{Fermi} for finite temperatures. Thus, an alternative expression for the work function is the following:[111]

$$\Phi = E_{vac} - E_{Fermi} \tag{1.2}$$

It was shown that there are two major contributions to the work function for an ideal metal surface.[112] The first is a bulk property, whereas the second is a surface specific energy contribution, caused by the electron density extending beyond the metal surface.[112,113] The electron cloud spills out above the surface up to a certain distance, which creates a negatively charged layer. This in turn gives rise to an

interface dipole with its negative end on top of the metal substrate. This dipole layer raises the electrostatic energy at the interface and generates an additional energetic barrier for extracting electrons from the bulk, thus increasing the work function.

This effect leads to the interesting phenomenon that the vacuum level actually depends on the distance from the metal surface.[114,115] The increased electrostatic energy at the metal surface leads to a slightly higher vacuum level close to the metal substrate, compared to the level at an infinite distance from the surface. For the sake of clarity the vacuum level just above the metal surface will be called E^s_{vac} and the vacuum level at an infinite distance from the substrate E^∞_{vac}. Due to the positive contribution to the electrostatic energy of the surface dipole layer, E^s_{vac} is generally higher than E^∞_{vac} (see Figure 4 of ref. [114]).

The quantity actually measured in experiments (like in UPS secondary cutoff measurements[116]) is E^s_{vac} not E^∞_{vac}.[114] This can be seen clearly as different work functions are measured for different surfaces of the same material.[114] Ref. [117] gives the nice example of a tungston single crystal, where work functions of 4.47 eV, 4.63 eV and 5.25 eV were measured for the (111), (100) and (110) surfaces respectively. A more detailed discussion of this topic can be found in refs [112, 114, 118].

Adsorbing a monolayer onto the substrate changes the work function significantly.[1] This is an effect of the molecular dipoles and the pushback effect. A regular arrangement of similarly oriented dipole moments changes the electrostatic potential in the SAM significantly,[119] which in turn affects the work function of the combined system. All sources of molecular dipoles contribute to this effect, the bond dipole,[28] situated at the substrate-SAM interface, the molecular dipole of the backbone and or embedded groups[24–26] and the terminal unit.[28] This change in potential, caused by dipole moments, depends on so called collective electrostatic effects.[120,121] Heimel et al.[119] showed that an array of dipoles, like in a densely packed SAM of dipolar molecules, causes a sharp drop in electrostatic potential between the substrate side of the SAM and the vacuum side of the SAM, which leads to effectively two different vacuum levels on each side of the SAM. This does not happen for an isolated molecule. The dipole of a single molecule disturbs the surrounding electrostatic potential just locally,[119] as illustrated in Figure 1.1.

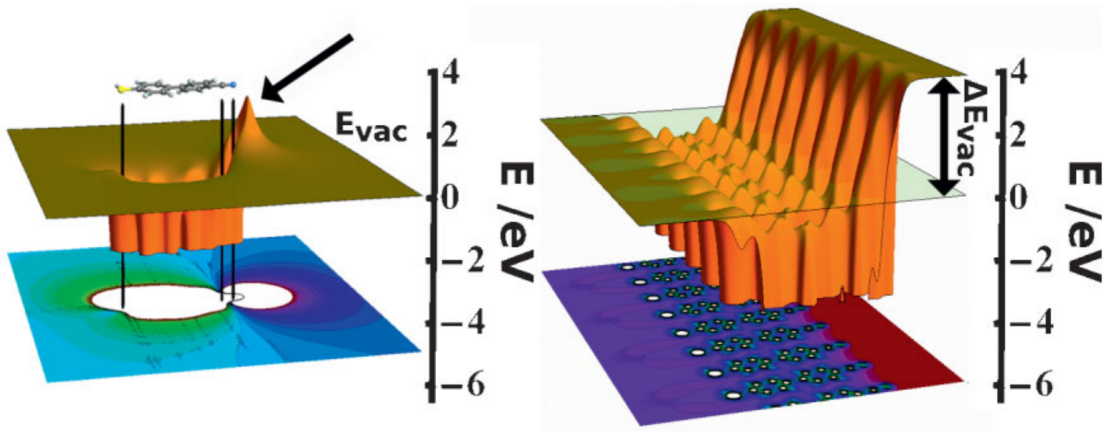

Figure 1.1.: The figure on the left shows the electron potential energy of an isolated biphenylthiol molecule with a terminal cyano group and the corresponding contour plot. The figure on the right shows the electron potential energy (and the corresponding contour plot) of an infinite, densely packed 2D arrangement of the same molecules. The isolated molecule disturbs the potential energy just locally (the black arrow indicating the effect of the polar cyano group), whereas the monolayer shown on the right behaves quite differently. It generates an overall shift of the potential energy due to the arrangement of dipoles. As a result the vacuum energy is different on both sides of the SAM as indicated by ΔE_{vac}. Reproduced with permission from ref. [119], © 2010 WILEY-VCH Verlag GmbH & Co. KGaA, Weinheim.

Furthermore, Natan et al.[122] have studied the decay length of electrostatic fields for isolated dipoles and dense dipole layers. They showed that while the electrostatic field of an individual point dipole reaches very far, the vertical decay length of the electrostatic field of a 2D square array of point dipoles is *"proportional to (and smaller by 2π than) the maximal lateral inter-molecular distance"*.[122] This means that the electrostatic field outside the monolayer decays to zero rapidly and a common, homogeneous electrostatic energy is established.[119,122] These collective electrostatic effects are crucial for describing the systems treated in this thesis and will be discussed in more detail in Chapters 5 to 7. They play an essential role in the interpretation of calculated and measured data, as will be explained in the respective Chapters.

A second collective electrostatic effect is the mutual depolarization of neighboring molecules with aligned dipole moments.[122,123] Each dipolar molecule is affected by the electrostatic field created by its neighbors, which leads to a decrease in the molecule's own dipole moment. This effect can be quite significant and is highly coverage dependent.[122,124] The subject of depolarization in SAMs and its impact on metal-organic interfaces is discussed in detail in the reviews [119, 122, 123, 125] and the original articles [120, 126, 127]. As shown in the above mentioned reviews, depolarization plays a crucial role in the electrostatic situation in a SAM. However,

it stands to reason that, depending on the specific SAM, depolarization could also have a significant impact on the molecular geometry and arrangement inside the SAM. This investigation is the topic of Chapter 8 of this thesis.

1.2. Systems investigated in this work

1.2.1. Alkyl thiolates with embedded dipolar ester groups

The primary systems of interest in this thesis are SAMs of alkyl thiolates with embedded dipolar ester groups on Au(111) substrate. The molecules studied have a thiol docking group, with which they bind dissociatively to the gold substrate. The molecular backbones consist of alkyl chains of varying lengths. As a terminal group they exhibit a plain CH_3 unit without any special functionalization. Instead, the alkyl backbone is modified by inserting a functional group, namely an ester group, which exhibits a significant dipole moment of 1.85 Debye[25] which is oriented at an angle of 101° from the (α-carbon) - (carbonyl carbon) bond axis (see Figure 1 of ref [25]). This inserted dipole effectively divides the backbone into two distinct segments: the bottom segment below the ester group and the top segment above (see Figure 1.2).

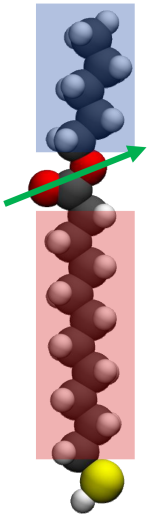

Figure 1.2.: Schematic depiction of a C10EC5 molecule (naming convention see below) with the green arrow indicating the orientation of the electric dipole moment introduced by the ester group. The ester dipole separates the molecule into two distinct parts: the bottom segment below the ester group (marked in red) and the top segment situated above the ester group (marked in blue).

As will be shown in Chapters 5 and 6, this electrostatic separation has significant influence on the properties of SAMs consisting of molecules of this type. They behave quite differently from SAMs of pure alkyl thiolates without embedded groups.

On top of the electrostatic implications, the ester group introduces a kink in the molecule, meaning the top alkyl segment is tilted ≈9° with respect to the bottom alkyl segment.[25]

The naming convention used for the molecules in this work is the following: number of carbon atoms in the bottom segment - E - number of carbon atoms in the top segment, e.g. C10EC5 for a molecule with ten carbon atoms in the bottom segment below the ester group and five carbon atoms in the top segment above the ester group (as shown in Figure 1.2).

A so-called reverse ester system is also studied in this thesis. It is named C10E*C10. This molecule is the same as the regular C10EC10 molecule except for the orientation of the ester group. In the reverse configuration, the ester is inserted 'upside - down' into the backbone, which reverses the orientation of the dipole moment, although not the absolute value (details about this system are given in Chapter 6).

SAMs of alkyl thiolates with embedded ester groups have already been subject of a thorough experimental study,[25] which revealed interesting properties, yet not all measured data could be interpreted at the time. This motivated us to revisit these systems in a theoretical investigation, employing density functional theory and molecular dynamics simulations, as well as comparing our theoretical data with new, additional, experimental results.

The feature that makes these systems interesting, namely the embedded functional group introducing an off-axis dipole moment also renders the data interpretation quite difficult and complex. The precise dipole orientation (and therefore also the electrostatic potential inside the SAM, which in turn influences atomic core level energies and the system's work function) depends sensitively on the exact tilt and twist angle of the molecules. Not only is there a strong dependence on these two individual quantities, but the combination of the two is paramount. Changing the twist angle slightly, while leaving the tilt angle fixed will already alter the orientation of the dipole moment drastically (as will be discussed in detail in Chapter 6). These effects in turn also affect the packing structure of the molecule concerning herringbone or non-herringbone packing structures. Additionally, the long, flexible alkyl backbones allow the molecules lots of degrees of freedom to move and reorient, yielding a highly complex configurational space. All these influences make this type of system a highly complex, and therefore most interesting and rewarding one to study. Detailed results of investigations of these alkylthiols with embedded ester groups and their according SAMs are described in Chapters 5, 6 and 8.

1.2.2. Pyrimidine-substituted terphenyls

The second group of systems that was studied in this thesis are terphenyl based SAMs on Au(111) substrates. These aromatic molecules basically consist of three phenylene rings and a thiol docking group to bind to the gold substrate. A dipolar element is introduced by substituting the middle phenylene ring by a pyrimidine

unit, which has a dipole moment of 2.3 Debye.[128,129] The orientation of the dipole moment depends on the positions of the nitrogen atoms in this pyrimidine unit. The dipole moment is oriented along the molecular axis in both cases, but it points toward the docking group and the substrate in one case (named TP1-down) and in the opposite direction, away from the thiol group and the substrate in the other case (named TP1-up). The naming convention chosen in this work follows the orientation of the pyrimidine dipole.

As a reference system a pure terphenyl molecule without pyrimidine substitution is used (named TP1). The chemical structures of all three molecules are depicted in Figure 1.3.

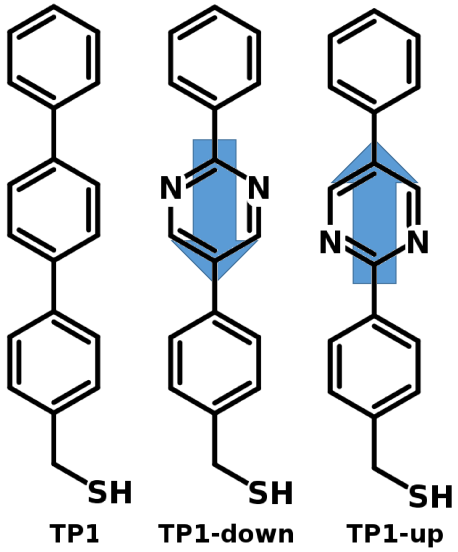

Figure 1.3.: Chemical structures of the three terphenyl-based molecules studied in this work. The reference molecule TP1, without a dipolar middle ring is shown on the left. The molecules, functionalized with an embedded dipolar pyrimidine unit are shown next to it. The pyrimidine unit is inserted in both possible orientations, thereby determining the dipolar orientation, indicated by the blue arrows. TP1-down has a dipole moment pointing along the molecular axis towards the docking group, whereas the dipole moment of TP1-up is oriented in the exact opposite direction.

The TP1 molecule is the ideal reference case, because it is practically identical to the functionalized TP1-up and TP1-down molecules, save for the dipolar central unit. It has the same docking group and adsorption site on the substrate, the same molecular shape and the same terminal group. These similarities give rise to the same packing structure in the three SAMs (including packing density, tilt and twist angles of the molecules).[26] The lack of structural differences in the three described SAMs makes this trio of molecules an ideal case to study the influence of embedded dipolar units on electronic properties of the SAM without any spurious effects due to structural differences in the compared monolayers. An interesting, combined theoretical and experimental study on these systems was already performed by Abu-

Husein et al.[26] We decided to further investigate this set of molecules with special focus on the properties of mixed monolayers which have not been studied in the initial publication.[26]

These systems represent an ideal possibility to investigate the influence of mixing molecules with oppositely oriented dipolar units in a SAM, or of diluting the effective dipole density by creating mixtures of TP1-up/down molecules with TP1 molecules. In the latter case the structure of the SAM remains intact as the TP1 molecules stabilize the monolayer, but the effective dipole density is reduced. The results of these investigations are described in Chapter 7.

An advantage of SAMs of these aromatic molecules over the aliphatic SAMs with embedded dipolar ester groups described above is the relative structural simplicity of terphenyl-based SAMs. Compared to the long, flexible alkyl chains, the TP1, TP1-up/down molecules are quite unflexible due to their rigid backbones. They do not have so many degrees of freedom to reorient in the SAM. Producing mixed SAMs of ester containing and non-containing alkyl thiols would be quite challenging. The molecular arrangement inside mixed SAMs would be near certainly not identical to the structure of pure SAMs, which makes data interpretation unnecessarily complicated. The aromatic molecules described here, on the other hand, allow the formation and investigation of extremely well defined mixed SAMs over a wide range of mixing ratios. These well defined and characterized systems offer the possibility to study dipolar effects in mixed SAMs without spurious influences caused by structural differences in the films.

2. Molecular dynamics

A number of good textbooks about the intricacies of molecular dynamics simulations are available to the interested reader. For the writing of this thesis the following have been found helpful and were used for compiling the following chapter: [130–133].

Molecular dynamics (MD) is a simulation method based on solving Newton's classical equations of motion that is used to simulate large systems, consisting of up to several thousands of particles. It is currently widely applied in various scientific fields of research.[134,135] In molecular biology MD is employed to investigate the structural form and folding of proteins,[136–138] for modeling lipid bilayers,[139–141] especially their properties as the constituents of cell membranes[142–145] and for investigating the structure and functionality of ionic channels in cell membranes.[146–148] Even entire viruses have already been described with MD simulations.[149–151] Molecular dynamics is also used in the simulation of nucleic acids in the investigation of DNA sequences.[152,153] Another, closely related application is pharmaceutical research, where MD is used for the development of new drugs[154–157] which typically consist of small organic compounds. But molecular dynamics has also found applications outside of the field of biology and medicine, foremost in the study of crystal structures for bulk materials,[158–160] liquid crystals,[161,162] thin films and self-assembled monolayers.[163–169]

With molecular dynamics, systems containing over 100,000 atoms can be simulated for time frames of tenths of nanoseconds.[134,135] These system sizes and time spans are far beyond the possibilities of current quantum mechanical (QM) calculations, but can still be treated with force field based MD with manageable computational effort.

However, interactions on a molecular and atomistic scale are dominated by quantum mechanical phenomena. Classical equations of motions, which are the basis of MD simulations do not include any QM effects per se. So to be able to describe large systems on the atomic and molecular level with enough accuracy, atomic interactions are modeled by so-called force fields. They are a compromise between accurate modeling and computational efficiency. A force field is a function describing the potential energy of a system combined with an appropriately chosen set of parameters. This set of parameters is generated by fitting to experimental data or ab-initio quantum mechanical calculations and therefore includes QM effects up to a certain point. A more detailed description of force fields and parameter sets is given in Section 2.3.

This clever combination of classical equations of motion with force fields that include a certain degree of QM effects makes molecular dynamics a very powerful tool to study systems, that are too large for a purely quantum mechanical treatment.

2.1. Time integration

This Section is based on refs. [130–133]

The basis of molecular dynamics simulations are Newton's equations of motion

$$m_i\ddot{\mathbf{x}}_i(t) = \mathbf{F}_i(t) = \mathbf{F}_i = -\nabla_{\mathbf{x_i}} V(\mathbf{x}_1, ..., \mathbf{x}_N), \text{ for } i = 1, ..., N \text{ particles}, \tag{2.1}$$

where m_i is the mass of particle i, $\ddot{\mathbf{x}}_i(t)$ is the second derivative of particle i's position, $\mathbf{F}_i$ is the force acting on particle i, which can be expressed as the derivative of the potential $V(\mathbf{x}_1, ..., \mathbf{x}_N)$ created by all surrounding particles in the system. To solve this set of equations for N particles time discretization $t \rightarrow t_n = t_0 + n\delta t$ is introduced by the finite difference method. With this discretization the system of $3N$ differential equations of second order is transformed into a set of $3N$ difference equations. The time discretization is an approximation of the real situation restricting the evaluation of the equations to the specific time steps t_n.

The first derivative of a time dependent function $\mathbf{x}(t)$ can be approximated by the central difference operator, yielding the following result

$$\left(\frac{d\mathbf{x}}{dt}\right)_{t_n} = \frac{\mathbf{x}(t_{n+1}) - \mathbf{x}(t_{n-1})}{2\delta t} \tag{2.2}$$

where the derivative at time step n is determined by the values at the "neighboring" time steps t_{n-1} and t_{n+1}.

Analogously, the following expression approximates the second derivative

$$\left(\frac{d^2\mathbf{x}}{dt^2}\right)_{t_n} = \frac{\left[\frac{\mathbf{x}(t_{n+1})-\mathbf{x}(t_n)}{\delta t}\right] - \left[\frac{\mathbf{x}(t_n)-\mathbf{x}(t_{n-1})}{\delta t}\right]}{\delta t} = \frac{\mathbf{x}(t_n + \delta t) - 2\mathbf{x}(t_n) + \mathbf{x}(t_n - \delta t)}{(\delta t)^2} \tag{2.3}$$

The second derivative of a particle's position with respect to time, however, is an expression for the particle's acceleration $\mathbf{a}(t_n)$. This allows to write down the new particle positions $\mathbf{x}_i(t_n + \delta t)$ using the forces $\mathbf{F}_i(t_n)$ acting on it at time step t_n and the particle's previous two positions $\mathbf{x}_i(t_n)$ and $\mathbf{x}_i(t_{n-1})$. The particle velocities at time step t_n can be calculated again using the central difference operator of Equation 2.2. This updating procedure is called the Verlet algorithm.[170]

A superior updating algorithm is provided by the velocity Verlet approach[170] which updates the velocities at the same time step as the particle positions. The

final set of update equations for the velocity Verlet algorithm is:

$$\mathbf{x}_i(t+\delta t) = \mathbf{x}_i(t) + \mathbf{v}_i(t)\delta t + \frac{\mathbf{F}_i(t)}{2m_i}(\delta t)^2 \tag{2.4}$$

$$\mathbf{F}_i(t+\delta t) = -\nabla_{\mathbf{x}_i} V\left[\mathbf{x}_i(t+\delta t)\right] \tag{2.5}$$

$$\mathbf{v}_i(t+\delta t) = \mathbf{v}_i(t) + \frac{\mathbf{F}_i(t+\delta t) + \mathbf{F}_i(t)}{2m_i}\delta t \tag{2.6}$$

The velocity Verlet algorithm is possibly the most widely employed updating algorithm in molecular dynamics simulations. It is also the method of choice in the LAMMPS[171] code used to perform MD simulations in this thesis.

The choice of an appropriate time step δt is important for the success of an MD simulation. It needs to be small enough, so that the fastest oscillations in the system are still resolved by the time integration. More precisely the relation $\delta t \ll 1/f_{max}$, with f_{max} the highest vibrational frequency in the system should hold. Generally, bond stretching vibrations are the fastest in a system, especially of bonded hydrogen atoms. Bond bending oscillations have lower frequencies. Bond rotations, i.e. oscillations of dihedral angles and other geometrical reorientations happen on an even larger time scale. Therefore, the fastest movements that need to be captured by the time integration method are bond stretching vibrations. For this, a time step of the order of 1 fs is appropriate.

As mentioned above, hydrogen bond stretching oscillations typically happen much faster than oscillations of other, heavier atoms. In order to treat these fast movements without decreasing the overall time step drastically the, so-called SHAKE[172] algorithm can be employed. This method imposes certain constraints on specified atoms during the time integration. Basically, all atoms are moved according to the update regime and the hydrogens are then updated to the appropriate positions according to their "parent" atoms, defined by the equilibrium bond distances and angles.

2.2. Statistical ensembles and thermostats

This Section is based on ref. [173].

In MD simulations one wants to describe physical systems with external constraints imposed, for example fixed particle number, a certain temperature profile or restrictions concerning the pressure of the system. These considerations are handled by choosing different statistical ensembles for the simulation. If the equations of motion are integrated as described in the previous Section 2.1 and the potential V is not explicitly time dependent then a microcanonical ensemble (NVE) is sampled.

In this ensemble the number of particles, the volume and energy of a system are conserved.

For other physical situations other ensembles are appropriate. The most common are the canonical (NVT), conserving the system's temperature T as well as particle number and volume, the grand canonical (μVT), μ being the chemical potential and the isothermal-isobaric (NPT), which is the correct choice if the system's pressure P and temperature T need to be controlled.

The implementation of these different statistical ensembles into MD simulations works by employing so-called thermostats. The simplest thermostat is probably the Berendsen thermostat[174] which controls temperature by directly scaling particle velocities. This thermostat is most often used to describe heating or cooling of a system, while the Nosé-Hoover thermostat[175,176] is predominantly employed to describe a canonical ensemble once the target system temperature is reached. The Nosé-Hoover method is based on coupling a heat bath to the system, which is modeled by introducing an additional degree of freedom to the system's Hamiltonian.[175,176] This basically introduces an imaginary particle with an artificial mass and velocity which represents the heat bath and is coupled to the other particle velocities.

The system's pressure can be controlled by the Berendsen,[174] the Andersen[177] or the Parrinello-Rahman[178] thermostat.

2.3. The force field

This Section follows refs [134, 135] Other recommended books and review articles about force fields and their current development are [179–181].

Basically, one has to distinguish between all-atom and extended, also called united atom, force fields. All-atom force fields explicitly treat all atoms in the system as individual particles. In contrast, in united atom force fields hydrogen atoms are neglected as individual particles. To account for their presence, the nonbonded parameters of the atoms to which the hydrogens are attached are modified accordingly to enable a correct description of their movements. Such united atom force fields are a compromise to computational resources. Nowadays, the most common force fields are all-atom type, treating the movement of hydrogen atoms explicitly.

One further can distinguish between Class I and Class II all-atom force fields. Class II[182–188] is more sophisticated than Class I, including additional higher order terms for angle bending and stretching and/or cross terms.[188–193]

In the following, I will discuss the general structure of a Class I all-atom additive force field on the example of the CHARMM36[194] force field, as this is the main force field used for MD simulations in this thesis. Class II force fields have the same basic structure as Class I type (described below) with a few extra terms added. Thus, the following description is still relevant for the more specialized Class II force fields.

As already mentioned briefly at the beginning of this Chapter, a force field consists

of a potential energy function describing the relation between the system's structure and its total energy, and a set of parameters used in the potential energy function. This combination of functional form and choice of appropriate parameters defines a force field. In fact, the careful and system specific parametrization is the most crucial part of developing a force field for MD simulations.

Parameters are obtained by fitting to experimental data or to ab-initio quantum mechanical calculations. There are several different parametrization philosophies. The main goal can be to create a specific force field, most accurate for describing a restricted number of special systems, which lacks transferability to other systems (for example to describe protein folding,[195] DNA structures[196,197] or cell membranes[198]). On the other hand, one can parametrize a force field so that it is applicable to a wide range of different systems (for example CGenFF[194] for a broad range of small organic molecules), therein losing some accuracy. Both approaches, and combinations thereof, are valid. The decisive factor here is the intended final range of applications of the new force field.

The general functional form of a Class I additive potential energy function is given by the following equation:[135]

$$\begin{aligned} E = & \sum_{bonds} K_b(b-b_0)^2 + \sum_{angles} K_\theta(\theta-\theta_0)^2 + \sum_{\substack{improper\\dihedrals}} K_\phi(\phi-\phi_0)^2 + \\ & \sum_{dihedrals} \sum_{n=1}^{6} K_{\Phi,n}\left[1+\cos(n\Phi-\delta_n)\right] + \\ & \sum_{\substack{nonbonded\\pairs\ i,j}} \epsilon_{ij}\left[\left(\frac{\sigma_{ij}}{|\mathbf{r}_i-\mathbf{r}_j|}\right)^{12} - \left(\frac{\sigma_{ij}}{|\mathbf{r}_i-\mathbf{r}_j|}\right)^{6}\right] + \\ & \sum_{\substack{nonbonded\\pairs\ i,j}} \frac{q_i q_j}{4\pi\epsilon_0|\mathbf{r}_i-\mathbf{r}_j|} \end{aligned} \tag{2.7}$$

Equation 2.7 can be split up into two main contributions, namely the bonded and non-bonded terms. The first four sums make up the bonded interactions, whereas the last two terms describe the non-bonded ones. The individual terms are discussed in the following.

2.3.1. Bonded contributions to the potential

Figure 2.1 graphically depicts the individual bonded contributions to the total energy.

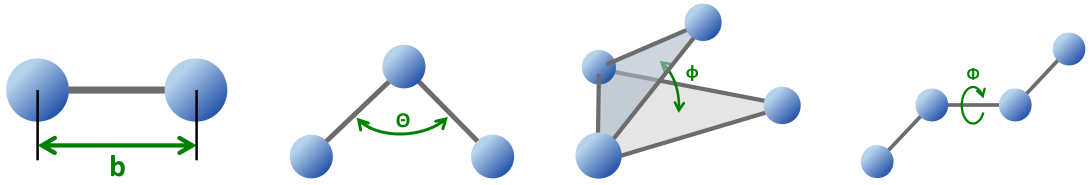

Figure 2.1.: Schematic depiction of the bonded contributions to the potential energy function of Equation 2.7: (a) bond stretching, (b) bond angle bending, (c) out-of-plane bending described by improper dihedral angles and (d) proper dihedral rotation.

Bond stretching, bond angle bending and improper dihedrals

The first two terms of the bonded contributions correspond to variations of the bond length and angle. Both are modeled by a harmonic potential with the equilibrium distance b_0 and equilibrium angle θ_0. K_b and K_θ are the corresponding force constants.[135] The use of such harmonic potentials is sufficient in most cases, where the variables do not deviate too strongly from their respective equilibrium values. When the latter is the case, higher order terms have to be included.

On a side note it should be mentioned that harmonic potentials do not include the possibility of bond breaking, i.e. dissociation of a bond. If such events are to be included into the MD simulation a Morse potential[199]

$$E_{Morse} = D_e \left[1 - e^{-\alpha(b-b_0)}\right]^2 \quad , \tag{2.8}$$

which inherently includes a dissociation energy D_e and equilibrium bond distance b_0 in its functional form, is more suitable.

The third term of the CHARMM[194] force field represents the out-of-plane distortions of molecules, described by improper dihedral angles (as shown schematically in Figure 2.1). It is also modeled by a harmonic potential with the equilibrium dihedral angle ϕ_0 and the force constant K_ϕ.

Dihedral angles

This brief discussion of dihedral angles is based on ref [200].

Dihedral angles describe the out-of-plane rotation of the last of four consecutive, chemically bound atoms (see Figure 2.1). The potential energy associated with this rotation cannot be described by a simple harmonic potential, nor by a Taylor expansion as the energetic barriers for dihedral rotation are usually comparatively low and dihedral angles therefore can vary quite significantly from their equilibrium value. Furthermore, from a geometric perspective the dihedral potential needs to have a 360° periodicity, which suggests some sinusoidal basic form, as also used in

Equation 2.7. There, Φ is the dihedral angle, $K_{\Phi,n}$ is the amplitude and δ_n is the phase for each multiplicity n. The multiplicity n gives the number of maxima and minima present in the potential for one 360° rotation.

2.3.2. Non-bonded contributions to the potential

The non-bonded contributions to the potential energy function are comprised by van der Waals forces (5th term of Equation 2.7) and electrostatic interactions between atoms, which are described by Coulomb forces (6th term of Equation 2.7).

Van der Waals forces

Van der Waals (vdW) forces in MD simulations are typically (as is also the case in Equation 2.7) described by a Lennard-Jones (LJ) potential, with the potential well depth ϵ_{ij} and σ_{ij}, the atomic distance corresponding to the potential minimum. It includes all non-bonded interactions except electrostatic ones and consists of an attractive term (depending on $|\mathbf{r}_i - \mathbf{r}_j|^{-6}$) and a repulsive term, proportional to $|\mathbf{r}_i - \mathbf{r}_j|^{-12}$. The attractive interaction is due to so-called London dispersion forces[200–204] which describe fluctuations of molecular dipole moments, which induce dipoles in neighboring molecules. The dipole fluctuations average to zero overall, but locally they cause attractive interactions between original dipoles and induced dipoles, which decrease with molecular distance to the power of six.

The repulsive term is due to Coulombic and Pauli repulsion. It should be stated that the distance dependence of this term, namely $|\mathbf{r}_i - \mathbf{r}_j|^{-12}$, is chosen for computational reasons. The $|\mathbf{r}_i - \mathbf{r}_j|^{-6}$ dependence for the attractive term has clear physical justifications and it is computationally convenient to calculate $|\mathbf{r}_i - \mathbf{r}_j|^{-12}$ as the square of $|\mathbf{r}_i - \mathbf{r}_j|^{-6}$.[135] A more accurate choice would be a $|\mathbf{r}_i - \mathbf{r}_j|^{-9}$ dependence for the repulsive part.[134] Alternatively, a Buckingham potential[205] can be used

$$E_{Buck} = A_{ij} e^{-B_{ij} r_{ij}} - C_{ij} r_{ij}^{-6} \ , \tag{2.9}$$

which replaces the repulsive power law by an exponential dependence on the particle distance r_{ij}. These and other alternative treatments of the repulsive term[134] describe the repulsive part more realistically than the LJ-term used in a standard Class I force field. It has to be stated though that the standard LJ description is quite adequate for most simulations of biomolecules and organic compounds around room temperature.[134]

The two parameters of the vdW potential, ϵ_{ij} and σ_{ij}, are typically provided as parameters for one atom type ϵ_i and σ_i and are then combined to create the ϵ_{ij} and σ_{ij} parameters used to describe interactions between different atom types.[134] The most common mixing rules employ the geometric mean or the arithmetic mean. The

CHARMM36 force field uses the geometric mean for the well depth[134]

$$\epsilon_{ij} = \sqrt{\epsilon_i \epsilon_j} \ , \tag{2.10}$$

and the arithmetic mean for the minimum energy distance:[134]

$$\sigma_{ij} = \frac{\sigma_i + \sigma_j}{2} \tag{2.11}$$

Transferring parameters between force fields that employ different mixing rules is not recommended.[134]

Electrostatic interactions

Electrostatic interactions are modeled by Coulomb forces between partial charges assigned to each atom. This is also what is meant by "additive" force field. Electrostatic interactions are treated as an additive term to the rest of the potential energy function.[134] In Equation 2.7, q_i and q_j denote the partial atomic charges, ϵ_0 is the electric permittivity of vacuum and $|\mathbf{r}_i - \mathbf{r}_j|$ is the distance between atoms i and j. Coulomb forces, with their $1/r$ dependence, are long-range interactions, which makes their calculation quite difficult. Essentially, the interaction between all atom pairs in the system needs to be calculated for each simulation step. This is prohibitively computationally demanding. Therefore, special computational routines are employed to treat different short- and long-range atomic interactions as will be briefly discussed in Section 2.3.3.

Assigning point charges to each atom, which can be treated in a simple additive Coulomb term, is a huge simplification of the actual situation, but it was computationally necessary for a long time. Typically the atomic point charges are calculated for an individual molecule in vacuum on a quantum mechanical level, and are then used in the MD simulation.[134]
This rather crude approximation wrongly assumes that firstly the atomic charges of an isolated molecule are the same as for a molecule inside a densely packed layer. This is not true, as depolarization plays an important role in SAMs, significantly decreasing molecular dipole moments.[119,124]

Secondly, this approach is inaccurate for systems with regions of different dielectric properties like lipid bilayers.[135]

Thirdly, the fixed point charge approach implicates that atomic charges remain the same throughout the entire MD simulation, which is also not the case as polarization phenomena depend on the precise molecular geometry and packing configuration at each time step. This is especially relevant if molecular processes are to be simulated, a prominent example being the field of molecular biology, where the function of ionic channels in cell membranes or the workings of lipid bilayers in general is studied.[134,181]

There is a general agreement in the MD community that the explicit inclusion

of polarizability is the next necessary step to improve the quality and accuracy of MD simulations even further.[134,135,181] To this aim, so called polarizable force fields are currently under development. There are several different approaches, varying in accuracy, computational cost and applicability to different systems. The topic of treating polarization phenomena in molecular structures, the available methods to do so, and the implications on simulation results are the subject of Chapter 8, where further information is given.

2.3.3. Computational methods to treat non-bonded interactions

Short-range interactions

This Subsection is based on refs [133, 206]

Short-range interactions can be tackled by introducing so-called neighbor lists and cutoff radii, up to which atomic interactions are considered. Employing a cutoff radius reduces the number of actual evaluations of the specific energy term. However, the simulation still needs to check each atom position individually, to find out whether atom j is within the cutoff radius of atom i. This is still highly computationally demanding. This issue can be addressed by introducing Verlet lists and the linked-cell method. The Verlet list method is based on constructing lists for each atom, including all neighboring atoms within a certain cutoff radius. Contributions to the potential energy term only have to be calculated for atoms within the lists. However, the lists need to be updated in every time step to keep track of atoms moving out of one "neighborhood" and into another.

Therefore, the linked-cell method is preferable for large system sizes. It is based on dividing the simulation cell into smaller units, called bins and keeping lists of which particles are situated in which bins. To evaluate pairwise interactions for each atom only particles in the same bin plus a limited number of neighboring bins have to be considered. This reduces the computational demands of evaluating pairwise interactions significantly.

The combined use of Verlet lists and the linked-cell method is even faster than the individual methods on their own. In this way, pairwise interactions are calculated using Verlet lists and linked cells are employed to update these Verlet lists. This reduces the computational effort compared to a pure linked-cell method, because only a small fraction of the atoms in neighboring bins are actually within the cutoff radius of the considered, original atom in the central bin.

Long-range interactions

This Subsection is based on refs [133, 206].

The above described linked-cell and Verlet list methods cannot be employed to treat long-range potentials like the Coulomb potential as they cannot simply be truncated at a cutoff radius. The contributions from far away atoms are still too significant to neglect. An additional difficulty in treating the Coulomb potential is its strong variation at small distances. The basic concept employed to computationally treat the Coulomb potential in MD simulations is to divide it into two additive parts, a possibly strongly varying short-range term and a smoother long-range part. Then both parts are treated with different, suitable methods. To be precise, for the short-range part the particle-particle method is used, employing once again the linked-cell method described above in real space. The long-range term on the other hand is tackled by transition into reciprocal space using a Fourier transformation, where it can be more easily solved using just a few **k**-vectors. This imposes the condition on the long-range term that it must be a smooth function and involve only slow variations at all distances.

This separation into two terms which are solved individually in real and reciprocal space, is the basis of the so-called particle-particle particle-mesh (P3M or PPPM) method[206,207] which is one of the most widely employed approaches to treat Coulomb interactions in MD simulations. The LAMMPS[171] code, employed in this thesis, also makes use of the P3M method to calculate Coulombic pairwise particle interactions.

2.4. Details of molecular dynamics simulations specific to this work

In the following, some specific details of the MD simulations presented in this work are given.

For MD simulations of alkyl thiolates on Au(111) substrate ten layers of gold are used to simulate the surface plus underlying bulk metal. The gold atoms are kept fixed during the simulation run. The system is treated with periodic boundary conditions in x- and y-direction. The LAMMPS[171] code (version 14 Feb 2013) is used to perform all MD simulations. It uses the velocity Verlet[170] algorithm for time integration in time steps of 1 fs, with the SHAKE[172] algorithm employed to treat hydrogen atoms. Long-range interactions are treated with the particle-particle particle-mesh (P3M) method.[206] For heating and cooling phases an NVE ensemble together with a Berendsen[174] thermostat is employed. To describe the system in equilibration phases, when the target temperature is reached an NVT ensemble in combination with a Nosé-Hoover[175,176] thermostat is used.

2.4.1. Partial atomic charges

Partial atomic charges, needed to calculate pairwise Coulomb interactions (as described in Section 2.3) are assigned according to the ESP charge partitioning scheme.[208,209] This method fits point charges to the atoms in a molecule so that the electro-

static potential at points around the molecule (defined by the Merz-Singh-Kollman scheme[208,209]) is reproduced. This calculation of atomic partial charges is carried out with the Gaussian09[210] code making use of the B3LYP functional[211–214] and an aug-cc-pVTZ basis set.[215–218] Finally the charges of indistinguishable atoms, like two hydrogens bound to one carbon atom in an alkyl chain are assimilated manually by using the mean value of the two calculated individual atomic charges for both.

In the MD run the hydrogen of the thiol group is removed as the molecules bind dissociatively to the gold substrate. To avoid treating molecules with a net charge the calculated partial atomic charge of this hydrogen is added to the partial charge of the sulfur atom in the MD input file.

2.4.2. Force fields

For most atomic interactions the CHARMM36 general force field "CGenFF"[194] (version 2b7) is used. This force field is parametrized to enable calculations of a diverse range of small organic molecules and drug like compounds.[135,194] To describe the gold-organic interactions the GoIp force field[219] is used. The gold-sulfur interaction is also described by a special force field, since the possibility of dissociation of the Au-S bond needs to be taken into account. The SAM molecules should be allowed to move freely on the Au(111) surface during the MD simulation, which necessitates the use of a breakable Au-S bond. This is provided by the force field developed by Jang et al.[220] which is based on a modified Buckingham potential. For the Au-S interaction a cutoff radius of 12 Å is chosen for pairwise contributions. The Lennard-Jones potential used in the CHARMM force field is assigned an inner and outer cutoff radius of 12 Å and 14 Å.

3. Density functional theory

In theoretical chemistry and solid state physics the aim is most often to describe the electronic structure of some complex many-body system, e.g. of individual molecules, monolayers or bulk structures. For an accurate description of these systems at atomic levels a quantum-mechanical approach is essential. However, treating such large systems of hundreds of atoms with state of the art wavefunction based methods is computationally challenging if not impossible. Density functional theory (DFT), in contrast, relies on the fundamental principle that any ground state system property can be expressed as a functional of the ground state electron density $n_0(\mathbf{r})$. With this basic approach the whole system can be described with only one scalar function of 3 spatial coordinates instead of having to consider $3N$ variables for a system of N electrons, as in wavefunction based methods.

This significant difference has made DFT the standard method of choice for investigating molecular systems on a quantum-mechanical level. Theoretical solid state physics employing DFT has developed into an incredibly large and diverse field enabling amazing insights into the electronic structures of numerous systems. In combination with experimental methods, DFT has been paramount in the investigation of molecular assemblies and their structural and electronic properties.

A lot of recommendable literature describing DFT in every detail and special aspect is available. Thus, in the following only the very basic aspects of DFT will be discussed. For a more detailed description the reader is referred to any one of the vast number of comprehensive textbooks about DFT. For the writing of this thesis the following references have been consulted and were found to be very instructive and helpful: [221–224] together with the brief but concise summary of density functional theory given in [225]. Additionally, the original articles of Hohenberg and Kohn [226], Kohn and Sham [227] and Kohn's nobel lecture [228] are recommended.

3.1. Basics of density functional theory

This Section 3.1 is based on refs [221, 223, 224].
For additional aspects, not discussed in these books, individual references are provided.

3.1.1. Schrödinger equation and Hamiltonian

The time-independent Schrödinger equation for a many-electron wave function Ψ,

$$\hat{H}\Psi(\mathbf{r}_1, ..., \mathbf{r}_N, \mathbf{R}_1, ..., \mathbf{R}_M) = E\Psi(\mathbf{r}_1, ..., \mathbf{r}_N, \mathbf{R}_1, ..., \mathbf{R}_M) \tag{3.1}$$

is the basis of most theoretical approaches in chemistry and solid state physics. It describes the system with the help of the Hamiltonian $\hat{H}$ for an interacting system of M nuclei and N electrons, which are situated at positions $\mathbf{R}_I$ and $\mathbf{r}_i$ respectively:

$$\hat{H} = \frac{\hbar^2}{2m_e}\sum_{i=1}^{N}\nabla_i^2 - \frac{\hbar^2}{2M_I}\sum_{I=1}^{M}\nabla_I^2 - \sum_{i=1}^{N}\sum_{I=1}^{M}\frac{Z_I e^2}{|\mathbf{r}_i - \mathbf{R}_I|} + \frac{1}{2}\sum_{i=1}^{N}\sum_{\substack{j=1\\ j\neq i}}^{N}\frac{e^2}{|\mathbf{r}_i - \mathbf{r}_j|} + \frac{1}{2}\sum_{I=1}^{M}\sum_{\substack{J=1\\ J\neq I}}^{M}\frac{Z_I Z_J e^2}{|\mathbf{R}_I - \mathbf{R}_J|} \tag{3.2}$$

In Equations 3.1 and 3.2 upper case indices correspond to properties of nuclei, while lower case indices describe electronic properties.

In Equation 3.2 the first two terms describe the kinetic energy of the electrons and nuclei respectively. The following terms give the electrostatic interactions between (i) electrons and nuclei (attractive) (ii) electrons and electrons (repulsive) and (iii) nuclei and nuclei (repulsive).

At this point the Born-Oppenheimer approximation[229] can be used to simplify the Hamiltonian. This approximation concerns the second term of Equation 3.2. As the nuclei are much heavier than the electrons, and thus move much more slowly, electron and nucleus movements can be separated. Electrons are essentially described as moving in the field created by nuclei at "fixed" positions in space. In this way the kinetic energy term of the nuclei is eliminated from Equation 3.2. Also, the electrostatic interaction between nuclei yields a significant, but constant term, so it will not be included explicitly in the following considerations.

The remaining Hamiltonian for the electronic system consists of only three terms

$$\hat{H} = \hat{T} + \hat{V}_{ext} + \hat{V}_{int} \ , \tag{3.3}$$

with the kinetic energy operator for the electrons $\hat{T}$, the external potential acting on the electrons $\hat{V}_{ext}$ (created by the nuclei) and the electron-electron interaction $\hat{V}_{int}$.

With the Born-Oppenheimer approximation the original Schrödinger equation has been reduced to its electronic part. However, the many-electron wavefunction still depends on $3N$ variables for N considered electrons. These are still far too many variables to consider for actually interesting physical systems consisting of hundreds of atoms. A step towards addressing this issue is made by the Hohenberg-Kohn theorems described next.

3.1.2. The Hohenberg-Kohn theorems

Theorem I[221] states that the external potential $V_{ext}(\mathbf{r})$ of Equation 3.3 is uniquely defined by the ground state particle density $n_0(\mathbf{r})$ (except for a constant). As the external potential determines the many-body wavefunction for all states of the system, this means that *"all properties of the system are completely determined given only the ground state density $n_0(\mathbf{r})$"*.[221]

Theorem II[221] states that a universal functional for the energy $E[n]$ can be defined by the electron density $n(\mathbf{r})$, which is valid for any external potential $V_{ext}(\mathbf{r})$. This functional allows to determine the exact ground state energy and density of the system by the variational principle. The ground state electron density is the one that minimizes the functional $E[n]$.

The important assertion of the Hohenberg-Kohn theorems is that the ground state electron density alone determines all properties of a system. Thus, one can describe the whole interacting system with the electron density, which depends on only 3 variables instead of $3N$.

It follows from theorems I and II that the total energy of the system can be expressed as a functional of the electron density $n(\mathbf{r})$

$$E[n] = T[n] + E_{int}[n] + \int d^3r V_{ext}(\mathbf{r}) n(\mathbf{r}) \tag{3.4}$$

$$= F_{HK}[n] + \int d^3r V_{ext}(\mathbf{r}) n(\mathbf{r}) \ , \tag{3.5}$$

in which the Hohenberg-Kohn functional

$$F_{HK}[n] = T[n] + E_{int}[n] \tag{3.6}$$

is defined. It includes all internal energies, both kinetic and potential, of an interacting electron system. The remaining term of Equation 3.4 describes the interaction of the electron density with the external potential $V_{ext}(\mathbf{r})$ created by the nuclei. The Hohenberg-Kohn functional $F_{HK}[n]$ is universal by construction, meaning it is independent of the external potential and valid for any interacting system of electrons. The ground state energy E_0 of a system can, in principle, be found by minimizing the energy functional with respect to the electron density. The corresponding density, yielding the minimum energy is then the ground state electron density $n_0(\mathbf{r})$.

This minimization can be treated as a two-step process as considered by Levy and Lieb.[230–234] This consideration also provides an alternative definition of the universal functional and is quite instructive. For this reason the next subsection gives a brief overview of the Levy-Lieb approach.

Levy-Lieb formulation of the universal functional

We start again with the total energy of a system, given by the expectation value of the Hamiltonian, in this case:

$$E = \frac{\langle\Psi|\hat{H}|\Psi\rangle}{\langle\Psi|\Psi\rangle} = \langle\hat{H}\rangle = \langle\hat{T}\rangle + \langle\hat{V}_{int}\rangle + \int d^3r V_{ext}(\mathbf{r})n(\mathbf{r}) \tag{3.7}$$

Minimizing the energy with respect to all variables in the wavefunction Ψ yields the ground state. The idea of Levy and Lieb was to split up the minimization into two parts. First one only considers wavefunctions, which all produce the same electron density $n(\mathbf{r})$ and minimizes over those wavefunctions:

$$E_{LL}[n] = \min_{\Psi\to n(\mathbf{r})}[\langle\hat{T}\rangle + \langle\hat{V}_{int}\rangle] + \int d^3r V_{ext}(\mathbf{r})n(\mathbf{r}) \tag{3.8}$$

$$= F_{LL}[n] + \int d^3r V_{ext}(\mathbf{r})n(\mathbf{r}) \tag{3.9}$$

Equation 3.9 defines the Levy-Lieb functional

$$F_{LL}[n] = \min_{\Psi\to n(\mathbf{r})}[\langle\hat{T}\rangle + \langle\hat{V}_{int}\rangle] \tag{3.10}$$

This first minimization step finds the wavefunction corresponding to the energy minimum for every considered electron density $n(\mathbf{r})$. In the second step of the Levy-Lieb approach the energy functional $E_{LL}[n]$ can then be minimized with respect to the electron density. The one electron density, which minimizes the energy functional is the ground state density, and the minimum energy value represents the ground state energy.

The Levy-Lieb formulation is thus a restatement of the Hohenberg-Kohn functional. It also clarifies the meaning of the universal functional in the form of Equation 3.10 as *"the minimum of the sum of kinetic plus electronic interaction energies for all possible wavefunctions having the given density $n(\mathbf{r})$"*.[221]

Secondly, the two-step minimization approach shows a way, in which the exact universal functional could be determined in principle.

In practice however, neither the Hohenberg-Kohn theorems nor the Levy-Lieb formulation provide a practical way to solve the interacting electron problem. This is where the Kohn-Sham ansatz comes into play, which is discussed in the next Section.

3.1.3. The Kohn-Sham approach

In the Kohn-Sham approach, suggested by Walter Kohn and Lu Sham in 1965[227] the complex interacting many-body system is replaced by an auxiliary non-interacting electron system. The Kohn-Sham ansatz assumes that there is an auxiliary system

which has the same ground state electron density as the original, interacting one. With the use of this transition the problem is simplified to treating independent-particle equations with all complicated many-body terms included into a so-called exchange-correlation functional.

Thus, the functional of the total energy can be written in the following form

$$E[n] = T_S[n] + \int d^3r V_{ext}(\mathbf{r}) n(\mathbf{r}) + E_{Hartree}[n] + E_{xc}[n] \ , \tag{3.11}$$

where $T_S[n]$ is the kinetic energy functional of the non-interacting auxiliary system and $E_{Hartree}[n]$ describes the classical Coulomb interaction energy of the electron density $n(\mathbf{r})$ with itself:

$$E_{Hartree}[n] = \frac{1}{2} \int d^3r d^3r' \frac{n(\mathbf{r}) n(\mathbf{r}')}{|\mathbf{r} - \mathbf{r}'|} \tag{3.12}$$

Equation 3.11 defines the exchange-correlation functional $E_{xc}[n]$, which includes all many-body effects not described by the other three terms

$$E_{xc}[n] = F_{HK} - (T_s[n] + E_{Hartree}[n]) \tag{3.13}$$

$$= \langle \hat{T} \rangle - T_s[n] + \langle \hat{V}_{int} \rangle - E_{Hartree}[n] \ , \tag{3.14}$$

where the definition of the Hohenberg-Kohn functional $F_{HK}[n]$ of Equations 3.5 and 3.6 was used. Equation 3.14 shows that the exchange-correlation functional is the difference in kinetic and potential terms between the interacting and non-interacting system, where the electron-electron interactions have been replaced by the Hartree term.

By minimizing the total energy functional with respect to electron density one ends up with the non-interacting single-particle Kohn-Sham equations

$$\hat{H}_{KS} \Psi_i(\mathbf{r}) = \epsilon_i \Psi_i(\mathbf{r}) \ , \tag{3.15}$$

with the Kohn-Sham Hamiltonian

$$\hat{H}_{KS} = -\frac{1}{2} \nabla^2 + V_{KS}(\mathbf{r}) \ , \tag{3.16}$$

which includes the effective Kohn-Sham potential $V_{KS}(\mathbf{r})$:

$$V_{KS}(\mathbf{r}) = V_{ext}(\mathbf{r}) + \int d^3r' \frac{n(\mathbf{r}')}{|\mathbf{r} - \mathbf{r}'|} + \frac{\delta E_{xc}[n(\mathbf{r})]}{\delta n(\mathbf{r})} \tag{3.17}$$

$$= V_{ext}(\mathbf{r}) + V_{Hartree}(\mathbf{r}) + V_{xc}(\mathbf{r}) \tag{3.18}$$

The electron density $n(\mathbf{r})$ is connected to the Kohn-Sham wavefunctions Ψ_i by:

$$n(\mathbf{r}) = \sum_{i}^{N} |\Psi_i(\mathbf{r})|^2 \tag{3.19}$$

To solve the Kohn-Sham equations (3.15) one requires the Kohn-Sham potential (Equation 3.17), which depends on the electron density via the exchange-correlation functional. The electron density, however, is determined by the Kohn-Sham wavefunctions (see Equation 3.19). Thus, one is faced with a set of single-particle equations, dependent on a potential that must be solved self-consistently with the electron density. In practice, one starts with an initial guess for the density, with which the Kohn-Sham potential is determined. Then the Kohn-Sham equations are solved for this potential, which results in a new electron density, calculated from the new Kohn-Sham wavefunctions. This process is repeated until some convergence criterion is met. The final ground state electron density also determines the ground state energy.

At this point it should be noted that the Kohn-Sham equations describe the interacting system exactly. If the exchange-correlation functional were known, solving the Kohn-Sham equations would lead to the exact solution. In practice, however, approximations for the exchange-correlation interactions are required, the accuracy of which determines the quality of the whole calculation. Consequently, a lot of effort has been put into the development of suitable exchange-correlation functionals. The simplest and yet quite successful and widely applied ones are the local density approximation (LDA) and the generalized gradient approximation (GGA).

3.1.4. Exchange-correlation functionals

In this Section, the two most widely used forms of the exchange-correlation functional, namely the local density approximation (LDA) and the generalized gradient approximation (GGA) are briefly described.

One great advantage of the Kohn-Sham approach is the separation of the non-interacting electron kinetic energy and the long-range Hartree term from the remaining exchange-correlation term. Due to this separation the exchange-correlation functional can be approximated in a *local* form

$$E_{xc}[n] = \int d\mathbf{r}\ n(\mathbf{r})\epsilon_{xc}(n(\mathbf{r}), \mathbf{r})\ , \tag{3.20}$$

where $\epsilon_{xc}(n(\mathbf{r}), \mathbf{r})$ is the exchange-correlation energy per electron at point $\mathbf{r}$, which only depends on the electron density in close vicinity of point $\mathbf{r}$.

The local density approximation (LDA) is based on Equation 3.20, where now the exchange-correlation energy density of the homogeneous electron gas is used as an

approximation for $\epsilon_{xc}(n(\mathbf{r}), \mathbf{r})$:

$$E_{xc}^{LDA}[n] = \int d\mathbf{r}\ n(\mathbf{r})\epsilon_{xc}^{hom}(n(\mathbf{r})) \tag{3.21}$$

The generalized gradient approach[235] goes one step further by not only considering the local electron density, but also taking the gradient of the electron density into account:

$$E_{xc}^{GGA}[n] = \int d\mathbf{r}\ n(\mathbf{r})\epsilon_{xc}(n(\mathbf{r}), \nabla n(\mathbf{r})) \tag{3.22}$$

The Perdew-Burke-Ernzerhof[235,236] (PBE) functional, which was used for calculations in this thesis, also belongs to the GGA class of exchange-correlation functionals.

As a last note it should be stated that, of course, the development of functionals has not stopped with the generalized gradient approach. Ever more precise, yet also computationally more demanding functionals have been developed, among them hybrid functionals like the popular B3LYP[214] and range-separated hybrid functionals,[237] which have proven to be quite successful.

3.2. DFT calculation details specific to this work

For DFT calculations presented in this work the program VASP[238–241] (version 5.3.2) has been used. The code is periodic in all 3 spatial directions. The systems studied in this work, however, are 2D periodic (infinite slabs extended in the x- and y-direction represented by a repeated unit cell). To be able to use the code a large vacuum gap is introduced into the unit cell along the z-axis.[119] With this approach an infinite number of 2D slabs are created along the vertical axis. As the individual layers have different potentials on both sides, a spurious potential gradient is introduced into the system. To compensate this a dipole correction in z-direction is implemented into the VASP code. This, in effect, places a dipole layer at the top of the unit cell, which exactly compensates the potential difference present in z-direction between repetitions of the unit cell (see Figure 3.1). In this way the individual layers are decoupled electrostatically and can be viewed as isolated slabs. The vacuum gaps used for the SAMs described in this work are in the range of 20 Å to 25 Å.

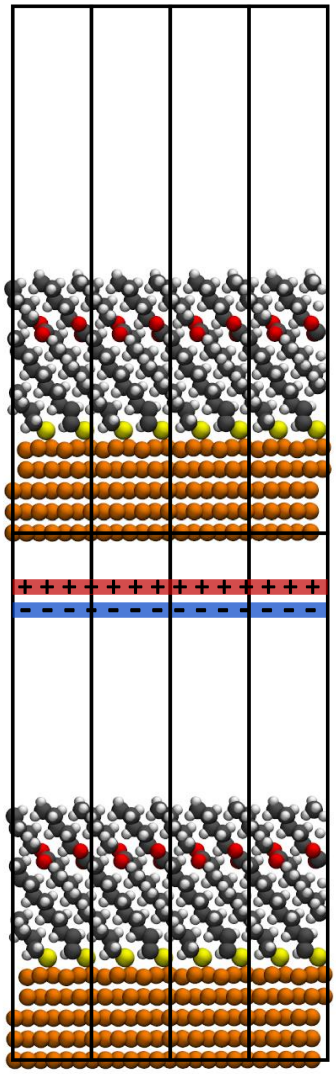

Figure 3.1.: Schematic illustration of the repeated slab approach used to simulate a 2D slab with the 3D-periodic code VASP[238–241]. To decouple the individual layers electrostatically a large vacuum gap is included in the unit cell and a dipole correction is employed during the calculation. This essentially places a self-consistently determined, artificial dipole layer (indicated as red and blue bars) near the top of the unit cell (indicated as black boxes) to compensate the electrostatic field of the slab.

As a sidenote it should be mentioned that this dipole correction is available in VASP for all three spatial directions. A full correction is needed for example for describing an isolated molecule in vacuum. In this case a large unit cell containing just one molecule and no substrate with dipole corrections in x-, y- and z-direction would be the appropriate approach.

To describe exchange-correlation effects, the Perdew-Burke-Ernzerhof[235,236] (PBE)

functional is used. The interaction between core and valence electrons is treated with the projector-augmented wave[242] (PAW) formalism, which is an advancement of the pseudopotential method.[243] Depending on how accurately the region near the core is described, the available PAW potentials are called "soft", "normal/standard" or "hard", the latter being the most precise and, therefore, the computationally most expensive ones. The specific atomic PAW potentials used for individual calculations are given in the respective sections of this work.

In conjunction with the PAW method, VASP uses a plane wave basis set, for which the cutoff energy can be chosen. In this work a cutoff energy of 300 eV is used for soft potentials . In the case of "standard" potentials it is increased to 400 eV. Higher cutoff energies are only used for special tests and are stated explicitly.

Van der Waals interactions are included in the calculation by the vdW^{Surf} method, developed by Ruiz et al.[244] in the implementation of Al-Saidi et al.[245]

To describe the system in reciprocal space an automatic Monkorst-Pack[246] k-point grid is chosen.

The convergence criterion for the total energy in the electronic self-consistent cycle is chosen as 10^{-6} eV. For geometry optimizations the forces between atoms are converged to 10^{-2} eV $Å^{-1}$.

In certain cases the total energy of the unit cell is already converged, while the total z-dipole moment of the cell is not. Accurately calculated dipole moments are however a necessity in further data evaluation. Therefore, an additional convergence check for the dipole moment of the unit cell is introduced and the convergence criterion is set to 10^{-4} eÅ. This dipole convergence loop is a customized addition to VASP used in our working group. It was implemented by Elisabeth Wruß.

3.3. Calculating core level energies within the DFT framework

There are two methods available to calculate core level energies within the DFT framework. The initial state and the final state approach. In the following I will briefly describe the basic principles of both and compare them with respect to usability for the systems studied in this thesis. Finally, I will give the reasons why the initial state method was chosen for calculations throughout this thesis.

3.3.1. The initial state method

The initial state method in VASP is based on a standard DFT calculation, performed with all electrons present in the molecule, where the Kohn-Sham eigenvalues of the core states are recalculated after the charge density of the valence electrons has been

determined in a self-consistent cycle.[247,248] These Kohn-Sham eigenvalues are then interpreted as core level energies.

This is not a completely accurate description of the system (and an XPS measurement process, which we desire to describe), as a molecule with all its electrons present is modeled with this approach. In a real XPS measurement however, an electron is removed from an atomic core shell and a so-called core hole is generated. In the initial state approach the existence of this core hole is ignored.[247,248] This introduces an inaccuracy as the electronic ground state of a molecule with a core hole is different from the ground state of the same molecule with all electrons present.[249]

Secondly, screening effects of the highly polarizable metal substrate are also not explicitly treated in the intial state calculation method.[250,251] This introduces an additional inaccuracy, which mostly affects atoms nearest to the metal substrate as they interact strongest with it.[252] The influence of substrate screening effects on atoms farther away from the interface is already quite weak.

3.3.2. The final state method

If atomic core level energies are calculated using the final state method, a separate DFT calculation is needed for every atom of interest in the unit cell. This is different from the initial state approach, where the core level energies of all atoms in the unit cell can be obtained in one single DFT calculation. This difference stems directly from the underlying methodological approach of the two procedures.

In the final state approach[248,249,253–258] one (or one half of a) core electron is removed from one atom in the unit cell and placed in the valence region[248], which, in the cases treated in this thesis, is described by states in the metal directly above the Fermi energy. Note that by this approach the unit cell remains charge neutral. A DFT calculation is then performed with this electronic configuration in the unit cell. This also explains, why a separate calculation is needed for every atom of interest in the unit cell. An individual DFT run has to be performed with the core electron removed from the one atom in question. The final state approach represents the situation of an XPS measurement more realistically than the initial state method, as the core hole is explicitly included into the calculations in this way. Secondly, screening effects of the metal are also intrinsically treated with this approach.[248,249] Therefore, in principle, binding energies can be calculated more accurately with the final state method than with the initial state approach.

However, for describing the systems of interest in this thesis the final state method has one crucial disadvantage. The very fact that it is more accurate by introducing an actual core hole into the calculation poses the problem. The electron is removed from its atom to the valence region, and a core hole is created. This transfer of charge creates an effective dipole inside the molecule. Dipoles are equally created in real XPS measurements, where photons remove electrons from atomic core shells and a screening charge builds up in the metal substrate. However, in experiments

this happens only to a small fraction of the molecules inside the SAM. In DFT calculations, the infinite 2D array of molecules inside a SAM is described by a small unit cell making use of periodic boundary conditions (see Section 3.2). So if a quantity is modified in the unit cell it is repeated over and over infinitely. Therein lies the problem. Due to the small unit cell size the dipole moment created in one molecule of the unit cell is repeated in every "neighboring" unit cell, which creates an unrealistically high dipole density in DFT calculations compared to the actual situation in an XPS experiment.

As was previously mentioned in Section 1.1, a regular array of dipoles leads to collective electrostatic effects, changing the electrostatic potential inside the SAM, which in turn shifts the atomic core level energies drastically (see Chapter 5).

To avoid this artifact the unit cell size needs to be large enough as to represent the actual electrostatic situation in an XPS experiment. Specifically, the distance between the core hole induced dipoles (which is essentially the size of the unit cell, as only one molecule per unit cell is "assigned" a core hole) would have to be large enough, so that collective electrostatic effects play a negligible role compared to the shifts in core level energies one wants to study. Such unit cell sizes, however, remain far beyond current computational possibilities.

Finally, it should be repeated that the dipolar density does not pose a problem in real life XPS experiments. The artificially high dipole density in calculations is a sole artifact of the use of periodic boundary conditions in combination with the restricted unit cell size and does not represent the actual experimental situation.

3.3.3. Reasons for choosing the initial state method

The inherent inclusion of screening effects of the metal in the final state method is important if one wants to accurately describe atoms near the metal surface[252,253], as in the investigation of surface core level shifts.[254,259] However, in this thesis, only SAMs of long, upright standing molecules are treated. The aim is to compare calculated results with experimentally obtained XP spectra. The XPS signal of atoms, however is damped exponentially with increasing distance of the atom in question from the surface of the SAM.[260] This means, the signal of the lowest lying atoms in the SAM, the ones closest to the metal substrate, and therefore the ones most affected by metallic screening, contribute to the XP signal intensity hardly at all, due to the strong damping effects caused by the monolayer above. Therefore, for the specific systems described in this thesis the advantages of the computationally more sophisticated final state methods are not essentially needed. Additionally, the error introduced by the above mentioned unrealistic dipole density inherent to the final state method renders results obtained with this approach untrustworthy for the systems discussed in this thesis. The slight errors associated with the initial state method on the other hand are acceptable. They do not qualitatively change the results.

Additionally, to make the calculations more realistic, a customized procedure was

developed, which allows to include screening effects of the metal substrate that are neglected in the initial state approach, into our data evaluation. These screening effects are treated in a data-processing step after the DFT calculation is finished. Core-level energies are shifted according to an electrostatic image charge model[261,262] which is described in detail in Chapter 5. XP spectra are then calculated from the individual, screened atomic core level energies as superposed, damped Gaussian functions (details see Chapter 5). To test this method it is applied to two different SAM-substrate systems and the calculation results are compared to measured data. Details of this study can be found in Chapter 5.

This computational procedure to obtain atomic core level energies and XP spectra was also employed for the calculations presented in Chapters 6 and 7.

4. Geometry optimization

To calculate specific system properties one first needs to know the exact molecular geometry and arrangement of the SAM on the substrate. This configuration can be found by employing geometry optimization techniques. As quantum mechanical effects play a crucial role in the systems investigated in this thesis, one cannot neglect them in the geometry optimization procedure. Thus, in this work geometry optimization is performed within the DFT framework. A standard conjugate gradient method[200,263,264] seems suitable for the task and is available within the program packages used in this work.

However, when applying this standard technique of geometry optimization to SAMs of long alkyl thiolates on gold substrate the simulation nearly inevitably gets stuck in some local minimum geometry instead of converging toward the global energetic minimum. In other words, the final geometry of the simulation depends heavily on the starting geometry. This is a dramatic drawback of the method, practically rendering it useless for the systems of interest here. Figure 4.1 shows two examples of such local minimum structures.

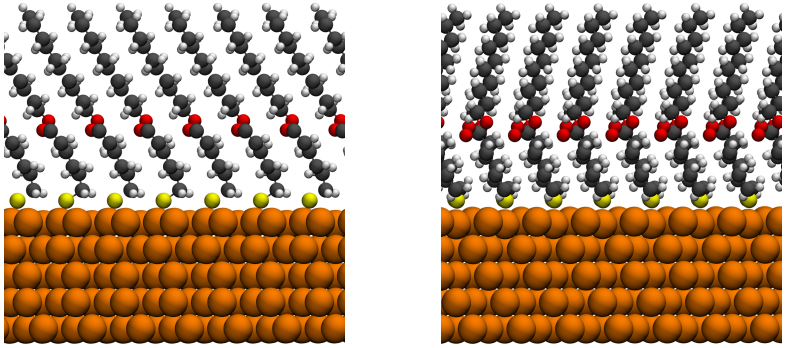

(a) **(b)**

Figure 4.1.: Examlpe of two local minimum geometries obtained with a conjugate gradient procedure for a full coverage C5EC10 SAM. The global minimum structure was not found in both cases. The simulations got stuck in local minima, which heavily depend on the starting geometry. In (a) the molecules show an unrealistic kink at the docking group, while they are strongly bent in (b).

The structure on the left of Figure 4.1 has a kink directly at the docking group, whereas the arrangement on the right shows strongly bent molecules. In these two cases it is quite obvious that the simulation did not converge to the global minimum structure. This might not be the case for all "end geometries".

The reasons why the conjugate gradient method fails for this type of SAM can be found in its structural properties. These SAMs consist of molecules with rather long alkyl backbones, which are highly flexible and can easily twist and bend. On top of that, alkyl thiolates on Au(111) substrate are relatively loosely packed, even at full coverage. There is enough space left in the SAM for the molecules to move quite a lot. In simulations we encounter molecules rotating around their main axis quite freely. They can also change their tilt angle to a certain degree or partially bend over. Cis-trans deformations, also called gauche defects[1,163,164,166,265,266] can also occur in the backbone. This freedom of movement leads to a rather complex potential energy surface (PES) with many local minima. The conjugate gradient method is not specialized to overcome high potential barriers, which is necessary to effectively sample the potential energy surface of these complex systems and reach the global minimum structure. Thus, I found the standard conjugate gradient procedure not effective to find the global minimum structures for the systems presented in this work. Instead the finally obtained geometry heavily depended on the initial starting geometry of the optimization procedure.

A solution to this dilemma is the following: Combining density functional theory with molecular dynamics simulations to access the advantages of both methods. This combined approach is applied for calculations of alkyl thiolates presented in this thesis.

Molecular dynamics is good at sampling the potential energy landscape for several reasons.[200] Firstly it allows the use of larger unit cells than DFT. Secondly one has the option of controlling the temperature of the sample in the simulation. Thus by heating the SAM one can introduce thermal energy into the system and energy barriers can be overcome. Molecules can get out of a present configuration more easily and make larger structural changes during the simulation. Thus the influence of the starting geometry on the outcome of the optimization can be eliminated. Not even the molecular binding sites on the gold substrate have to be predetermined during MD runs. The choice of a suitable force field for the gold sulfur interaction allows the molecules to stay mobile on the substrate. For the calculations presented in this work the force field of Jang et al.[220] was used, as it allows breaking of the gold sulfur bond (for details see Chapter 2). The heating phase in the simulation is followed by an elongated equilibration period at room temperature to allow the system to settle in the minimum geometry at this temperature, which also represents experimental conditions. To remove thermally introduced defects from the SAM, the sample can also be artificially cooled to basically $T = 0\,K$ in the simulations. A customized temperature profile can be introduced for a specific system. Total simulation times of several tens of nanoseconds are possible. Depending on the unit cell size, the computational cost is still reasonable for quite extended simulations.

These are clear advantages of the MD method. However, one has to bear in mind that classical force fields are employed in this method. Still, as already previously

stated, quantum mechanical effects are vital for correctly describing the systems of interest in this work and must not be neglected. Thus for SAMs of alkylthiols, both methods (MD and DFT) are used complementary for geometry optimization. An initial geometry optimization within the MD framework is performed to reach the vicinity of the total global minimum. Then, using the SAM geometry found in this MD simulation as a starting point, a quantum mechanical geometry optimization using density functional theory is performed in a second step. In the following the details of this procedure are given.

4.1. Details of the geometry optimization procedure

In this Section the specific procedure of the geometry optimization combining MD and DFT is described.

The exact parameters (including force fields, functionals, basis sets etc.) used for the individual MD and DFT steps are the same as stated in the respective Chapters 2 and 3. This procedure has been applied for all geometry optimizations of SAMs of functionalized and unfunctionalized alkyl thiolates on gold substrate described in the Chapters 5 and 6. It was not necessary for SAMs of aromatic molecules as described in Chapter 7. Terphenyls are quite rigid molecules compared to the long alkyl thiolates, restricting the molecular movement in the SAM. Additionally, these molecules are packed much more densely at full coverage than alkyl thiolates on gold, thus leaving them even less room to reorient inside a SAM. These two reasons combined explain why a standard quantum mechanical geometry optimization using VASP[238–241] in conjunction with GADGET[267] (described below) is sufficient for the terphenyl SAMs described in Chapter 7. The procedure employed for alkyl thiolate SAMs on gold substrates is described in the following.

The geometry optimization process is started with an MD run using a unit cell containing ten layers of gold substrate with a Au(111) surface on which 16 molecules are placed. All gold atoms were kept fixed throughout the entire simulation. The starting geometry of the molecules is chosen with zero tilt angle and the same random twist angle for all. This arrangement however does not at all influence the outcome of the simulation due to the temperature profile used during the MD run.

The MD process was started at T=0 K with a fast heating phase up to T=750 K over t=0.2 ns to introduce thermal energy and allow the molecules to move freely, also enabling lateral motion on the substrate. This heating phase is followed by a slow cooling to room temperature (T=300 K) over t=1.3 ns with a constant cooling rate and subsequent equilibration at room temperature for t=5 ns. This allows the molecules to find and settle in the minimum energy structure within the used MD framework. At this stage the general molecular arrangement is nearly satisfactory for subsequent DFT optimization, but it is still affected by thermally induced defects. These include bent molecules, cis-trans defects and a certain variation in the twist angles of the molecules. These defects are caused by random motions of

the molecules at finite temperature and are not representative of the ground state described in the subsequent DFT calculations. For the specific application in this work they are an obstacle, as the aim is to use the final configuration for DFT optimizations in which a cis-trans defect, for example, would remain present.

Thus, following the equilibration phase at room temperature, the sample is artificially cooled down to T=5 K to get rid of the defects. This is done quite slowly over a timespan of t=4 ns to give the molecules enough time to straighten out at these low temperatures. The finally obtained geometry creates the starting point for the subsequent DFT geometry optimization.

As the MD unit cell is way too large to be handled in a quantum mechanical DFT calculation, four representative, neighboring molecules are picked from the end geometry obtained with MD and placed on a gold substrate of five layers. The DFT optimization of this smaller unit cell is then performed using VASP[238–241] (version 5.3.2) in conjunction with the program GADGET[267] developed by Tomáš Bučko.

GADGET is a tool that enables optimizing the geometry in internal coordinates instead of cartesian coordinates and offers alternative initial guesses for the Hesse matrix (for this work Fischer's model[268] was used).

Without these features geometry optimization of SAMs of long, flexible alkyl thiolates is not successful as the molecular tilt angles do not deviate from the initial configuration during the course of the optimization procedure. Changing the tilt angle of a whole molecule, or even several, interacting, neighboring molecules in cartesian coordinates means that all atomic (x,y,z) coordinates have to change by rather a big amount in the same geometry step. Such a step is not chosen in optimization algorithms, where mostly small changes from one geometry to the next are made. When the system is treated in internal coordinates, however, altering the tilt angle of a whole molecule requires just one coordinate to change. Such a small variation is a standard step in geometry optimization procedures.

For this reason we have found geometry optimizations performed in cartesian coordinates completely unsuccessful for SAMs of long, upright standing molecules on substrates. Optimizing in internal coordinates using GADGET[267], in contrast, yielded good results for the same systems.

Part II.

Results and Discussion

5. Understanding chemical vs. electrostatic shifts in X-ray photoelectron spectra of organic self-assembled monolayers

In the first part of this thesis the working principle of density functional theory, including the initial and final state methods to calculate core level energies have been presented. In this chapter these methods are applied to the investigation of self-assembled monolayers of alkylthiols, functionalized with dipolar groups. A general procedure to correctly calculate core level energies and XP spectra for these systems in devised and presented. The method is tested on two different SAMs, one including a terminal dipolar unit, while the other one is characterized by an embedded dipolar group. The effects of chemical and electrostatic influences on XP spectra are studied and verified by comparison to experimental data.

This Chapter has been published in the Journal of Physical Chemistry C, see ref [269]. It is reproduced here without changes.

Author Contributions:
The work presented in this chapter was a collaborative effort between Thomas Taucher, Iris Hehn, Oliver Hofmann, Michael Zharnikov and Egbert Zojer and the work was published in the Journal of Physical Chemistry C.[269] Thomas Taucher and I are equally contributing first authors of this publication.

The idea to use partially fluorinated alkylthiolate SAMs and mid-chain ester functionalized alkylthiolate SAMs for this study was conceived by Egbert Zojer. Michael Zharnikov provided the initial incentive to write a paper comparing the effects of chemical versus electrostatic shifts in XP spectra. Thomas Taucher and I performed all calculations and theoretical evaluations shown in this chapter. Specifically, Thomas Taucher performed all calculations of the partially fluorinated system (F8H11SH) and I performed all calculations of the ester-functionalized system (C10EC5) including the MD preoptimization. The postprocessing step to include substrate screening effects and exponential damping was developed jointly by

Thomas Taucher and me, with greatly appreciated input and help from Oliver Hofmann and Egbert Zojer. Thomas Taucher performed extensive preliminary tests to establish the initial state method as the more suitable one to calculate core level energies of the studied systems. Michael Zharnikov provided the measurement data and contributed to data interpretation in numerous lively discussions. The first draft of the manuscript was written jointly by Thomas Taucher and me. Its final version also contains valuable input and contributions by Oliver Hofmann and Egbert Zojer, concerning data presentation and wording of the manuscript. I wrote the Supporting Information Section (Section 5.6) and prepared all figures for this section. The figures depicting the chemical structures and unit cells of the main paper (Figures 5.1 and 5.2) were prepared by Thomas Taucher. Egbert Zojer made the schematic figure depicting the energy levels in the system (Figure 5.5). I prepared all figures depicting calculation results (Figures 5.3, 5.4, 5.6 and 5.7).

5.1. Introduction

A convenient way of tuning the properties of a given substrate is by covering it with covalently-bonded self-assembled monolayers (SAMs).[1,4,76] Such interface-modifiers have been applied in numerous ways, e.g., for controlling the wettability of surfaces,[270–272] for providing protection from corrosion,[273],[274] for enabling adhesion of biological cells,[275] as sensors,[48],[47] for nanopatterning,[276–278] and in organic electronics. In the latter context, they were applied for modifying electrode-semiconductor[24,27,53,61,62,64,72,74] and dielectric-semiconductor[63,66] interfaces. SAMs were even used as active layers in organic transistors.[58–60] Of crucial importance for electronic applications are changes of the substrate work function induced through SAMs bearing polar terminal groups[28,61–63,114,279,280] or polar units embedded into the molecular backbones.[24–26,281] Embedded dipolar groups also directly impact the electronic states within the SAMs and their alignment relative to the Fermi-level.[21,22]

A common approach for characterizing the properties of such SAMs is X-ray photoelectron spectroscopy (XPS).[116,282] By means of chemical shifts (i.e., shifts in the core-level binding energies induced by the immediate chemical environment of an atom) it is possible to verify the chemical integrity of the SAM, to understand details of its composition, and to explore its homogeneity.[110] Recently, in addition to chemical shifts, a variety of factors affecting the XPS binding energies have been mentioned.[15,25,26,283–285] For ionic crystals it is known that the Madelung energy needs to be taken into account to correctly describe shifts in binding energies.[122,286] A related effect of particular interest in the present case is that for SAMs containing dipolar elements within the molecular backbones binding-energy shifts can be associated with changes of the local electrostatic energy due to potential shifts caused by the dipoles.[25,26] Indeed, collective electrostatic effects arising from the superposition of the fields of periodically assembled dipoles have been discussed extensively in the context of the valence electronic structure of organic adsorbate layers.[119,122,123] They are also crucial for understanding adsorbate-induced

work-function changes[28,119,121–123,287] and, more recently, their exploitation as a tool for designing monolayers with highly complex electronic properties has been suggested.[22] As XPS is very sensitive to such effects it provides a highly valuable tool for characterizing the local electrostatic energy in complex adsorbate structures. However, for such a task it is absolutely crucial to understand how collective electrostatic effects and chemical shifts interact to give rise to the finally measured XPS signals.

Consequently, the purpose of the present paper is to obtain a coherent understanding of the interplay between these two effects. This is achieved by performing density functional theory (DFT) calculations on carefully selected model SAMs and comparing the results to high resolution XPS (HRXPS) measurements.[25,288] In this way we show that both chemical and collective electrostatic effects have to be taken into account to fully interpret XP spectra. The presented results imply that when chemically identical entities are incorporated into complex adsorbate layers their XPS signature can serve as an efficient probe for variations in the local energy landscape.

5.2. Investigated systems

The interplay between chemical and electrostatic shifts for core-level energies is relevant far beyond the field of self-assembled monolayers and applies to all systems in which assemblies of polar elements occur. Still, their discussion is most straightforward for extended and typically very well-ordered chemically bonded SAMs, where complications such as core-hole screening effects become less relevant (vide infra). Thus, we chose two SAMs, whose properties and chemical integrity are very well characterized.[25,288] They belong to the most established type of SAMS, namely substituted alkyl thiolates on Au(111),[1] and, therefore, serve as prototypical model systems for the present study. They comprise a partially fluorinated alkyl thiolate and a similarly long alkyl thiolate containing a polar ester group embedded into the aliphatic backbone. Their structures and the used surface unit cells are shown in Figure 5.1 and 5.2, respectively. Their full experimental characterization is contained in the above-mentioned references.

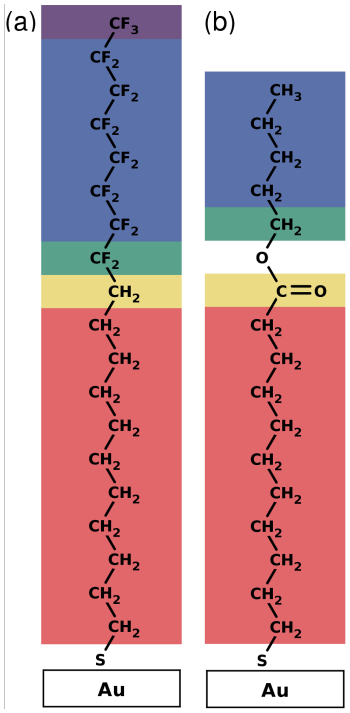

Figure 5.1.: Chemical structures of (a) 12,12,13,13,14,14,15,15,16,16,17,17,18,18,19,19,19-heptadecafluorononadecane-1-thiolate (F8H11SH) and pentyl-11-sulfanylundecanoate (C10EC5) bonded to a Au surface. The different background colors refer to C atoms with chemically clearly distinct environments (see Results and Discussion section 5.4).

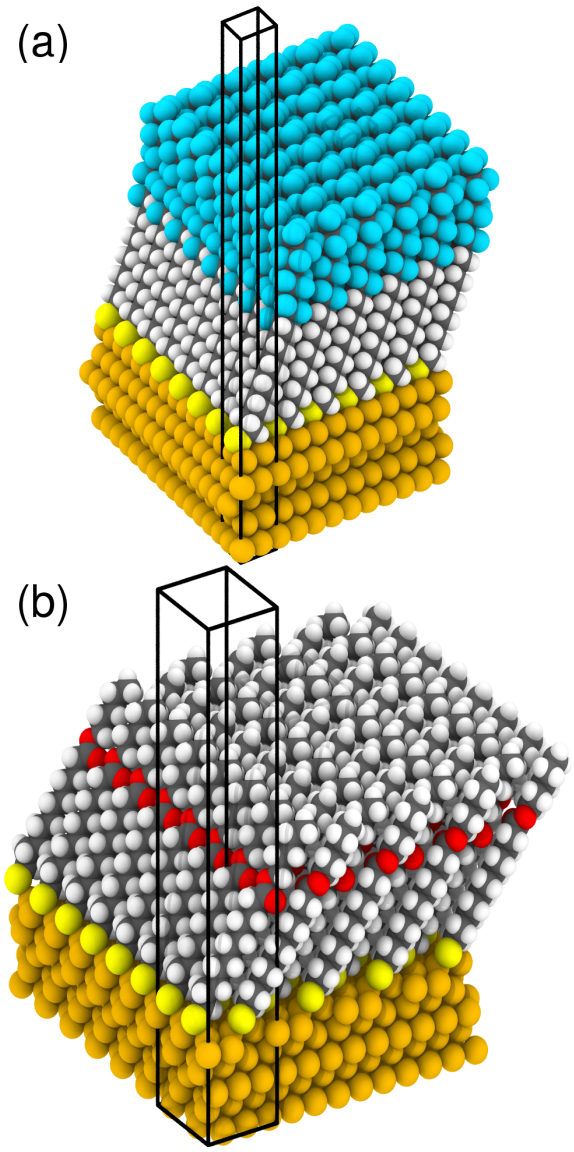

Figure 5.2.: Schematic pictures of the Au(111)/SAM interface are shown for F8H11SH (a) and C10EC5 (b). The surface unit cell is indicated by the black parallelepiped, showing the applied periodic boundary conditions used in the simulations as well as the vacuum gap to decouple the periodic replicas in z-direction (for details see main text).

Both layers are bonded to Au(111) surfaces. The choice of the partially fluorinated alkyl thiolate (hereafter referred to as F8H11SH consistent with ref. [288]) is motivated by the presence of five chemically different carbon species, that can be identified in high-resolution XP spectra.[288] This makes this SAM an ideal candidate for studying chemical shifts and for benchmarking the applied methodology. The alkyl thiolate (hereafter referred to as C10EC5 consistent with ref. [25]) contains a polar ester group and is an example of a system for which electrostatic shifts in the XP spectra have been suggested.[25] An important aspect of C10EC5, in which it conceptually differs from F8H11SH, is that the alkyl chains above and below the ester group (blue and red in Figure 5.1a) are chemically identical, i.e. there are two chemically equivalent segments of the chains, which are separated by a dipole. Both in ref. [288] and [25] several chain lengths, degrees of fluorination and different ester positions have been investigated; we chose the present systems because they are of comparable lengths. Moreover, the C5 segment above the ester in C10EC5 is short enough that in experiments an appreciable signal from the bottom chain can still be detected (with similar intensities for C5 and C10 segments for a photon energy of 580 eV), while it is long enough to be well ordered.[25]

The F8H11SH SAMs on Au(111) have been shown to grow in a commensurate p(2x2) arrangement with one molecule in the unit cell.[288] This structure is also chosen in the present study (cf. Figure 5.1). In passing we note that also a c(7x7) cell containing 17 molecules and non-commensurate structures have been reported.[289–292] These are not considered here. For the ester containing alkyl thiolates we used a (3 x $2\sqrt{3}$) unit cell containing four non-equivalent molecules in a herringbone arrangement[293] in analogy to a structure commonly reported for non-substituted alkyl thiolates.[13,294–298] The above choice of unit cells results in a molecular footprint, A, of 29.70 $\mathring{A}^2$ for F8H11SH and 22.27 $\mathring{A}^2$ for C10EC5. Note that the reduced packing density for the F8H11SH SAM is a consequence of the larger size of the fluorine atoms compared to the hydrogens. Accordingly, a chiral arrangement of the CF_2 groups is favored in the respective segment,[288] while for all alkyl segments a coplanar, *all trans* conformation is obtained.

For the reduced-coverage calculations of F8H11SH a 4x4 super-cell was chosen and all molecules but one were removed, yielding A = 475.2 $\mathring{A}^2$. This corresponds to a nominal coverage $\Theta = 1/16$. In the C10EC5 case, the unit cell was doubled in the longer direction and quadrupled in the shorter one and again all molecules but one were removed. Nominally, this yields $\Theta = 1/32$ (note that here the primitive unit cell contained four molecules), but as the packing density in the full coverage monolayer is significantly higher, the molecular footprint increases only to 712.8 $\mathring{A}^2$. In this context it is important to note that we kept the molecules fixed at the adsorption geometries of $\Theta = 1$, in order to isolate the impact of diluting the dipoles from the massive changes of the molecular orientation occurring at low coverages, where alkyl thiolates are known to lie flat on the Au substrate.[13]

5.3. Theoretical methods

5.3.1. Computational details

We performed slab-type band structure calculations based on density functional theory using the Vienna ab initio simulation package (VASP v5.3.2)[238–241] and employing the Perdew-Burke-Ernzerhof (PBE) functional[235,236] in conjunction with the projector augmented-wave method (details on the potentials are specified in the SUI).[242,299] Long-range van der Waals interactions were accounted for using the vdWSurf method[244] in the implementation of al Saidi et al.[245] The used cutoff energy for the plane-wave basis set was 400 eV and the total energy was converged to 10^{-6} eV. Γ-centered k-point meshes with 8x8x1 and 4x4x1 k-points were used for F8H11SH and C10EC5 SAMs at full coverage (bearing in mind the different sizes of the respective surface unit cells). When increasing the unit-cell size, the k-point mesh was scaled accordingly.

In all simulations the surfaces were represented by slabs consisting of five layers of Au to model the Au(111) surface with the SAM adsorbed to only one side of the slab. To avoid spurious surface relaxations the Au lattice constant was determined by applying the same methodology as used for calculating the surfaces. It was found to be 4.141 Å , which is very close to measured (4.079 Å[300]) and calculated values (4.154 Å[301]) reported in literature. The geometry optimizations were started with thiolates placed at fcc hollow sites of the Au(111) surface; periodic replicas of the slab were decoupled by a vacuum gap of ca. 30 Å and a self-consistently determined dipolar layer.[302] In the simulations, the topmost two layers of the Au slab were allowed to relax, while the other three layers were fixed at the bulk geometry. In the geometry optimization the forces were converged to $10^{-2}\,\mathrm{eV\,Å^{-1}}$.

The geometry update was performed via the GADGET[267] tool, which (i) enables the use of internal coordinates for describing the adsorbate layer and (ii) provides advanced algorithms[267] for the initial guess of the Hesse matrix, where, in the present work, Fischer's model[268] was applied. To sample the very rich configurational space of the highly flexible mid-chain ester-functionalized alkyl thiolates, we did a pre-optimization using molecular dynamics (for details see the Supporting Information).

5.3.2. Calculating XPS core level shifts

Relative XPS core-level shifts were calculated within the initial-state approach, which in VASP relies on a recalculation of the Kohn-Sham eigenvalues of the core states subsequent to the self-consistent determination of the charge density associated with the valence electrons.[247] Relative shifts of these energies are often found to reproduce very well the experimentally obtained results .[28,303–305] In passing we note that we compared the results obtained using this approach to full potential calculations employing the FHI-aims code,[306] which yielded quantitatively consistent core-level shifts (for details see the Supporting Information).

For the present systems, where we are primarily interested in core-level excitations of atoms relatively far away from the metal surface, the initial-state approach is preferable over the a priori more sophisticated final state approaches.[248,249,253–258] In the latter, screening effects especially by the metal atoms are considered explicitly in the quantum-mechanical simulations. This is particularly important for atoms very close to the metal surface, i.e., the sulfur atoms[252] and the first few carbons. It would, however, result in serious artefacts in the present case: Final state approaches rely on calculating the energy for a situation with one or one-half of an electron (employing Slater's transition state theory[307]) excited from the core into the valence region. In our systems, the unoccupied valence region is represented by states in the metal right above E_F. This means that any carbon core-level excitation is associated with a charge transfer from an atom within the SAM into the metal substrate (i.e., over an appreciable distance especially for carbon atoms near the surface of the SAM). This gives rise to a significant dipole moment, which would not pose a significant problem if the excitation happened only in individual molecules (as in the experiments). Due to the periodic boundary conditions one, however, deals with an excitation-induced large dipole in every unit cell resulting in an artificial potential gradient and in a shift of the core-level energies due to collective electrostatic effects (vide supra). Hence, for including screening effects via the final-state approach, one would need to converge the size of the unit cell until the excitation-induced dipoles are dilute enough such that the described artefacts become significantly smaller than the shifts in core-level energies that one intends to describe. This would require intractably large unit cells.

As in the here-applied initial-state approach the screening of the core-hole by the highly polarizable metal substrate is not directly considered in the calculations of the core-level energies,[250,251] it needs to be accounted for by an electrostatic image charge model.[261,262] There the core-level energies including screening are expressed as:

$$\varepsilon_{C1s,screened} = \varepsilon_{C1s} + \frac{1}{4\varepsilon(z - z_0)} \tag{5.1}$$

Here, ε is the dielectric constant of the SAM. We chose $\varepsilon = 2.26$ for both systems for the full coverage case.[25] This approach neglects that the SAMs are of only finite thickness, which is expected to have a negligible effect on the results. Also direct screening effects within the dielectric SAM are not accounted for. For the low coverage calculations $\varepsilon = 1.0$ was used, since they represent essentially isolated molecules on the substrate. The constant z_0 is the position of the image plane. It was set to 0.9 Å above the average z-position of the top gold layer.[308,309] z is the position of the atom whose core-level is excited. The screening shifts core-level energies to less negative values (smaller binding energies) and affects the atoms closest to the substrate most. As the molecules we investigated consist of rather long alkyl chains, the overall impact of screening on the XP spectra is comparably small, since the atoms in the SAM far away from the substrate, for which screening is least relevant,

contribute most strongly to the experimental signals. To compare the results of the calculations directly to the experiments, we simulated XP spectra by associating each C 1s core level with a Gaussian peak[i] centered at $\varepsilon_{C1s,screened}$ and subsequently summing over the contributions of all atoms weighted by an exponential attenuation function to account for the finite escape depth of the photoelectrons:[260]

$$w_i(d) = w_0 \exp\left(-\frac{d}{\lambda}\right) \ , \tag{5.2}$$

The individual weights $w_i(d)$ depend on d, the vertical distance between atom i and the topmost layer of atoms in the SAM, and the damping factor, λ. w_0 is a scaling constant, which does not affect the shape of the spectra. λ is given by[260]

$$\lambda = 0.3 * E_{kin} * e^{\beta} \ , \tag{5.3}$$

where E_{kin} is the kinetic energy of the escaping electron, which is determined by the energy of the incident photon (in our case 580 eV) minus the binding energy of the electron (calculated C 1s energy). The empirical attenuation factor β was chosen such that experimental relative peak heights were reproduced by our calculations. We used $\beta = 0.638$ for ester SAMs and $\beta = 0.55$ for partially fluorinated SAMs, where the smaller value in the latter case accounts for the stronger damping due to the significantly increased electron density in the fluorinated SAM.

5.4. Results and discussion

5.4.1. XP spectrum of the partially fluorinated SAM (F8H11SH) – dominance of chemical shifts

The calculated core-level energies are shown together with the simulated and measured XP spectra for densely packed F8H11SH SAMs in Figure 5.3. It is well established that calculated core-level energies are better suited to reproduce core-level shifts rather than reproduce absolute binding energies.[303–305,310] Therefore, while the core-level energies in the left panel of Figure 5.3 are reported as calculated, the simulated spectrum in the right panel of Figure 5.3 is stretched by a factor of 1.15 and shifted by 20.1 eV to align them with the experimental curve. This is analogous to the strategy commonly applied when comparing calculated energies of Kohn-Sham orbitals with experimentally measured binding energies in the valence region.[311] In this context it needs to be stressed that, while this procedure improves the quantitative agreement between the measured and simulated curves, it is by no means necessary for reproducing the experimentally observed trends in our calculations.

[i] Variance = 0.135 eV and 0.1 eV for C10EC5 and F8H11SH, respectively; adapted to best fit to the experimental spectra.

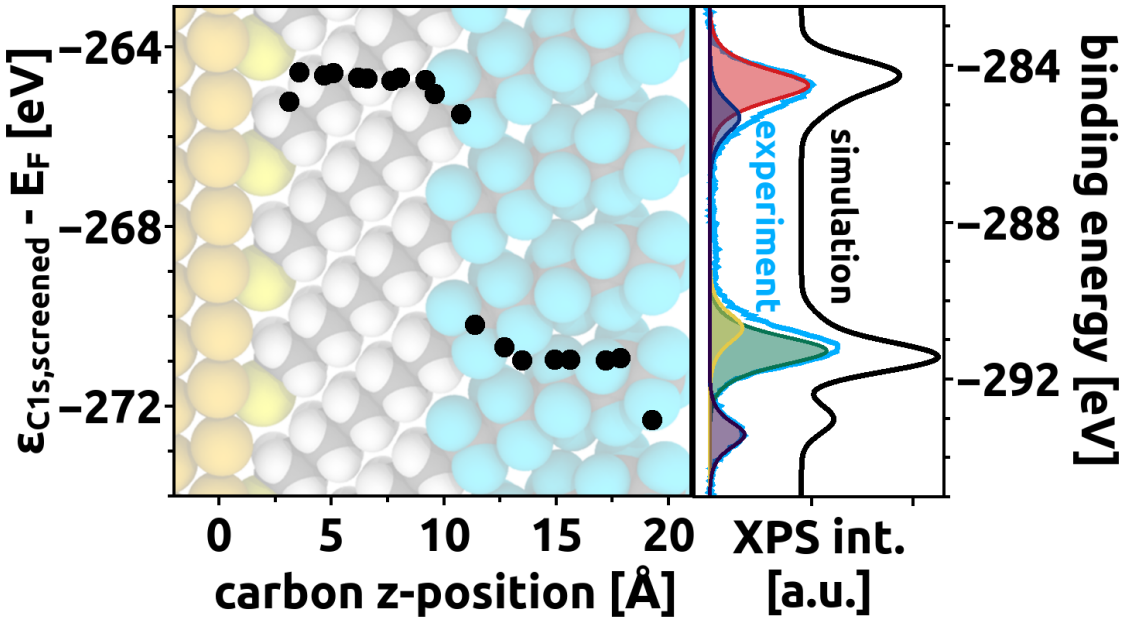

Figure 5.3.: DFT-calculated (screened) C 1s core-level energies relative to the Fermi energy for each carbon atom in a full coverage F8H11SH SAM (left panel). The right panel shows the XP spectrum calculated from the individual C 1s energies of the SAM (black). Additionally, the measured HRXP spectrum[288] of a full coverage F8H11SH SAM on Au(111) is shown (light blue). The measurements were performed with an incident photon energy of 580 eV. Five Gaussian peaks are fitted to the measured spectrum; the assignment of these peaks is discussed in the main text. While the core-level energies in the left panel are reported as calculated, the simulated spectrum has been stretched by a factor of 1.15 and subsequently shifted by 20.1 eV (binding energy $= [\varepsilon_{C1s,screened} - E_F] * 1.15 + 20.1eV$). As a consequence of that, the left and right scales do not cover the same range of values. The experimental spectrum is reprinted with permission from (Lu, H.; Zeysing, D.; Kind, M.; Terfort, A.; Zharnikov, M. Structure of Self-Assembled Monolayers of Partially Fluorinated Alkanethiols with a Fluorocarbon Part of Variable Length on Gold Substrate. J. Phys. Chem. C 2013, 117, 18967–18979). Copyright (2013) American Chemical Society.

For understanding the details of the calculated as well as measured XP spectra it is useful to identify groups of carbon atoms with chemically different environments along the chain. In ref. [288] five chemically distinct carbon species have been assigned to various features of the high-resolution XP spectra (cf., Figure 5.3): (1) The terminal carbon atom bonded to three fluorine atoms giving rise to the peak at the most negative binding energy (violet curve); (2) the carbon atoms in the fluorinated segment having two fluorinated carbon atoms as nearest neighbors and associated with the highest intensity feature in the spectrum (green curve); (3) the other terminal carbon atom in the fluorinated segment adjacent to the hydrocarbon segment visible as an asymmetry of the line shape of the main peak (yellow

curve); (4) the terminal carbon atom of the hydrocarbon segment, adjacent to the fluorinated segment (dark blue); and (5) the carbons in the other CH_2 groups with only CH_2 carbons and sulfur (see below) as neighbors causing the main feature at least negative binding energies (red curve). These assignments are fully confirmed by a comparison between the simulated and measured spectra and by tracing back the features in the simulated XP spectrum to the core levels of individual carbon atoms in the left panel of Figure 5.3. The simulations also clearly reveal a slightly shifted binding energy of the very first carbon atom due to the bonding to the sulfur atom. Moreover, we observe increasingly less negative core-level binding energies for the CH_2 carbon atoms upon approaching the metal surface, which is a consequence of the increasing screening. The latter two effects are not resolved in the experiments due to the close values of the binding energies for the respective carbon atoms as well as the progressively strong attenuation of the photoelectron signal for the deeply located atoms. Overall, the excellent agreement between theory and experiment for the F8H11SH SAM confirms that the used methodology is capable of reliably describing chemical shifts in photoemission for self-assembled monolayers.

5.4.2. XP spectrum of the alkyl thiolate SAM containing an embedded ester group (C10EC5) – significance of electrostatic shifts

As can be clearly seen in Figure 5.4, also for the C10EC5 SAM the main features of the measured XP spectra, namely the relative peak positions and the relative peak intensities are very well reproduced in the simulations. The peak associated with the carbonyl carbon (marked yellow in Figure 5.4) at the most negative binding energy is clearly resolved in the experiments. This is a clear consequence of the modified chemical environment of that particular carbon atom that is bonded to two oxygen atoms. Right next to it we find the peek associated with the ether C (marked green in Figure 5.4), which is still significantly chemically shifted with respect to the emission from the carbon atoms in the aliphatic chain segments, albeit to a lesser degree than for the carboxylic C atom. As in the F8H11SH case, we find that the peak associated with the first carbon directly bound to the sulfur docking group is slightly shifted to more negative binding energies in the calculations. The feature due to the terminal CH_3 carbon is not resolved as a separate peak in the simulated and measured XP spectra as the associated shift is much smaller than for the CF_3 carbon in the F8H11SH example.

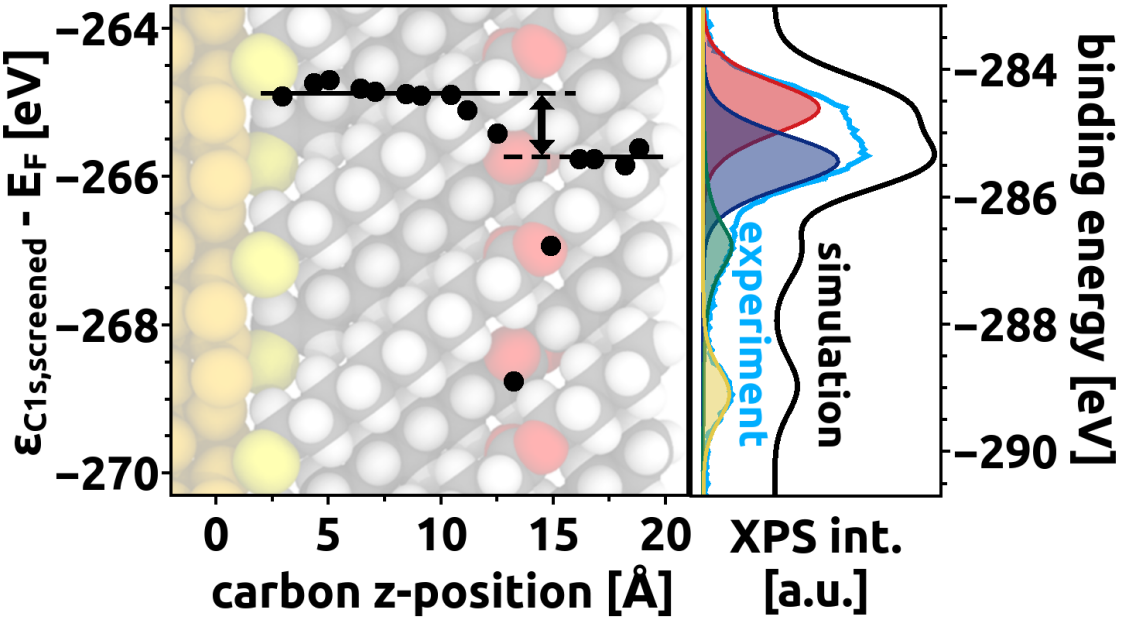

Figure 5.4.: DFT-calculated (screened) C 1s core level energies relative to the Fermi energy for each carbon atom in a full coverage C10EC5 SAM (left panel). The reported C 1s energies and z-positions are averaged over the four molecules in the unit cell. The impact of this averaging is negligible, with typical (maximum) variations on the order of 0.01 eV (0.1 eV). The right side of the figure shows the XP spectrum calculated from the individual C 1s energies of the same SAM (black). Additionally the measured HRXP spectrum[25] of a full coverage C10EC5 SAM on Au(111) is shown (light blue). The measurements were performed with an incident photon energy of 580 eV. Four Gaussian peaks are fitted to the measured spectrum; the assignment of the obtained peaks is discussed in the main text. While the core-level energies in the left panel are reported as calculated, the simulated spectrum has been stretched by a factor of 1.15 and subsequently shifted by 20.1 eV (binding energy $= [\varepsilon_{C1s,screened} - E_F] * 1.15 + 20.1eV$). As a consequence of that, the left and right scales do not cover the same range of values. The experimental spectrum is reprinted with permission from (Cabarcos, O. M.; Shaporenko, A.; Weidner, T.; Uppili, S.; Dake, L. S.; Zharnikov, M.; Allara, D. L. Physical and Electronic Structure Effects of Embedded Dipoles in Self-Assembled Monolayers: Characterization of Mid-Chain Ester Functionalized Alkanethiols on Au111. J. Phys. Chem. C 2008, 112, 10842–10854). Copyright (2008) American Chemical Society.

While all these differences in core-level energies can be understood as a consequence of different chemical environments, this is not the case for the shift between the two most prominent peaks of the spectrum located around -285 eV. They can be unambiguously assigned to the CH_2 groups in the bottom and top segments of the molecule (below and above the ester group). These two segments are chemically equivalent, but still the associated average C 1s core-level energies differ by as much as 0.86 eV. In passing we note that this difference is not caused by different degrees

of screening of the core holes in the upper and lower segments, as can be gauged by experiments on non-substituted alkyl thiolate SAMs[16] and also from a simulation in which a difference of 0.71 eV is still present when this screening is switched off.

Thus, there must be another origin for that shift in core-level energies. As already suggested by Cabarcos et al.,[25] this has to be related to the regular arrangement of the ester dipoles. Although the dipole moments originating from the polar ester groups are strongly inclined relative to the surface normal,[25] their components perpendicular to the substrate are still sizable. This can be shown by calculating the dipole moments per molecule perpendicular to the film surface in hypothetical free-standing SAMs arranged in the geometry the molecules adopt on the surface (but after replacing the polar thiol group by a hydrogen to isolate the polar contribution of the ester). The obtained perpendicular dipole moments per molecule then amount to 0.51 Debye at full and to 0.76 Debye at 1/32 coverage. The smaller value at full coverage is the consequence of well-known depolarization effects. The horizontal components of the dipoles are compensated by a polarization of the metal (cf., mirror charges).

The individual electric fields originating from the ester dipole perpendicular to the substrate add up and cause a sharp drop in the electrostatic energy.[119] The drop is very strongly localized, as, contrary to the situation of isolated dipoles, electric fields decay rapidly in densely packed SAMs.[122] As also the core-levels are strongly localized at individual carbon atoms their energies directly follow the dipole-induced change of the electrostatic energy. This results in very different binding energies of the core-levels of the upper and lower alkyl segments relative to the Fermi-level of the metal and, consequently, in strongly different kinetic energies of the photoelectrons. This is illustrated schematically in Figure 5.5. In that sense, the core-level energies serve as very sensitive probes of the local electrostatic energy within the SAM.

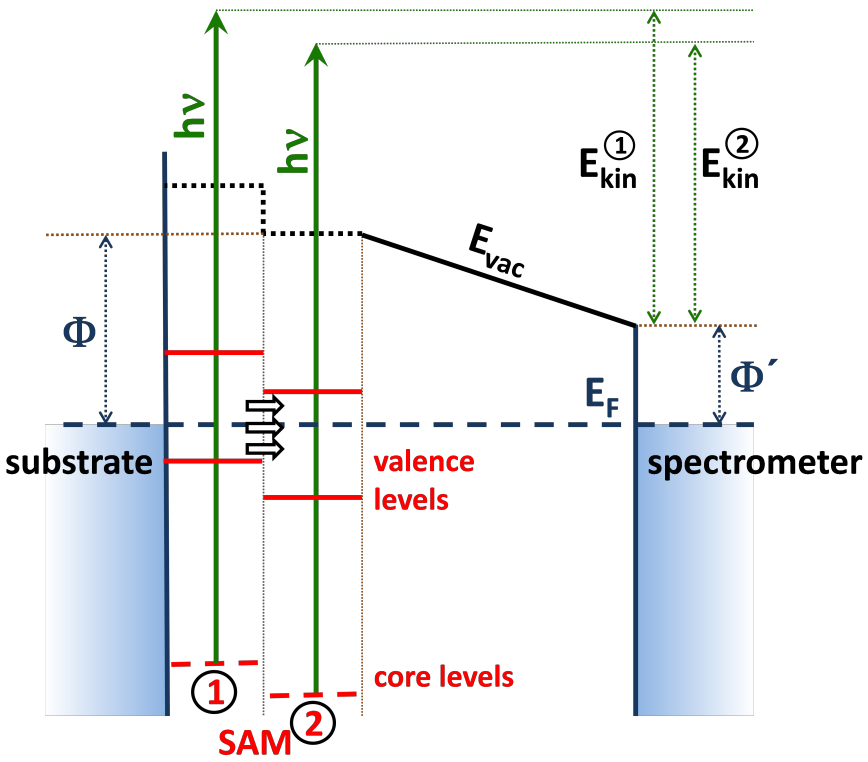

Figure 5.5.: Schematic illustration of the energy level alignment in the C10EC5 SAM. The core and valence levels of the bottom segment (1) and top segment (2) of the molecules are separated by an ordered two-dimensional array of dipoles. The associated shift in energy results in two different measured electron kinetic energies at the detector (E^1_{kin} and E^2_{kin}). The green arrows symbolize the XPS measurement process with the incident photon energy $h\nu$. E_F denotes the Fermi energy, which is the same on the sample and detector side of the setup[282] in contrast to the vacuum energy E_{vac}. The work function of the clean gold substrate is modified by the applied SAM to the resulting value Φ. For the sake of clarity we assume an infinitely extended sample and detector; i.e., no distinction between the vacuum level directly above the sample and at a distance much larger than the sample dimensions is made, as this again would not affect the differences in the kinetic energies of the photoelectrons.

Since this shift in the electrostatic potential arises from the collective superposition of the fields of the 2D arranged dipoles, it is (i) directly proportional to the dipole density and (ii) expected to diminish for individual dipoles, where instead of the highly localized[122] step in the electrostatic energy a much smaller and smeared out shift in the binding energy of the core levels due to the electric field of an individual dipole is to be expected.[119] This provides an efficient handle for testing the above hypothesis that such electrostatic effects indeed impact measured core-level energies: Upon reducing the coverage of the SAM (with - in this computer-experiment

- maintained geometry and dipole orientation, vide supra), XPS core-level shifts induced by collective electrostatic effects should decrease and for very low coverages essentially disappear. In contrast, chemically induced shifts ought to persist.

5.4.3. XP spectra at reduced coverage – turning off collective electrostatic effects

In the following, we discuss core-level energies at strongly reduced coverages (cf., section 5.2) for the C10EC5 and F8H11SH systems. The evolution of the spectra for gradually reducing the coverage can be found in the Supporting Information. A conceptually related situation, at least as far as the impact of the ester-dipoles is concerned, would be a homogeneously mixed SAM consisting of a minority of C10EC5 molecules embedded into alkyl thiolates.

Figure 5.6a compares the core-level energies of C10EC5 molecules in full and low coverage SAMs. The most important result of this comparison is that for the low coverage SAM the shift between the core level energies of the upper and lower alkyl segments has essentially disappeared. As a consequence, in the simulated XP spectra the main peak is no longer the superposition of two clearly resolved maxima, but is rather dominated by a single feature. This very much supports the above hypothesis that the shift in the full-coverage SAM is of purely electrostatic origin. Consistent with this scenario, the carbonyl carbon and the ether carbon core level energies are still shifted with respect to the rest of the chain, as the origin of that shift is "chemical" in nature.

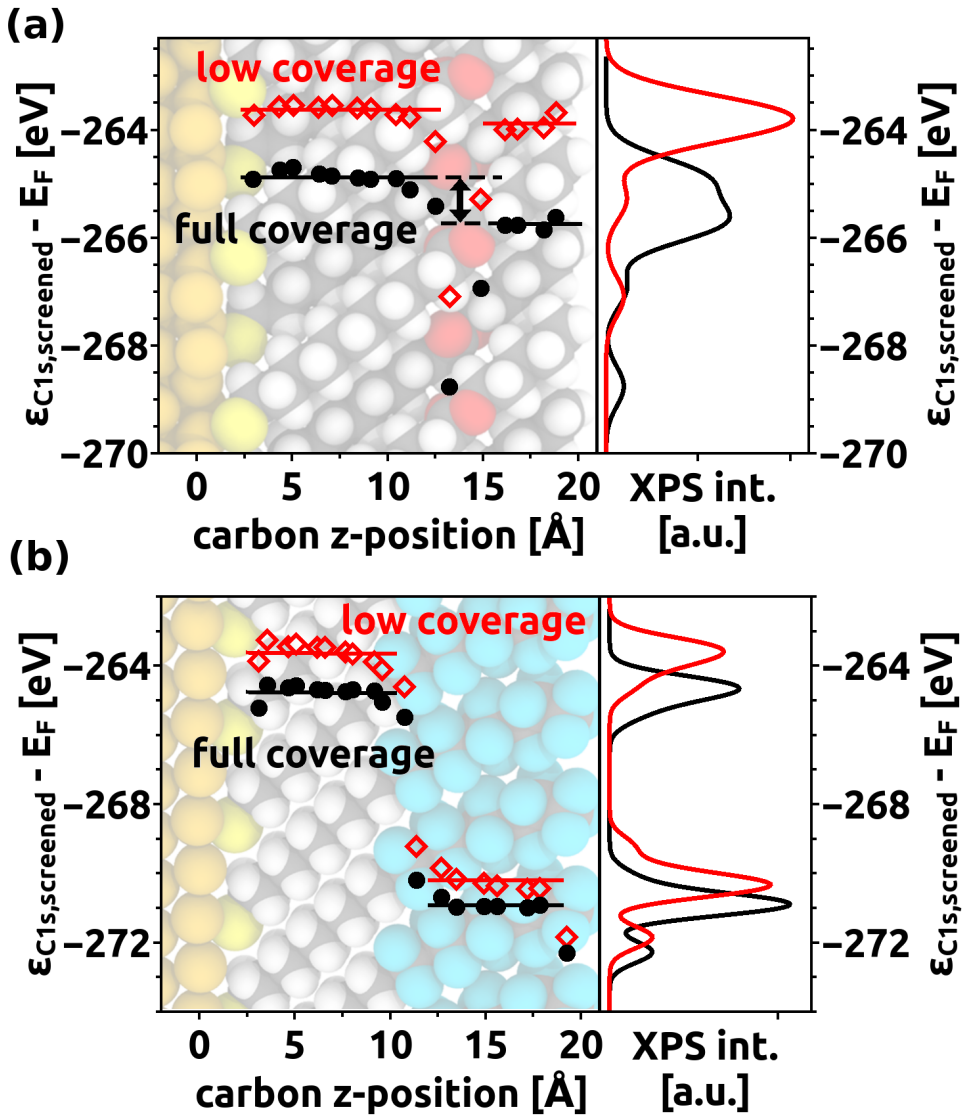

Figure 5.6.: Calculated C 1s core level energies of (a) C10EC5 and (b) F8H11SH in the full coverage SAMs (black) compared to the low-coverage situation (red). The molecular geometries are kept the same at both coverages (for further details see section 5.2). The right plot shows the XP spectra calculated from the individual 1s orbital energies of all carbons in the unit cell plotted without shifting and stretching of the original data, as we do not compare to experimental spectra here.

What still remains to be explained is why the positions of all C 1s core levels are shifted to smaller binding energies in the low-coverage SAMs. This can again be traced back to collective electrostatic effects (or rather the lack thereof) in the low-coverage situation: One must not forget that also at the metal/SAM interface a significant dipole is present (i) due to the thiolate group and (ii) as a consequence of bonding-induced charge rearrangements. This second ordered dipole layer causes a potential drop at the metal/SAM interface at full coverage. This results in an

electrostatic shift of the core-level energies of all atoms situated above the docking group, i.e., all carbon atoms within the SAM, for the same reasons as in the case of the ester dipole. At low coverage that step-like change in the electrostatic energy diminishes and is replaced by the much weaker potential energy modification due to an individual dipole. Noteworthy, the rigid shift of the C 1s core-levels in the bottom segment far from the dipoles between the two different coverages allows a determination of an upper limit for the shift in the electrostatic energy due to the thiolates (including the bonding to the metal), which for the present configuration of the chains amounts to 1.25 eV. The reason for this value representing only an upper limit is that it is affected also by differences in the core-hole screening (cf., section 5.3.2). When neglecting screening effects, the shift is reduced to 0.94 eV.

The above "electrostatic" view is fully corroborated by the electron electrostatic energy within the SAM at full and low coverages, which is shown in Figure 5.7. There one clearly sees the significantly higher electrostatic energy around the isolated molecule (right) compared to the densely packed monolayer (left). What is also clearly resolved is that the top and bottom segments of the C10EC5 molecule at low coverage experience a very similar electrostatic environment, while there is a significant shift in energy between the regions around the top and bottom segments at full coverage. I.e., the polar ester groups induce a potential energy step at high coverages, while the potential modifications associated with the ester group are very local for the isolated molecule.

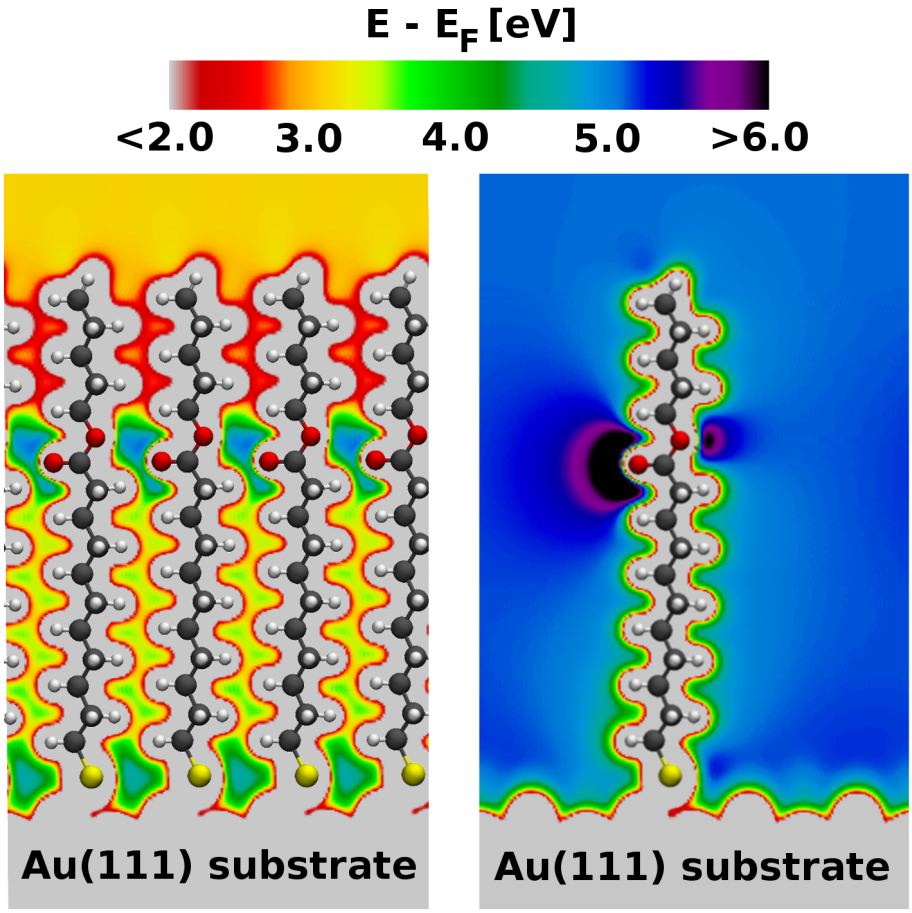

Figure 5.7.: Calculated electron electrostatic energy for the full coverage C10EC5 SAM (molecular footprint of 22.3 Å^2) shown on the left, and the low coverage C10EC5 SAM (molecular footprint of 712.8 Å^2) shown on the right; the potential is plotted in the plane containing the (essentially parallel) long molecular axes of two (of the four) neighboring molecules in the unit cell. The electrostatic energy is given with respect to the Fermi level of each system.

When comparing the F8H11SH high- and low-coverage SAMs a picture evolves that is consistent with the above considerations (see Figure 5.6b): There is a rigid shift of all C 1s core-level energies to lower binding energies in the low-coverage case. Again, the reason is that the step in the electrostatic energy due to the thiolates diminishes at low coverages. The effect is somewhat smaller for the F8H11SH SAM (only 1.0 eV compared to 1.25 eV for the C10EC5 SAM). This is a consequence of (i) the lower density of docking groups in the latter case (c.f., section 5.3.1) and (ii) the somewhat different docking geometry for a situation with all molecules parallel (F8H11SH) compared to a herringbone packing (C10EC5).[ii]

[ii]Note that we see similar changes in work-function modifications when studying pure alkyl thiolates in the respective geometries.

Interestingly, the differences in core-level energies for the two coverages are smaller in the fluorinated section of the SAM. This can be understood as the consequence of a small dipole component pointing towards the surface that is localized in the interface region between the fluorinated and non-fluorinated sections of the SAM (cf., molecular dipole contribution in ref. [17]). This causes a comparably small upwards-shift of the core level energies in the fluorinated section of the SAM; i.e., also in F8H11SH electrostatic shifts do play a role, but they are very small compared to the chemical shifts and, therefore, typically not accounted for when interpreting the experiments. When reducing the coverage, these electrostatic shifts again disappear explaining the smaller net-shift to lower binding energies in the fluorinated section of the SAM.

5.5. Conclusions

The considerations in this paper show that shifts in the core-level binding energies measured for thin organic films by x-ray photoelectron spectroscopy are not only determined by the chemical environment of the atoms of interest. Additionally, variations in the electrostatic energy caused by collective electrostatic effects (albeit often overlooked) play an equivalently important role. This is shown by a comparison between experimental and theoretical XP spectra combined with an in-depth analysis of the local electrostatic situation in two prototypical thiolate-bonded self-assembled monolayers. As a consequence, great care has to be taken when exclusively associating experimentally observed changes in core-level binding energies with chemical changes occurring in an adsorbate layer. Peak shifts of several tenths of an eV or more can be caused either by interfacial charge rearrangements (here due to the bonding of the thiolates) or by polar groups incorporated into the studied molecules. As a consequence, when using chemically identical species in different spatial regions of an adsorbate (i.e., when ruling out chemical shifts), XPS can become a powerful tool for probing local variations in the electrostatic energy, making it a highly promising technique for studying nanoscopic electronic devices even beyond its well-recognized capabilities.

5.6. Supporting information

5.6.1. Simulation details of the pre-optimization using molecular dynamics

The potential energy surface (PES) of the C10EC5 alkyl thiolate SAM is rather complex including many local minima. To efficiently sample this PES we combined the DFT-based geometry optimization as described in the main manuscript with a pre-optimization using molecular dynamics (MD). To run the simulations the program package LAMMPS[171] (v. 14 Feb 2013) was applied. The Verlet[170] algorithm was used to solve the equations of motion in time steps of 1fs. The

SHAKE[172] algorithm was employed for constraining the mobility of the hydrogen atoms during the simulation. For temperature slopes we chose an NVE ensemble (Berendsen thermostat)[174] and in the equilibration phase an NVT ensemble with the Nosé-Hoover[175,176] thermostat was used. Coulomb interactions were calculated in reciprocal space with the particle-particle-particle-mesh (PPPM)[206] method. The atomic charges needed were calculated for an isolated molecule using the ESP charge-partitioning scheme,[208,209] where the charges are assigned to reproduce the quantum-mechanically calculated electrostatic potential at points selected according to the Merz-Singh-Kollman scheme.[208,209] Gaussian09[210] with the B3LYP[211,213,214,312] functional and an aug-cc-pVTZ[215–218] basis set were used for this calculation.

For most interactions the CHARMM36 general force field[194] (v. 2b7) was used. However, the gold-organic interactions were described with the GoIp[219] force field, which we found to be most appropriate for modelling organic adsorbates, and the Au-S bond was described with the potential designed by Jang et al.[220] This potential is of a modified Buckingham type and allows bond breaking, thus allowing the molecules to move on the substrate. Hence, we do not predetermine the bonding sites already with the starting configuration. The cutoff radius for pairwise interactions was chosen as 12 Å for Au-S. The Lenard-Jones potential (lj/charmm/coul/long) used for the CHARMM force field had an inner cutoff radius of 12 Å and an outer one of 14 Å.

The Au(111) surface in the MD run was represented by ten layers of gold. The positions of the gold atoms were kept fixed during the simulation. Periodic boundary conditions in x- and y-direction were employed, creating a 2D infinite slab. The lateral extension of the periodic unit cell was chosen such that it contained 16 C10EC5 molecules in dense packing. At the start, all molecules were oriented upright with the same twist angle (i.e., not introducing any bias towards a herringbone arrangement of the molecules). To reach the global minimum we employed a temperature ramp, first heating the sample to T = 750 K (over a timespan of t = 0.2 ns). This allows the molecules to move freely on the substrate and lifts any bias incurred by the arbitrarily chosen starting configuration. The sample was then cooled to room temperature (T = 300 K) over t = 1.3 ns with a constant cooling rate and equilibrated there for t = 5 ns. Afterwards the system was slowly cooled to T = 0 K over a timespan of t = 4 ns to prevent thermal motion of the molecules, thus giving us straight molecular geometries without thermally induced "defects" in the final geometry. From the final structure, four representative molecules were picked and a unit cell containing five layers of gold substrate and four molecules was created for further geometry optimization using density functional theory (DFT).

5.6.2. Details of the PAW potentials used for VASP calculations

Table 5.1 lists the PAW potentials used for all VASP calculations in this work, except the "VASP soft PAW" test calculation shown in Figure 5.8. For this test calculation soft PAW potentials were used for carbon and oxygen atoms.

Table 5.1.: List of PAW potentials used for VASP calculations in this work.

element	potential
Au	PAW_PBE Au 06Sep2000
S	PAW_PBE S 17Jan2003
C	PAW_PBE C 08Apr2002
H	PAW_PBE H 15Jun2001
O	PAW_PBE O 08Apr2002
F	PAW_PBE F 08Apr2002

5.6.3. Testing different PAW potentials and comparison to a full potential code

In Figure 5.8 we compare C1s energies of the C10EC5 SAM calculated with different PAW potentials to estimate the influence of the set of used potentials. As a reference we use results obtained with the full potential code FHI-aims[306] for the same system.

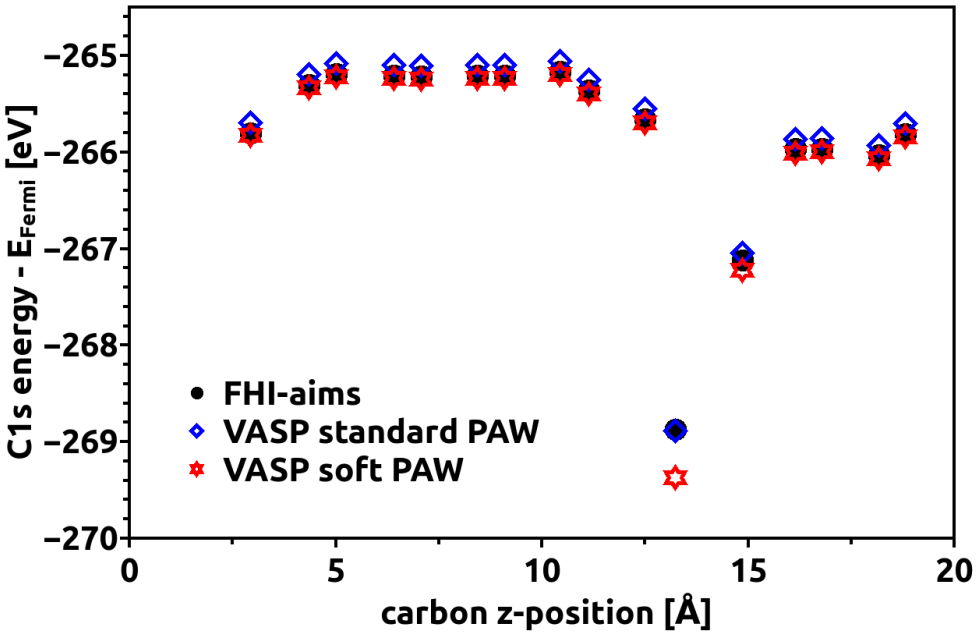

Figure 5.8.: C1s energies of the full coverage C10EC5 SAM calculated with VASP using standard PAW potentials (Au, S, C, H, O) (open blue diamonds) and partially soft PAW potentials (Au, S, C_s, H, O_s) (open red stars). The results are compared to those obtained using the full potential code FHI-aims[306] (full black dots) employing "tight" settings for all elements, except sulfur, for which "light" settings have been used. For the sake of comparing the different calculation methods all core level energies shown in this plot are unscreened energies.

The result of the VASP calculation using standard PAW potentials is nearly identical to the FHI-aims calculation, save for a small rigid offset. The calculation performed with soft PAW potentials for carbon and oxygen, however, differs noticeably from the other two calculations at the carbonyl carbon (the carbon lowest in energy and chemically most different).

5.6.4. The impact of screening on calculated C1s energies

Figure 5.9 shows a scatter plot of the carbon 1s core level energies of a full coverage F8H11SH SAM. We compare the unscreened values with the ones including screening effects.

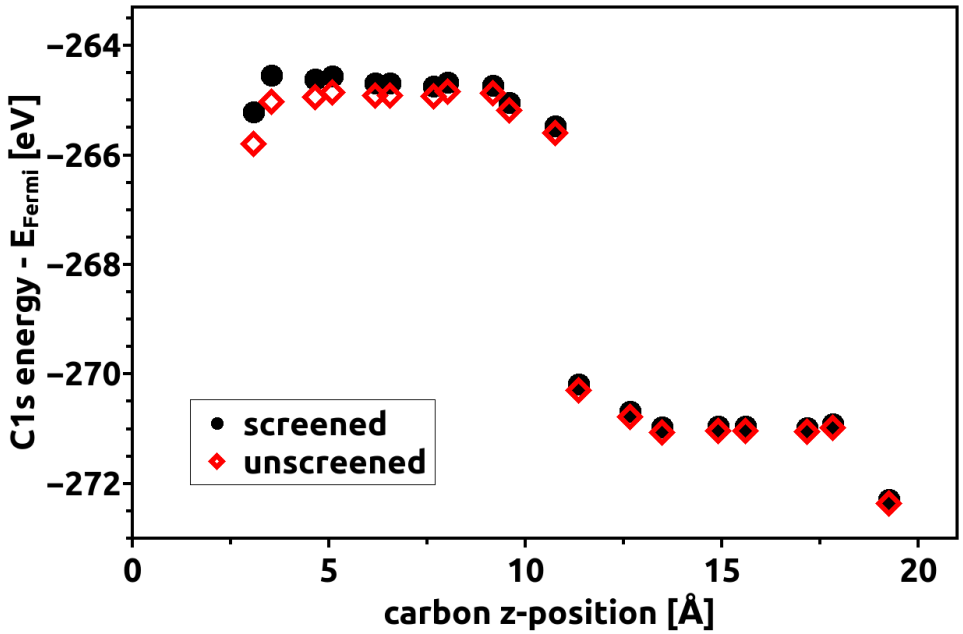

Figure 5.9.: Calculated C 1s core level energies of a full coverage partially fluorinated alkyl thiolate SAM (F8H11SH) including (full black dots) and excluding (open red diamonds) screening effects by the metal.

We see that the screening of the metal substrate shifts core level energies to less negative values. Atoms closest to the substrate are affected the most, whereas there is practically no influence on atoms near the top of the SAM. Combined with the strong damping of the XPS signal of deep lying atoms (see next section) the impact of screening on the systems portrayed in this work is rather small.

5.6.5. Impact of damping on calculated C1s spectra

Figure 5.10 shows calculated XP spectra of the F8H11SH system including and excluding attenuation effects for the photoelectrons.

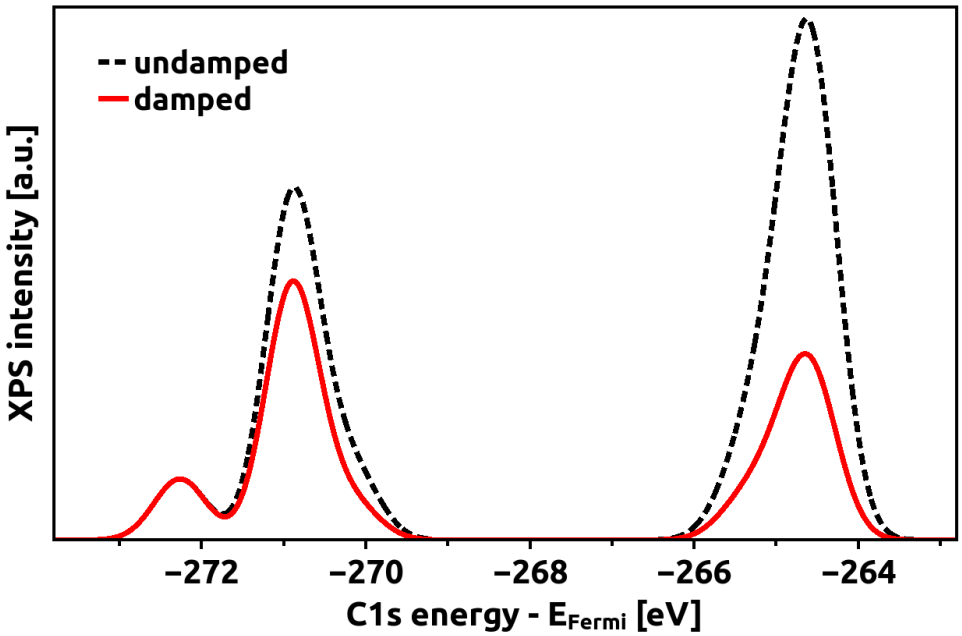

Figure 5.10.: Calculated XP spectra of a full coverage F8H11SH SAM, comparing a spectrum which takes an exponential attenuation of the signal into account (red solid line) and one neglecting it. Both curves include screening effects of the metal as described in the main article.

We see that attenuation effects are significant. The intensity of the peak assigned to the bottom alkyl chain (at ≈ -265 eV) is reduced to about one third. The intensity of the fluorinated part of the molecule (≈ -271 eV) is only slightly reduced, as it constitutes the top part of the SAM. The CF_3 signal (≈ -272.5 eV) is unaffected by attenuation effects, because this carbon is situated right at the top of the SAM.

5.6.6. Comparing non-stretched calculated XP spectra to experiments

Figures 5.11 and 5.12 compare the experimental XP spectra of full coverage F8H11SH and C10EC5 SAMs with calculated spectra which were only shifted and not stretched. They are included here for the sake of comparison to stress that the reproduction of the experimental trends/shifts by the simulations is by no means related to the commonly applied stretching of the energy scale of the Kohn-Sham eigenstates.

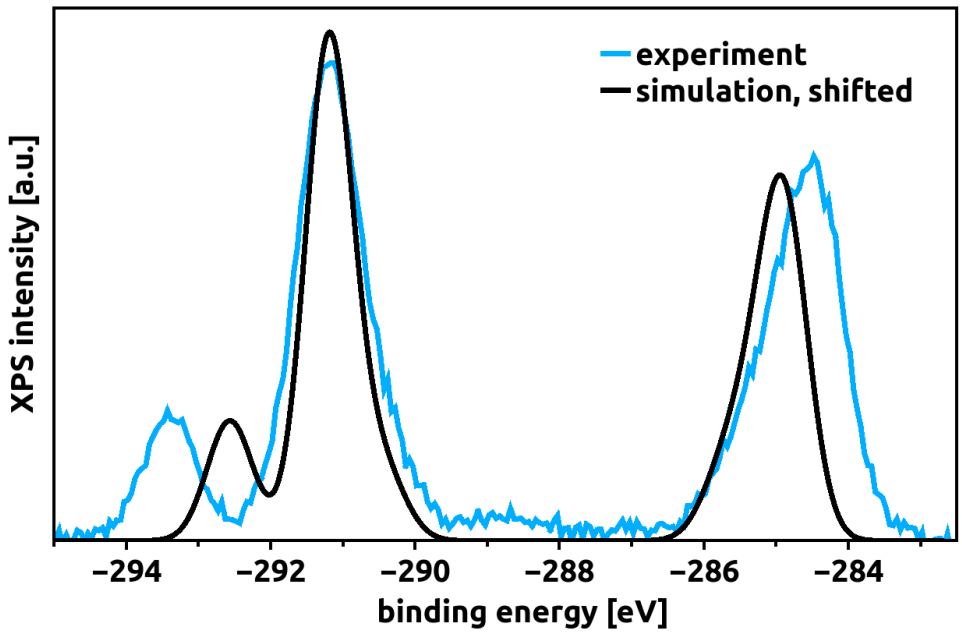

Figure 5.11.: Comparison of the measured HRXP spectrum[288] of a full coverage F8H11SH SAM on Au(111) (light blue) with the calculated spectrum (black). The calculated spectrum was rigidly shifted by -20.3 eV to align the main peak with the experimental one, but not stretched. The measurements were performed with an incident photon energy of 580 eV. The experimental spectrum is reprinted with permission from (Lu, H.; Zeysing, D.; Kind, M.; Terfort, A.; Zharnikov, M. Structure of Self-Assembled Monolayers of Partially Fluorinated Alkanethiols with a Fluorocarbon Part of Variable Length on Gold Substrate. J. Phys. Chem. C 2013, 117, 18967–18979). Copyright (2013) American Chemical Society.

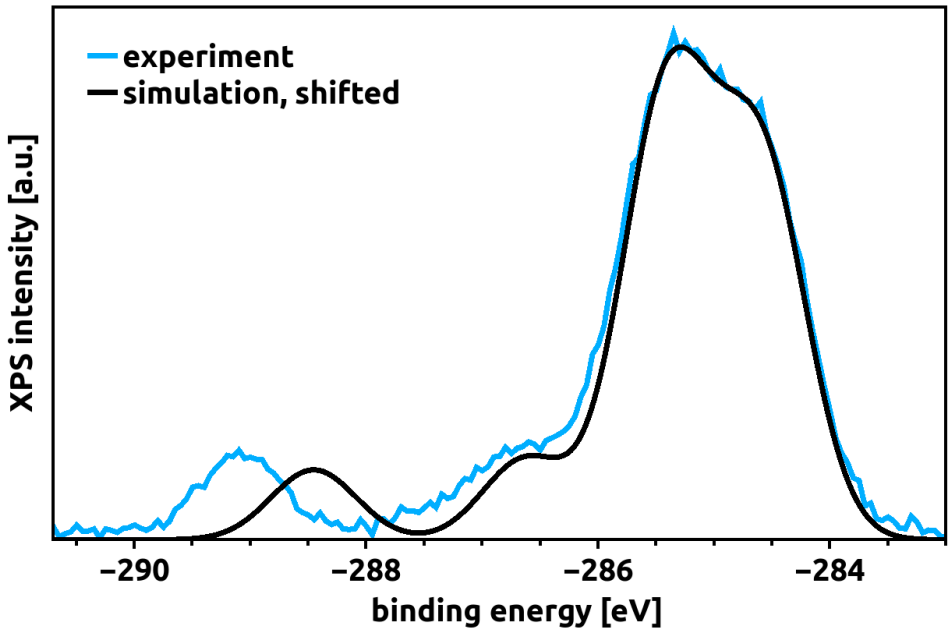

Figure 5.12.: Comparison of the measured HRXP spectrum[25] of a full coverage C10EC5 SAM on Au(111) (light blue) with the calculated spectrum (black). The calculated spectrum was rigidly shifted by -19.7 eV to align the main peak with the experimental one, but not stretched. The measurements were performed with an incident photon energy of 580 eV. The experimental spectrum is reprinted with permission from (Cabarcos, O. M.; Shaporenko, A.; Weidner, T.; Uppili, S.; Dake, L. S.; Zharnikov, M.; Allara, D. L. Physical and Electronic Structure Effects of Embedded Dipoles in Self-Assembled Monolayers: Characterization of Mid-Chain Ester Functionalized Alkanethiols on Au111. J. Phys. Chem. C 2008, 112, 10842–10854). Copyright (2008) American Chemical Society.

From Figures 5.11 and 5.12 we see that the calculated spectra, when only shifted rigidly without any stretching, qualitatively reproduce the measured ones quite accurately. All peaks found in the experimental spectra are present in the calculations and the relative peak intensities match. There are only slight differences regarding the exact values of the XPS peak shifts.

5.6.7. Intermediate coverages

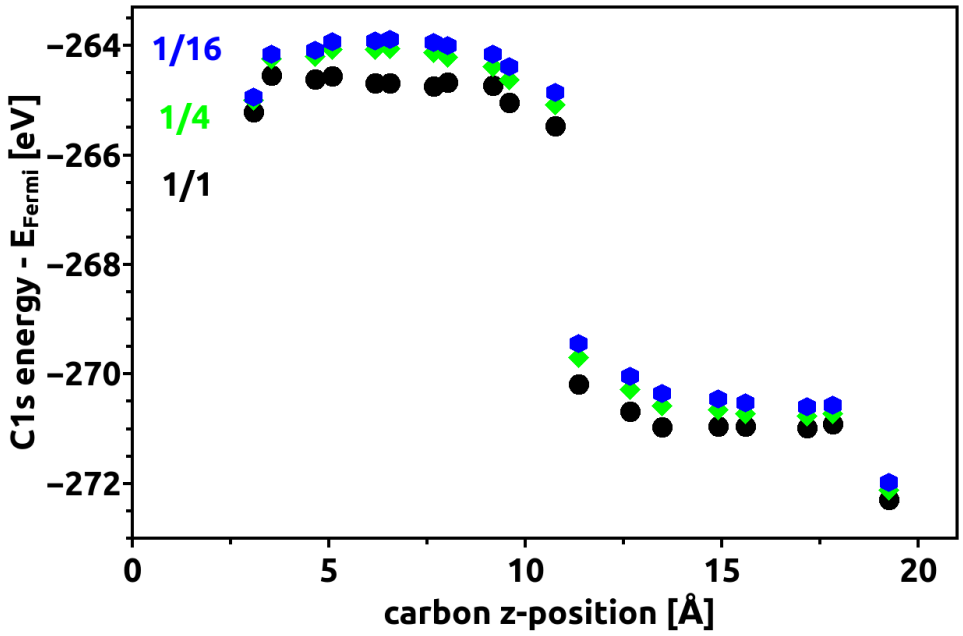

Figure 5.13.: Calculated C 1s core level energies of F8H11SH SAMs at different coverages. We show three different coverages in this plot: full coverage (black dots), a coverage of 1/4 (green diamonds) and a coverage of 1/16 (blue hexagons). For the sake of comparison $\varepsilon = 2.26$ was used for calculating screening effects in all three cases shown here (in contrast to the main manuscript, where $\varepsilon = 1$ was used at the lowest coverage).

In Figure 5.13 we see that the results for full coverage and a coverage of 1/4 are still quite different from one another. However, coverages of 1/4 and 1/16 yield already pretty similar results. We therefore interpret a coverage of 1/16 as dealing with isolated molecules on the substrate for the F8H11SH system. The case is a bit different for the C10EC5 SAM discussed next (see Figure 5.14), where it was necessary to reduce the coverage even more to eliminate collective electrostatic effects.

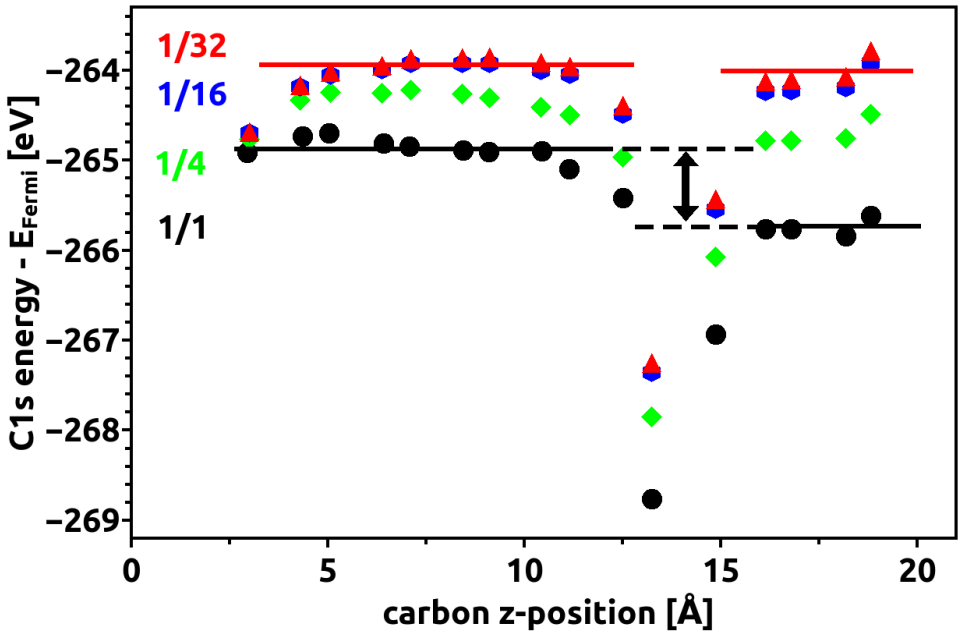

Figure 5.14.: Calculated C1s core level energies of C10EC5 SAMs with different coverages. The intermediate coverages that were calculated are included in this plot: full coverage (black dots), a coverage of 1/4 (green diamonds), a coverage of 1/16 (blue hexagons) and a coverage of 1/32 (red triangles). For the sake of comparison $\varepsilon = 2.26$ was used for calculating screening effects in all four cases shown here (in contrast to the main manuscript, where ε =1 was used at the lowest coverage).

We see a trend going from full to low coverage, with the energetic difference between bottom and top segment gradually decreasing. The electrostatic shift of the bond dipole also vanishes gradually from full to low coverage. The results for coverages 1/16 and 1/32 are already nearly identical. The electrostatic situation does not change anymore, the molecules behave as if isolated in both cases. For a coverage of 1/4 there still is some collective electrostatic interaction present, but much weaker than in the full coverage system. Thus, an electrostatic shift between bottom and top chain can still be seen, but it is much smaller than in the full coverage system.

6. Effects of embedded electric dipole layers in alkanethiolate self-assembled monolayers

In the previous chapter a method to calculate core level energies of dipolar alkylthiol SAMs, based on DFT and the initial state approach, has been presented and applied to two different test cases, namely a partially fluorinated alkylthiol and an alkylthiol with an embedded, dipolar ester group. On the example of these two functionalized SAMs the impact of chemical and electrostatic effects on XP spectra has been demonstrated. Now that we are confident about the applicability of the method described in the previous chapter, the same method is employed to study SAMs of ester-functionalized alkylthiols in more detail. Especially the impacts of chain length, and molecular orientation on electronic properties like the work function and core level energies are of interest and are addressed in this chapter. The systems are studied employing DFT calculations as well as numerous experimental techniques.

Author contributions:
The work presented in this chapter was a collaborative project between experimental and theoretical partners. It was initiated by the experimental groups of David L. Allara and Michael Zharnikov. Egbert Zojer and I contributed the simulation part of this work. We are currently preparing a manuscript about this work for publication in a scientific journal. As the experimental and theoretical results are closely connected and rely on each other for data interpretation I decided to include both parts of the joint work in this thesis. Only presenting my theoretical contribution would mean leaving out a significant and very important part of the overall findings of this project. I.e., the inclusion of the experimental results is crucial for putting the simulations into a proper scientific context. I, therefore, included the experimental sections of our joint manuscript, which is currently in preparation, in this thesis. I want to state that I did not perform the measurements presented in these sections, nor did I write the text. The detailed author contributions to the work presented in this chapter are stated in the following.

Nichole Sulliven, Peng Peng Zhang, Masato Maitani, Jean-Francois Morin, Paul S. Weiss and David L. Allara contributed to synthesizing the molecules and were also partly involved in measurements. Swen Schuster, Orlando Cabarcos and Michael Zharnikov prepared the SAMs, performed all shown XPS, NEXAFS, IR and work-function measurements and evaluated the experimental data. I performed all DFT

and MD calculations presented in this work. Manuel Vieider and Otello Roscioni taught me how to run MD simulations, which was crucial for the geometry preoptimization performed with MD in this work. Interpretation of the experimental and calculation results proved quite difficult and I enjoyed numerous extensive and lively discussions with Swen Schuster, Michael Zharnikov, David L. Allara and Egbert Zojer about the subject. The original idea to investigate mid-chain ester functionalized SAMs was conceived by David L. Allara and Michael Zharnikov. Egbert Zojer supervised the theoretical part of this work.

All sections related to experimental techniques and results, as well as the introduction, were written by Michael Zharnikov. He and Swen Schuster also prepared the figures depicted in these sections. Specifically, these sections are 6.1, 6.2, 6.3 and 6.4. These sections are directly taken from our joint manuscript, which is currently under preparation for future journal publication. I wrote the other sections, namely 6.5, 6.6, 6.7 and 6.8 and prepared all figures shown in these sections.

6.1. Introduction

It is well known that molecules can be adsorbed onto metal or semiconductor surfaces to form highly organized, oriented self-assembled monolayers (SAMs).[1,313] Molecular engineering of solid surfaces by SAMs to adjust a wide range of physical and chemical properties has been of interest for many applications, including sensors,[47,48] electronic devices,[314,315] selective crystal growth,[316,317] and nanolithography.[49–51] Recently, there has been growing interest in exploiting SAMs specifically to tailor the interfacial electronic properties on metal and semiconductor surfaces for device applications such as organic solar cells, light emitting diodes and organic thin film transistors.[24,47,58,59,61,62,64,72,74,114,280,315,318–325] The strategy involves self-assembly on an electrode surface via a precursor SAM molecule containing a functional group with an electric dipole to form a dipole layer which will in turn modify the electrode work function and its energy level alignment to the levels of the organic active layer and thereby impart significant improvements in charge injection and transport during device operation.[61,62,72,114,321,323,324] In addition to work function modifications in the case of metal electrodes, SAMs on semiconductor surfaces also can modulate electric transport of the sub-surface channel via introduction of a local electric field or new surface states.[47,319,320,322] This phenomenon is now utilized in sensor technology and field effect transistors.[48,319,326]

Within the above, SAM-based strategy of the work function tuning, a functional group with an electric dipole is usually attached to the molecular backbone as the terminal moiety.[17,27,28,61,101,115,279,327] The surface potential and work function (Φ) shift correlate well with the polarity of this moiety, following simple trends providing a practical recipe for work function engineering. Additional factors such as a contribution related to the bonding to the substrate and the effect of the molecular backbone were considered to be either more difficult to vary (bonding to the

substrate)[328] or of a minor importance (molecular backbone),[329,330] so that the adjustment of the terminal polar group became the most popular and frequently used strategy.

This approach has, however, essential drawbacks since the variation of the terminal polar group not only changes the work-function of the substrate, but, simultaneously, has the potential to modify the growth mode of the semiconductor film. The latter also has significant implications on the performance of the entire device. In addition, the terminal groups of the intermediate SAM can be affected by the growing semiconductor, especially if these groups are reactive, resulting in a change of their polarity and, consequently, diminishing their positive effect.

An alternative strategy to avoid the above drawbacks is the embedding of a polar group into the molecular backbone,[24,26,331] as in particular has been demonstrated recently by the example of thioaromatic SAMs with the embedded pyrimidine moiety.[26] Depending on the orientation of this group in the backbone, the work function of the system could be changed by either +0.57 or -0.42 eV (with respect to an unfunctionalized thioaromatic reference SAM) without changing the chemistry for docking to the substrate or the chemical composition of the SAM-ambient interface.[26] Significantly, the tuning of the work function is not the only effect of the embedded pyrimidine group, since it also induces a potential discontinuity inside the monolayer, electrically shifting the core-level energies in the regions above and below the dipoles relative to one another. The respective shift could be observed directly by X-ray photoelectron spectroscopy (XPS), reflected as the different binding energies (BEs) for the emissions associated with the both regions. This observation, along with a few others,[51,283–285] questions the generally accepted chemical shift model[282] in its specific applications to monomolecular films, and suggests that electrostatic effects are important as well. I.e., such electrostatic shifts are superimposed on the chemical ones and can even play a dominant role in certain cases.

Interestingly, the respective electrostatic effects in photoemission associated with embedded dipoles have been observed before for SAMs of mid-chain ester functionalized alkanethiols (ATs) on Au(111), and explained tentatively within a simple phenomenological model combined with DFT calculations of isolated molecules to determine the direction and magnitude of the ester group dipole in internal molecular coordinates.[25] Significantly, both the phenomenological model and the calculations were based on the structural data obtained by a careful characterization of the SAMs by quantitative infrared reflection spectroscopy (IRS), near-edge X-ray absorption fine structure (NEXAFS) spectroscopy, and ancillary ellipsometry. These measurements enabled to definitively establish the molecular chain structures and ester group orientations, along with film thickness.[25]

Given the success of the above study and considering the recent progress in theory regarding the understanding of electrostatic properties of SAMs,[22,26,281,330] we have decided to revisit the mid-chain ester functionalized ATs on Au(111). Along these lines, we have further expanded both the set of dipole-containing SAM precursors and the types of experiments used to characterize the electrostatic behavior of the SAMs, most importantly, performing work function measurements in addition to

studying core-level excitations. These measurements were performed by two different techniques, viz. via the secondary electron cut-off in ultraviolet photoelectron spectroscopy (UPS) and by non-contact, atomic force microscopy (NC-AFM). Note that the NC technique, applicable to metal, semiconductor and even insulator surfaces at near-atomic resolution,[332] provides a powerful, non-invasive way to obtain spatial surface information complementary to UPS work function data.[327,333] To provide further insight, the experimental studies are now combined with up-to-date quantum-mechanical modeling of actual metal-SAM interfaces.

6.2. Experimental methods

6.2.1. Sample preparation

Details for the synthesis of the ester molecules have been described previously.[25] The compounds studied and the abbreviations for their SAMs are listed in Table 6.1.[i] Note that to designate different systems, we will use the nomenclature CnECm for the mid-chain ester functionalized alkanethiols, where n and m denote the number of CH_x segments below and above the ester group. Additionally, C10E*C10 refers to a system in which the ester group has been reversed and C10EC4EC5 contains two ester groups. The -$(CH_2)_n$- segment close to the substrate will be referred to as the bottom segment, and the one at the ambient side as the top segment. Note also that the monolayers of C5EC10, C10EC5, C10EC10, C15EC5 have already been described to some extent in our previous publication,[25] whereas SAMs of C10EC15, C15EC10, C10E*C10, and C10EC4EC5 are new.

[i] In the final manuscript, which we are currently preparing for journal publication, this table will be placed in the Supporting Information.

Table 6.1.: SAM precursor molecules and their abbreviations used in this study.

compound	**abbreviation**
$SH(CH_2)_{11}CH_3$	C12
$SH(CH_2)_{15}CH_3$	C16
$SH(CH_2)_{17}CH_3$	C18
$SH(CH_2)_{19}CH_3$	C20
$SH(CH_2)_{21}CH_3$	C22
$SH(CH_2)_5COO(CH_2)_9CH_3$	C5EC10
$SH(CH_2)_{10}COO(CH_2)_4CH_3$	C10EC5
$SH(CH_2)_{10}COO(CH_2)_9CH_3$	C10EC10
$SH(CH_2)_{10}COO(CH_2)_{14}CH_3$	C10EC15
$SH(CH_2)_{15}COO(CH_2)_4CH_3$	C15EC5
$SH(CH_2)_{15}COO(CH_2)_9CH_3$	C15EC10
$SH(CH_2)_{20}COO(CH_2)_4CH_3$	C20EC5
$SH(CH_2)_{10}OOC(CH_2)_9CH_3$	C10E*C10
$SH(CH_2)_{10}COO(CH_2)_4COO(CH_2)_4CH_3$	C10EC4EC5

Vacuum deposited Au on a mica substrate (Agillent / Molecular imaging, Tempe, AZ) was used for the AFM studies. After hydrogen flame annealing, the substrate was immersed into a 0.1 mM thiol solution in absolute ethanol (Pharmco) for 24 h. Upon removal from solution, the surface was thoroughly rinsed with dichloromethane, acetone and ethanol, then dried under a nitrogen flow, and immediately loaded into the UHV AFM chamber. Thermally evaporated Au/Cr (200 nm/10 nm thickness, respectively, ≈1-1.5 nm rms surface roughness of the final Au film) on native oxide covered Si wafers was used for the IRS and photoemission studies. The pressure of the thermal evaporator system was kept at or below 5 x 10^{-8} Torr during the entire deposition process. The substrate was immersed directly into the thiol solution after removal from the thermal evaporator. For transport to synchrotron for the XPS and UPS data collection, the freshly made samples were immediately put into clean fluoroware wafer containers and packed in plastic bags

sealed under argon purge for transport. This procedure has proven to be very effective for keeping the sample integrity.

6.2.2. Sample characterization: General comments

The mid-chain functionalized and reference SAMs were characterized by infrared reflection spectroscopy (IRS), high resolution XPS (HRXPS), UPS, AFM, and Kelvin probe measurements using NC-AFM. All experiments were performed at room temperature. The HRXPS, UPS, and NC-AFM measurements were conducted under ultra-high vacuum (UHV) conditions (base pressure < 5 x 10^{-10} Torr). The experiments were complemented by theoretical simulations.

6.2.3. Infrared reflection spectroscopy and associated spectral simulations

IR spectra were obtained using a customized Fourier transform infrared spectrometer (BioRad FTS-7000, Digilab, Randolph, MA) with the sample and detector optics housed in an external N_2 purge box. The signal was collected by a liquid N_2 cooled MCT detector. Spectra were obtained using p-polarized light at an 86° incidence angle with 2 cm^{-1} resolution and averaged over 800 scans to improve the signal to noise ratio.

Details of the spectral simulation procedures have been previously presented[25] and the procedures in the present case follow the previous work in exact detail. The simulations utilize a combination of experimental and theoretical data. In brief, isotropic optical function spectra were obtained from transmission spectra of pressed KBr pellets containing precisely known concentrations of pure, polycrystalline thiol (or disulfide as was convenient). Vibrational assignments and transition moment directions were made with the help of spectra calculated from DFT theory for isolated molecules fixed in a planar, all-trans conformation. The isotropic optical function spectra were converted to anisotropic tensor spectra by use of the transition moment directions and the tensor spectra were then used to simulate spectra of an assembly of oriented molecules at selected chain tilt angles to the surface normal and twist angles of the chain planes around the long molecular axis.

6.2.4. Photoemission experiments

HRXPS measurements were performed at the bending magnet beamline D1011 of the MAX-IV synchrotron radiation facility in Lund, Sweden, using a SCIENTA SES200 electron energy analyzer. The spectra were recorded in the Au 4f, S 2p, C 1s, and O 1s regions with a special emphasis on the C 1s range to monitor the electrostatic effects. The spectra acquisition was performed in normal emission geometry, at photon energies (PEs) of either 350 or 580 eV. The binding energy (BE) scale of every spectrum was individually calibrated using the Au $4f_{7/2}$ emission line of the underlying Au substrate at 83.95 eV.[334] The energy resolution was 70-100 meV,

which is noticeably smaller than the full width at half maximum (fwhm) of the spectral features relevant in this study. The spectra were fitted by symmetric Voigt functions and either Shirley-type or linear backgrounds. For all samples, the same fit parameters were used for identical spectral regions for a given photon energy.

6.2.5. UPS experiments

Work functions of the samples were determined by measuring the secondary electron cutoff of the UP spectra following a standard approach.[283] The experiments were performed at the Max IV facility, using the same beamline and experimental station as in the case of the HRXPS measurements. The photon energy was set to 50 eV. The samples were biased by -25.6 V relative to ground so that the low energy portion of the spectrum could be observed. The positions of the cutoffs in the samples were referenced to those of C16/Au and freshly sputtered gold.

6.2.6. AFM measurements: lateral force imaging

Molecular lattice images were taken by contact mode AFM using a RHK 350 AFM/STM scan head with force modulation probes (PPP-FMR, Nanosensors, Switzerland; cantilever force constant $\approx$ 2.8 N/m). Typical images were obtained at $\approx$ 5 nN normal force (including the capillary force between the tip and the sample) at scan rates from 50 to 200 nm s^{-1}. Due to the stick-slip friction characteristics, lateral force images can display atomic features that are not necessarily shown in the topography.

6.2.7. Surface potential (Kelvin probe) measurements

Experiments were conducted in a Jeol JSPM-4500A AFM system equipped with SPM 100 electronics and a PLL Pro universal AFM controller (RHK technologies, Troy, MI). All data were taken using conducting Pt-Ir coated Si cantilevers (PPP-NCHPt, Nanosensors, Switzerland) with typical spring constants and Q-factors of 40 N/m and 330 kHz in air (Q-factor $\approx$20 k in UHV). The tips were thoroughly rinsed by anhydrous dichloromethane and absolute ethanol before loading into the UHV system to remove any organic contaminants from the surface and then blown dry by nitrogen gas. The probe was further degassed under UHV at 150°C for 2 h by heat radiation from a nearby tungsten filament. This provided a constant probe tip surface which gave reproducible CPD measurements on a standard alkanethiolate SAM.

During each experiment, the approach of the tip to the surface was done cautiously to avoid any damage or crashing into the surface. To ensure that the tip condition was unchanged, the work function of a clean Au{111} surface, preloaded and stored in the UHV chamber, was measured before and after characterization of each SAM. Differences between the surface potential values of the SAMs and Au{111} references yielded a consistent set of data for all the SAMs.

The tip was scanned in non-contact mode by oscillating it close to its resonant frequency with the tip-surface interaction detected by either a change of its vibrating

amplitude or a shift of its oscillating frequency. For the reported measurements, the frequency modulation (FM) mode was used , in which the vibrating amplitude is kept constant by a phase shifter and automatic gain controller applied on the probe drive. The frequency shift is then measured by a phase lock loop (PLL). Simultaneous topography images were achieved by regulating the tip-sample distance to keep a constant frequency shift. Data were obtained from at least three independent samples for each SAM on ≈10 different spots on each surface and the final values of the intercept for each SAM taken as the average over all the measurements. Each measurement gives the contact potential difference (CPD) between the tip and the sample surfaces. The work functions ($\Delta\Phi_{\mathrm{work}}$) for each SAM were further calculated as as $\Delta\Phi_{\mathrm{work}}$ = $(\mathrm{CPD})_{\mathrm{SAM}}$ - $(\mathrm{CPD})_{\mathrm{Au}}$, where the bracketed quantities represent the averaged CPD values for multiple measurements of a given SAM and its companion Au{111} reference.

6.3. Experimental results

6.3.1. SAM structure

In our previous study, the orientation of the alkyl chain segments and the embedded ester moiety in the CnECm SAMs were deduced from the best fits of spectral simulations, based on classical electromagnetic theory, to experimental IRS data along with the analysis of the NEXAFS spectra.[25] The results of both procedures agreed within experimental error to give an overall average of alkyl chain tilt from the surface normal of 31(±4)° and a chain twist around the long axis of 60(±5)° (see Figure 6.1). Note that the above values are more strict for the bottom -(CH_2)- segments which, within experimental error, exhibit conformational ordering and orientation identical to those reported previously for the alkyl chains in non-substituted AT (NSAT) SAMs on Au(111), while the top segments are significantly more conformationally disordered. However, the both segments are generally aligned in an extended form as shown in Figure 6.1, where a schematic of the orientation of the CnECm molecules in the respective SAMs is given, along with the definitions of the tilt and twist angles (right hand side).

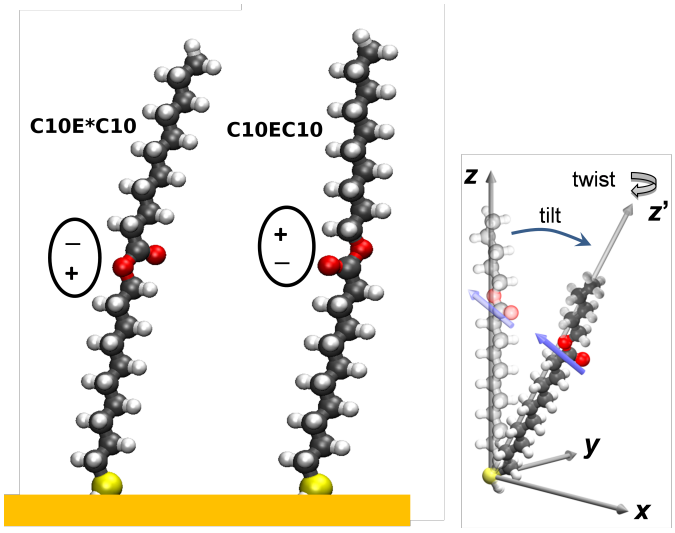

Figure 6.1.: Schematics of a fully extended all-trans isolated chain for an embedded ester molecule positioned on a substrate surface plane. The coordinate system on the right shows the molecule on a surface (xy-plane) with the long axis of the molecule tilted away from the z-axis and the chain plane twisted around the long molecular axis. When the molecule is fully upright along the z-axis and not twisted the CH_2 plane lies in the xz-plane. The directions of the z-projections of the molecular dipoles for the C10EC10 and C10E*C10 molecules are shown on the left.

In addition, the experimental data of the previous study[25] suggest that the O=C=O ester group is coplanar with the C-C-C plane of the bottom and top -(CH_2)- segments (a certain degree of conformational disorder notwithstanding).

Significantly, the above geometry defines the orientation of the ester group and, consequently, the direction of the related dipole moment which appears to be strongly tilted with respect to the surface normal, as shown in Figure 6.1. Consequently, its projection on the z-axis (i.e. the surface normal), defining the potential discontinuity within the SAM, depends strongly on the exact adsorption geometry which, even though similar on the average (see below), can differ to some extent for the different, mid-ester functionalized films.

In the present study all the IR spectra of the CnECm SAMs have nearly identical patterns to those in the previous study.[25] Applying the same methods of analysis as used previously gives chain orientations within experimental error of the values above, viz. -(CH_2)- chain tilt from the surface normal of 31($\pm$4)° and a chain twist around the long axis of 60($\pm$5)°. Since the IR spectral pattern of the reversed ester film, C10E*C10 however, was slightly different than for the CnECm SAMs, we present here the respective experimental spectra and best fit simulations (Figure 6.2).

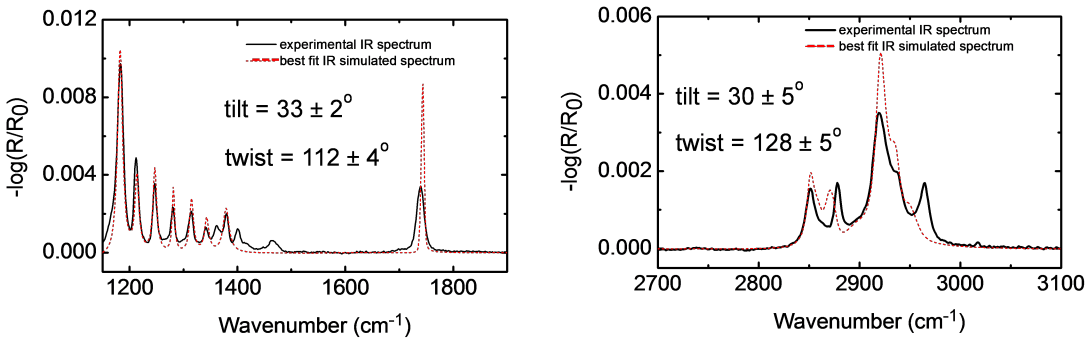

Figure 6.2.: IR spectra of the C10E*C10 reverse ester SAM: experimental (full black line), best-fit simulation (dashed red line). The best fit values for the tilt and twist angles of the -(CH_2)- chain parts with estimated errors are shown in the graphs. The low frequency data (left) shows modes for both the alkyl chains and the ester group while the high frequency data shows the C-H stretch modes. The best fits represent global fits so not all modes have equal errors as noted particularly for the C=O stretch near 1730 cm^{-1}.

The overall result is that, on the average, the -(CH_2)- segments of the C10E*C10 film are tilted from the surface normal at 32(±4)° with a chain twist around the long axis of 120(±4)°, which can also be considered as -60 (±4)° in view of the symmetry. These values are, within the error ranges, very close to those obtained for the set of CnECm monolayers and establish that inverting the ester group orientation in the alkyl chain has a negligible effect on the overall SAM structure.

In order to definitively establish if there is a uniform molecular arrangement in both the standard (CnECm) and reverse ester SAMs on the substrate surface, lateral force AFM measurements were performed. Typical images for the C10EC10 and C10E*C10 monolayers are shown in Figure 6.3.

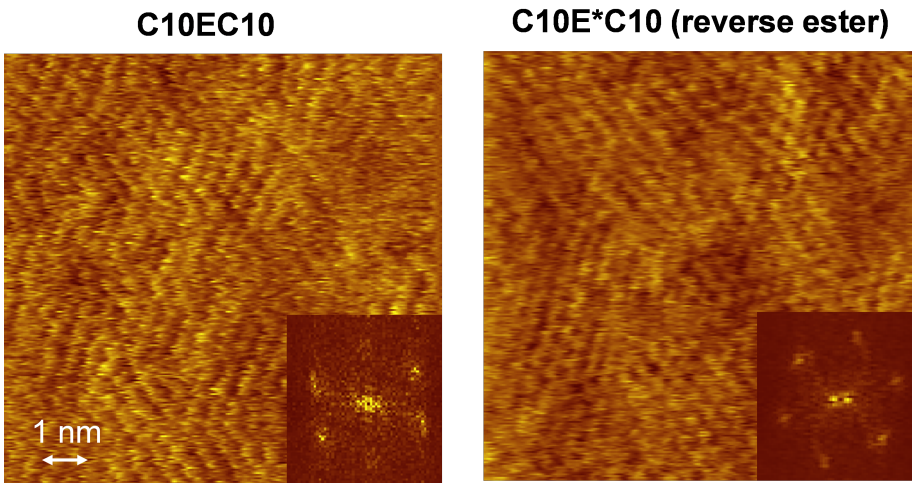

Figure 6.3.: Lateral force AFM topography images of the C10EC10 and C10E*C10 SAMs with 2-D Fourier transforms shown in the insets. Both images clearly show a hexagonal pattern which corresponds to the standard $\left(\sqrt{3}\text{ x }\sqrt{3}\right)$ R30° arrangement with a lattice spacing of ≈0.50 nm.

Both images confirm an ordered arrangement with the adsorbates in a $\left(\sqrt{3}\text{ x }\sqrt{3}\right)$ R30° hexagonal lattice with the expected ≈0.50 nm nearest neighbor spacing, which corresponds to a surface density of ≈4.60 molecules nm^{-2}. Such a lattice is typical of the NSAT SAMs on Au(111) surface, apart from the c(4 x 2) modulation of the $\left(\sqrt{3}\text{ x }\sqrt{3}\right)$ R30° structure, resulting in the $\left(2\sqrt{3}\text{ x }3\right)$rect arrangement.[87,335,336] It is difficult to say whether such a modulation occurs in the given case. The main conclusion is, however, that both standard and reverse ester SAMs exhibit long-range structural order, with the structure being nearly identical to that of the non-substituted alkylthiol SAMs on the same substrate. Another important finding is that the reverse ester SAM has a virtually identical arrangement on the Au(111) surface as the standard embedded ester monolayers, which is expected given the almost identical average orientation of the -(CH_2)- segments in these two types of SAMs.

6.3.2. Electrostatic effects: photoemission

The C 1s XP and HRXP spectra of the NSAT SAMs on the Au(111) substrate exhibit a single emission at a BE of 284.85 - 285.0 eV, accompanied by two weak shoulders, which are hardly perceptible, especially in the XPS case, and can only be recognized within a very detailed analysis.[16,110] The binding energy of the emission depends slightly on the length of the molecular backbone and increases somewhat with chain length (≈17 meV per C atom).[16] In contrast to these reference systems but in agreement with our previous study[25] and a recent work on mid-chain substituted thioaromatic SAMs[26] the C 1s HRXP spectra of all the CnECm SAMs exhibit not one but two major -(CH_2)- related emissions. The two peeks are associated with the bottom and top segments. In Figure 6.4, where the C 1s HRXP spectrum of the

C10EC10 SAM is presented as a representative example of the entire CnECm series, they are clearly resolved along with the peaks associated with the carbonyl and ether carbon. The individual emissions are color-coded according to the schematics of the C10EC10 molecule shown in the inset of Figure 6.4 with individual parts of the molecule marked by specific colors.

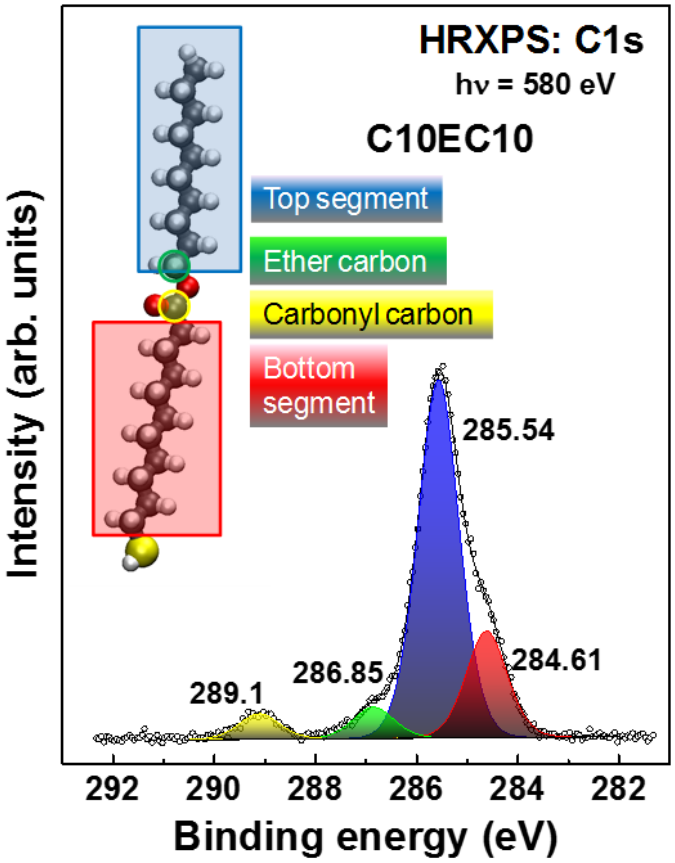

Figure 6.4.: Decomposition of the C 1s HRXP spectrum of the C10EC10 SAM, representative of the entire CnECm series. The individual emissions associated with individual parts of the C10EC10 molecule are color-coded using a schematics of this molecule with the individual parts marked by specific colors. Binding energies of the characteristic emissions are given.

The difference between the BE positions of the emissions associated with the bottom and top -(CH_2)- segment is ∼0.9 eV. This difference cannot be explained within the general concept of chemical shifts since both segments are chemically identical. The reason for the difference is, as mentioned above, a pure electrostatic effect, viz. a potential discontinuity inside the monolayer associated with the embedded dipolar ester groups.

The occurrence of two different emissions for the chemically identical top and bottom -(CH_2)- segments is additionally illustrated by Figure 6.5, where the C 1s HRXP spectra of the CnEC5 series are presented. Analogous data for another

representative series (C10ECn) can be found in Figure 6.6.[ii]

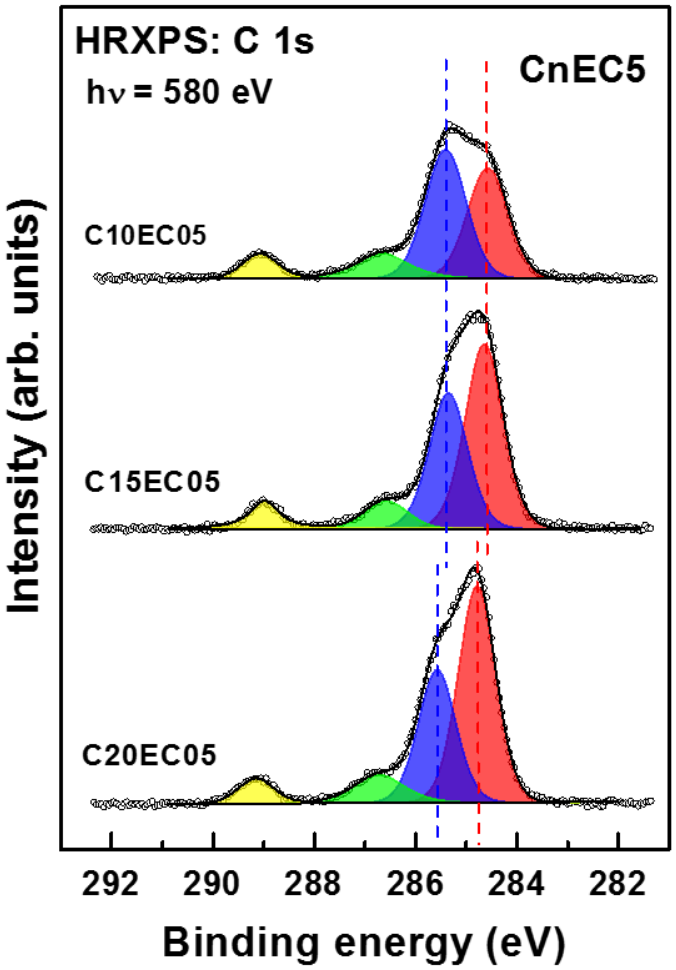

Figure 6.5.: C 1s HRXP spectra of the CnEC5 SAMs with n = 10, 15 and 20. The spectra are decomposed into individual emissions which are color-coded, viz. bottom -(CH_2)- segment (red), top -(CH_2)- segment (blue), ether carbon (green), and carbonyl carbon (yellow). The vertical dashed lines mark the BE positions of the emissions associated with the top and bottom -(CH_2)- segments as a guide to the eye.

[ii] In the final manuscript, which we are currently preparing for journal publication, this figure will be placed in the Supporting Information.

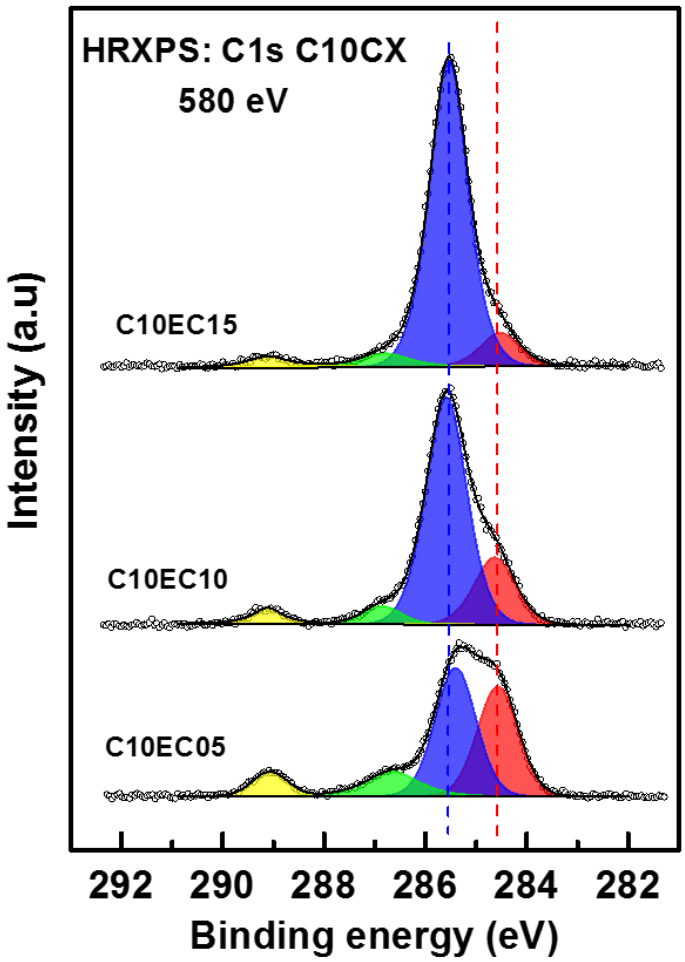

Figure 6.6.: C 1s HRXP spectra of the C10ECn SAMs at n = 5, 10 and 15. The spectra are decomposed into individual emissions which are color-coded, viz. bottom -(CH_2)- segment (red), top -(CH_2)- segment (blue), ether carbon (green), and carbonyl carbon (yellow). The vertical dashed lines mark the BE positions of the emissions associated with the top and bottom -(CH_2)- segments.

Whereas the BE positions and intensities of the ether and carbonyl peaks are persistent over the CnEC5 series (Figure 6.5), as can be expected (apart from a minor shift in C20EC5, which will be explained later on) - since the positions of these atoms with respect to the SAM-ambient interface do not change, there is a noticeable intensity redistribution within the major feature comprised of the emissions related to the -(CH_2)- top and bottom segments. According to the spectral decomposition procedure performed consistently over the entire series (see Section 6.2), this redistribution stems from the increasing contribution of the bottom segment with increasing n, whereas the contribution of the top segment, appearing at a ∼0.8 eV higher BE, does not change. Such a behavior is understandable since the photoemission signal from the top segment of the constant length is persistent over the series, whereas the photoemission signal from the bottom segment increases

with increasing n. This signal is, however, strongly attenuated by the top segment overlayer resulting in its comparably low intensity even though the bottom segment is considerably longer than the top one. The case of the reverse ester is presented separately in Figure 6.7, along with the data for the C10EC10 and C16 SAMs given for comparison.

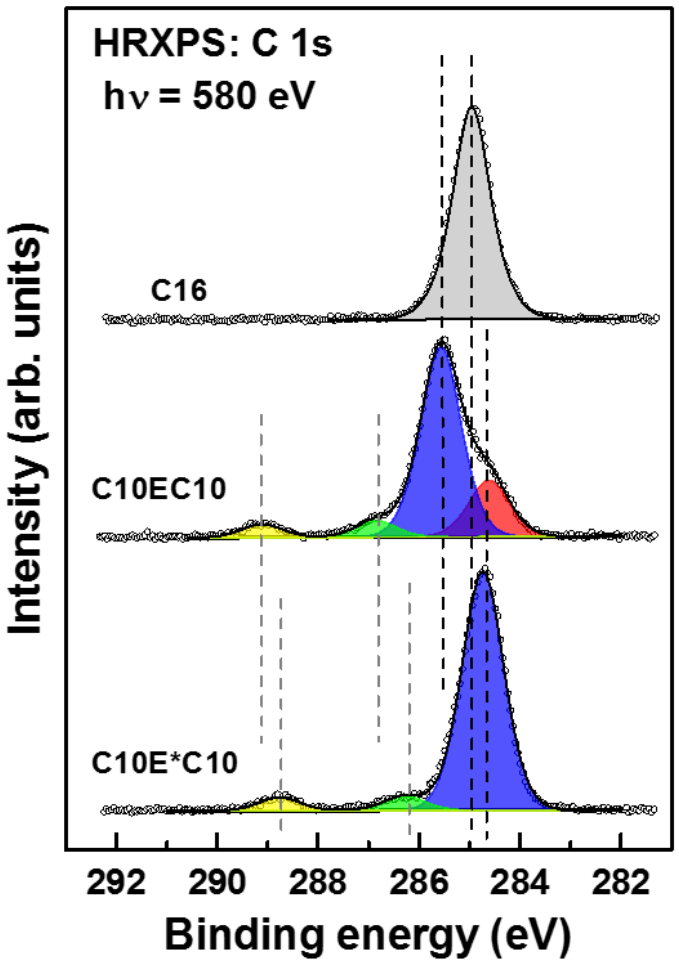

Figure 6.7.: C 1s HRXP spectra of the C16, C10EC10, and C10E*C10 SAMs. The spectra of the two latter films are decomposed into individual emissions which are color-coded, viz. bottom -(CH_2)- segment (red), top -(CH_2)- segment (blue), ether carbon (green), and carbonyl carbon (yellow). The vertical dashed lines mark the BE positions of the emissions as a guide to the eye.

The spectrum of the C16 film, representative of the NSAT films, exhibits a single emission peak at a BE of 284.95 eV. The spectrum of the C10EC10 SAM shows the two major emissions at 284.61 and 285.54 associated with the bottom and top -(CH_2)- segments, respectively, with much lower intensity of the former feature because of the strong attenuation of the respective signal by the top-segment overlayer at the given kinetic energy of the photoelectrons. In addition, there are the less intense but clearly perceptible ether and carbonyl peaks. In contrast, the spectrum

of the C10E*C10 monolayer is dominated by a single emission at ∼284.65 eV which, presumably, contains contributions from both bottom and top -(CH_2)- segments, with the latter contributions being much more intense, similar to the C10EC10 case. The presence of the single emission only suggests that there is almost no BE shift between the peaks associated with bottom and top -(CH_2)- segments for the C10E*C10 SAM implying that the reverse ester does not create a potential discontinuity inside the film . The effect of the reversal is, however, well visible (Figure 6.7) since the major emission, representative of the top -(CH_2)- segment, and the ether and carbonyl peaks shift to lower binding energies considerably upon the reversal of the ester group. As to the absolute BE shift associated with the embedding of the reverse ester, it is just a matter of reference. In particular, instead of the BE of the bottom segment peak for the CnECm and C10E*C10 films, the BE of the sole C 1s peak for the NSAT SAMs with the same total number of C atoms in the backbone can be considered. Such a reference will diminish the upward BE shift associated with the standard ester orientation (C10EC10) but results in a reasonable downward BE shift in the case of the reverse ester, as seen in Figure 6.7. A careful analysis of the HRXP spectra acquired at both 350 and 580 eV gives values of +0.57 and -0.4 eV for the shifts of the top segment C 1s emission for the C10EC10 and C10E*C10 SAMs, respectively, as compared to the C20 monolayer.

The above shifts can also be monitored in the overview diagram in Figure 6.8, presenting the C 1s BEs associated with the -(CH_2)- chain or segments for all SAMs studied.

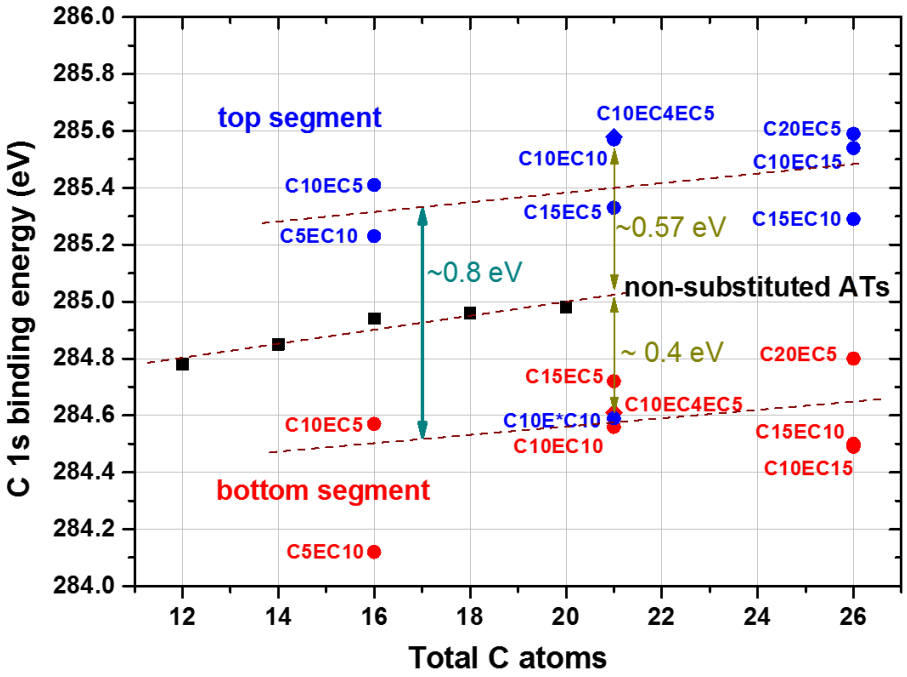

Figure 6.8.: Graphical summary of the C 1s BE data for the emission associated with the alkyl chain in the NSAT SAMs (black squares) as well as the emissions related to the top and bottom -(CH_2)- segments in the mid-ester functionalized AT SAMs (blue and red symbols respectively): CnECm and C10E*C10 (full circles), C10EC4EC5 (rhombus). The dashed straight lines are guides for the eyes. The energy differences between the individual peaks, viz. the average value for CnECm and the derived values for C10EC10 and C10E*C10 with respect to C20 are shown by the vertical arrows.

According to this diagram, the C1s BE shift between the bottom and top segments is ∼0.8 eV for most of the mid-ester functionalized SAMs, with some scattering within ±0.2 eV for the different systems. The C 1s BEs for the top and bottom -(CH_2)- segment of the ester SAMs display a similar dependence on the total backbone length as the C 1s BE for the NSAT monolayers with a slight increase of the binding energy with increasing backbone length.

The overview diagram in Figure 6.8 contains also the results for the double ester SAM, C10EC4EC5, which have not been discussed so far. The C 1s HRXP spectrum for this system is presented in Figure 6.9, along with the data for the C10EC10 and C15EC5 monolayers given for comparison.

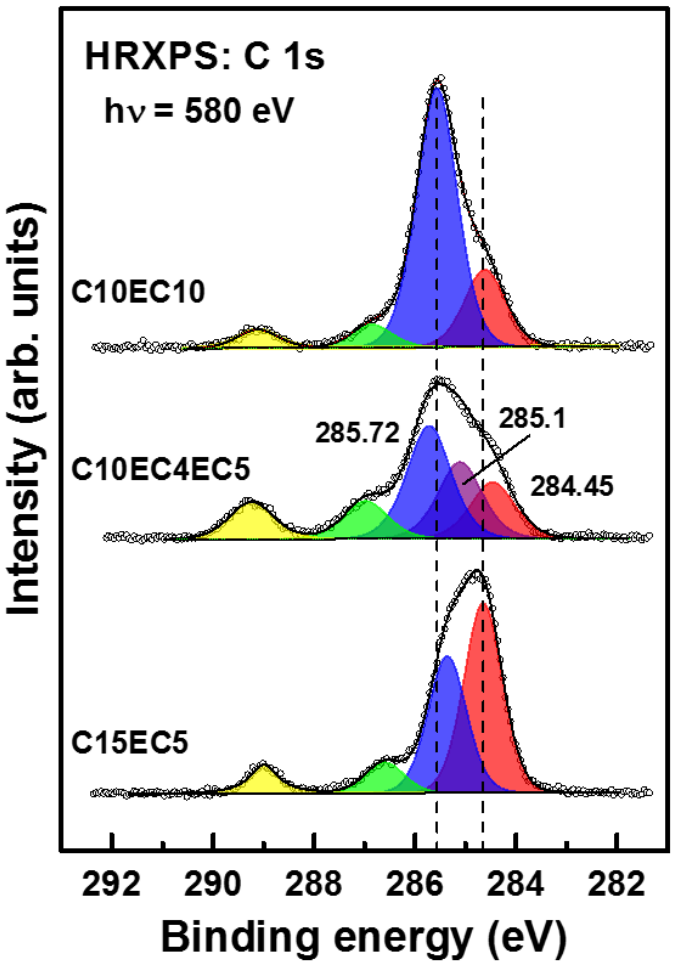

Figure 6.9.: C 1s HRXP spectra of the C10EC10, C10EC4EC5, and C15EC5 SAMs. The spectra are decomposed into individual emissions which are color-coded, viz. bottom and middle (C10EC4EC5) -(CH_2)- segment/segments (red), top -(CH_2)- segment (blue), ether carbon (green), and carbonyl carbon (yellow). The vertical dashed lines mark the BE positions of the emissions as a guide to the eye.

The spectrum of the C10EC4EC5 SAM is dominated by a broad, asymmetric feature related to the -(CH_2)- segments and accompanied by the ether and carbonyl peaks. The latter peaks are more intense than the analogous emissions in the spectra of the C10EC10 and C15EC5 monolayers, which is understandable since the C10EC4EC5 SAM contains two ester groups instead of one. As to the major broad feature, its decomposition in individual emissions is non-trivial and, in our opinion, cannot be performed in non-equivocal fashion but only tentatively, since these emissions are undistinguishable in the overall spectral envelope. Following general logics and based on the data for the CnECm SAMs, three emissions associated with the bottom, middle, and top -(CH_2)- segments can be assumed within the joint envelope, with the intensity relations mimicked from the spectra of the C10EC10 and C15EC5 monolayers. Indeed, the top/bottom relation for C10EC10 corresponds to

the (top+middle)/bottom relation for C10EC4EC5. Also, the top/bottom relation for C15EC5 corresponds to the (top)/(middle+bottom) relation for C10EC4EC5. The resulting decomposition of the asymmetric broad feature for the C10EC4EC5 SAM by three emissions is presented in Figure 6.9. Whereas the BE energy shifts with respect to the middle segment emission can be considered as tentative only (see e.g. a decomposition by two emissions only in Figure 6.10[iii]), the BE energy shift between the emissions associated with the top and bottom -(CH_2)- segments, ∼1.25 eV is presumably more reliable since it is closely related to the overall spectral shape. This value is noticeably higher than the maximum shift for the CnECm films (∼1.05 eV) but smaller than the double average shift in these films (∼1.6 eV), suggesting a clear but limited effect of the double embedded ester.

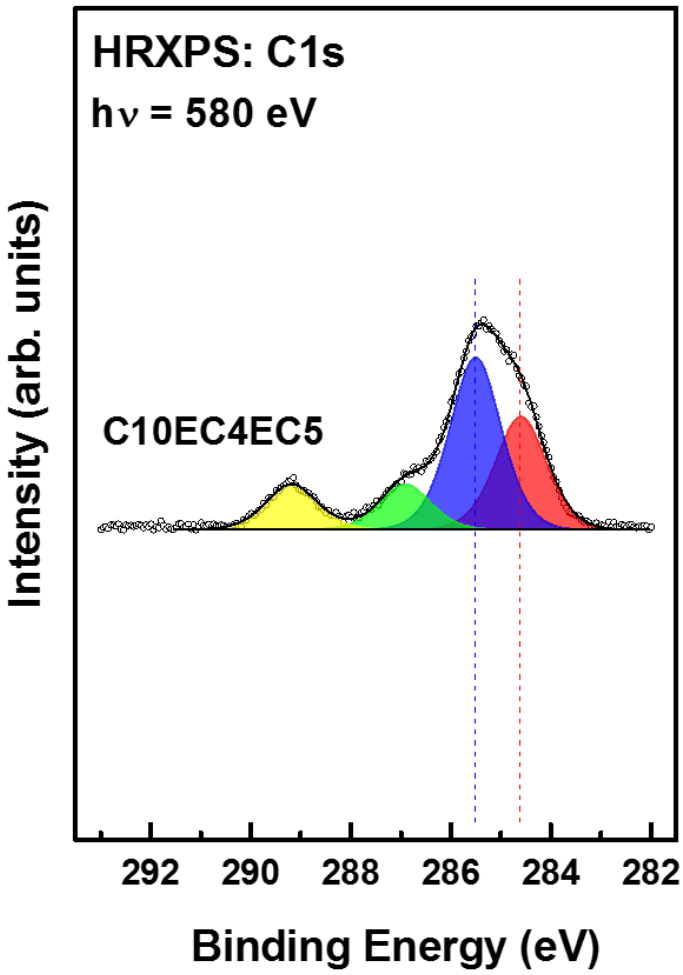

Figure 6.10.: C 1s HRXP spectra of the C10EC4EC5. The spectra are decomposed in individual emissions which are color-coded, viz. bottom + middle (red), and top -(CH_2)- segments (blue), ether carbon (green), and carbonyl carbon (yellow). The vertical dashed lines mark the BE positions of the emissions as a guide to the eyes.

[iii] In the final manuscript, which we are currently preparing for journal publication, this figure will be placed in the Supporting Information.

6.3.3. Electrostatic effects: work function

The embedding of the dipolar ester group into the alkyl backbone should affect the work function of the entire system. An overall graphical summary of $\Delta\Phi$ values (relative to the value for the C16 monolayer, viz. -0.85 eV with respect to the clean gold substrate) is provided in Figure 6.11 where both the main data set taken from the UPS cutoff measurements and the limited set obtained from surface potential AFM are shown in separate graphs.

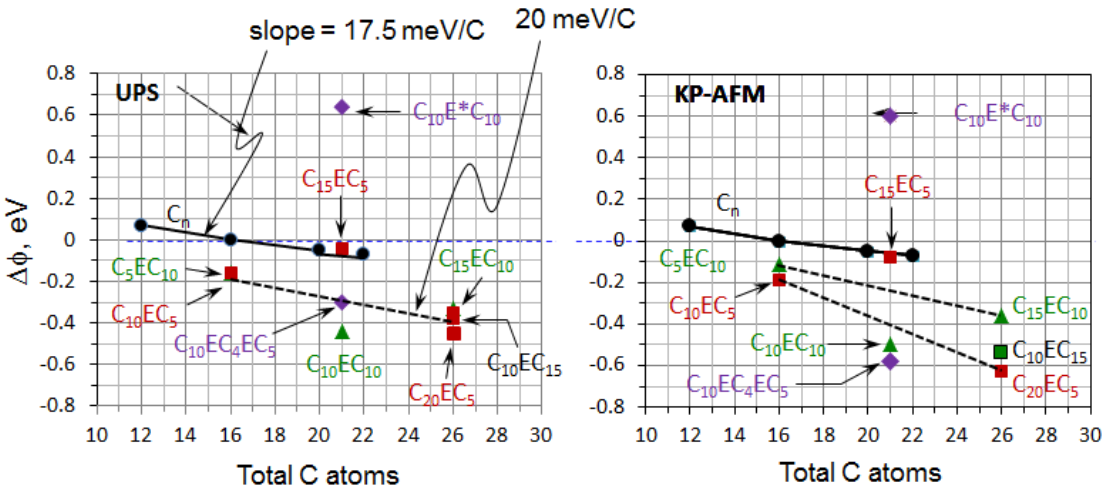

Figure 6.11.: Graphical summary of work function (Φ) data. In both panels the values of Φ are given in terms of $\Delta\Phi$, defined as the difference between the work function of each SAM and the work function of a corresponding unsubstituted alkanethiolate SAM (Cn) with the same number of carbon atoms in the molecule. Thus for SAMs with values along $\Delta\Phi$=0 there is no shift relative to the alkanethiolate SAM while values with $\Delta\Phi$<0 correspond to SAMs with lower work functions than the alkanethiolate SAMs. The black dots represent unsubstituted alkanethiolate SAMs and the other data points are labelled with the specific ester functionalized SAM. **Left panel:** the major set of data which was obtained by PES measurements at two different photon energies (see text for details). The slopes of the two main linear correlations are shown by arrows. **Right panel:** the smaller set of data obtained from surface potential AFM measurements.

The agreement between the UPS and AFM derived values is quite good considering intrinsic differences between these two techniques and the fact that the experiments were absolutely independent and performed on different samples.

The work function of the NSAT SAMs decreases with increasing length of the molecular backbone, which can be tentatively explained by a progressive change in the polarizability of the alkyl matrix.[122,329] A similar general tendency is observed for the ester SAMs. Significantly, there is a noticeable $\Delta\Phi$ shift of -(0.2-0.35) eV between the values for the NSAT films and CnECm SAMs, manifesting the effect of the embedded ester group. The only exception is the C15EC5 monolayer for

which no shift is observed. The $\Delta\Phi$ values for the C10EC10 and C10E*C10 SAMs exhibit qualitatively symmetric behavior with respect to the reference value for the NSAT film with the same total amount of C atoms in the backbone: $\Delta\Phi$ is negative for C10EC10 (-0.4 eV) and positive for C10E*C10 (+0.65 eV) . Quantitatively, the absolute values of $\Delta\Phi$ are not equal for the standard and reverse positions of the embedded ester group, similar to the asymmetry observed for the C 1s BE shift, but in the different direction. As to the double ester system, the $\Delta\Phi$ value for the C10EC4EC5 SAM is, on average, comparable to that of the C10EC10 monolayer (almost the same total number of C atoms), so that the effect of the additionally embedded ester group on the work function of the entire system is very weak, if any at all.

6.4. Discussion of experimental results

All mid-chain ester functionalized AT SAMs of this study exhibit pronounced electrostatic effects associated with the embedded dipole group, in agreement with the results of the previous work dealing with some of these systems[25] as well as of a recent study of analogous thioaromatic monolayers with embedded pyrimidine groups.[26] The electrostatic effects are manifested in two ways, viz. as a BE shift of the C 1s emissions related to the bottom and top -(CH_2)- segments of the molecular backbone and as a change in the work function of the entire system.

A BE shift of the C 1s emissions related to the chemically identical bottom and top -(CH_2)- segments is of particular importance for the correct description of photoemission from SAMs since it suggests that the general concept of the chemical shift can be applied to these systems to a limited extent only. In some selected cases, as e.g. in the given study and some recent work,[25,26,51,269,283–285] this concept is not sufficient for the adequate description of the XP spectra and should be combined with electrostatic considerations. The reason for this behavior is the insulator character of the SAM matrix, enabling creation of an electrical potential distribution, including its discontinuity, inside the monolayer. Such a discontinuity can be in particular created by a layer of dipolar groups embedded into the backbone of the SAM constituents at a certain position, as occurs in the given case, for the mid-chain ester functionalized AT SAMs. Accordingly, the core-level energies in the region above and below the dipoles differ relative to one another, which is reflected in the kinetic energy of the photoelectrons and, subsequently, in the BE of the respective emissions in C 1s XP spectra. Such a BE difference observed experimentally for most of the CnECm SAMs is ∼0.8 eV (see Figure 6.8), correlating nicely with a simple theoretical estimate of 0.81 (±0.06) eV based on the orientation of the ester groups in the SAMs and their dipole moment.[25] A certain variation in the BE difference value (±0.2) eV observed for the CnECm SAMs can be tentatively explained by specific deviations from the average adsorption geometry. Since the dipole associated with the embedded ester group is strongly inclined with respect to the surface normal, even small structural differences can result in noticeable change of its projection onto this normal, redefining the value of the potential discontinuity.

An alternative reference for the C 1s BE shift in the ester SAMs is the BE of the analogous emission in the NSAT monolayer with the same total number of C atoms in the backbone. Surprisingly, the latter BEs, lie approximately halfway between the values for the bottom and top segments in the ester SAMs, as shown in Figure 6.8. A close analysis of this figure suggests that the introduction of the ester moiety into the AT backbone does not only result in the C 1s BE shift between the bottom and top -(CH_2)- segments but also in a lowering of the BE of the bottom segment (by 0.2-0.3 eV) with respect to the value for the NSAT monolayer with the same number of C atoms as the bottom segment of the ester SAM. This is illustrated by Figure 6.12 where the C 1s BE values for the ester SAMs are arranged according to the length of the bottom -(CH_2)- segment and compared to the NSAT of the same length.

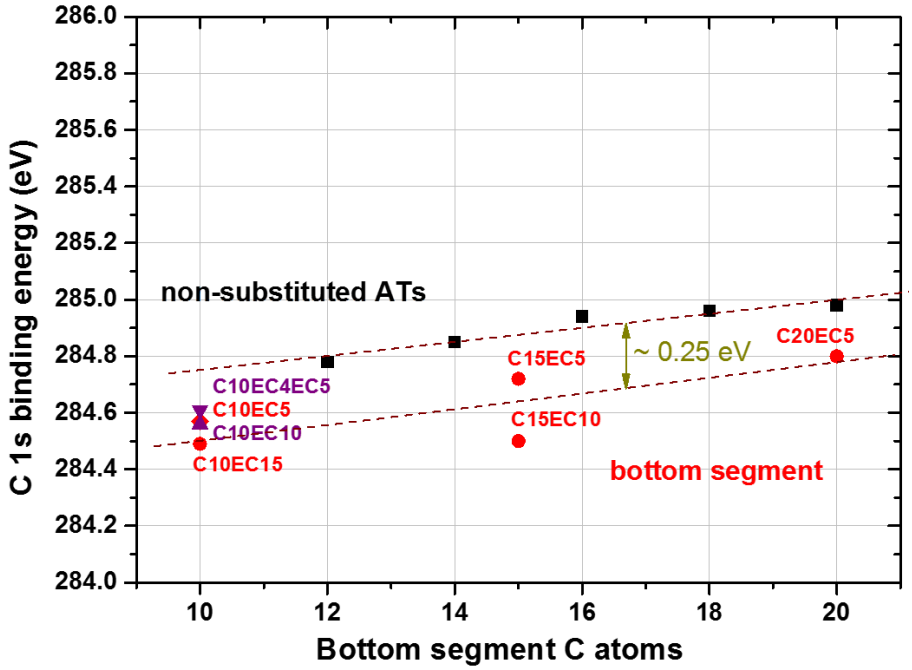

Figure 6.12.: Graphical summary of the C 1s BE data for the emission associated with the alkyl chain in the NSAT SAMs (black squares) as well as the emissions related to the bottom -(CH_2)- segments in the mid-ester functionalized AT SAMs (red and lilac symbols). The symbols are arranged either in accordance with the number of C atoms in the backbone (NSAT SAMs) or in the bottom alkyl segment (ester SAMs). Different symbols are used for C10EC4EC5 (lilac down triangle) and C10EC10 (lilac up triangle) to distinguish from the other systems.

A probable explanation for this BE difference, which is also substantiated by the theoretical results discussed in the following sections, is a difference in the bond dipole between ester SAMs and NSAT monolayers. If the Au-S-C bond varies slightly for different SAMs this will affect the effective z-dipole component, energetically shifting the binding energies of the whole molecule independently of the ester dipole effect. Thus, the BE difference manifests itself already in the respective bottom

segments and not only in the top alkyl part. As to screening of the photoemission hole by the substrate electrons, it is especially strong for the short chain molecules, following the standard 1/r dependence of the Coulomb potential, explaining, in particular, the exceptionally low C 1s BE value for the bottom -(CH_2)- segment in the C5EC10 film (Figure 6.8).

The use of the NSAT SAMs as the reference results in the smaller value of the electrostatic shift associated with the top -(CH_2)- segment in the ester SAMs, viz. +(0.3-0.55) eV, but is more consistent with the behavior of the "reverse ester", C10E*C10 film. With respect to the NSAT reference, the reversal of the embedded dipole direction, performed in this system, results in a shift of ca. -0.4 eV, in contrast to the value of +0.57 eV for the C10EC10 monolayer. Such a quasi-symmetric behavior following the direction of the embedded dipole is logical and expectable, in contrast to the lack of any perceptible C 1s BE shift for the top -(CH_2)- segment of the C10E*C10 SAM with respect to the bottom segment (see Figure 6.7).

The quasi-symmetric behavior of the photoemission shift with respect to the direction of the embedded dipole correlates nicely with the $\Delta\Phi$ values for the C10EC10 and C10E*C10 SAMs, viz. -0.4 eV for C10EC10 and +0.65 eV for C10E*C10 (see Figure 6.11). Apart from this correlation, the above results for $\Delta\Phi$ suggest that the work function of AT SAMs can be varied in a controlled fashion within $\pm$(0.4-0.65) eV range by the embedded dipole strategy. Significantly, this variation is not accompanied by a significant change in the molecular orientation and the SAM structure with respect to the "parent" NSAT films, as follows from the IR (Figure 6.2), NEXAFS spectroscopy,[25] and AFM (Figure 6.3) data. Also, the physical and chemical identities of both SAM-substrate and SAM-ambient interfaces remain persistent. Thus, the dipole control can be fully decoupled from the interfacial chemistry, which represents a useful practical tool for molecular engineering of interfaces. Both aliphatic (this work) and aromatic[26] SAMs can then be used for this purpose within the embedded dipole strategy.

A change in the work function upon the embedding of the dipolar ester group was also observed in all other CnECm SAMs studied, except for the C15EC5 monolayer (see Figure 6.11). The value of $\Delta\Phi$, measured with respect to the NSAT SAMs with the same total number of C atoms in the backbone, varies between -0.2 eV and -0.35 eV depending on the particular system, which is most likely related to the minor structural differences between the different films. The work function modification with respect to NSAT SAMs is comparatively small because the difference in bond dipole between ester SAMs and NSAT SAMs partially cancels the effect of the ester dipole. Apart from this shift, the CnECm SAMs follow a linear trend of $\Delta\Phi$ with the total number of C atoms, as observed in Figure 6.11, mimicking the behavior of the NSAT films which exhibit similar trend, with a slope of -17.5 meV/C.

The reason for the special behavior of the C15EC5 SAM, in terms of the practically non-existent work function modification with respect to an NSAT SAM is unclear at the moment. According to the spectroscopic analysis this film has a sim-

ilar structure as all other CnECm monolayers of this study.

The $\Delta\Phi$ effect observed for the CnECm films should, at the first glance, redouble in the case of the "double ester", C10EC4EC5 monolayer. However, the $\Delta\Phi$ value for this system -(0.4-0.5 eV) is comparable to that for the C10EC10 SAM (ca. -0.4 eV) which has the same total number of C atoms but only one embedded ester group. A reason for this behavior can be specific orientation of one or both ester groups of the C10EC4EC5 monolayer, so that the projection of the respective dipole onto the substrate normal is small. Note that the single-ester-group-like value of $\Delta\Phi$ for the C10EC4EC5 SAM correlates well with the behavior of the second "fingerprint" of the electrostatic effects, viz. the C 1s HRXP spectrum (Figure 6.9). Even though a nonequivocal decomposition of this spectrum is not possible (see e.g. Figure 6.10), the BE difference between the C 1s emission stemming from the bottom and top -(CH_2)- segments, limited by the spectral envelope, is very close to that of the C10EC10 SAM.

Apart from the above discussion, specific for the C10EC4EC5 SAM, the correlation between the electrostatic effects of the embedded dipole in photoemission and work function should also be considered for the other mid-ester functionalized AT monolayers. As far as the NSAT SAMs with the same total number of C atoms in the backbone are taken as the reference, the direction of the C 1s BE shift for the top -(CH_2)- segment emission in the HRXP spectra correlates fully with the sign of $\Delta\Phi$ and is determined by the electrostatic energy shift associated with the embedded dipolar ester group.

Also the absolute value of the BE shift with respect to the NSAT reference, viz. +(0.3-0.55) eV correlates well with the absolute value of $\Delta\Phi$, viz. (0.4-0.65) eV, even though a perfect agreement for the individual systems could not be achieved. Both the BE shift and $\Delta\Phi$ are determined by the extent of the potential discontinuity associated with the embedded dipole combined with the effect of the interfacial Au-S dipole. The work function modification additionally depends on the orientation of the terminal methyl groups which carry a certain dipole moment.[328] Differences in the average orientation of the methyl groups are well possible, both related to the parities of the top and bottom -(CH_2)- segments (so called odd-even effects) and different degrees of the conformational and orientational disorder in the top segment part of the SAMs. Note, however, that the analysis of the $\Delta\Phi$ data in Figure 6.11 did not allow to make any reliable conclusions regarding the impact of the odd-even effects in the ester SAMs. They should be present but, most likely, work together with a variety of other factors and are therefore hardly traceable.

6.5. Theoretical methods

For this work we performed slab type density functional theory (DFT) calculations to gain insight into the electronic structure of the systems of interest. To arrive at the minimum energy configuration we employed a pre-optimization step using molecular

dynamics (MD) simulations, making use of the program package LAMMPS.[171] In this step 16 molecules were placed on 10 layers of gold substrate and a simulation run was performed, including heating up to T=750K, annealing at T=300K and subsequent slow cooling to T=5K to get rid of the thermal motion of the molecules. Throughout the simulation the gold substrate was fixed. The molecules were mobile on the gold substrate. Details of the preliminary MD runs are the same as described in Chapters 4 and 5. With this temperature profile we were able to find the minimum energy geometry within the classical MD method and use it as a starting point for subsequent quantum mechanical (QM) geometry optimization using DFT. For this second optimization step a $\left(3 \text{ x } 2\sqrt{3}\right)$ unit cell containing four molecules adsorbed on the fcc hollow sites of a Au(111) substrate was used (see Figure 5.2 of Chapter 5). It is the same unit cell that was already employed for calculations of the C10EC5 SAM presented in Chapter 5. This unit cell, as well as a simple $\left(\sqrt{3} \text{ x } \sqrt{3}\right)$ R30° unit cell containing one molecule are reported in literature for alkylthiolates on gold substrate.[13] We chose the larger one to include the possibility of a herringbone arrangement of the molecules. The gold substrate was modeled using five layers, of which the top two were kept mobile during the geometry optimization. The bottom three layers were fixed to simulate bulk gold. The gold lattice constant was d=4.141 Å. A 6x6x1 Monkhorst-Pack[246] k-point grid was employed in reciprocal space.

For the quantum mechanical geometry optimization the program package VASP[238–241] (version 5.3.2) in combination with GADGET,[267] a tool that enables optimizing in internal coordinates, was used. Due to the 3D periodic nature of the code, we employed a dipole correction in z-direction to electrically decouple the individual slabs.[302] To that end a vacuum gap of 25Å to 30Å was introduced in the z-direction of the unit cells. The exchange-correlation functional chosen was the PBE functional,[235,236] van der Waals interactions were included with the vdW$^{\text{Surf}}$[244] method in the implementation of Al-Saidi et al.[245] The projector-augmented wave (PAW)[242,299] formalism was used to describe core-valence interactions and a plane wave basis set with a cutoff energy of 400 eV was used for all calculations. The convergence criterion for the total energy in the self-consistent cycle was 10^{-6} eV and the ionic relaxation was concluded if forces acting on the ions were lower than 10^{-2} eV Å^{-1}. The total z-dipole moment of the unit cell was converged to 10^{-4} eÅ.

After obtaining the minimum energy geometry in this way, core-level energies were computed following the initial state[247] approach. This method does not intrinsically include screening effects of the substrate. We accounted for them in a postprocessing step in the form of a classical image charge potential[261,262] $V_{im} = -\frac{1}{4\varepsilon(z-z_0)}$, with the position of the image plane z_0=0.9Å above the top gold layer.[308,309] The dielectric constant was ε=2.26.[25] To calculate XP spectra from the pure core-level energies, individual Gauss curves were calculated and summed up including exponential damping according to.[260] The incident photon energy was chosen as hν=580eV, in accordance with the experimental data presented in the previous section and a value of β=0.638 was used to describe damping effects. The details of this data evaluation are described in Section 5.3 of Chapter 5 (see also ref [269]).

6.6. Simulation results

6.6.1. Comparison to experiment on the test system C10EC5

As was already shown in Chapter 5, the calculation method employed in this work is able to quite accurately reproduce experimental XPS results for the C10EC5 SAM, see Figure 5.4. We see the experimentally observed splitting of the main peak into two subpeaks (ΔC1s = -0.79 eV), which can be directly assigned to the bottom and top segment of the chain. Additionally, the peaks of the chemically shifted ether and carbonyl carbons are reproduced correctly. Complementary to measurements, calculations give information about the binding energies of individual atoms inside the SAM. This data is not available in such local detail through XPS measurements and gives valuable insights into the effects happening inside the layer.

In the following we also calculated the work function modification of the C10EC5 SAM with respect to a SAM of pure alkyl thiolates on Au(111) substrate. This reference SAM has a backbone of 16 carbon atoms, to give it equal overall length as the C10EC5 SAM. The calculated work function modification of the C10EC5 SAM with respect to this C16 reference SAM is -0.76 eV. This value agrees quite well with the calculated peak splitting in XP spectra. For evaluating the electrostatic shift in core level energies one can also calculate the difference between the screened and damped average core level energy of the carbons in the top and bottom chain instead of using an unfunctionalized alkylthiol reference SAM. This shift is $\Delta\text{C1s}_{\text{top}-\text{bot}}$ = -0.79 eV for C10EC5.

6.6.2. Changing the twist angle - horizontal ester orientation

Rotating the mid-chain ester functionalized alkylthiols around their main axis by 180° results in a changed orientation of the ester dipole without affecting the main structural properties of the SAM like tilt and azimuth angle. (see Figure 6.13 which shows a sketch of this reorientation) Thus, such a rotation of the molecules could easily occur inside a SAM. As the molecules do not need more space or disturb their neighbors in this configuration a certain fraction of the molecules could reorient in this way inside a SAM either as individual molecules or in patches. Indeed we do find such twisted molecular orientations in the MD pre-optimization for most of the studied systems.

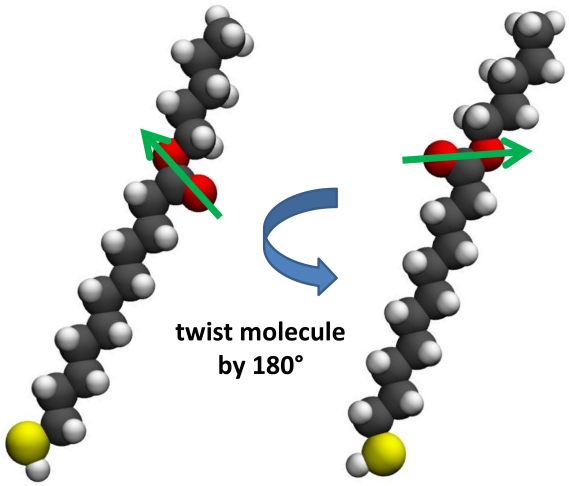

Figure 6.13.: Left: schematic depiction of a C10EC5 molecule with regular orientation of the ester dipole. Right: C10EC5 molecule rotated by 180° around the main molecular axis. This rotation around the molecular axis results in a nearly horizontal orientation of the ester dipole, indicated as a green arrow. The z-dipole component is drastically reduced.

This reorientation, however, can have a drastic impact on the electronic properties of the SAM, even though the structural consequences, regarding the molecular packing and tilt angles are minimal. In the following we will illustrate this using the C10EC5 system as a representative example. Figure 6.14 shows the calculated C1s core level energies of a C10EC5_twisted SAM, where all four molecules in the unit cell were rotated by 180° as described above and of a regular C10EC5 SAM for comparison. The difference in calculated total energies for "twisted" and "regular" C10EC5 SAMs is ≈0.16 eV per molecule, the regular being lower in energy.

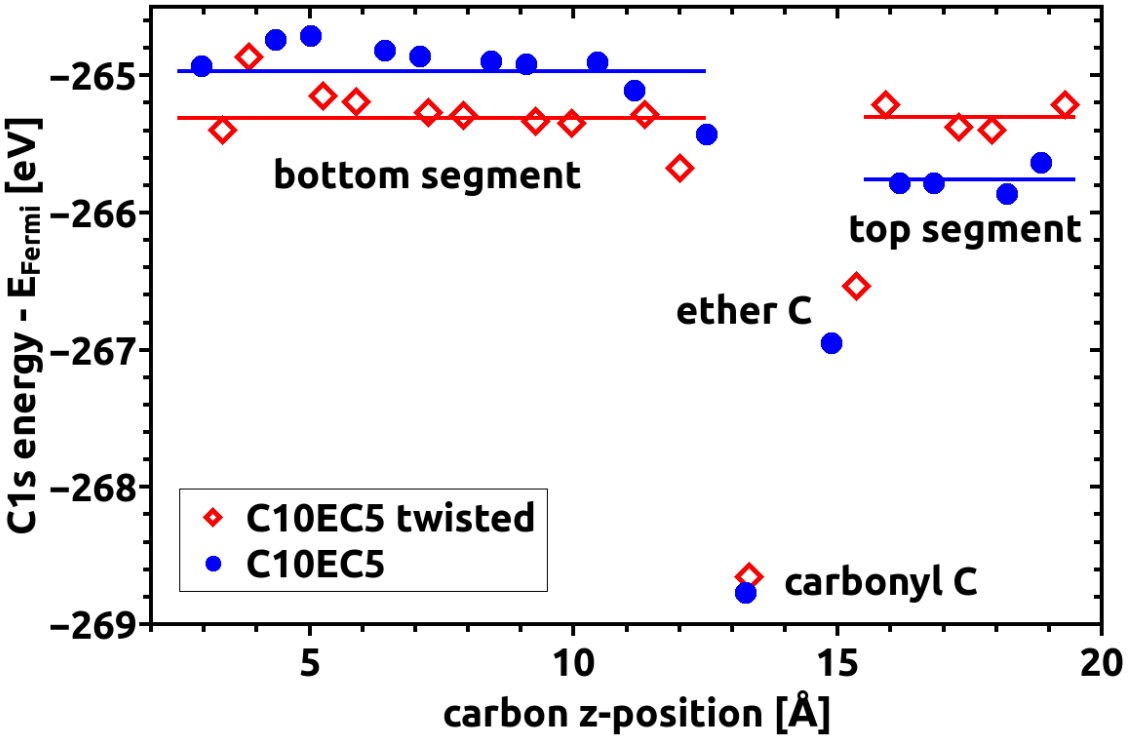

Figure 6.14.: Calculated C 1s core level energies relative to the Fermi energy for a full coverage C10EC5 SAM (full blue dots) and a full coverage C10EC5 SAM with all molecules twisted by 180° (open red diamonds) are shown. The carbon z-position is given relative to the position of the top gold layer (z=0 Å). The depicted C1s energies and z-positions are averaged over all four molecules in the unit cell. The impact of this averaging is, however, negligible, as the maximum difference in energy between equivalent C atoms amounts to 0.09 eV.

In Figure 6.14 we see that the bottom and top segment of the C10EC5_twisted SAM have nearly identical core level energies (shift top-bottom segment = 0.01 eV). This result is in stark contrast to the regular C10EC5 SAM, which shows a significant drop in core level energies from the bottom to the top segment. We attribute this lack of energetic difference to electrostatic origins. In the C10EC5 SAM the difference in core level energies is caused by the regular arrangement of the ester dipoles in the SAM. The densely packed, parallel z-dipole components cause a drop in potential and the core level energies follow. In the case of twisted molecules, however, the ester dipole moment happens to be oriented in a nearly perfectly horizontal fashion. Due to this lack of effective z-dipole moment, the potential landscape sees no sharp drop at the position of the ester group and thus also the core-level energies remain unaffected.

To test this explanation we take a look at the potential landscape inside the SAM. This should offer further insight. Figure 6.15 shows the plane-averaged electron electrostatic energy of a C10EC5 horizontal SAM, a C10EC5 regular SAM and a

reference C16 SAM.

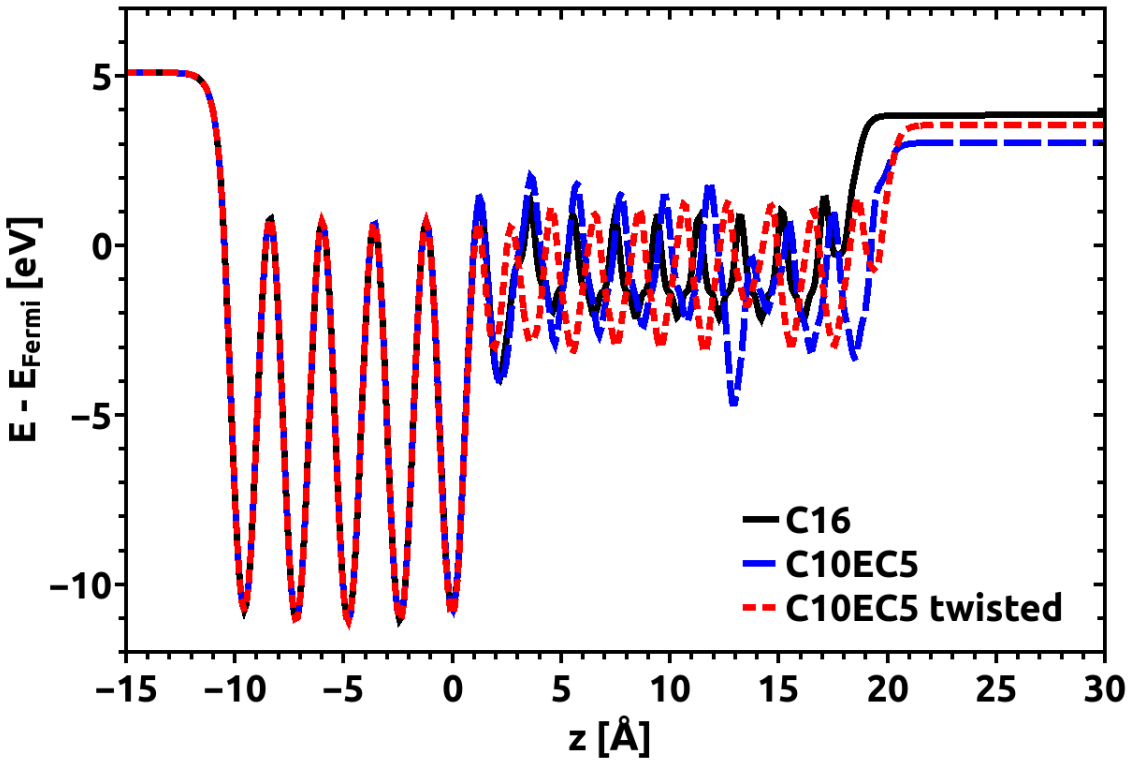

Figure 6.15.: Plane-averaged electrostatic energy of an electron calculated for three different systems: a regular C10EC5 SAM (dashed blue line), a C10EC5_twisted SAM, where all molecules are twisted by 180° (dotted red line), which results in a horizontal orientation of the ester dipole moments and a C16 reference SAM (solid black line) without any ester group. All three SAMs are densely packed. The energy is plotted as a function of the z-position in the SAM relative to the top gold layer (z=0 Å). The first five distinct peaks on the left show the five layers of gold substrate, the smaller peaks after that represent the SAM. The top of the SAMs is reached at a z-position of about 20 Å above the top gold layer.

The leftmost five peaks (minima) visible in Figure 6.15 are assigned to the five layers of gold substrate. They are identical for all three shown systems. However, the systems differ significantly in the vacuum side potential (rightmost side of the Figure 6.15). The regular C10EC5 SAM shows a distinct drop in potential relative to the C16 reference. This drop appears already at the ester group ($z \approx 12$ Å above the top gold layer) and leads to the shift in core level energies, which results in the double peak structure found in XPS measurements and calculations (see Figures 6.5 and 6.14). The work function modification for C10EC5, calculated as the difference of the vacuum side electrostatic potentials of the C10EC5 SAM and the C16 reference SAM is $\Delta\Phi$ = -0.76 eV. The twisted C10EC5 SAM, however, shows a qualitatively different behavior. In this case the vacuum side potential is practically identical to the one of the C16 reference SAM. In Figure 6.15 we see that the potential for

C10EC5_twisted lacks the distinctive minimum indicating the ester group, which is present for the C10EC5 SAM. This means that, due to the reorientation of the ester group, there is no vertical dipole component left, thus no potential drop occurs in z-direction. This also explains the lack of electrostatic XPS peak splitting for this SAM. The different potential landscape should also be reflected in the work function modification. For the twisted C10EC5 SAM it is calculated as $\Delta\Phi$ = -0.24 eV (with respect to a C16 reference). Contrary to expectations it is not exactly zero. This discrepancy is, however, not caused by the ester group. This can be seen, when taking a look at the core level energies again. The shift between top and bottom segment is 0.01 eV. Thus, no electrostatic shift happens between the two segments. Therefore, the ester group does not cause a potential difference in this case. However, the XPS shift between the bottom segment of C10EC5_twisted and a reference C16 SAM is -0.35 eV, the same discrepancy we find in the vacuum side potential and the work function modification. Thus we can assume that the cause for this core level energy and potential difference between C10EC5_twisted and C16 is located at the gold-SAM interface. As we will show later, it is caused by the bond dipole.

6.6.3. C5EC10 - a system with preferred horizontal ester orientation

In the previous section we have shown that the molecular twist angle can have a significant impact on the electrostatic potential inside the SAM and consequently on the work function of the system and on atomic core level energies. We have shown the impact of horizontal orientation of the ester dipole on the example of the C10EC5 SAM.

In the following we discuss the C5EC10 system in the light of this aspect. For this system the molecular dynamics pre-optimization step finds the majority of molecules in the SAM oriented with horizontal ester dipoles. Only a few are found with "regular" dipole orientation. Thus we chose this molecular orientation with horizontal ester dipole as a starting point for the subsequent quantum mechanical optimization. It was found to persist throughout the QM optimization. Figure 6.16 shows a schematic depiction of the ester orientation for a C10EC5 and C5EC10 molecule with the same twist angles, taking into account the tilt angle found inside SAMs.

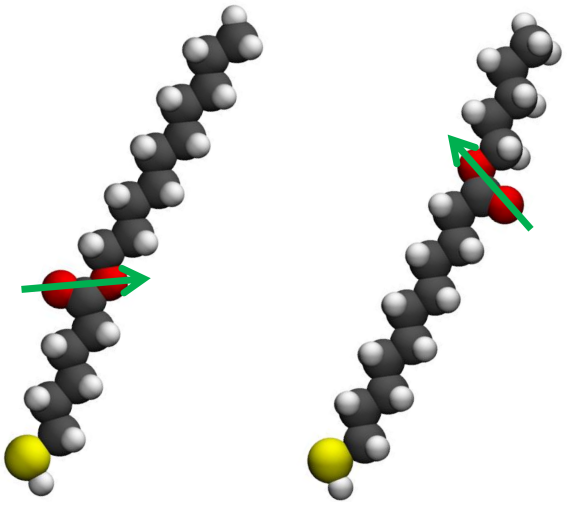

Figure 6.16.: Schematics of a C5EC10 molecule (left) and C10EC5 molecule (right) with the same twist and tilt angles. Dipole moment orientations are indicated for both molecules as green arrows. Due to the odd number of carbons in the lower segment of the C5EC10 molecule and the zig-zag nature of the carbon backbone the dipole moment of this molecule is oriented practically horizontally at this tilt angle, which is representative of the general molecular orientation inside a SAM. Only isolated molecules are shown here to better illustrate the orientation of the ester group.

The fact that the C5EC10 SAM favors a horizontal ester dipole orientation is caused by the odd number of carbons in the lower chain for this system in contrast to the even number in the C10EC5 SAM, which shows the opposite behavior. The zig-zag structure of the alkyl chain combined with an odd number of carbons in the lower chain leads to a different orientation of the ester group, if the tilt and twist angles are assumed to be similar in both cases. Apparently, in the C5EC10 case the combination of these factors leads to a preferred horizontal orientation of the ester dipole in our calculations.

The regular configuration of C5EC10 (with near horizontal ester dipole) was found to have lower total energy in DFT calculations than the twisted ester orientation by ≈0.3 eV per unit cell, which results in an energetic difference of ≈0.075 eV per molecule. This makes it plausible that this is the preferred molecular orientation for the C5EC10 molecule. Presumably both orientations are present with a certain mixing ratio in experimentally studied SAMs.

For comparison, the difference in total energy for ”twisted” and ”regular” C10EC5 SAMs (in this case ”twisted” has the near horizontal ester dipole orientation) is ≈0.62 eV per unit cell, the regular being lower in energy. The energetic difference per molecule is ≈0.16 eV. This is a larger energetic difference than encountered for the C5EC10 SAM. Figure 6.17 shows the calculated C1s core level energies of a C5EC10 SAM, compared to the reference C16 SAM.

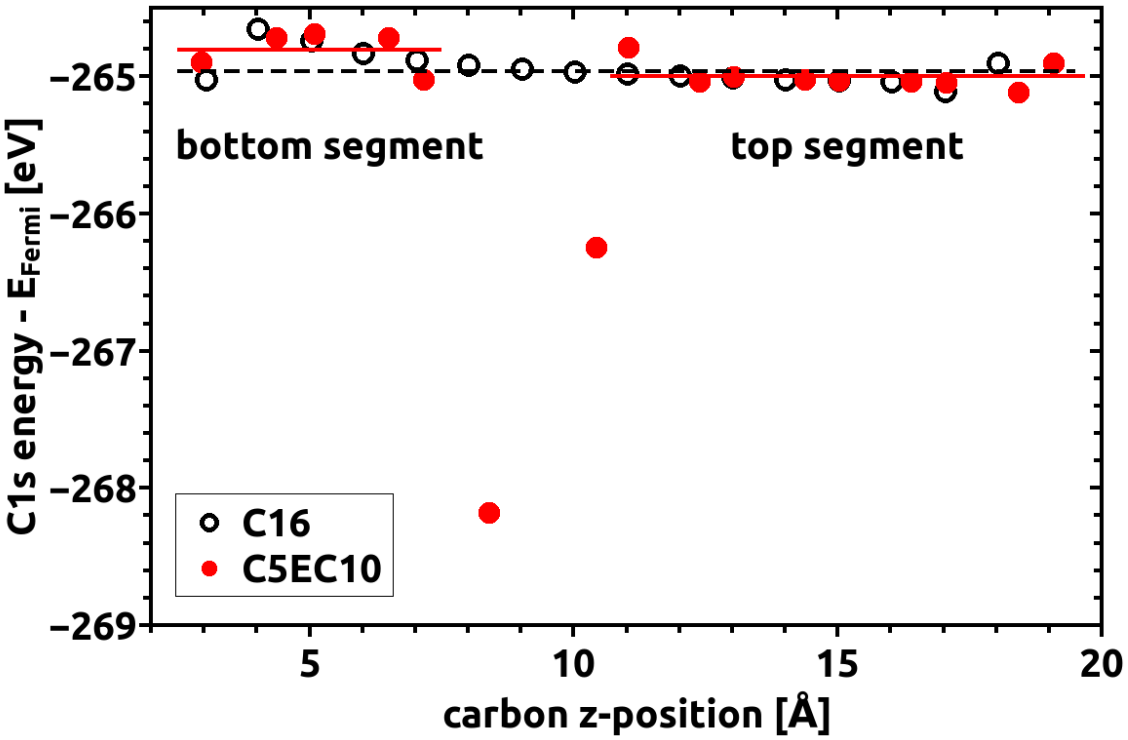

Figure 6.17.: Calculated C1s core level energies of a densely packed C5EC10 SAM (full red dots), with all molecules oriented with near horizontal ester dipole and of a C16 reference SAM (open black circles). The depicted C1s energies and z-positions are averaged over all four molecules in the unit cell. The impact of this averaging is, however, negligible, as the maximum difference in energy between equivalent C atoms amounts to 0.09 eV. The core level energies are given relative to the Fermi energy. We find only a slight difference in the core level energies of the top and bottom segment carbons of C5EC10. The ether and carbonyl carbons in contrast remain shifted with respect to the rest of the chain.

Figure 6.17 shows the same basic effects as already discussed for the horizontal C10EC5 system (compare Figure 6.14). There is only a minimal potential drop at the ester group, due to the mostly lacking z-dipole component. Therefore the core level energies are very close for the bottom and top segment carbons. Only the chemically different ether and carbonyl carbons exhibit significantly different 1s energies. The lack of potential drop can be seen in Figure 6.18, which shows the plane-averaged electron electrostatic energies of a regular C10EC5 SAM, a C5EC10 SAM with horizontal ester dipole orientation and a C16 reference SAM.

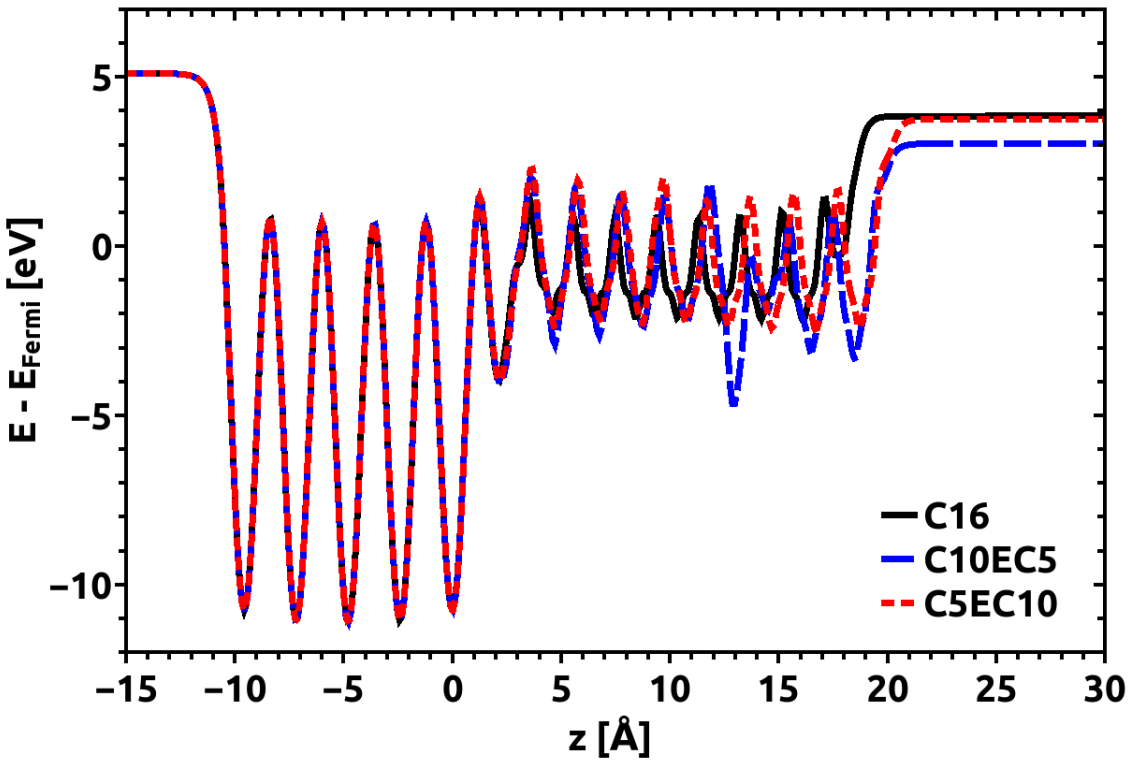

Figure 6.18.: Plane-averaged electron electrostatic energy of a regular C10EC5 SAM (dashed blue line), a C5EC10 SAM (dotted red line) and a C16 reference SAM (solid black line). The energy is plotted as a function of the z-position in the SAM relative to the top gold layer. The first five distinct peaks on the left show the five layers of gold substrate, the smaller peaks after that represent the SAM. The top of the SAM is reached at a z-position of about 20Å above the top gold layer.

In Figure 6.18 we see that C5EC10 and C16 have practically identical vacuum side potentials (right hand side of Figure 6.18), as C5EC10 exhibits no drop in potential at the horizontally oriented ester group (explained above). The C10EC5 SAM shows a potential drop at the ester group and thus has a different vacuum side potential than C16 and C5EC10. The XPS shift found between bottom and top segment for the C5EC10 system, however, is not exactly zero. It is calculated as ≈0.19 eV, so apparently, the ester dipole is not oriented exactly horizontally. A small z-dipole component is still present. If a C16 SAM is used as a reference for calculating the XPS shift though ($C1s_{top}$ - $C1s_{C16}$), instead of the bottom segment ($C1s_{top} - C1s_{bot}$), we find an XPS shift of only -0.04 eV. This leads us to the assumption, that the bond dipole difference between C5EC10 and C16 is compensated by the still slightly present ester z-dipole of C5EC10 in this comparison. This can also be seen if we compare the average top and bottom segment C1s energies of C5EC10 with the average C1s energy of C16 (see full and dashed lines in Figure 6.17). There the C16 and the C5EC10 SAM differ by about -0.19 eV in the bottom segment and by only -0.04 eV in the top segment. The influence of the bond dipole is explained in more

detail in Section 6.6.5. The work function modification of C5EC10, determined as the difference between the vacuum side electrostatic potentials of C5EC10 and C16 is $\Delta\Phi$ = -0.03 eV.

Combining the results given above we come to the conclusion that C5EC10 shows a qualitatively different behavior than we see in the C10EC5 SAM. It is more analogous to the twisted C10EC5 system. With the C5EC10 system we could show that SAMs with different chain lengths can orient in different ways and thus change properties and measurement results quite significantly due to different ester orientations. This might play an interesting role not just in calculations but also in experimental studies of SAMs.

C5EC10 twisted

As an additional test of the interpretation put forward in the section above, a second calculation on a C5EC10 SAM was performed. For this all four molecules in the unit cell of the C5EC10 system described above were rotated by 180°. According to our theory this should reorient the ester dipoles inside the SAM so that they have a significant z-component again, similar to the regular C10EC5 system.

In the according simulation of this second C5EC10 system, which we call C5EC10_twisted we find a significant electrostatic shift between bottom and top segment of the SAM in accordance with expectations. The calculated C 1s core level shift between the two segments is ΔC1s = -0.79 eV. The calculated work function modification for this SAM, $\Delta\Phi$ = -0.87 eV. It agrees with the shift in core level energies and is as significant as for the C10EC5 SAM.

6.6.4. Reverse ester system

After studying the influence of reorienting the ester group by changing twist angles, we now take a look at what happens, when we chemically alter the orientation of the molecular dipole. For this test the ester group is inserted reversely into the carbon backbone (indicated as E* in the naming convention used in this work). In this case the z-dipole moment is oriented towards the substrate instead of away from it as in the regular ester-functionalized SAM. Figure 6.19 shows a schematic depiction of a C10EC10 and a C10E*C10 molecule with the ester dipole moment indicated, considering the molecular tilt angle inside a SAM.

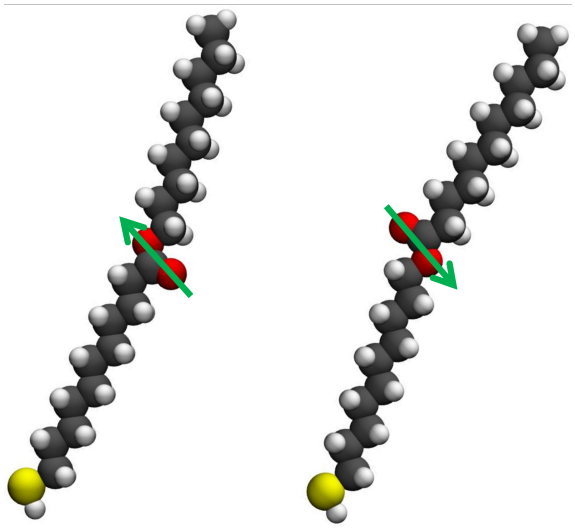

Figure 6.19.: Schematic depiction of a C10EC10 molecule (left) and a C10E*C10 molecule (right) with a reverse ester group embedded into the backbone. The dipole moments of the ester groups are indicated by green arrows. Only isolated molecules instead of SAMs are shown here to schematically illustrate the orientation of the dipolar group more clearly.

In the following, we study the implications of reversed ester groups on the example of the C10E*C10 system and compare it to the regular C10EC10 case. We choose these SAMs, because of their equal chain lengths below and above the dipolar group. In this way we try to exclude the influence of non-identical chain lengths on the results. In calculations and experiments (see Section 6.3.1) both SAMs are found to have the same bonding sites to the substrate resulting in the same packing density of the film. Also the tilt angles of both SAMs are found to be comparable. So we can assume with reasonable certainty that any differences in the behavior of the two systems are connected to the electrostatic presence of the reversed ester group and are not solely caused by a drastically different SAM structure. In Figure 6.20 we compare calculated C1s core level energies for both systems. The corresponding plane-averaged electron electrostatic energies are shown in Figure 6.21.

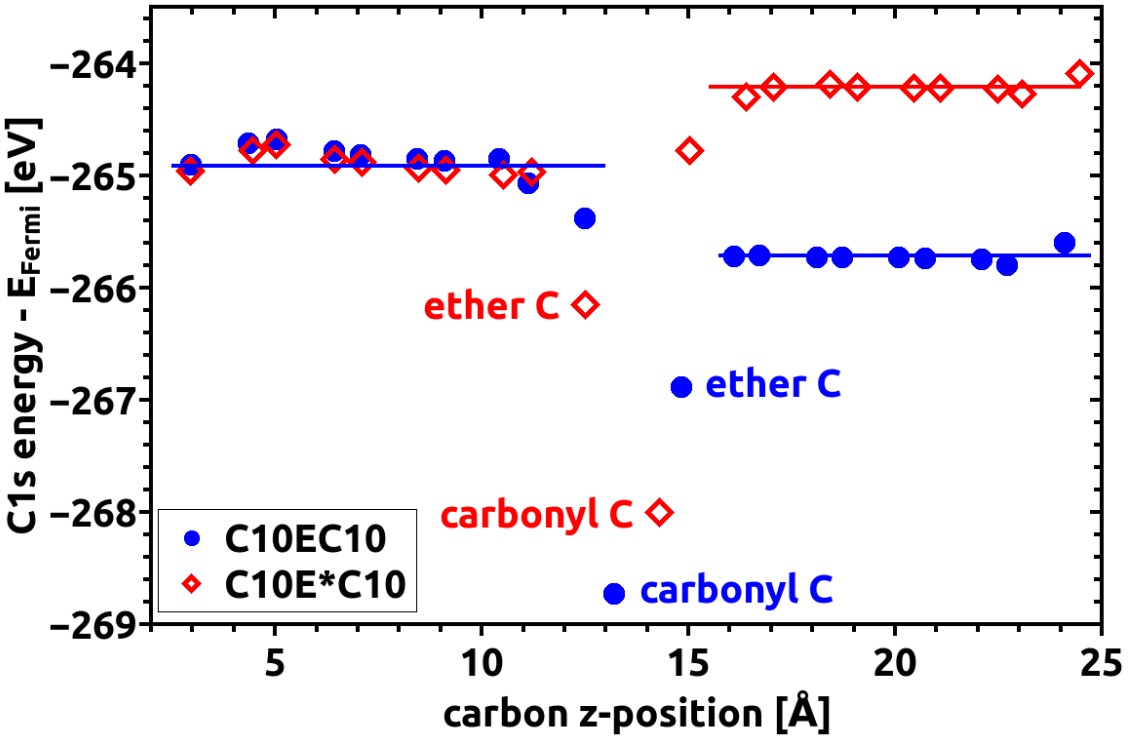

Figure 6.20.: Calculated C1s energies of a densely packed C10EC10 SAM (full blue dots) and a C10E*C10 SAM (open red diamonds), which contains a reverse ester component. Core level energies are given with respect to the Fermi energy as a function of the z-position of the respective carbon atoms relative to the position of the top gold layer (z=0 Å). The depicted C1s energies and z-positions are averaged over all four molecules in the unit cell. The impact of this averaging is, however, negligible, as the maximum difference in energy between equivalent C atoms amounts to 0.09 eV. We find the C1s energies in the bottom segment to be identical for both systems, the top segments differ significantly however.

In the C10EC10 SAM the top segment is shifted downward in energy by -0.79 eV compared to the bottom segment and by -0.75 eV with respect to the C16 reference. This is the same trend we already encountered in the C10EC5 system. The C10E*C10 SAM in contrast shows an upward shift of the top segment of +0.70 eV (+0.75 eV with respect to the C16 reference). This agrees well with the simple electrostatic picture. The reverse orientation of the ester group leaves the ester dipole moment pointing toward the substrate instead of away from it. The z-dipole component is inverted compared to a regular C10EC10 molecule. Thus, the jump in electrostatic potential also changes direction and the core level energies follow this trend. Considering the chemical shifts in Figure 6.21 one has to keep in mind that in the reverse ester system the ether and carbonyl carbon have reversed z-positions along the backbone compared to C10EC10, the ether C being situated at lower z-position than the carbonyl C. The chemical shifts in both systems happen independently of the electrostatic shifts. Both effects simply add up to result in

the overall C 1s core level energy of each carbon atom. Due to the reversed dipole in C10E*C10 the core levels of the carbonyl and ether carbon get shifted upward compared to C10EC10. The according plane-averaged electron electrostatic energies of the C10E*C10, the C10EC10 and the reference C16 SAM are shown in Figure 6.21.

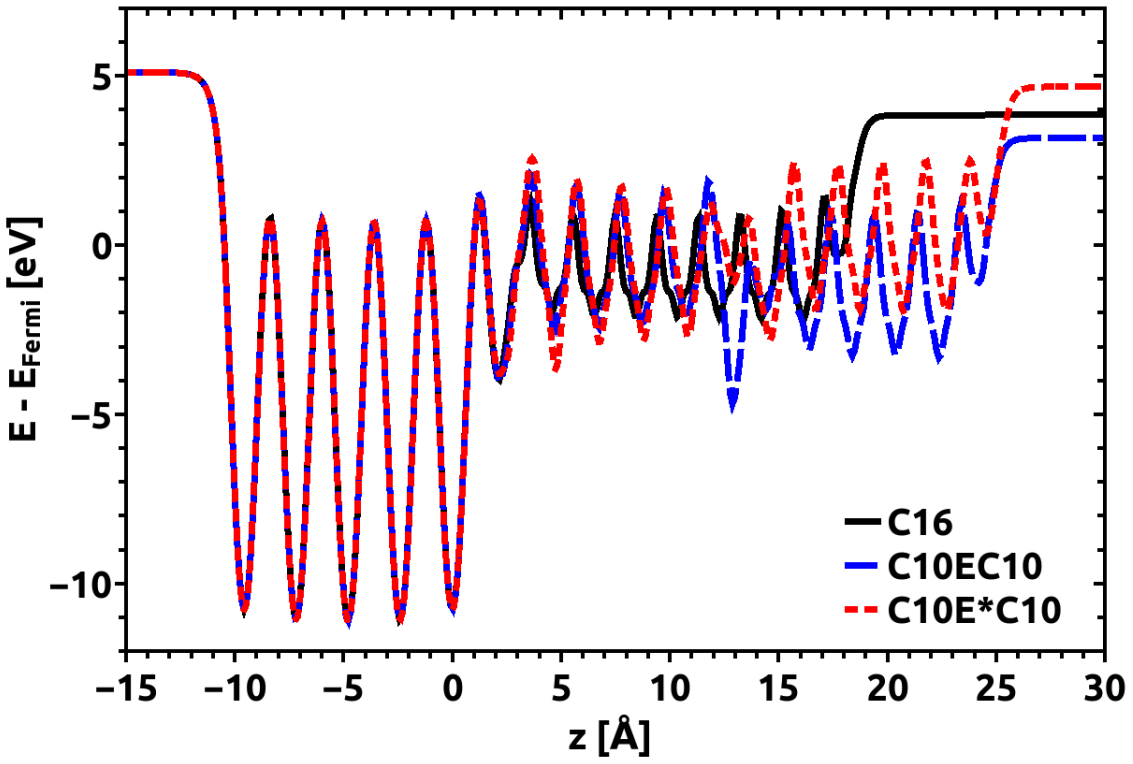

Figure 6.21.: Plane-averaged electron electrostatic energy of a C10EC10 SAM (dashed blue line), a C10E*C10 SAM (dotted red line) and a C16 reference SAM (solid black line). The energy is plotted as a function of the z-position in the SAM relative to the top gold layer (z=0 Å). All energies are given relative to the Fermi energy. We see an opposite shift of the vacuum side potential for C10EC10 and C10E*C10 compared to the C16 reference SAM.

The vacuum side potential shifts in opposite directions for C10EC10 and C10E*C10 compared to the C16 reference, due to the inversely oriented ester group. This is clearly visible, as the C10EC10 and C10E*C10 potentials already start to differ at the ester group (z ≈12 Å), the former shifting down in energy, the latter up. The work function modifications for these systems, calculated from the vacuum side potentials, are $\Delta\Phi$ = -0.62 eV for C10EC10 and $\Delta\Phi$ = +0.88 eV for C10E*C10, both compared to the C16 reference SAM. The calculated work function modifications and XPS shifts agree qualitatively. Quantitatively they differ by about 0.13 eV for both C10EC10 and C10E*C10, the work function modification having the more positive value in both cases. This trend is also observed in other calculated and measured systems (see previous sections for calculation results and Figures 6.8 and

6.11 for the experimental binding energy shifts and work function modifications).

6.6.5. Influence of the bond dipole

Above, we have extensively described the potential and core level shifts caused by the ester dipole layer in various systems. The ester dipole, however, is not the only one present in the studied systems. At the gold-SAM interface we find the bond dipole (caused by the polar sulfur-carbon bond), which is nearly as prominent and must not be neglected to arrive at a comprehensive picture. The densely packed molecules create a regular arrangement of similarly oriented dipoles also at this interface, analogous to the ester dipole layer described in more detail above. In contrast to the ester dipole, however, the bond dipole affects the whole molecule, not just the top segment. In fact, in the top segment, the two influences are superimposed and may enhance or partially cancel each other, as was already briefly discussed in Chapter 5 (see also ref [269]). Apart from the tilt angle (which is very consistent throughout all calculations) the bond dipole is influenced by the twist angle of the molecule as this changes the Au-S-C bond angle noticeably. Therefore, we performed tests on pure alkyl thiolate SAMs to get an estimate of the influence of the twist angle on the bond dipole. These systems allow us to study the impact of the bond dipole without having to separate ester dipole from bond dipole effects. We chose the C16 molecule for these tests, as it is the one mostly used as a reference throughout this paper and, thus, is of special interest to us. Secondly, it has about the same length as the theoretically studied ester functionalized molecules. Therefore we can be reasonably certain that chain length effects do not play a role when interpreting the obtained data with regard to alkyl thiols with embedded dipolar units. We started with a densely packed C16 SAM, with all molecules arranged identically (no herringbone structure) and tested geometries with all molecules rotated by 90°, 180° or just half the molecules rotated by 90°, which creates a herringbone pattern. We expect the strongest deviations at a change in twist of 90°. In these tests we find the maximum influence of ≈0.4 eV on core level energies and work function indeed for this case. Rotation by 180° showed surprisingly little variations in work function and core level energies, only ≈0.06 eV, from the original SAM. The original and the 180° rotated configuration apparently have a quite similar bond dipole component in z-direction. With this small test series we found that the bond dipole can vary work functions and core level energies up to about 0.4 eV in the studied systems. Considering that the ester dipole shifts are of the order of 0.6 to 0.8 eV, we deem the bond dipole influence highly non-negligible. Its effect may be especially serious when ester SAMs are compared with other alkyl thiolate reference SAMs as the bonding geometry is not guaranteed to be the exact same in both cases. Thus, when XPS shifts or work function modifications are calculated with respect to a Cn SAM (for example: top chain of C10EC5 vs. C16 reference) different bonding situations might introduce deviations of up to around 0.4 eV. At this point we want to suggest that different bond dipoles might be the reason for apparent minor discrepancies found between results presented so far in this work (further discussion see below).

Different surface reconstructions are a second possible cause for changes in the bond dipole. The study of such surface reconstructions and their influence on system work functions was not the object of the investigation presented here. However, careful studies on this subject have already been published. Literature reports variations of the work function on the order of 0.5 eV caused by different surface reconstructions.[337]

6.6.6. Correlation between molecular chain length and work function

To investigate the experimentally found influence of the total chain length on the work function we performed calculations of alkyl thiolate SAMs with lengths between 9 and 18 carbon atoms, both in herringbone and non-herringbone configuration. In our calculations we do not see an influence of the chain length on the sample work function. Neither for herringbone arrangement, nor for non-herringbone packing. However, we find a slight difference between odd and even number of carbons in the alkyl chain. The work function modification changes by 0.05 eV between alkyl thiolates with odd and even carbon numbers, odd numbers showing larger work function modifications (compared to a pristine Au(111) surface). As we do not find the overall molecular geometry (tilt, twist and azimuth angle) altered with increasing chain length in our calculations, we attribute the slight difference to the orientation of the terminal CH_3 unit. Due to the zig-zag structure of the carbon chain the CH_3 group is oriented differently for odd and even numbers. This influence, however, seems negligible (0.05 eV) compared to other, electrostatic effects found in ester functionalized alkyl thiolate SAMs ($\approx$ 0.8 eV work function modification due to the presence of the ester dipole).

6.6.7. Calculation data summary

Table 6.2 summarizes the calculated data for the systems discussed above. Core level shifts and work function modifications are given.

Table 6.2.: Calculated core level shifts and work function modifications for the systems described above. All values are given in eV.

top-bot ... shift in average core level energies between the top and bottom segment of one system
bot-C16 ... shift in average core level energies between the bottom segment of the specified system and the C16 reference SAM
top-C16 ... shift in average core level energies between the top segment of the specified system and the C16 reference SAM
Φ_i - Φ_{C16} ... work function modification of the specified system with respect to the C16 reference SAM

system	**top-bot**	**bot-C16**	**top-C16**	$\mathbf{\Phi_i - \Phi_{C16}}$
C10EC5	-0.79	0.00	-0.80	-0.76
C10EC5_twisted	0.01	-0.35	-0.34	-0.24
C5EC10	-0.19	0.16	-0.04	-0.03
C5EC10_twisted	-0.79	0.04	-0.75	-0.87
C10EC10	-0.79	0.04	-0.75	-0.62
C10E*C10	0.70	0.06	0.75	0.88

Please note that two systems of Table 6.2 show horizontal ester dipole orientation, namely C10EC5_twisted and C5EC10, as discussed in more detail in the previous sections. Table 6.2 shows that the top-C16 C1s shift agrees reasonably well with the work function modification for all investigated systems.

Furthermore we find that the top-C16 shift is the sum of the individual bot-C16 and top-bot shifts. This means the total electrostatic shift between the core level energies of each system's top segment and the reference C16 SAM is given by the individual contributions of the bond dipole shift (bot-C16) and the ester dipole shift (top-bot), which simply add up.

6.7. Discussion of simulation results and comparison to experiment

The calculated results are consistent within themselves. The top/bottom core level shifts (column top-bot of Table 6.2) correspond to the ester orientation. The top chain is shifted downwards by $\approx$ -0.8 eV for regular esters, upwards ($\approx$ +0.7 eV) for reverse esters and not at all for horizontal orientation of the ester dipole. These core level shifts for SAMs with different ester orientation are in line with basic electrostatic considerations.

The calculated work function modification (column "Φ_i - Φ_{C16}" of Table 6.2) generally agrees with the calculated top/bottom core level shift. At first glance the C10EC5_twisted and the C5EC10 SAMs seem to be an exception of this finding. In these two cases the top/bottom shift does not exactly correspond to the work function modification but deviates by about 0.15 to 0.25 eV. This apparent inconsistency however can be explained by the bond dipole contribution (column "bot-C16" of Table 6.2). The work function modification is calculated with respect to the C16 reference SAM. When the top segment core level shift is also evaluated using the C16 SAM as a reference instead of the bottom segment of the same molecule these shifts correspond exactly to the work function modification. In fact the difference in core level energies between C10EC5_twisted (and C5EC10 respectively) and C16 is already found in the bottom segment (column "bot-C16" of Table 6.2). This substantiates the explanation that different bond dipole contributions of C10EC5_twisted (and C5EC10 respectively) and C16 are responsible for the discrepancy between top/bottom core level shift and work function modification found for those systems.

Tests performed on non-functionalized alkyl thiolate SAMs (specifically C16) showed that the maximum influence of twist angle induced changes of the bond dipole on the work function for these systems is on the order of$\approx$0.4 eV. This maximum influence was achieved by rotating all molecules in the unit cell by 90° around the main molecular axes.

The overall work function modification of the system and the core level energy of the top segment are defined by the superposed influences of the bond dipole and the ester dipole. Both can add up or partially compensate depending on the exact molecular orientation. See for example the calculations for the C10EC5_twisted and the C5EC10 SAMs in Table 6.2. Notice that the core level energies of the bottom segments vary for these systems compared to the other listed SAMs, which can be attributed to different bond dipole contributions due to rotation around the main molecular axes in these cases.

An experimental indication of different bond dipole situations being present in different systems can be found in Figure 6.8 which shows the measured C 1s binding energy of Cn SAMs and the separate binding energies of the bottom and top segments of ester functionalized alkyl thiolate SAMs. In this graph we find the bottom segments of the functionalized SAMs and the non-substituted Cn SAMs rigidly shifted with respect to each other. This shift cannot be caused by the ester dipole as its electrostatic influence only affects the top segment. Therefore we surmise that experimental Cn SAMs and ester functionalized alkyl thiolate SAMs have a slightly different bonding geometry to the substrate, resulting in different z-components of the bond dipole, which shifts the binding energies of both types of SAMs relative to each other. The experimentally observed shift between the binding energies of bottom segments and Cn SAMs is on the order of 0.2 to 0.4 eV, which is exactly the same energetic variation we find in our test calculations concerning the energetic influence of the bond dipole described above. The shift between bottom and top segment binding energies seen in Figure 6.8 is attributed to the electrostatic influ-

ence of the ester dipole.

The influence of the bond dipole raises the question of which reference to use for determining XPS shifts. Comparing the average core level energies of the top and bottom segment of the molecule has the advantage that both parts have the same bond dipole influence. However, the bottom segment is subjected to stronger screening effects of the metal substrate than the top segment (compare Figure 5.9 of Chapter 5). This might increase the calculated XPS shift. The second possibility is to compare the top segment to a pure alkyl thiolate reference SAM of similar overall chain length (C16 in our case). In this case, screening effects should be similar enough in both systems. However the bond dipole situation is not guaranteed to be identical in both SAMs, which could possibly introduce deviations in XPS shift evaluations of up to around 0.4 eV.

For comparing XPS shifts to work function modifications, which are calculated using a C16 reference SAM it seems reasonable to also use a C16 reference to evaluate the XPS shifts, always bearing in mind the above mentioned bond dipole issue. This choice of reference system is supported by experimental data. For the C10EC10 SAM for example the XPS shift between the bottom and top segment is -0.93 eV. If a Cn SAM of the same chain length (C20 in this case) is used as a reference the shift reduces to -0.60 eV. The former shift is much larger partially due to the fact that the bottom segment is screened more strongly by the substrate than the top segment, which increases the calculated shift. And partially the large difference of 0.33 eV can also be attributed to different bond dipoles in the C10EC10 and the C20 SAM. The XPS shift calculated with the Cn reference however agrees much better with the measured work function modification of -0.44 eV which is also obtained using a Cn reference. The same qualitative trend is also found in the other measured systems. In the C10EC5 SAM for example the top/bottom shift of -0.84 eV is reduced to -0.51 eV using a C16 reference. The effect is even more drastic in the case of C5EC10 where the XPS shift is altered from -0.89eV (top/bottom) to only -0.27 eV (top/C16). The rather strong change in this case could be partially attributed to the short bottom segment. It consists of only five carbon atoms which are all rather close to the substrate so all experience strong screening effects. This creates a stronger influence than for a molecule with a longer bottom segment, where the averaging over all bottom segment carbons reduces the screening effects to some extent, as atoms experience noticeably less screening with increasing distance from the metal substrate. A strong screening influence for a short bottom segment could also explain the exceptionally low energetic position of the C5EC10 bottom segment in Figure 6.8. The molecule with the longest bottom chain (C20EC5) on the other hand shows an above average binding energy of the bottom segment. This seems to support the explanation put forward above. Generally, the difference between experimental top/bottom and top/Cn XPS shifts is smaller the longer the bottom segment of the molecule gets.

The influence of screening on the average C1s energy of the bottom segment can be tested straightforwardly in calculations. As we account for substrate screening

only in a postprocessing step after the actual DFT calculation (details see Section 5.3), we can compare C1s energies evaluated with and without taking screening into account. And indeed we find the same trend as encountered in experiments. For the C10EC5 SAM for example the average C1s energy of the bottom segment changes by 0.26 eV (from -265.23 eV to -264.97 eV), which increases the bot-top shift. The influence is larger for shorter bottom segments. For the case of the C5EC10 SAM for example the bottom segment energy is changed by 0.41 eV due to screening effects. The top segments on the other hand are much less affected, experiencing variations of 0.1 eV or less.

Another experimental indication of the influence of different bond dipole situations in different SAMs can be found in Figure 6.8. There we see a rigid shift of the whole C20EC5 HRXP spectrum to higher binding energies compared to the C15EC5 and C10EC5 spectra. The spectrum is shifted by about 0.2 to 0.3 eV, including the carbonyl and ether peaks. This finding could be explained by slightly different bonding situations in the different SAMs resulting in different z-components of the bond dipole. This would give rise to exactly such a rigid shift of the whole spectrum including the ether and carbonyl peaks as observed in Figure 6.5.

In contrast to experiments we did not find a dependence of the chain length on the work function. Neither in pure alkyl thiolate SAMs nor in SAMs with embedded ester groups. This justifies using the C16 SAM as a reference system for all theoretically investigated systems, even for the slightly longer C10EC10 and C10E*C10 molecules. In the light of the bond dipole influence it further seems reasonable to use just one reference system for all SAMs to reduce the risk of further confusing the results by having different bond dipole contributions in different reference systems.

The orientation of the CH_3 terminal moiety in odd-even numbered carbon chains was found to influence the work function by only 0.05 eV, playing just a minor role in the overall energetic situation inside the SAM. We therefore identify the ester dipole and the bond dipole as the two main contributing factors determining the work function and core level binding energies of the studied systems.

Although the general qualitative agreement between measurements and simulations is good, a few experimentally studied systems still show unexplained trends which we do not fully understand yet, even with the help of calculations. The C10E*C10 reverse ester system for example shows a work function modification of +0.64 eV in experiments. The HRXP spectrum (see Figure 6.7) however reveals only one major peak (apart from the small side peaks, unambiguously assigned to the ether and carbonyl carbons) situated at the binding energy normally assigned to the bottom segment in other ester functionalized alkyl thiolate SAMs. In contrast to measurements we find a pronounced XPS shift between the bottom and top segment of C10E*C10 in calculations (see Figure 6.20). The shift is of equal value but opposite in sign to the shift found in the regular C10EC10 system. We also observe

good qualitative agreement between XPS shift and work function modification. The absence of a double peak structure in the measured HRXP spectrum is particularly confusing in the light of the fully present work function modification. This significant, positive change in work function due to the adsorbed SAM renders the effect of horizontally aligned ester dipoles very unlikely as an explanation for the absent XPS peak splitting. If that were the case the work function modification would also be only very minor compared to the Cn reference SAMs. However the work function modifications of the C10EC10 (exp: -0.44 eV, calc: -0.62 eV) and C10E*C10 (exp: +0.64 eV, calc: +0.88 eV) systems are significant and agree reasonably well between experiment and calculation, calculations always producing a slightly larger modification than experiments. The asymmetry in work function modifications for these two SAMs could be explained by the bond dipole of the Cn reference SAM. As seen from the identical bottom segment core level energies in Figure 6.20 the bond dipoles of C10EC10 and C10E*C10 are similar. But the ester dipoles point in opposite z-directions for both cases. So using the same Cn reference for both systems results in the bond dipole difference between ester SAM and Cn SAM adding up to the ester contribution for the C10E*C10 system and partially compensating the ester influence in the C10EC10 SAM.

When comparing the measured and calculated binding energies of the C10EC10 and C10E*C10 SAM (Figures 6.7 and 6.20) in more detail we find the positions of the ether and carbonyl peaks shifted for the two different SAMs. Both these carbons are shifted to smaller binding energies for C10E*C10 (keeping in mind that ether and carbonyl carbon have exchanged z-positions for C10EC10 and C10E*C10 in Figure 6.20 due to the reverse ester orientation), the ether carbon experiencing a slightly larger shift than the carbonyl C. This can be explained by the superposition of chemical and electrostatic effects. The chemically shifted ether and carbonyl carbons already experience the electrostatic influence caused by the ester group, which is reversed in the C10EC10 and C10E*C10 SAM. Therefore also the energetic positions of the ether and carbonyl carbons is affected inversely in both. In the C10EC10 SAM the chemical and electrostatic influences add up, both shifting to higher binding energies (more negative core level energies). In the C10E*C10 SAM the electrostatic shift partially compensates the chemical shift. This explanation is in line with the electrostatic top segment energy shift found in calculations for C10E*C10. For experiments however, the absence of a HRXPS peak splitting is even more confusing considering the observed influence on the carbonyl and ether carbons, which can be plausibly explained by the electrostatic influence of the ester dipole.

A second, possibly additional influence might be again the bond dipole which can also cause a rigid shift of the whole spectrum. Such a bond dipole difference between C10EC10 and C10E*C10 is not found in our calculations as shown by the nearly identical average core level energies of the bottom segments of both systems: -264.92 eV for C10EC10 and -264.91 eV for C10E*C10. Such a bond dipole difference however might nevertheless be present in the experimental samples if the molecules are rotated slightly differently there.

In calculations we found that the C5EC10 system seems to prefer orienting with a horizontal ester dipole. This stimulates the question whether such configurations could also be present in experimental SAMs. Mixed SAMs consisting of molecules with both regular and horizontal ester orientation are imaginable, either separated into domains or intermixed. A distribution of molecules with varying twist angles inside the SAM would affect the system properties differently than a SAM in which all molecules have the same ester z-dipole moment. To be specific a mixed SAM, consisting of molecules with "regular" ester orientation and a certain fraction of molecules with horizontally oriented ester dipoles is expected to show a reduced work function modification as only the molecules with a z-dipole component would contribute to the measured average value of the work function. The XPS shift, however, would be unaffected. Molecules with a "regular" z-dipole moment would still show a full peak splitting of -0.8 eV, whereas molecules without z-dipole component would only give one signal corresponding to the energy of the lower segment (which, in this case would also be the energy corresponding to the now electrostatically not separated top segment). Such SAMs consisting of molecules with two different twist angles would be expected to change relative XPS peak intensities, but not peak positions compared to pure "regular" SAMs.

For such mixed SAMs one can imagine that the homogeneity of the film and the prevalent mixing ratio have significant influence on the actual behavior of the system. Therefore, this topic is addressed and studied in detail in the next Chapter. And indeed, one crucial result of this investigation is that the above described scenario of mixed "regular" and "horizontal" dipoles depends significantly on the homogeneity of the film. In fact, a full XPS peak-splitting and simultaneously reduced work function modification would only be observed in the case of separated domains with different dipole orientations. A homogeneously mixed SAM would result in a different XP spectrum (see Chapter 7 for more detailed information).

In the context of dipolar mixtures the C15EC5 SAM can be discussed. In experiments it showed a significant HRXPS peak shift between the bottom and top segment of -0.69 eV (-0.42 eV using a Cn SAM as reference) but practically no work function modification, only -0.05 eV compared to a Cn reference SAM. This behavior could possibly be understood in terms of a horizontal ester dipole orientation for a large fraction of molecules in the SAM. As described above this would not affect the position of the respective bottom / top segment XPS peaks. However, if a large fraction of molecules in the SAM were oriented in such a way that the ester dipole aligned parallel to the substrate this fraction would not contribute to the work function modification, thus reducing it noticeably.

A flaw in this explanation however is the fact that the work function modification is not simply reduced, but it is practically non-existent for C15EC5. For this to happen either nearly all molecules would need to have a horizontal ester dipole orientation, which we presume would affect the XP spectrum after all, in terms of signal intensity. If only very few molecules had an electrically separated top seg-

ment we would expect the according XPS peak to be of quite low intensity. An alternative, or possibly additional explanation could be once again the bond dipole contribution. It is conceivable that the difference in bond dipole between C15EC5 and the Cn reference SAM cancels the still present, although due to mostly horizontal ester dipoles reduced, work function modification. Such a combination of effects could be theoretically imagined. However it seems highly coincidental that both effects should exactly cancel each other. At the moment though we cannot offer a better explanation for the unusually small work function modification of C15EC5 observed in experiments.

The implications of horizontal orientation of the ester dipole could also possibly explain the measured HRXP spectrum and work function of the double ester system C10EC4EC5 (see Figures 6.8, 6.9 and 6.10 for the HRXPS data and 6.11 for the work function modification). If the molecule is oriented in a way that aligns the first (nearest to the substrate) ester group horizontally, this group will not produce a potential discontinuity in the SAM. And therefore no separate peak will show up in the XP spectrum. In this case only two instead of three peaks should be fitted into the measured main peak of the XP spectrum (see Figure 6.10): one assigned to the bottom and middle segment combined and one assigned to the top segment, separated from the lower parts by the second ester group. For this decomposition the XPS shift between bottom+middle and the top segment agrees with the one found for the C10EC10 SAM. The work function modification measured for the double ester system (-0.4 to -0.5 eV) is also comparable to the one measured for the C10EC10 (-0.4 eV) SAM. This is a further indication that one of the ester groups might be "electrostatically inactive" due to horizontal dipole orientation. Another observation corroborating this theory are the peak positions of the carbonyl and ether carbons in the HRXP spectrum of the double ester system (see Figures 6.9 and 6.10). Their peaks are increased in intensity compared to the C10EC10 and C15EC5 SAMs, but not shifted. The intensity increase is explained by the presence of two ester units instead of one. However, if the first ester group were to produce an electrostatic shift, the second ester group would be equally affected as the rest of the molecule, meaning the carbonyl and ether signals of the second ester group would be shifted. However, Figure 6.9 shows no indication of such a shift, which would be noticeable as a distinct peak broadening at the very least. This experimental finding further strengthens the hypothesis that in the double ester system the ester group closest to the substrate is oriented horizontally and therefore does not induce an electrostatic shift.

6.8. Conclusions

Mid-chain functionalized AT SAMs are an important system to study the electrostatic effects of the embedded dipolar groups, such as esters. Compared to aromatic monolayers, having quite large structural units (phenyl rings), AT SAMs provide better possibilities for parameter variation such as the identity of the embedded

dipolar group, its position and orientation in the molecular backbone, as well as the total length of this backbone. On the other hand, aliphatic SAMs are more prone to structural variations including conformational disorder induced by the embedded group, which makes it difficult to establish a correlation between the structural and electrostatic properties. Nevertheless a clear correlation between the presence of the embedded ester group and the work function and binding energies were found. The embedded dipolar group modifies both quantities by up to several tenths of eV. This electrostatic influence strongly depends on the precise orientation of the ester dipole and its resulting, effective z-component (perpendicular to the substrate). Reversal of the embedded dipolar group results in reversed electrostatic effects, while they simply vanish for horizontal orientation of the ester dipole. The bond dipole was identified as a second main electrostatic influence in the SAM, affecting electronic properties by up to 0.4 eV. Both effects combine in the top segment of the SAM, where they may enhance or partially cancel each other depending on the orientation of the ester dipole. Furthermore, it was found that bond dipole differences between functionalized AT SAMs and reference NSAT SAMs can introduce variations of the determined work function modifications and BE shifts of up to 0.4 eV. This influence is of special relevance in choosing a suitable reference system for data evaluation, e.g. using the bottom segment of the same SAM or an NSAT SAM as a reference to evaluate BE shifts of the top segment.

7. Mixed monolayers of aromatic molecules with embedded dipolar elements

In the previous chapter, SAMs of alkylthiols with embedded dipolar groups were extensively studied. The impact of chain length and dipole orientation was investigated. The implications of horizontal versus vertical dipole orientation were of special interest. In this context, the possibility of mixed SAMs containing molecules with both these dipolar orientations and the possible implications on film properties were briefly addressed. To answer these open questions a study on mixed, dipolar SAMs has been carried out, the results of which are presented in this chapter. However, SAMs of ester-functionalized alkylthiols are not an ideal system to test the effects of mixed dipolar SAMs. Their structural variations, off-axis dipole moments and varying bond dipole contributions make it unnecessarily challenging, or even impossible to determine the exact impact of individual contributions. Therefore, a system of functionalized, aromatic molecules was chosen as a test case. These molecules, although exhibiting dipoles with opposite orientation along the molecular backbone (or no dipole at all in the case of the reference system) form highly ordered SAMs with the same structural properties, independent of dipole orientation. This makes them an ideal test case to study the effects of mixing ratio and film homogeneity on the electronic properties of the SAM, while avoiding spurious effects caused by structural differences in the films.

Author Contributions:
The work presented in this chapter was a collaborative effort between experimental and theoretical partners. The individual contributions were as follows. Tarek Abu-Husein and Andreas Terfort synthesized the molecules. Swen Schuster, Tobias Wächter and Michael Zharnikov prepared the SAMs and performed all of the HRXPS, work function and concentration measurements and provided me with the according data. They also helped me in numerous discussions with interpreting the experimental data. I performed all calculations and theoretical evaluations shown in this chapter and analyzed the results. David A. Egger provided me with an initial unit cell for the calculations of the pure TP1-up, TP-down and TP1 SAMs, which I reoptimized to be consistent in the parameter settings for all calculations of this chapter. I wrote the text and made all the figures shown in this chapter. Egbert Zojer supervised the theoretical work and strongly contributed to the interpretation of the data in numerous discussions. Finally, the idea to study mixed self-assembled

monolayers of these molecules and to investigate the impact of homogeneity was conceived by Egbert Zojer and Michael Zharnikov. We aim to publish the results presented in this chapter in the form of a journal publication and are currently working on a manuscript. We plan to submit it to the Journal of Physical Chemistry Letters in the near future. This chapter of the thesis presents all results and analyses on mixed monolayers in detail, whereas the paper gives a compact account of the most important, central aspects of the study.

7.1. Introduction

Controlling and tuning surface and interface properties has been one of the major goals of research in the fields of chemistry, physics and nanotechnology for some time now. In this context, self-assembled monolayers offer unique possibilities to modify surface properties in a variety of ways. They can be employed for corrosion protection,[273,274] to change wetting properties[270,271] or to facilitate cell adhesion.[275,338] Also photosensitive films can be created by adsorbing for example azobenzenes[339–343] which change their conformation from trans to cis upon illumination. This is just a small range of possibilities SAMs provide for altering surfaces chemically and physically. They also find wide application in the field of organic electronics, enhancing the performance of organic transistors,[58,59,66] solar cells[53–55,57] and light emitting diodes.[344–346] They are included into the devices to purposefully modify contact-semiconductor[27,53,62] and dielectric-semiconductor[63–66] interfaces or to improve film growth.[64,347] SAMs have even been used as active layers themselves.[58–60]

For these electronic applications the electric dipole moment of the molecules building the SAM is of crucial importance. It strongly influences the electrostatic situation inside the SAM through collective electrostatic effects[25,28,119,121,122,269] and, therefore, can significantly alter device properties like substrate work functions[14,72–74] and charge injection barriers.[61,62,108,344] Molecules with large dipole moments are particularly useful for such applications. The usual way to employ molecular dipoles is in the form of terminal groups.[14,27,28,61,115,279,285] This functional group is chosen to provide the desired dipole moment for the application. Modifying the vacuum side end group of the SAM, however, will also change the interaction with the next layer, i.e. the chemical reactivity[348,349] might be altered, as well as the growth properties of the adjoining layer.[64,316] Considering the number of unwanted side effects, it seems undesirable to use the terminal group as a handle to tune the molecular dipole. On the contrary it would be preferable to find a way that enables separate tuning of the dipole moment and chemical interactions with the adjoining layer. This can be realized by introducing embedded dipolar units into the backbone of the molecule instead of at the end. In this way, the terminal group with its chemical, structural and wetting properties remains in place, while the molecular dipole can be changed at will to tune the work function of the substrate. The general concept of embedded functional groups has already been employed and described in several studies.[350–353] Dipolar functional units inside SAMs are a more recent topic of interest. Studied systems include ester groups inside alkylthiol SAMs[25] (described in detail in Chapters

5 and 6), pyrimidine substituted aromatic SAMs[26] as well as mixed monolayers of different carboranethiol isomers.[24] In ref [26] the impact of substituting the central ring of a terphenyl-4-methanethiol with a 2,5-pyrimidine group has been investigated in an extensive experimental and theoretical study. We revisit these aromatic SAMs with embedded dipolar groups in this work and investigate how they behave in mixed monolayers. The impact of mixing ratio on the work function and atomic binding energies in homogeneous mixtures is investigated. In a second step, we take a look at how SAMs with domain structures behave. We investigate how phase separation of molecules with different dipole moments affects the electronic properties of the SAM. In this work we complement density functional theory (DFT) calculations with high-resolution X-ray photoelectron spectroscopy (HRXPS) and work function (WF) measurements. Theoretical and experimental results are presented and compared.

7.2. Theoretical methods

All calculation results presented in the following were obtained with density functional theory (DFT) using the program package VASP[238–241] version 5.3.2. Periodic boundary conditions were used in all spatial directions including dipole correction and a vacuum gap of ≈20 Å in z-direction to decouple the individual 2D slabs[302] artificially produced by the periodicity in z-direction. For optimizing the geometry we used the program GADGET[267] in conjunction with VASP, which enables optimizing in internal coordinates. The PBE functional[235,236] was used in all calculations together with PAW[242,299] potentials and a cutoff energy of 300 eV for the plane wave basis set. For the geometry optimization we chose a convergence criterion of $10^{-2}\,\mathrm{eV\,\AA^{-1}}$ for the forces acting in the ionic relaxation. The total energy in the self-consistent cycle of each DFT step was converged to 10^{-6} eV. For the z-dipole moment of the unit cell a precision of 10^{-4} eÅ was required. Thus, the calculations were extended beyond already achieved energy convergence if necessary to converge the dipole moment to a sufficient level. Core-level energies presented were calculated in the XPS initial state approach[247] which does not by itself account for screening effects of the substrate. These screening effects were included in the form of a classical image charge model[261,262] in a postprocessing step as described in detail in Section 5.3 (see also ref [269]). The image plane position was chosen as 0.9 Å above the top gold layer[308,309] and the dielectric constant was ε=3.0. XP spectra were calculated from the individual core level energies by summing up Gaussian functions (variance=0.1 eV), accounting for the surface sensitive nature of XPS measurements by including exponential damping as described in detail in Section 5.3 (see also ref [269]). The incident photon energy was chosen in accordance with experiment as hν=580 eV and a value of β=0.65 for describing damping effects (see Section 5.3 for details) was chosen for yielding the best agreement of relative peak heights between calculated and measured XP spectra.

7.3. Experimental methods

This section on experimental methods was written by Michael Zharnikov. It is taken as is from our joint manuscript, which is currently in preparation for journal publication. Therefore, an italic font is used for this section. We plan to submit the manuscript to the Journal of Physical Chemistry Letters. It has not yet been submitted though.

"The gold substrates (Georg Albert PVD-Beschichtungen) were prepared by thermal evaporation of 100-200 nm of gold (99.99% purity) onto polished single-crystal Si(100) wafers (Silicon Sense) primed with a 5 nm adhesion layer of titanium or chromium. These substrates were polycrystalline, with predominant (111) orientation and a grain size of 20-50 nm. The SAMs were formed by immersion of freshly prepared substrates into a mixed solutions of TP1-up and TP1-down in tetrahydrofuran with a joint concentration of ∼0.1 mM for 24 h at room temperature. The mixing ratio was varied. After immersion, the samples were carefully rinsed with pure solvent and blown dry with a stream of N_2.

Work function measurements were carried out using a UHV Kelvin Probe 2001 system (KP technology Ltd., UK). The pressure in the UHV chamber was ∼10^{-10} mbar. SAMs of hexadecanethiol on Au and freshly sputtered gold were used as references. XPS measurements were carried out at the HE-SGM beamline (bending magnet) of the synchrotron storage ring BESSY II in Berlin, Germany. The spectra were acquired in normal emission geometry using a Scienta R3000 spectrometer. The photon energy was set to 350 eV. The energy resolution was 0.2-0.3 eV. The BE scale was referenced to the Au $4f_{7/2}$ emission of the gold substrate at 84.0 eV.[354] *The quality of the films was verified by additional XPS and X-ray absorption measurements."*

7.4. Investigated systems

We studied SAMs of three different terphenyl-based molecules, either in pure monolayers or mixed monolayers. The chemical structures of the studied molecules are depicted in Figure 7.1. They consist of a terphenyl-4-methanethiol reference system, named TP1 in this paper, and two TP1 based molecules where the central phenylene ring has been substituted with a 2,5-pyrimidine group (named TP1-down and TP1-up). The pyrimidine unit introduces a significant, embedded dipole moment (2.3 Debye)[128,129] oriented along the molecular axis. For the TP1-down molecule the pyrimidine dipole points towards the thiol docking group and the substrate, whereas it points in the opposite direction for the TP1-up molecule. The TP1 system has no pyrimidine unit and therefore lacks this dipolar contribution. This makes it an ideal reference system as it is otherwise identical to the TP1-up and TP1-down molecules. It has the same docking group, the same molecular length and, very crucially, the same terminal group. We therefore they form similar packing geometries for all SAMs.[26] Quantities like the vacuum side work function will not be affected

by the influence of chemically different terminal groups. This allows us to study the influence of the embedded dipole moment, reducing other spurious effects to a minimum.

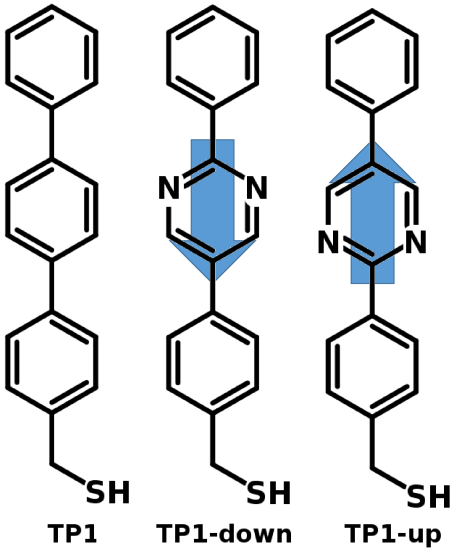

Figure 7.1.: Schematic chemical structures of the three molecules discussed in this paper. The arrows indicate the direction of the dipole moment of the central pyrimidine unit (drawn from the negative to the positive end), which points in opposite directions for TP1-down and TP1-up. The TP1 reference system without a pyrimidine unit lacks this significant dipolar contribution.

All calculated SAMs were full coverage films with molecules binding to the fcc hollow sites of the Au(111) substrate. The unit cells included five layers of gold substrate with the topmost two layers mobile in the geometry optimization. The bottom three layers were kept fixed during the optimization process to simulate bulk gold. For all described systems a herringbone packing was assumed.[26]

To calculate pure SAMs containing only one molecule type we used a $\left(\sqrt{3}\text{ x }3\right)$ unit cell containing two molecules (see Figure 7.2a) combined with a 8x5x1 Monkhorst-Pack[246] k-point grid. The $\left(\sqrt{3}\text{ x }3\right)$ unit cell is equivalent to the $\left(\sqrt{3}\text{ x }2\sqrt{3}\right)$ R30° structure reported for TP1 monolayers on gold in literature.[26,355–358]

We also performed calculations on mixed SAMs (TP1-up:TP1-down ; TP1:TP1-up ; TP1:TP1-down) with the mixing ratios 75:25, 50:50, 25:75. For these calculations we used a $\left(2\sqrt{3}\text{ x }3\right)$ unit cell containing four molecules (see Figure 7.2a). The mixing ratios were implemented as 3:1, 2:2, 1:3 molecules of each type per unit cell. The k-point grid was chosen according to the unit cell size as a 4x5x1 Monkhorst-Pack[246] grid. With these mixing ratios and the described choice of unit cell the calculations describe homogeneously mixed SAMs.

For comparison we also performed a calculation of an inhomogeneously mixed TP1-up:TP1-down SAM, showing phase separation into domains of one molecule type. To describe such an inhomogeneously mixed structure, a larger unit cell is

necessary. As a compromise between domain size and feasibility of the calculation we chose a $\left(6\sqrt{3}\text{ x }3\right)$ unit cell creating a striped structure (see Figure 7.2a). This unit cell includes six molecules of type TP1-down and TP1-up each; all TP1-down molecules are situated in the left half of the unit cell, while all TP1-up molecules are situated in the right half (see Figure 7.2b). Employing periodic boundary conditions on this unit cell creates infinitely extended striped domains of each molecule type of a width of three molecules. For this unit cell a 2x6x1 Monkhorst-Pack[246] k-point grid was used.

No geometry optimization of this large unit cell was performed, due to computational cost. Instead it was built from the individual, geometry optimized unit cells of the pure TP1-down and TP1-up SAMs respectively (see details above).

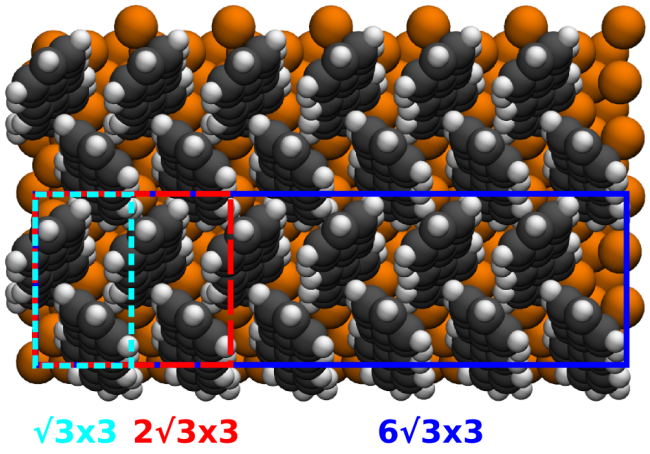

(a)

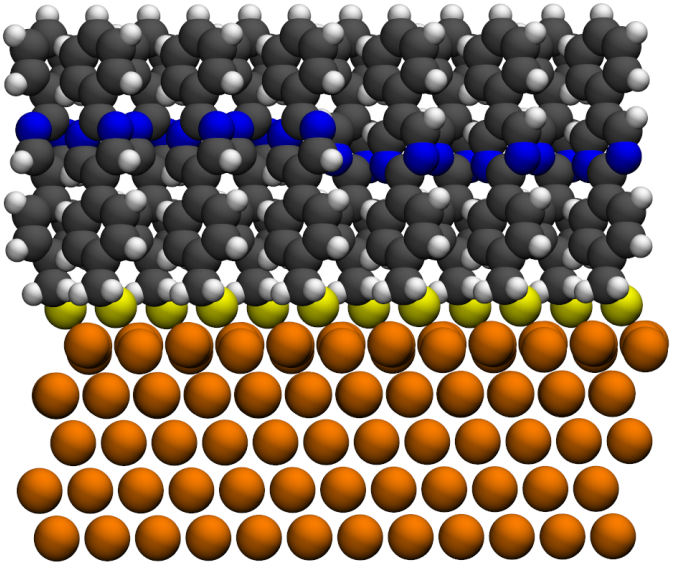

(b)

Figure 7.2.: (a) Top view of the terphenyl SAM structure on Au(111) substrate. The three different unit cells used for calculations in this work are indicated by colored boxes: $\left(\sqrt{3}\text{ x }3\right)$ (dotted cyan line), $\left(2\sqrt{3}\text{ x }3\right)$ (dashed red line) and $\left(6\sqrt{3}\text{ x }3\right)$ (solid blue line). (b) shows a sideview of the $\left(6\sqrt{3}\text{ x }3\right)$ unit cell used to create the inhomogeneously mixed 50:50 TP1-up:TP1-down SAM. The six TP1-down molecules are all situated in the left half of the unit cell, whereas the TP1-up molecules are situated in the right half, clearly distinguishable by the different positions of the nitrogen atoms (blue) in the respective molecules.

7.5. Results and discussion

7.5.1. Pure SAMs

It has already been shown in a number of publications, e.g. [24, 25, 252, 269] that a dipolar layer in a SAM leads to a highly localized drop in the electrostatic potential and consequently shifts the work function of the whole system due to collective electrostatic effects. The molecules treated in this work were already studied by Abu-Husein et al.[26], who investigated pure layers of TP1, TP1-up and TP1-down SAMs on Au(111) substrate. They showed in a combined experimental and theoretical study that the downward pointing dipole layer in the TP1-down SAM shifts the core level energies of the vacuum side carbon ring to less negative values and increases the work function of the system with respect to a pure TP1 reference SAM without this dipole layer. The TP1-up SAM with a layer of dipoles pointing in opposite direction, namely away from the substrate, showed the reverse trend. Core level energies are shifted to more negative values and the work function is decreased.

We take these unmixed systems as a starting point for our calculations. However, in contrast to calculations presented in ref [26], we include screening effects of the substrate as described in the method section. Additionally, we calculate XP spectra, including exponential damping of the signal. The calculated carbon 1s core level energies of a pure TP1-down, TP1-up and a TP1 reference SAM are depicted in Figure 7.3. We find a good qualitative and quantitative agreement with the results presented in ref [26].

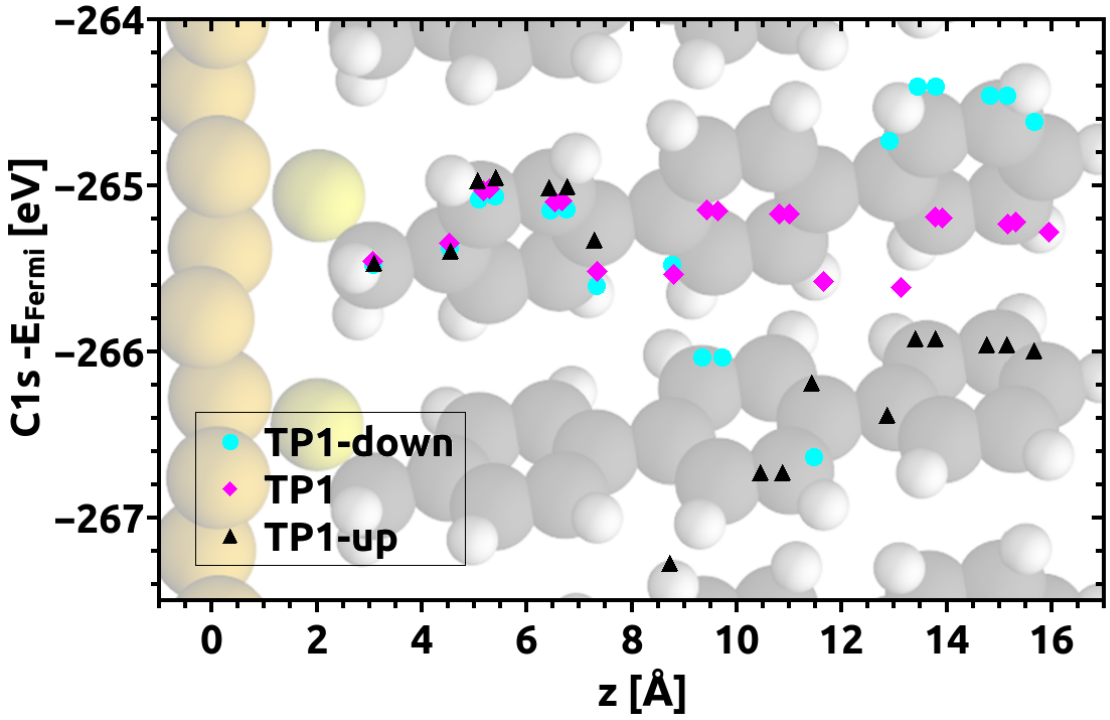

Figure 7.3.: Calculated carbon 1s core level energies of a pure TP1 SAM (pink diamonds) a TP1-down SAM (cyan dots) and a TP1-up SAM (black triangles) relative to the Fermi energy of the system. The given core level energies and z-positions of the carbon atoms are obtained as average values of the two molecules in the unit cell for each system. The maximum energetic difference in core level energies between equivalent atoms in a unit cell is 0.06 eV. In the TP1-up SAM the dipole layer shifts the C1s energies of the top ring downwards in energy. In the TP1-down SAM the situation is reversed, the core level energies are shifted upward. In the pure TP1 SAM no electrostatic shift takes place due to the lack of dipole moment. In this case, all three carbon rings are energetically equivalent, save for screening effects. These shift the 1s energies of the carbon ring nearest to the substrate to slightly less negative energies.

The 1s energies of the carbons in the vacuum side ring are shifted with respect to the substrate side ring according to the electric dipole introduced by the central pyrimidine unit. The downward pointing dipoles in the TP1-down SAM shift C1s energies upwards. In the TP1-up SAM the situation is reversed due to the opposite orientation of the molecular dipoles. To quantify the effect we calculate the average C1s energy of the carbons in the vacuum side ring (including screening and exponential damping of the XPS signal) for all three depicted systems. The shift between the top carbon rings of TP1-down/TP1-up and TP1 is symmetric for both functionalized SAMs. The core level shift for TP1-down is ΔC1s = +0.77 eV, while it is ΔC1s = -0.74 eV for TP1-up. These calculated values are in good qualitative agreement with the experimental shifts stated in ref [26], which are ΔC1s = -0.42 eV and

ΔC1s = 0.65 eV respectively for TP1-down and TP1-up. Note that calculated core level energies have a negative sign, while measured binding energies have a positive sign by convention. Therefore, the XPS shifts have different signs for calculated and measured values. A calculated shift to more negative core level energies corresponds to a measured shift to higher binding energies. The effect seems to be more pronounced in calculations than in measurement. This observation was already made and described in ref [26], where structural imperfections in the experimental SAM like grain boundaries are discussed as possible causes.

The carbon atoms in the middle ring, containing the nitrogen atoms are afflicted by chemical shifts and therefore show different core level energies than the carbons in the two phenylene units. So are the carbons connecting the substrate and vacuum side ring to the central pyrimidine unit. The electrostatic shifts between the carbons in the three rings and the mentioned chemical shifts manifest themselves in the calculated and measured XP spectra, see the spectra of the pure TP1-up and TP1-down SAMs shown in Figure 7.5. The main peak for these systems is created by the strong signal of the carbons of the vacuum side phenylene ring. Additionally there is a smaller "shoulder" to the right/left of the main peak for the TP1-up/TP1-down system. This shoulder is produced by the chemically shifted carbons in the pyrimidine unit and by the carbon atoms in the substrate side phenylene ring. This side peak is lower in intensity due to the stronger damping of the XPS signal of the deeper lying atoms creating it.

The systems' work functions are equally affected by the embedded dipole layers. The calculated work function modification (with respect to the work function of a pure TP1 SAM on Au(111) substrate) is $\Delta\Phi$ = +0.75 eV for the TP1-down SAM and $\Delta\Phi$ = -0.71 eV for the TP1-up SAM. These values agree qualitatively and quantitatively very well with the calculated shift of the core level energies. In measurements[26] work function modifications of $\Delta\Phi$ = +0.56 eV and $\Delta\Phi$ = -0.42 eV for the TP1-down and TP1-up SAMs were found.

Concluding this first introductory section we can state that our calculation method yields very good agreement with published data for the already studied pure TP1-down and TP1-up SAMs on Au(111). In general, effects are more pronounced in calculations than in experiments. This, however, was also already stated and its origin tentatively explained in ref [26]. We therefore are confident in applying this approach to mixed SAMs presented in the following.

7.5.2. Homogeneous mixtures of molecules with opposing dipoles

Now that we have defined how a pure SAM's properties are affected by the embedded dipolar group, we investigate how such molecules behave in mixed SAMs. We specifically are interested in how properties of the SAM can be influenced by varying the mixing ratio. First we take a look at a homogeneously mixed SAM consisting of

a 50:50 ratio of TP1-up and TP1-down molecules. The calculated carbon core level energies are depicted in Figure 7.4 and in the form of an XP spectrum in Figure 7.5.

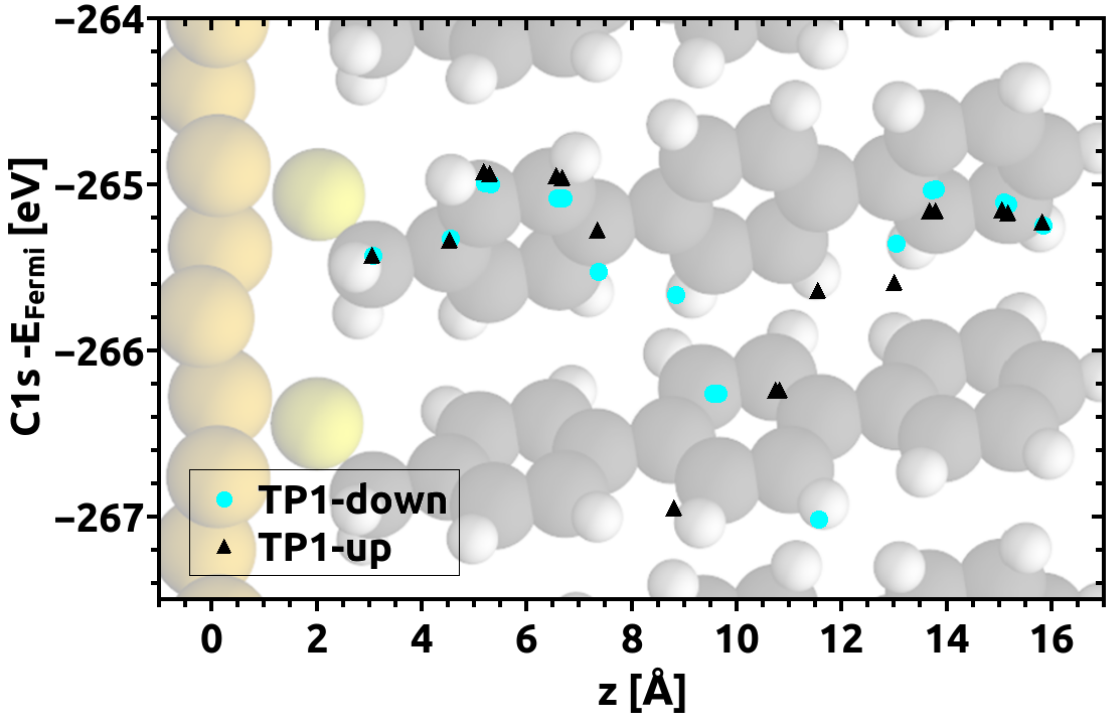

Figure 7.4.: Calculated C1s energies of a homogeneously mixed TP1-up : TP1-down SAM with the mixing ratio 50:50. The average atomic C1s energies of the TP1-down molecules (cyan dots) and TP1-up molecules (black triangles) in the SAM are shown relative to the Fermi energy of the system as a function of the average z-position of the individual carbon atoms.

In Figure 7.4 we see that the substrate side rings of both molecule types inside the SAM have the same C1s energies. This does not yet distinguish them from the pure SAMs described above. The vacuum side rings of TP1-up and TP1-down molecules in the mixed SAM, however, also have nearly identical C1s energies. This is a qualitatively different trend from the one encountered in pure TP1-up and TP1-down SAMs. In the homogeneous mixture, an upward pointing dipole of a TP1-up molecule is surrounded by the downward pointing dipoles of its TP1-down neighbor molecules and vice versa. Thus, we find no cluster of equally oriented dipoles in a homogeneously mixed SAM. This prevents the collective electrostatic effects responsible for the potential discontinuity and the associated shift in core level energies found in pure TP1-up and TP1-down SAMs. The lack of collective effects explains the missing electrostatic shift between the substrate and vacuum side ring for the mixed SAM. The qualitatively different behavior of pure and mixed TP1-up/down SAMs can be seen even more clearly in calculated XP spectra (shown in Figure 7.5).

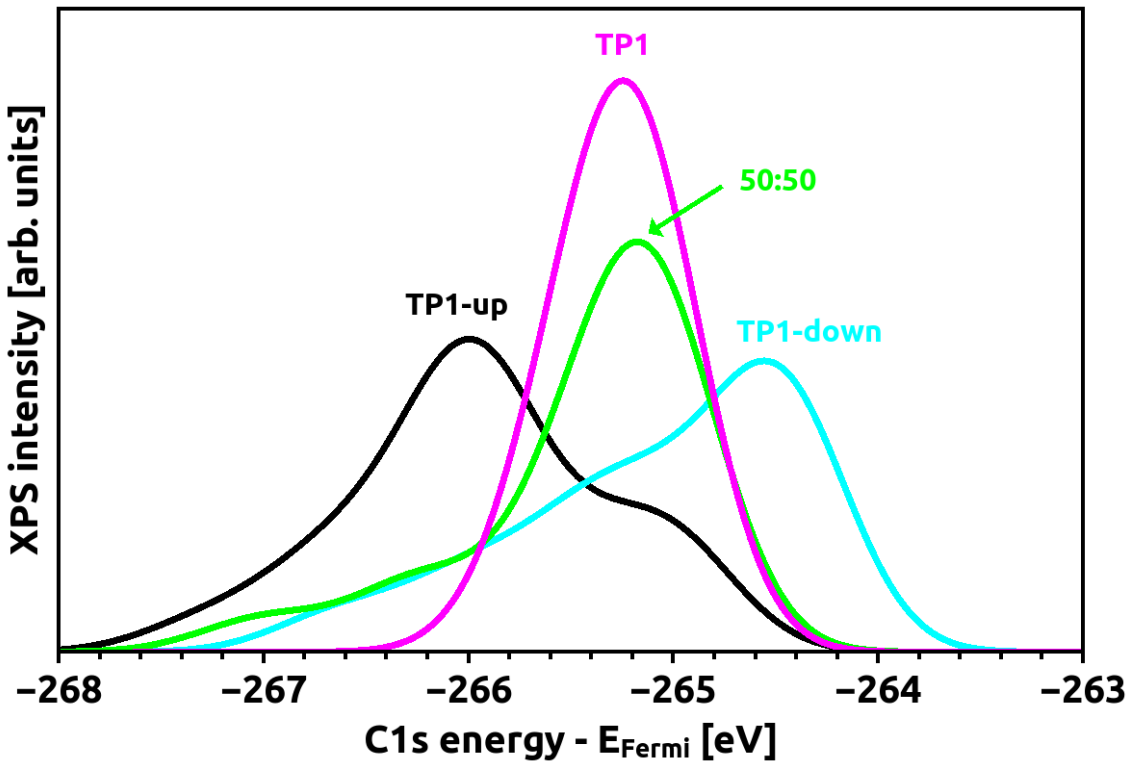

Figure 7.5.: Calculated XP spectra of a pure TP1-up (black), TP1-down (cyan), a homogeneously mixed 50:50 TP1-up:TP1-down (green) and a pure TP1 reference SAM (pink). The shown XP spectra were calculated from the calculated C 1s core level energies of the four shown systems according to the method described in Section 7.2. All four spectra are depicted relative to the respective Fermi energy of each system.

In Figure 7.5 we see that the main peaks of the pure TP1-up and TP1-down SAMs are shifted symmetrically with respect to the TP1 reference SAM. We also see the lower intensity "shoulders" next to the main peaks of the TP1-up and TP1-down SAMs already mentioned in the previous section discussing pure SAMs. They are caused by the carbons in the middle and substrate side rings, which are energetically different (due to chemical and electrostatic effects) from the carbons of the vacuum side ring creating the strong main peak.

The XPS peak of the homogeneous mixture and the TP1 reference SAM are found at the same energy, symmetrically in between the TP1-up and TP1-down peak. The electrostatic shift due to the pyrimidine unit does not happen for 50:50 mixed SAMs in the same way as for pure SAMs. No collective electrostatic shift is observed in the mixed case. The C1s energies of the bottom and top ring are the same. The peaks of the TP1 reference SAM and the 50:50 homogeneous mixture, however, have higher intensity than the other two pure SAMs, the TP1 reference having the highest signal intensity of those four spectra. This is caused by the carbons of the middle ring, which lie at the same energy as the two other rings for TP1, which is

not the case for TP1-up and TP1-down SAMs. In those cases, the carbons in the pyrimidine unit are chemically shifted. This leads to lower, more broadened peaks for pure TP1-up and TP1-down SAMs. The pure TP1 SAM in contrast creates a higher, narrower XPS peak. The 50:50 homogeneous mixture is an intermediate case. Here the substrate and vacuum side ring are not noticeably electrostatically shifted with respect to each other and do add up in the XPS signal. The carbons in the middle pyrimidine unit however are chemically shifted to different C1s core level energies and do not add to the main XPS signal of the other carbons. Therefore the XPS peak of the 50:50 mixtures is higher than the peaks of the pure TP1-up and TP1-down SAMs but still lower than the signal of the TP1 reference SAM.

For a complete picture we also take a look at the work function modification (vacuum side work function relative to the work function of a pure gold substrate) of the different SAMs. The value for the 50:50 homogeneous mixture $\Delta\Phi_{\mathrm{mix}}$ = -1.21 eV is practically the same as the work function modification of the pure TP1 SAM $\Delta\Phi_{\mathrm{TP1}}$ = -1.29 eV. These values lie essentially halfway between the work function modifications of the pure TP1-up $\Delta\Phi_{\mathrm{TP1-up}}$ = -2.00 eV and TP1-down SAM $\Delta\Phi_{\mathrm{TP1-down}}$ = -0.54 eV. These results agree nicely with the previously presented carbon core level energies.

Varying the mixing ratio

In this part we take a look at how the properties of the SAM can be influenced by varying the mixing ratio. We performed calculations of TP1-up : TP1-down mixed SAMs with the ratios 75:25, 50:50 and 25:75. XP spectra were calculated for these mixed SAMs and compared with spectra of the corresponding pure SAMs. Calculated results are also compared to measured spectra of the same mixed SAMs. The calculated and measured HRXP spectra are shown in Figure 7.6. The peakwidths (full width at half maximum = FWHM) of the calculated and measured spectra are summarized in Table 7.1. Note that the calculated XP spectra have been obtained using an extrinsic broadening with a variance of 0.1 eV. This value was chosen to fit the FWHM of the calculated pure TP1-up spectrum to the experimental spectrum of TP1-up. The same broadening has been used to obtain all other spectra (and FWHM) shown in Figure 7.6 and Table 7.1. This is the reason why the agreement in FWHM between experiment and calculation is perfect for TP1-up. For the other systems calculated and measured FWHM still agree quite well.

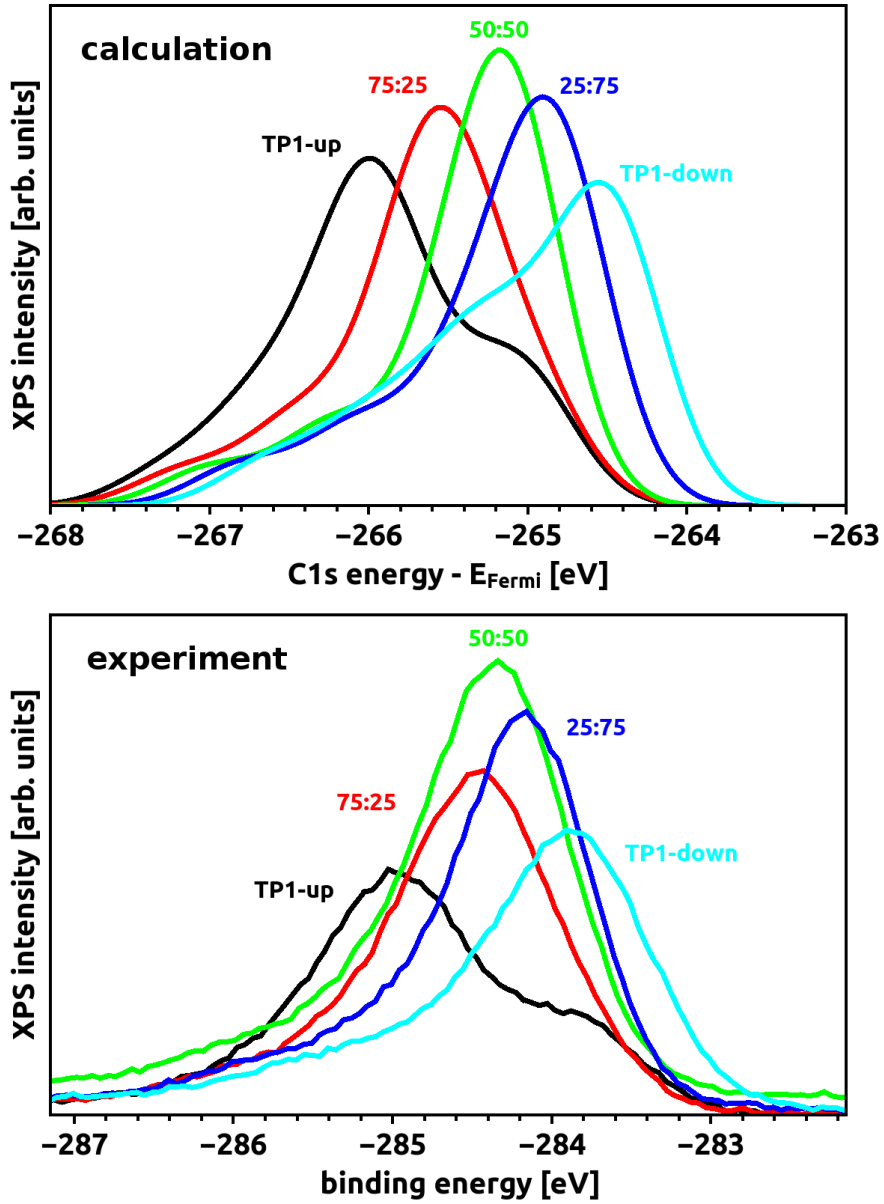

Figure 7.6.: Calculated (top) and measured (bottom) HRXP spectra of TP1-up : TP1-down mixed SAMs with different ratios: pure TP1-up (black), 75 up : 25 down (red), 50 up : 50 down (green), 25 up : 75 down (blue) and pure TP1-down (cyan). The calculated spectra are aligned relative to the Fermi energy of each system. The given mixing ratios for the experimental SAMs are the concentrations in the solution. Measurements were taken at BESSY with an incident photon energy of hν=580 eV. Notice the different x-axes in both graphs: C 1s core level energies relative to the Fermi energy for calculated spectra and electron binding energy for measured spectra. The two spectra are rigidly shifted by 19.15 eV with respect to each other. It is well know that calculated absolute core level energies are not suitable for comparison to absolute measured binding energies; instead relative energies and energy shifts are the quantities to be compared.[303–305,310]

Table 7.1.: Full width at half maximum (FWHM) of the calculated and measured XP spectra of pure and mixed TP1-up and TP1-down SAMs. FWHM values are given in eV.

TP1-up : TP1-down ... mixing ratio in the solution

$FWHM_{calc}$ ... full width at half maximum of the calculated spectra

$FWHM_{exp}$ ... full width at half maximum of the measured spectra

TP1-up : TP1-down	$FWHM_{calc}$	$FWHM_{exp}$
100 : 0	1.25	1.25
75 : 25	1.07	1.15
50 : 50	0.90	1.10
25 : 75	1.01	1.00
0 : 100	1.47	1.25

For varying mixing ratio we still find one dominant main peak associated with the vacuum side carbon ring. The low intensity "shoulder" caused by the carbon atoms in the middle ring (as already seen in pure TP1-up and TP1-down SAMs) is also present in the XP spectra of mixed SAMs. The main peak shifts linearly with mixing ratio from the TP1-up pure SAM towards less negative energies to the pure TP1-down SAM. The SAMs described with these calculations are all homogeneous mixtures, even the ones with 25:75 mixing ratio. The molecular dipoles do not form isolated clusters of one type but are intermixed with opposing dipoles. They do not produce combined collective effects, but interact on a local scale. They can fully or partially compensate each other's electrostatic effects. Thus, overall we encounter averaged effects, which manifest themselves in the linear shift of the distinct main peak with mixing ratio. The corresponding HRXPS measurements show the same trends that were found in calculations. Note that calculated absolute core level energies are not suitable for direct comparison to measured binding energies.[303–305,310] Instead relative core-level energies and energy shifts should be used for comparison.[303–305,310] Thus, the different x-axes in Figure 7.6 should be noted, giving the calculated C 1s core level energy and the measured binding energy respectively. The rigid energetic offset between those two quantities, however, is no hindrance for the interpretation of the data as we aim to find qualitative trends and compare only relative energies and not absolute values.

Another featured observed in the spectra shown in Figure 7.6 is the varying peak height for SAMs with different mixing ratios. This is equally found in calculation and in experiment, although the experimental spectra show a more pronounced effect. It has to be kept in mind though, that the experimental peak heights are not absolutely reliable as a certain variation is introduced in different measurements. The pure TP1-up and TP1-down SAMs produce the lowest and broadest peaks (FWHM = 1.25 eV and 1.45 eV), whereas the homogeneous 50:50 mixture has

the highest intensity and the narrowest peak (FWHM = 0.90 eV calculated, 1.10 eV measured). This can be explained by the XPS contributions of the individual carbon rings. The more pronounced the energy difference between the three rings, the broader and therefore lower the resulting main XPS peak gets. For the 50:50 homogeneously mixed SAM we already saw in the scatter plot (Figure 7.4) that the average C1s energy of carbons in the two phenylene rings is practically identical. Their respective contributions to the XPS signal lie at the same binding energy, adding up, thereby increasing the peak intensity. For SAMs with strong energetic difference between the carbon rings (like the pure TP1-up and TP1-down cases) the XPS signals of the individual rings are not positioned at the same energy, therefore creating a broader peak with lower maximum intensity. Intermediate mixing ratios behave accordingly (FWHM $\approx$ 1 eV).

One difference between measurement and calculation is that the main peak in measured XP spectra does not shift exactly linearly with mixing ratio. On that note one has to keep in mind that the mixing ratio given is the one of the solution used for producing the films. However, the concentration in the actual SAM can be quite different from the concentration in the solution. This is a commonly observed behavior in mixed SAMs.[24,359,360] In the case of the TP1-up : TP1-down mixture it is not possible to experimentally determine the actual mixing ratio in the adsorbed SAM. The usual approach is to compare relative nitrogen 1s signal intensities in XP spectra, to determine the concentration of nitrogen containing molecules in the film. However, in this case both molecules of the mixture contain two nitrogens each. Therefore, XPS peak intensities yield no information about the mixing ratio of this particular SAM. From the peak shifts, which are larger from pure to 75:25 (and 25:75) mixtures, than from 75:25 (25:75) to 50:50 we assume that all three mixed cases are actually closer to a 50:50 mixture than to a 75:25 mixture. This is plausible from an electrostatic point of view, as dipoles prefer antiparallel over parallel orientation as the energetically favorite one. This explanation is corroborated by our simulations, which show that the total system energy per molecule of the 50:50 mixture is 75 meV lower than for the 27:75 up:down mixture, and 60 meV lower than for the 75:25 mixture.

The non-linear shift observed in XPS peak position is analogously found in the measured work function modification, which also shows a non-linear behavior with respect to the concentration in solution (see Figure 7.8).

As a result of our calculations we also have knowledge about the electrostatic potential inside the SAM. It is shown in the form of the calculated plane-averaged electron electrostatic energy in Figure 7.7.

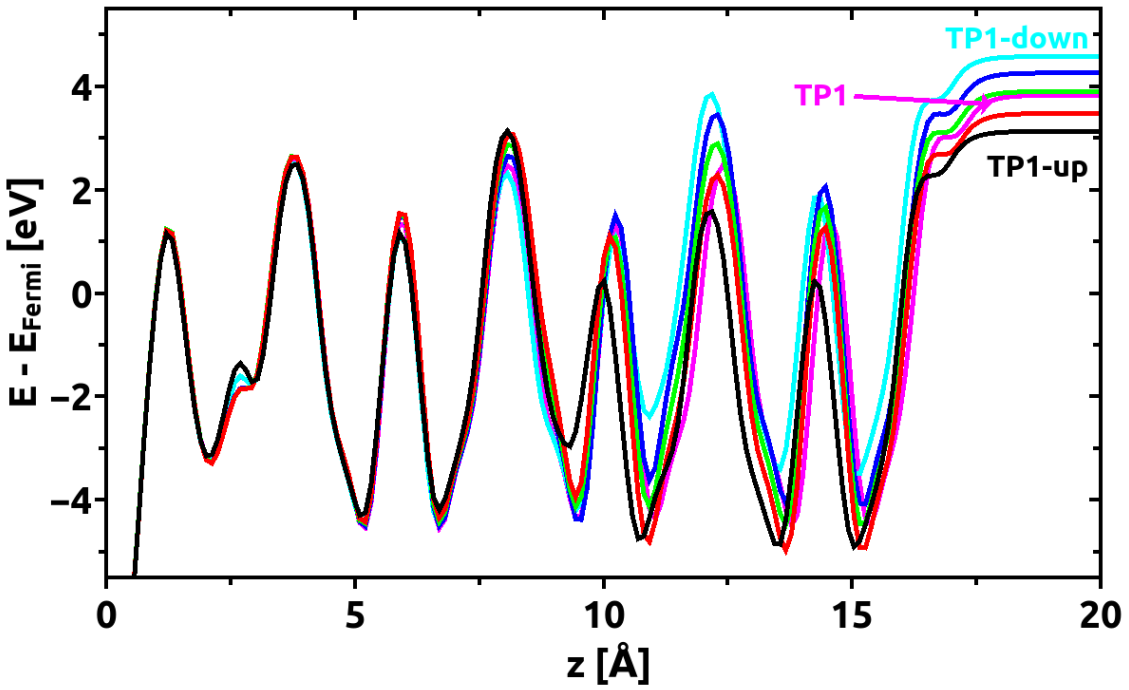

Figure 7.7.: Calculated plane-averaged electrostatic energy of an electron as a function of z-distance from the substrate given relative to the Fermi energy of each system. The data for the pure SAMs TP1-down (cyan), TP1 (pink) and TP1-up (black) and as well as for homogeneously mixed TP1-down : TP1-up SAMs with the mixing ratios 75:25 (dark blue), 50:50 (green) and 25:75 (red) is shown. The vertical distance is given relative to the average position of the atoms in the topmost gold layer (z=0 Å). The features situated between z=0 Å and z=18 Å correspond to the adsorbed SAMs. The electrostatic energy inside the gold substrate is not affected by the adsorbed SAMs[26] and is, therefore, not shown in this plot for the sake of clarity.

In Figure 7.7 we see that the electrostatic energy in the SAM below the pyrimidine unit is the same for all depicted systems. It only starts to differ at the pyrimidine unit situated at z ≈ 8 Å above the gold substrate. The essential feature of this plot, the electrostatic energy on the vacuum side of the SAM (shown on the right side of Figure 7.7) is directly linked to the mixing ratio. It shifts up linearly with increasing/decreasing TP1-down/TP1-up content in the SAM. Consequently the system with a 50:50 mixing ratio shows nearly identical vacuum side electrostatic energy as the TP1 reference SAM as the electrostatic influences of the TP1-up and TP1-down dipoles cancel in this case. The clearly visible shift in electrostatic energy, which is caused by the dipolar pyrimidine groups leads to the shifts in XP spectra described before and the work function modifications presented next.

Calculated and measured work function modifications for mixed SAMs are depicted in Figure 7.8. The values are given relative to a pure TP1 reference SAM.

The measured SAMs with mixing ratios of 10:90 and 90:10 were not reproduced in calculations due to computational cost. The unit cell sizes necessary to describe these mixing ratios render calculations prohibitively time consuming and expensive.

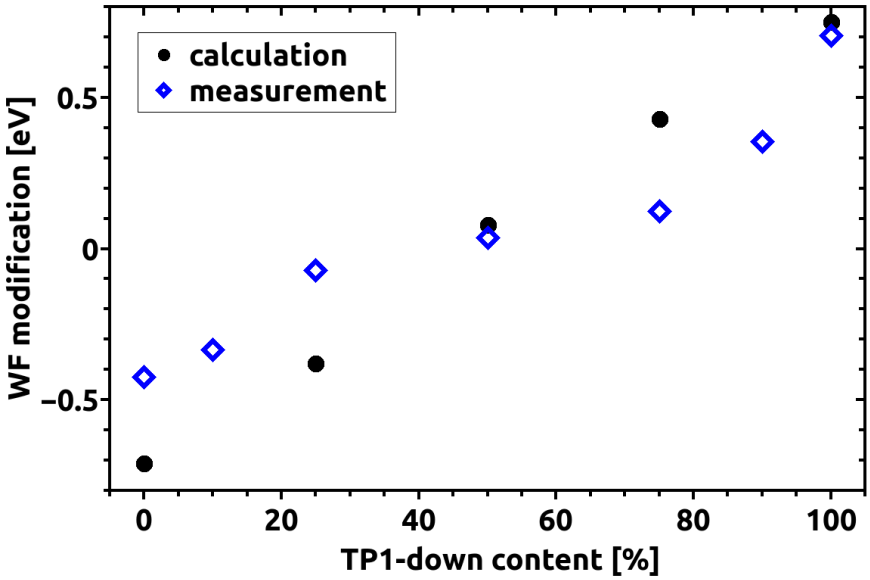

Figure 7.8.: Measured (red and blue open symbols) and calculated (full black dots) work function modification of TP1-up : TP1-down mixed SAMs of varying mixing ratio. The work function modification is given relative to the work function of a pure TP1 SAM.

As we see in Figure 7.8 the calculated work function modification follows the same trend as the calculated XPS peak positions described previously. It shifts gradually to more positive values for increasing TP1-down content in the SAM. The TP1-down molecules in the SAM increase the work function compared to TP1, whereas the TP1-up molecules decrease it. The actually observed work function is created by the combined contributions of both molecule types present in the SAM. For a homogeneous 50:50 mixture, the opposite shifts exactly compensate each other. In this case the work function modification is practically identical to the one of the pure TP1 reference SAM on gold substrate. We observe quite good qualitative agreement between calculation and measurement. In this context it should be stated that the given experimental concentrations are the concentrations present in the solution used for SAM preparation. The mixing ratio in the actual adsorbed SAM might vary from the ratio in the solution if one of the components adsorbs preferentially.[24,359,360] The concentration in the SAM, however, cannot be determined directly from measurements in this case as both molecule types contain two nitrogen atoms each. Thus, the XPS intensity of the nitrogen 1s peak does not give an indication of the actual molecule content in the SAM. Consequently, the lateral position of the experimental data points in Figure 7.8 is not to be fully trusted. If one takes into account the possibility that some of the measured data points should be shifted along the concentration axis to represent the actual concentration in the

SAM, even better agreement with the calculated data is conceivable. As already previously mentioned, such a non-linear shift with solution-concentration is also observed in the measured XPS peak positions of TP1-up : TP1-down mixed SAMs (see Figure 7.6). Both these observations can be explained by the assumption that the 75:25 and the 25:75 solutions probably create a mixture much closer to 50:50 in the adsorbed SAM as dipoles prefer antiparallel over parallel alignment. The calculated total system energies per molecule support this hypothesis. The energy of the 50:50 mixture is 75 meV lower than the one of the 27:75 up:down mixture, and 60 meV lower than the one calculated for the 75:25 mixture.

7.5.3. Reducing the dipole density

In the previous section the effects of homogeneously mixing upward and downward pointing dipoles in a SAM was studied.

In the following, we investigate what happens if we just use one dipole orientation in a SAM but vary the dipole density. The goal here is to change the distance between molecular dipoles inside the SAM, while the packing density of molecules is kept constant. This can be achieved by mixing the functionalized TP1-up or TP1-down molecules with the "pyrimidine-less" TP1 molecules. In this way we can produce SAMs with diluted dipole density, while keeping the same molecular packing and arrangement in the SAM. The TP1 molecules do not contribute electrostatically to the effects, but they keep the dipolar TP1-up/TP1-down molecules from reorienting or falling over.

Thus, mixed SAMs containing either TP1-up and TP1 or TP1-down and TP1 are investigated. In analogy to the previous section the mixing ratios 100:0, 75:25, 50:50, 25:75 and 0:100 are considered for both the TP1 : TP1-up and TP1 : TP1-down case. Contrary to the TP1-up : TP1-down mixtures discussed previously, these films allow a determination of the actual concentrations in the SAM as only one of the molecules contains nitrogen.

In experimentally studied SAMs we find a difference in concentration between the solution used for SAM preparation and the actually adsorbed SAM. Tables 7.2 and 7.3 list the respective concentrations present in solution and in the SAM for different mixing ratios. The molecular concentrations were determined separately from the intensity of the nitrogen 1s signal of the XP spectra and from NEXAFS measurements. The concentration values obtained from both measurements were then averaged.

Table 7.2.: Mixing ratio in the solution used for SAM preparation and in the actual adsorbed SAM for mixed SAMs of TP1 : TP1-up. Concentrations in the SAM were extracted separately from NEXAFS measurements and the intensity of the nitrogen 1s signal in XPS measurements. Values of both measurements were then averaged.

mixing ratio in the solution TP1 : TP1-up	**mixing ratio in the SAM** TP1 : TP1-up
100 : 0	100 : 0
75 : 25	77 : 23
50 : 50	54 : 46
25 : 75	32 : 67
0 : 100	0 : 100

Table 7.3.: Mixing ratio in the solution used for SAM preparation and in the actual adsorbed SAM for mixed SAMs of TP1 : TP1-down. Concentrations in the SAM were extracted separately from NEXAFS measurements and the intensity of the nitrogen 1s signal in XPS measurements. Values of both measurements were then averaged.

mixing ratio in the solution TP1 : TP1-down	**mixing ratio in the SAM** TP1 : TP1-down
100 : 0	100 : 0
75 : 25	68 : 32
50 : 50	36 : 64
25 : 75	12 : 82
0 : 100	0 : 100

First we take a look at the XP spectra for these systems. Figure 7.9 shows the calculated and measured spectra for both types of mixed SAMs with various mixing ratios.

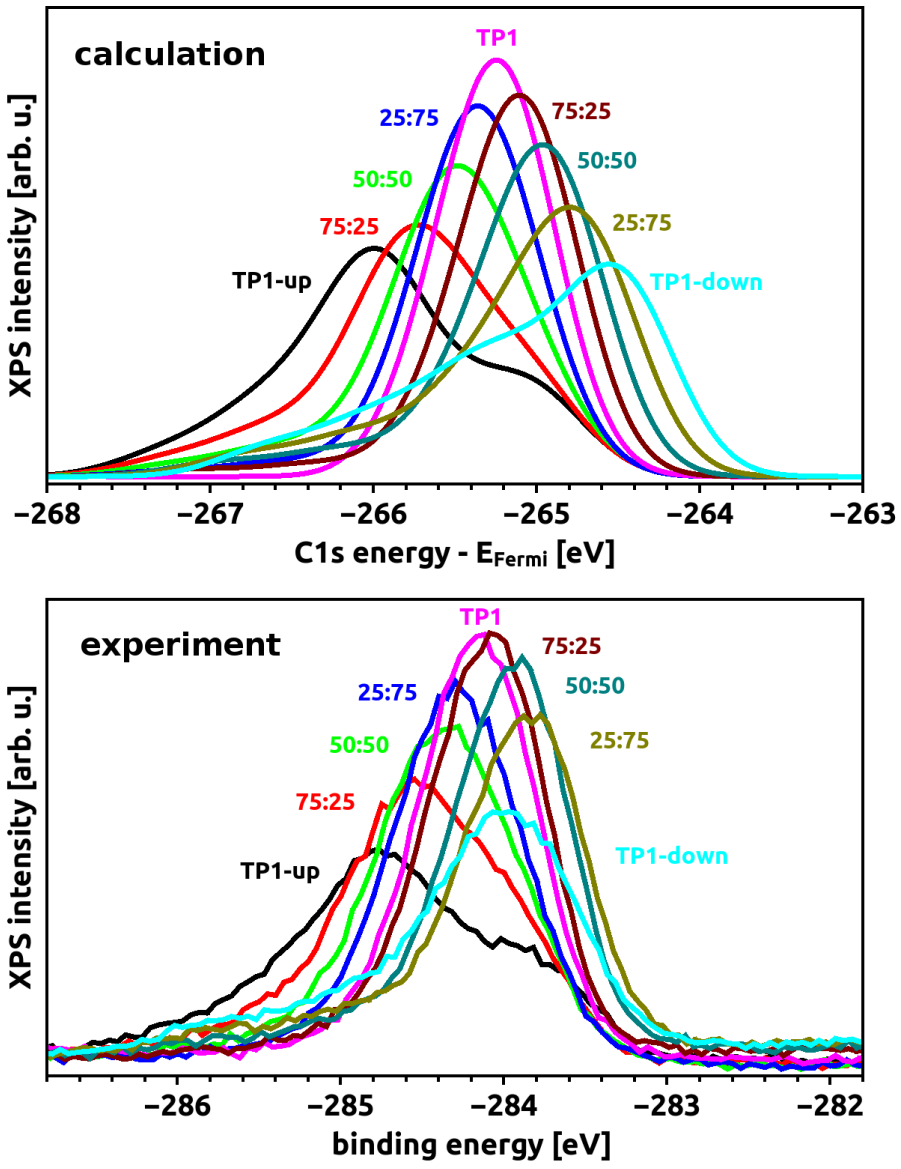

Figure 7.9.: Calculated (top) and measured (bottom) HRXP spectra of a pure TP1-up SAM (black), a pure TP1 SAM (pink) and a pure TP1-down SAM (cyan). Also shown are the spectra of mixed SAMs consisting of TP1-up : TP1 with mixing ratios 75:25, 50:50, 25:75 (red, green, blue) and TP1 : TP1-down mixtures with the ratios 75:25, 50:50, 25:75 (dark red, dark green, dark yellow). The depicted calculated spectra are aligned to the respective Fermi energies of each system. The mixing ratios stated for the experimental SAMs give the concentrations in solution. The corresponding concentrations of each component in the adsorbed SAM are listed in Tables 7.2 and 7.3. The HRXPS measurements were performed at MAX-Lab with a photon incident energy of 580 eV. Notice the different x-axes in both graphs: C 1s core level energies relative to the Fermi energy for calculated spectra and electron binding energy for measured spectra. The spectra are rigidly shifted by 18.8 eV with respect to each other. It is well know that calculated absolute core level energies are not suitable for comparison to absolute measured binding energies, instead relative energies and energy shifts are the quantities to be compared.[303–305,310]

In Figure 7.9 we find good qualitative agreement between experimental and calculated XP spectra. The same main features are encountered in both cases. The position of the main XPS peak clearly correlates with mixing ratio. Starting from the pure TP1-up SAM it gradually shifts to less negative energies with decreasing TP1-up content towards the signal of the pure TP1 SAM. The TP1 : TP1-down mixtures continue this trend seamlessly. The XPS peak shifts further to higher energies with increasing TP1-down content. The pure TP1-down SAM, however, introduces a slight inconsistency in this measurement series. Its main peak is situated at around -284 eV binding energy, when it should be placed at around -283.5 eV to fulfill the gradual trend. In the light of the previously presented data, especially the XP spectra of the TP1-up : TP1-down mixtures (Figure 7.6), where TP1-down perfectly agrees with the rest of the data we conclude that here we are faced with some sort of measurement error. Conditions in SAM preparation and/or measurement might have been slightly different from the other systems in this series. Therefore, in our interpretation of the data this TP1-down spectrum is not fully trustworthy and should be remeasured to clear up the situation. However, we do not have access to any new measurement data at the moment. This point however, will be addressed in the future. Nevertheless, in the light of the other presented data, we are reasonably confident in our interpretation of the measurement series and the identified trend.

The "shoulder", created by the energetically shifted carbons in the middle and substrate side ring is distinctly visible in the spectra of the pure TP1-up and TP1-down SAMs. For the depicted mixed SAMs though, it gradually vanishes with increasing TP1 content. Fewer and fewer molecules in the SAM have energetically shifted carbons in the middle and substrate side ring with increasing TP1 content. This reduces the peak width and increases the main signal intensity.

The according, calculated plane-averaged electron electrostatic energies of these mixed TP1 : TP1-up and TP1 : TP1-down SAMs are depicted in Figure 7.10.

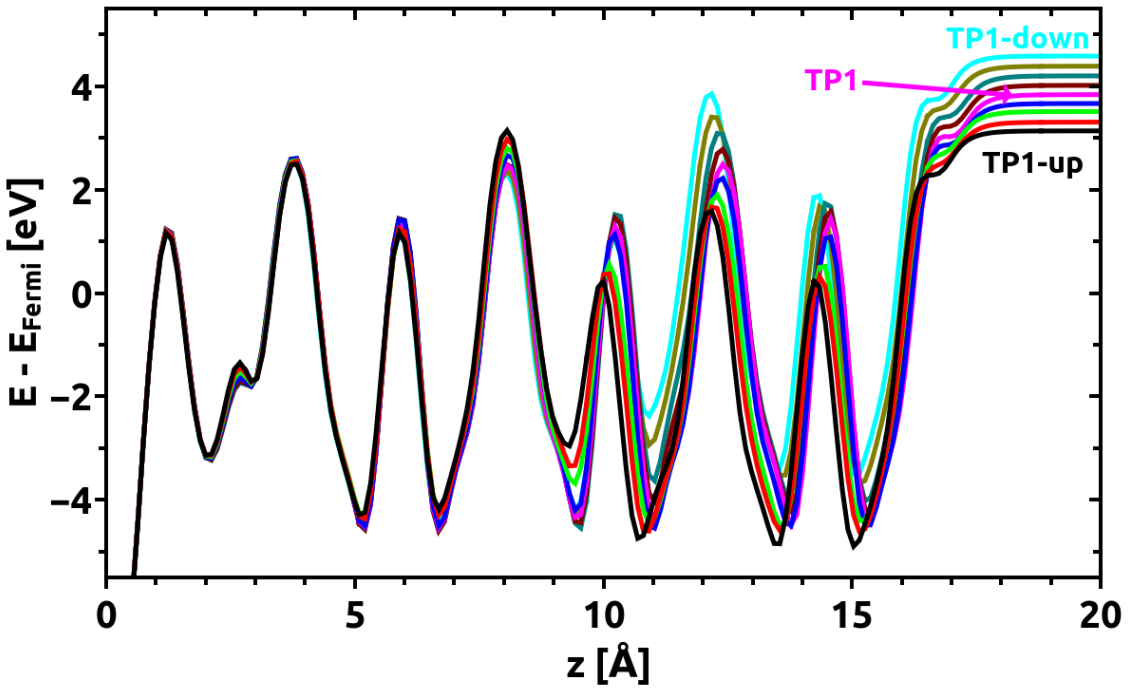

Figure 7.10.: Calculated plane-averaged electrostatic energy of an electron as a function of z-distance from the substrate given relative to the Fermi energy of each system. We show the data for a pure TP1-down SAM (cyan), a pure TP1 SAM (pink) and a pure TP1-up SAM (black). Also depicted are the spectra of mixed SAMs consisting of TP1-down : TP1 with mixing ratios 75:25, 50:50, 25:75 (dark yellow, dark green, dark red) and TP1 : TP1-up mixtures with the ratios 75:25, 50:50, 25:75 (blue, green, red). The vertical distance is given relative to the average position of the atoms in the topmost gold layer (z=0 Å). The features situated between z=0 Å and z=18 Å correspond to the adsorbed SAMs. The electrostatic energy inside the gold substrate is not affected by the adsorbed SAMs[26] and is, therefore, not shown in this plot for the sake of clarity.

There we see that all SAMs have the same electrostatic energy on the substrate side (left side of Figure 7.10), while the vacuum side potential (shown on the right side of Figure 7.10) shifts up linearly with increasing/decreasing TP1-down/TP1-up content in the SAM. The same trend as in the TP1-up : TP1-down mixture is found here. This shift in the electrostatic energy causes the peak shifts found in XP spectra for these mixed SAMs and the work function modifications presented next in Figure 7.11.

Figure 7.11 shows the measured and calculated work function modifications for TP1 : TP1-up and TP1 : TP1-down mixtures. The work function modifications are given relative to the work function of a pure TP1 reference SAM.

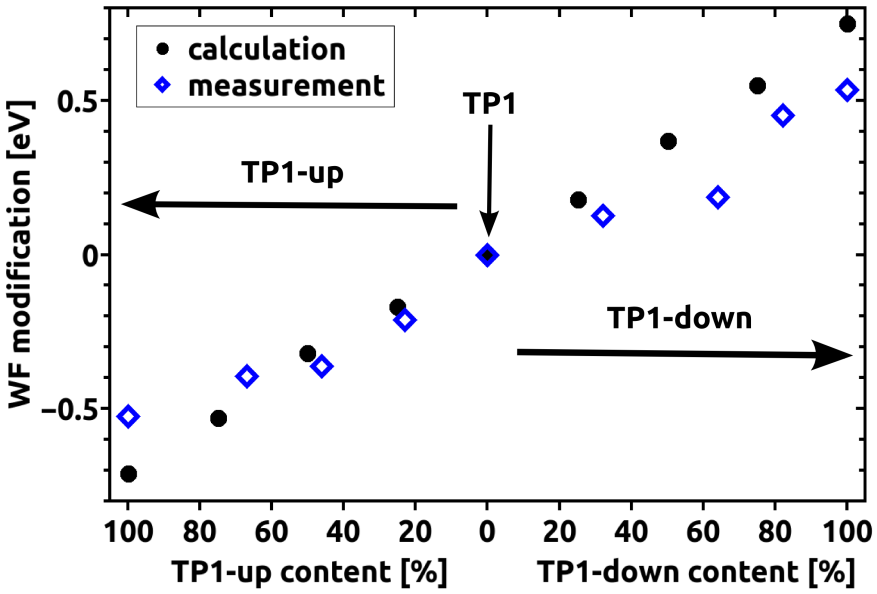

Figure 7.11.: Measured (open blue diamonds) and calculated (full black dots) work function modifications of TP1:TP1-up mixed SAMs (left half of the plot) and TP1:TP1-down mixed SAMs (right half of the plot), given relative to the work function of a pure TP1 reference SAM. The work function modification is depicted as a function of the TP1-up/TP1-down content in the SAM for both experimental and calculated data. Note the inverted x-axis on the left half of the plot. The TP1-up content in the SAM increases going from the center of the plot towards the left.

The workfunction modification increases linearly with decreasing TP1-up and increasing TP1-down content. This is in accordance with XPS measurements. It also adheres to expectations as TP1-up shifts the potential down and vice versa for TP1-down. The workfunction modification is therefore affected accordingly. We find a good qualitative agreement between calculation and experiment. The slope of the linear increase found in calculations is again slightly higher than in experiments. This was already seen for the TP1-up : TP1-down mixed SAMs (see Figure 7.8).

7.5.4. Inhomogeneous mixtures - dipolar domains

In the previous sections homogeneous mixtures of upward and downward pointing dipoles were studied quite thoroughly. We also depicted the consequences of diluting the dipole concentration inside the SAM. What is still missing so far is an assessment of the influence of phase separation. It is conceivable that some systems do not mix homogeneously but rather form isolated domains of similar dipole orientation. This could happen, for example, when structurally different molecules are mixed or influences other than electrostatics favor phase separation of dipolar molecules.

To test the impact of such dipolar phase separation, we make use of the same studied molecules as before. In calculations we have the possibility to arrange the

individual molecules into separate domains with upward and downward pointing dipoles and study the effects of this alternate arrangement. All other structural parameters, like packing density, docking sites, orientation of the molecules inside the SAM remain the same as in the previously studied homogeneous mixtures. Additional side effects of structural reorientation can be excluded in this way. Thus we can give an estimation of how phase separation influences XP spectra or measured work functions. By comparing calculated and measured data we can then gain information about the exact structure of a SAM and the distribution and orientation of dipoles. At this point it should be mentioned that the unit cell used to simulate the inhomogeneous mixture represents the situation of short-range phase separation. Using a large enough unit cell to capture long-range phase separation in the SAM is not possible due to the prohibitively high computational demand.

Figure 7.12 shows the calculated C1s core level energies of a 50:50 TP1-up : TP1-down mixed SAM with separate up and down domains. The average of the respective middle molecules of each domain is shown, which is less affected by domain boundary effects. In this way we can get an estimate of the electrostatic situation inside the domain while reducing the spurious effects of the domain boundaries. This is a reasonable approach, as in real SAMs domains are larger than is possible to handle in DFT calculations. There are many more molecules inside a domain than at the boundary. So to get a representation of the situation inside a domain from DFT calculations we use the data obtained from the central molecules of each domain and evaluate molecules at the domain boundary separately.

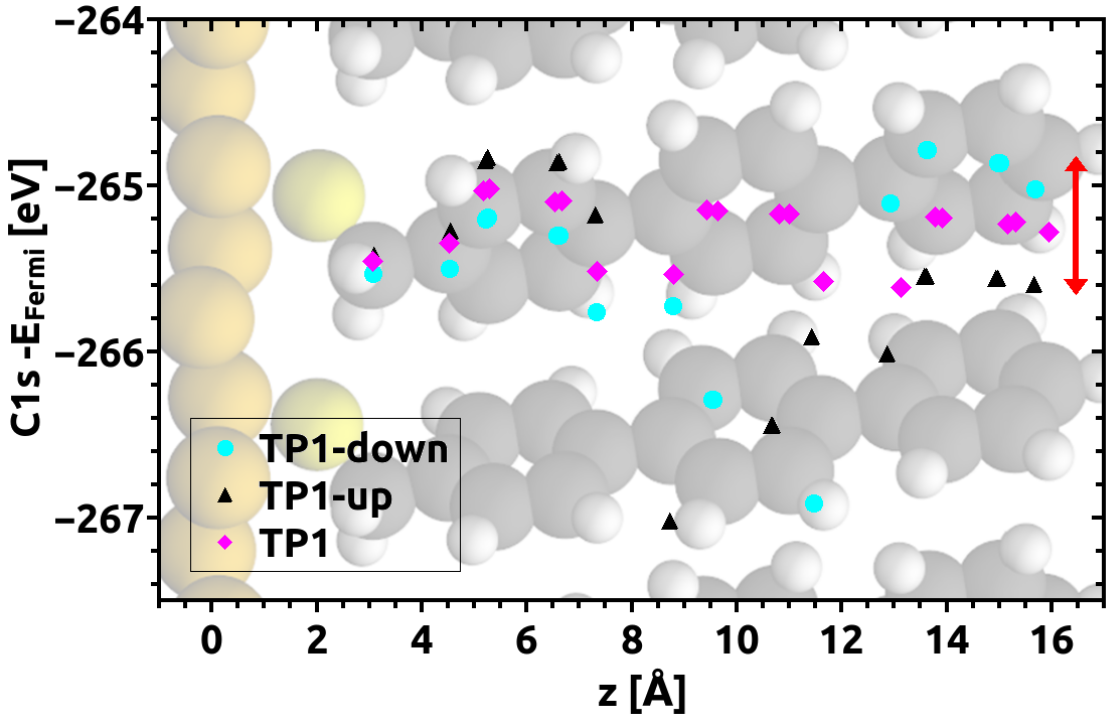

Figure 7.12.: Calculated C1s core level energies of a full coverage SAM with separate TP1-up and TP1-down domains. The mixing ratio is 50:50. The average C1s energies of the central two TP1-down molecules (cyan dots) and TP1-up molecules (black triangles) are shown relative to the Fermi energy of the system as a function of the average z-position of the individual carbon atoms. Individual atomic C1s energies of the two equivalent molecules of each domain used for averaging deviate by less than 0.05eV. Additionally, the C1s energies of a pure TP1 SAM (pink diamonds) are included in the figure for comparison.

In contrast to the homogeneously mixed TP1-up : TP1-down SAM we see a different energetic situation for TP1-up and TP1-down molecules in this inhomogeneous mixture. In the TP1-down domain C1s energies of the vacuum side ring are shifted upward by ≈ +0.38 eV compared to a pure TP1 reference. In the TP1-up domain the reversed effect is observed, namely a shift downward in energy by ≈ -0.35 eV. These shifts are smaller than in pure TP1-down and TP1-up SAMs, but they are still substantial.

The existence of opposite electrostatic shifts is an indication that the molecules in both domains are sufficiently screened from the respective neighboring domains to show collective electrostatic effects. The molecules inside a domain primarily feel the influence of their immediate neighbors, which have similar dipole orientation. This does not hold for the molecules situated directly at the domain border. These molecules have neighbors with both possible dipolar orientations and, therefore, no clear electrostatic shift is found for these molecules. Their C1s energies are influenced by local fields that yield no useful information about the general overall electrostatic

picture in the SAM and are therefore not included in Figure 7.12.

As an additional feature in Figure 7.12 we see that the C1s energies of the substrate side phenylene rings are not completely identical for molecules in the up and down domain. This is an effect of the striped SAM geometry. The TP1-up stripes can be thought of as embedded in the potential of their neighboring TP1-down stripes and vice versa,[23] which, consequently, influences core level energies. As this effect also affects the central molecules of each domain, we can surmise that stripes of a width of three molecules apparently do not shield the central molecules completely from the potential of the neighboring domains.

Figure 7.13 shows the corresponding, calculated XP spectrum of this inhomogeneous TP1-up:TP1-down mixed SAM. Additionally the spectra of the homogeneous 50:50 mixture and the pure TP1-up and TP1-down SAMs are depicted.

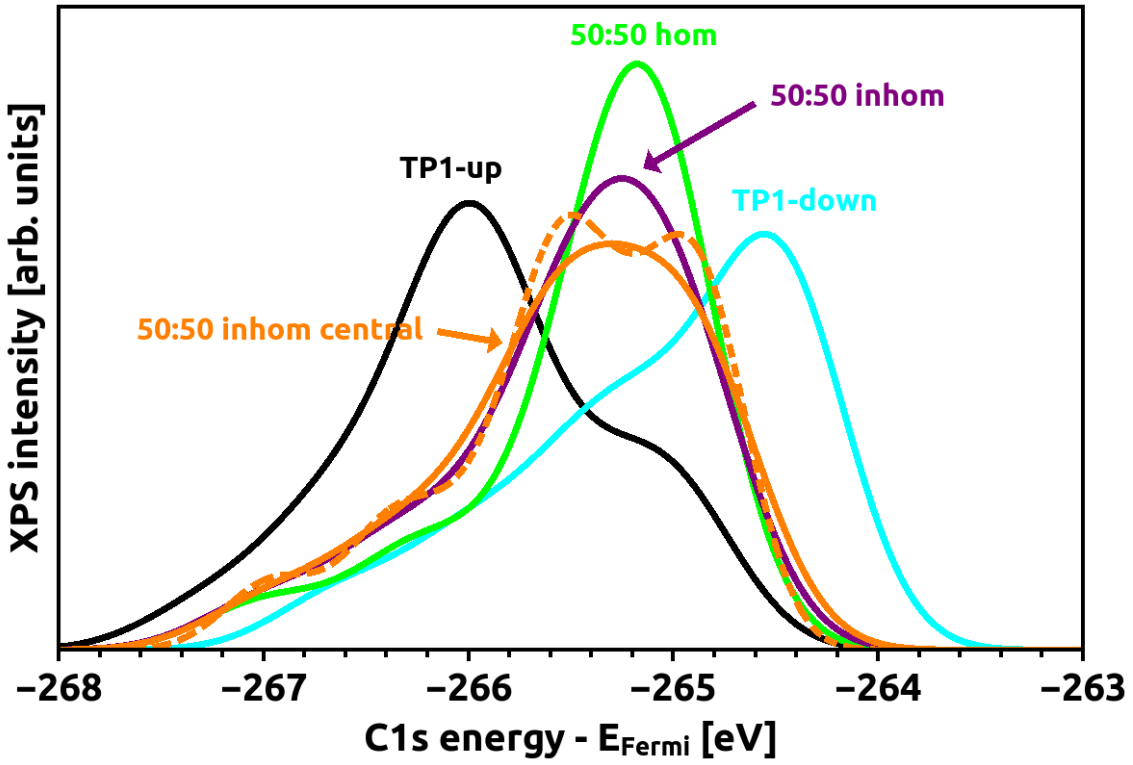

Figure 7.13.: Calculated XP spectrum for an inhomogeneous 50:50 TP1-up:TP1-down mixture exhibiting separate domains for each molecule type (violet curve). Additionally, the calculated spectra of a homogeneously mixed 50:50 TP1-up:TP1-down SAM (green) and a pure TP1-up (black) and a pure TP1-down (cyan) SAM are shown. The orange curves show the spectra obtained from the inhomogeneous 50:50 mixture only using the central two molecules of each domain for evaluation, thereby reducing the influence of domain edges. The spectrum evaluated with an extrinsic broadening of variance 0.1 eV is shown as an orange solid line, whereas the dashed orange line depicts the same spectrum evaluated with a reduced variance of 0.05 eV to show the two peak contributions of the separate domains more clearly. All other depicted spectra were evaluated with a variance of 0.1 eV.

The peaks of both 50:50 mixtures lie right in the middle between the peaks of the pure SAMs. The peak of the inhomogeneous SAM (violet) is noticeably broader (FWHM = 1.19 eV) and lower in intensity than the peak of the perfect molecular mixture (FWHM = 0.90 eV). It is comprised of two separate main contributions, namely TP1-up and TP1-down. TP1-up shifts the vacuum side ring down in energy, TP1-down shifts it up. This results in peak broadening. The domain sizes are rather small in the used unit cell, due to computational restrictions mentioned above. This results in the unrealistic situation that many molecules are situated at the edge of the domains and comparatively few at the center. The molecules at the boundaries are influenced by the neighboring domain and local electrostatic fields. To distinguish the signal contributions of the molecules inside the domain from the ones at the

domain boundaries we show the orange curves in Figure 7.13, which show the XP spectra of the same inhomogeneous SAM, however, only using the C1s energies of the central molecules of each domain for evaluation. The spectrum shown as a solid orange line was evaluated with a variance of 0.1 eV for the Gaussian functions. The spectrum included as the dashed orange line was obtained using a reduced variance of 0.05 eV to show the two separate peak contributions of the individual domains more clearly. Comparison of the different XP spectra of 7.13 shows that an inhomogeneous mixture leads to a significant increase in the FWHM or even to a clear double peak feature if the domains are large enough. The effect of peak broadening can be seen even more clearly when normalized spectra a plotted (see Figure 7.14).

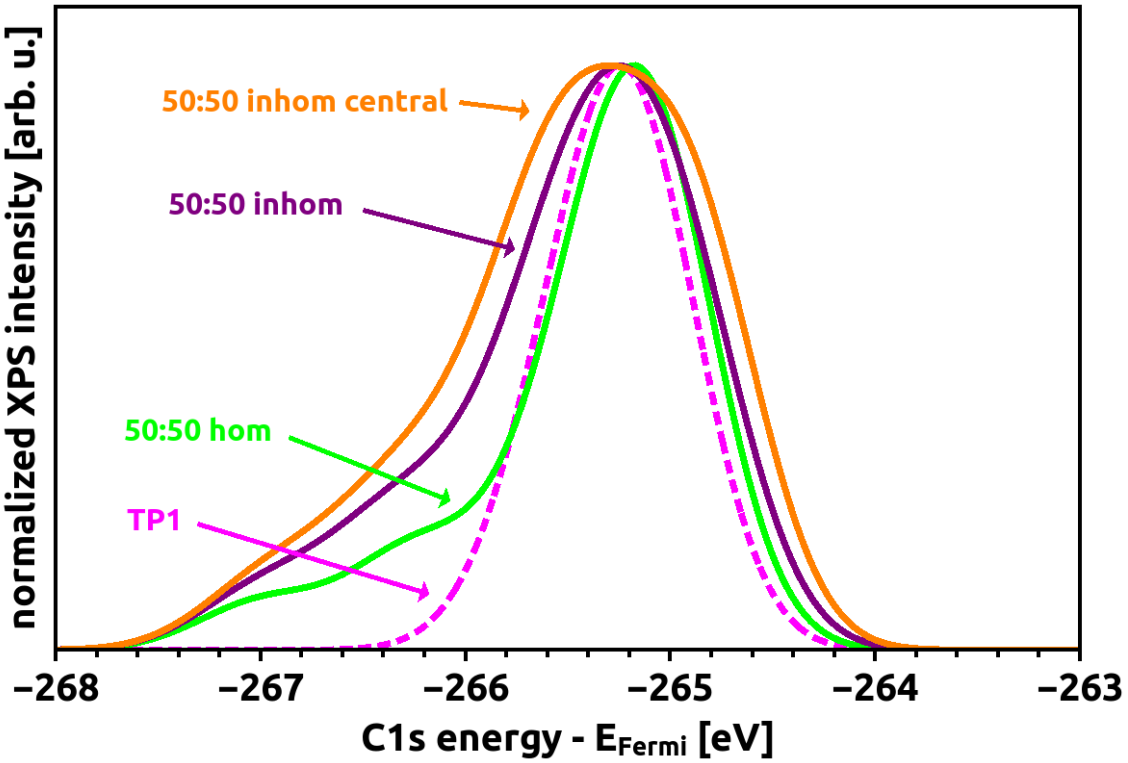

Figure 7.14.: Normalized, calculated XP spectra of a TP1 SAM (pink), a homogeneous 50:50 up:down mixture (green), the striped 50:50 mixture (violet) and the striped 50:50 mixture using only the central two molecules of each domain for evaluation (orange). All spectra shown in this figure are evaluated with an extrinsic broadening using a variance of 0.1 eV.

Figure 7.14 shows that the homogeneous up:down mixture (FWHM = 0.90 eV) and the TP1 reference SAM (FWHM = 0.85 eV) have nearly identical peakwidths. This is not the case for the inhomogeneous, striped SAM. For the spectrum including all molecules a heavily increased FWHM of 1.19 eV is observed. When eliminating edge effects by only including the central molecules in the evaluation (orange curve) the FWHM increases even more to a value of 1.45 eV.

To get an idea of the XP spectrum a SAM with larger domains would create, we show the 50:50 weighted superposition of the spectra of the pure TP1-up and TP1-down SAMs in Figure 7.15. In this case the double peak structure is even more pronounced. The XP spectra of the homogeneous 50:50 mixture and the pure TP1 SAM are included for comparison.

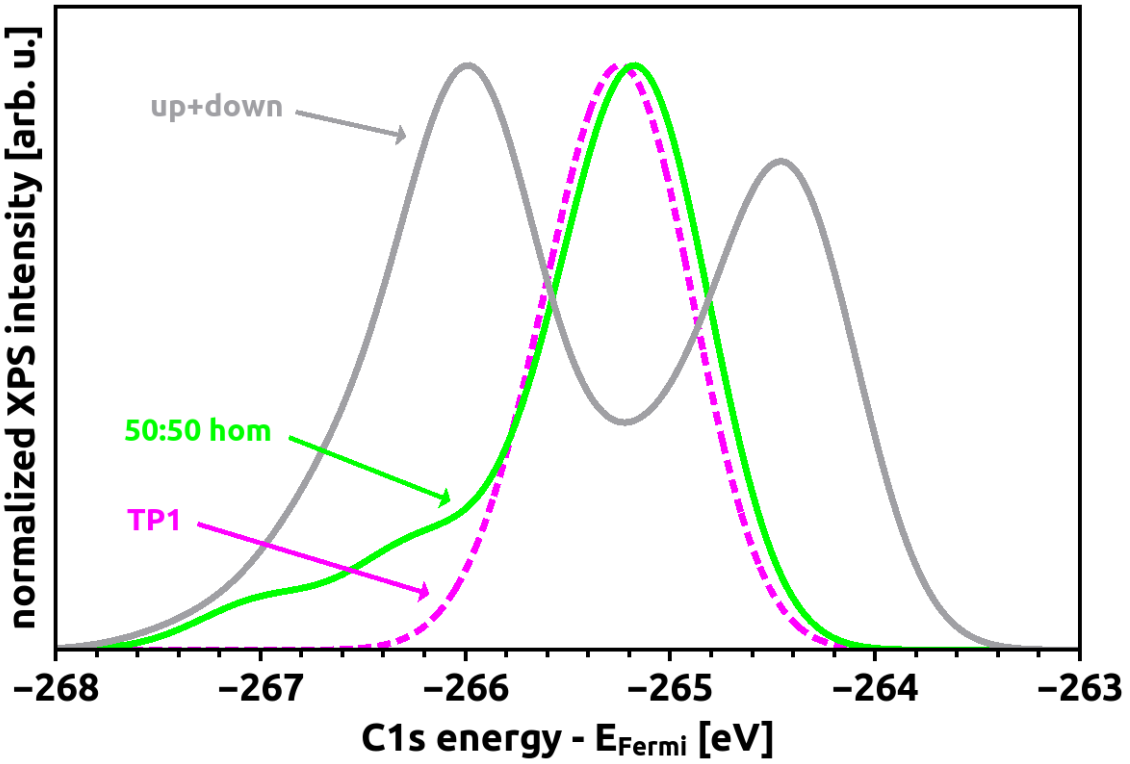

Figure 7.15.: Normalized, calculated XP spectra of a TP1 SAM (dashed pink line), a homogeneous 50:50 up:down mixture (green), and the 50:50 weighted superposition of the spectra of the pure TP1-up and TP1-down SAMs (gray). All spectra shown in this figure are evaluated with an extrinsic broadening using a variance of 0.1 eV.

The results presented in Figures 7.13 to 7.15 indicate that with increasing domain size the XPS peak splitting gets more and more distinct.

From these results we conclude that core level energies are qualitatively very different in homogeneously and inhomogeneously mixed SAMs. The precise molecular arrangement heavily influences C1s energies. We therefore believe that XPS could be used to probe the homogeneity of a SAM. Phase separation of dipolar molecules on the substrate should result in a distinctively different signal (significant peak broadening or even clear double peak features in case of large domains) and, therefore, be detectable in XPS.

In the next paragraph we investigate how the formation of dipolar domains affects the work function of the system. Pure dipolar SAMs are compared with homogeneous and inhomogeneous mixtures. Table 7.4 summarizes the calculated work function modifications of various systems. The values are calculated as the difference

between the average vacuum side electrostatic potential (more than 10 Å distance to the top of the sample) of the SAM in question and the reference system. Values are given relative to a pristine Au(111) substrate and relative to a pure TP1 SAM on Au(111) substrate.

Table 7.4.: Calculated work function modifications $\Delta\Phi$ of various systems, given in eV. The work function modification is given relative to a pristine Au(111) substrate and relative to a pure TP1 SAM on Au(111) substrate.

system	**$\Delta\Phi$** relative to Au(111)	**$\Delta\Phi$** relative to TP1
TP1	-1.29	0.00
TP1-up	-2.00	-0.71
TP1-down	-0.54	0.75
50up:50down hom	-1.21	0.08
50up:50down inhom	-1.26	0.03

From Table 7.4 we see that the work function of the inhomogeneous SAM shows a qualitatively different behavior than the core level energies (XP spectrum) of the same system. In the XP spectra a clear distinction between homogeneous and inhomogeneous mixtures is found. The work function modification, however, is nearly identical for both mixtures and the TP1 reference SAM. Neither the homogeneous, nor the inhomogeneous 50:50 TP1-up:TP1-down mixture affects the work function of the gold substrate any differently than the pyrimidine-less TP1 SAM does. We further see that the calculated values for these systems lie in the middle between the work function modifications of the pure TP1-up and TP1-down SAMs. From this comparison we conclude that the work function apparently is not affected by the domain structure in the inhomogeneous SAM. From pure SAMs on the other hand we know, that the work function is significantly shifted by the adsorption of dipolar monolayers. We therefore conclude that, as the work function is averaged over the extension of the domains, the opposite effects of the TP1-up and TP1-down domain cancel each other.

To better understand this behavior we take a look at the potential directly above the SAM for this inhomogeneous system. Figure 7.16 shows the electron electrostatic energy of horizontal cut planes at increasing z-distances from the top of the SAM.

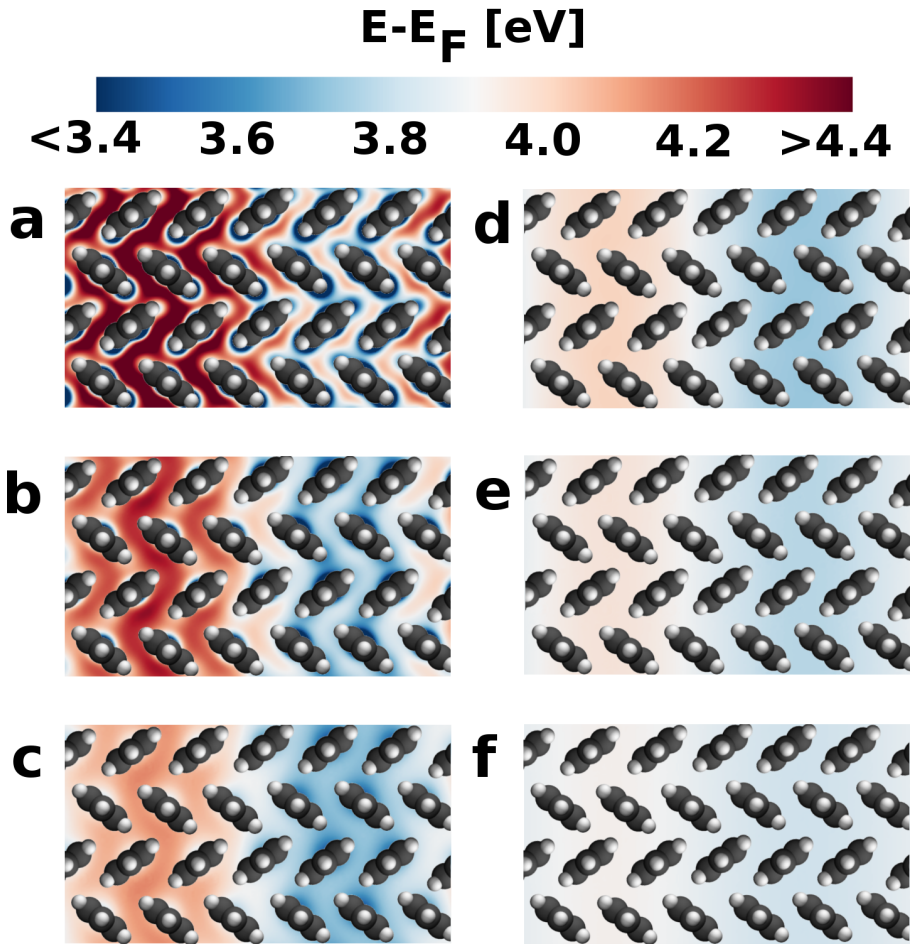

Figure 7.16.: Electron electrostatic energy at horizontal cut planes (parallel to the substrate) at increasing z-distances from the top of the inhomogeneous TP1-up : TP1-down SAM. The TP1-down domain is situated on the left half of the plots, the TP1-up domain on the right. Subfigures a to f give the electrostatic energy at the following z-distances from the top of the SAM (determined as the average z-position of the topmost hydrogen atoms): (a) z=0 Å, (b) z=1 Å, (c) z=2 Å, (d) z=4 Å, (e) z=6 Å, (f) z=9 Å. The lateral positions of the molecules in the SAM below are indicated as a guide to the eye.

Close to the SAM the electrostatic energy above the TP1-down stripe (left halfs of Figures 7.16 a-f) is noticeably higher than in the TP1-up stripe (right halfs of Figures 7.16 a-f). TP1-down molecules collectively shift the potential upwards, while TP1-up molecules, due to their reversed dipole orientation, shift it downwards by the same amount. The difference in electrostatic energy between the TP1-up and TP1-down domain gradually vanishes with increasing z-distance from the SAM. The electrostatic potential above both regions assimilates gradually. At a distance of z $\approx$ 8 Å from the top of the SAM the electrostatic energy can be considered

homogeneous. The opposite influences of the dipolar domains are averaged at this distance.

With this insight into the potential situation above the SAM the calculated work function modifications can be understood much better. The individual domains influence the potential significantly, but the effects compensate each other already at small distances above the top of the SAM. Thus, the work function modification yields just averaged information about the electrostatic situation in the SAM. XPS on the other hand probes the film much more locally as is apparent from the clear influence of the homogeneity of the SAM on core level energies.

Discussion: homogeneous vs. inhomogeneous mixtures

From the results presented above for pure dipolar SAMs as well as homogeneous and inhomogeneous mixtures we draw the following conclusions. Apparently electrostatic XPS shifts are generated already in small domains, whereas the work function is averaged over a much larger area. Thus the work function modification for the domain structure is the same as for a homogeneous mixture. So when measuring a SAM that consists of individual patches with different dipolar orientation one could expect to see this in the form of significantly broadened or even split peaks in XP spectra. Work function measurements, however, would not reveal a phase separation of dipolar molecules.

In this light we can interpret the experimental data presented in this work from an additional angle. XPS measurements of all presented mixed SAMs showed neither double peak structures nor peak broadening. Furthermore, the binding energy of the single main peak shifts linearly with mixing ratio. Thus we conclude that all experimentally studied SAMs of varying mixing ratios form homogeneous mixtures. No separation into domains of one molecule type takes place.

Such a homogeneous dispersion of TP1-up and TP1-down molecules also seems plausible from an electrostatic perspective. Dipoles prefer to align antiparallel to each other, as this is the energetically favored arrangement. If no other, stronger influences (for example steric or conformational restrictions) compensate this trend, molecules can be expected to prefer antiparallel dipolar alignment. This leads to quite homogeneous mixtures of TP1-up and TP1-down molecules. This argument also holds for mixtures with just one strongly dipolar molecule type (see TP1 : TP1-up and TP1 : TP1-down mixtures). Also in this case the dipolar molecules will try to distribute evenly on the substrate instead of all clustering together as this would be energetically unfavorable. The tendency to homogeneous intermixing of molecules for TP1:TP1-up and TP1:TP1-down is observed in calculations and experiments alike as presented above.

7.6. Conclusions

Self-assembled monolayers of pyrimidine-substituted terphenyls on gold substrate have been investigated with experimental and theoretical means. The impact of

dipole orientation on work function and core level energies in pure and mixed SAMs has been studied. Both quantities were found to be in good agreement in calculations and experiments. A clear correlation with the mixing ratio of the SAMs was found. Homogeneous and inhomogeneous mixtures result in qualitatively different XP spectra. In contrast, such a clear distinction between homogeneous and inhomogeneous SAMs was not found in the systems' work functions.

This suggests that XP spectra give more localized information about the film than work function measurements. XPS can be used to assess the homogeneity of a film as well as the chemical composition and electrostatic situation in the SAM. Work function measurements on the other hand yield information averaged over a larger area of the sample and, therefore, cannot provide such localized information about short range variations of the electrostatic potential inside the SAM.

For the specific systems investigated in this work no double peak structure was revealed in XP spectra, independent of mixing ratio. We therefore deduce that the investigated molecules show no tendency to form separate domains. Instead molecules with opposing dipole moments readily intermix on the substrate to form homogeneous SAMs. This is in accordance with the simple electrostatic picture of dipoles favoring antiparallel orientation as the energetically preferable configuration over parallel alignment.

8. Accounting for depolarization effects in molecular dynamics simulations of self-assembled monolayers

In the previous chapters, density functional theory (DFT) has been used as the main method to study structural and electronic properties of self-assembled monolayers. Molecular dynamics (MD) was only employed as a tool for geometry preoptimization, albeit a crucial one. In fact, as explained in more detail in Chapter 4, geometry optimization of alkylthiol SAMs without the preoptimization step, resulted in completely arbitrary and wrong final geometries. This shows that MD is a powerful tool to investigate self-assembled monolayers, especially their structural properties. Large scale systems, containing a few hundred molecules can be studied. The investigation of disorder or domain structures in the film, even including the effects of temperature variations is possible. However, quantum-mechanical effects, like the phenomenon of depolarization are neglected in classical, force field based MD. This is a significant setback, especially for the study of self-assembled monolayers on metal substrates, where this effect is reported to influence molecular dipoles quite strongly. To address this issue we devised and tested a method to account for depolarization effects in MD simulations of self-assembled monolayers, which is presented in this chapter.

Author contributions:
The work presented in this chapter was a joint effort of Iris Hehn, Manuel Vieider, Luca Muccioli, Claudio Zannoni, Egbert Zojer and Otello M. Roscioni. The basic idea to account for depolarization effects in MD simulations and study the impact on self-assembled monolayers was put forward by Egbert Zojer. Otello M. Roscioni came up with the concept of using electrostatic embedding to describe depolarization effects and to combine it with MD simulations in an iterative process to self-consistently update atomic partial charges and molecular structures. The details of individual calculations steps and the total final process were developed, tested and improved by Otello M. Roscioni and me jointly. I performed the test calculations and the comparison to the analytical Topping model presented in Section 8.3, as well as the test calculations and comparison between the embedding procedure and a periodic boundary DFT code presented in Section 8.5. Otello M. Roscioni performed the calculations applying the full procedure on four different systems presented in

Section 8.6. The results were evaluated jointly between Otello M. Roscioni and me. Manuel Vieider performed preliminary MD simulations on mid-chain ester functionalized alkylthiol SAMs and he and Otello M. Roscioni taught me how to set up and evaluate MD simulations. Luca Muccioli and Claudio Zannoni provided advice during the development of the procedure. Egbert Zojer provided valuable advice and constant support during the development and testing of the method. The data was interpreted jointly between Otello M. Roscioni, Egbert Zojer and me.

The text of this chapter was written by me. Otello M. Roscioni provided an outline of the simulation procedure that I used as a basis for writing Section 8.2. He also prepared the flowcharts depicted in Figures 8.1 and 8.2. I prepared all other figures and tables of this chapter.

8.1. Introduction

Dipolar molecules in dense, regular arrangements behave quite differently from individual molecules. This is due to the collective interaction of aligned dipole moments.[119,122] Individual dipole moments get reduced by the influence of the electric field created by all neighboring dipolar molecules. This phenomenon is called depolarization and it can have a significant effect, potentially reducing molecular dipole moments by as much as a factor of three.[17,61,124] This is of special importance for SAMs of molecules with large initial dipoles. The overall dipole moment of a SAM most significantly influences system properties like the potential inside the monolayer, the system's work function or atomic binding energies (see Chapters 5 to 7). Additional to the influence of depolarization on electronic properties one could expect some impact on the structural properties of SAMs. Especially in cases where molecular dipoles are not exclusively oriented along the molecular axes but have also horizontal components one might expect depolarization to indirectly have an influence on the SAM structure. By depolarization the orientation of the dipole moment relative to the molecular axis can be changed. This can influence how the molecules arrange with respect to each other inside the SAM. Such structural reorientations involving possibly larger spatial scales like order-disorder effects can be best studied using molecular dynamics (MD) simulations, as this method allows the use of much larger unit cells than purely quantum mechanical calculation methods like density functional theory (DFT).

However, as described in Chapter 2 conventional molecular dynamics simulations use additive force fields. They treat electrostatic interactions using Coulomb potentials of partial atomic charges, which are included as purely additive terms to the potential energy function of the force field. The atomic charges are calculated for an isolated molecule in vacuum on a quantum mechanical level according to one of several available charge partitioning schemes like ESP[208,209], Hirshfeld[361–363], Mulliken[364] or any other required one. Furthermore, the atomic charges remain unchanged throughout the entire MD simulation. This electrostatic description completely neglects polarizability of molecules and, therefore, depolarization effects are

not accounted for in conventional MD simulations.

However, for many systems (including SAMs, thin films, bulk materials or biological systems like proteins, lipid bilayers or cell membranes) polarization phenomena can be expected to have a crucial influence on structural, electronic and functional properties.[365–369]

This is the reason why currently considerable effort is being dedicated to the development of so-called polarizable force fields.[134,135,181,367,369–371] These force fields try to substitute the conventional additive approach of treating electrostatic interactions by explicitly including polarization effects into the functional form of the force field.[372–375] Several different approaches defined by different levels of accuracy, applicability to various types of systems and computational demands are under development.[135,181,376–386]

These force fields have been designed in the last couple of years and are now available for the first time. However, they are still in the crucial state of testing and parameters have to be optimized to correctly treat various systems. So far they have been successfully applied to a few selected systems.[135,181,387–394] It also has to be mentioned that difficulties have been encountered and some system properties have been described incorrectly by the new force fields.[395–397]

According to refs [134, 135, 181, 369, 373] there seems to be a general agreement within the MD community that firstly the further development of polarizable force fields is the next crucial step in improving the quality of MD simulations. Secondly, these new force fields need to undergo the same rigorous testing and improvement processes as the standard additive force fields, which already have gone through several iterations of adapting and improving parameter sets.[135,373] Thirdly, there seems to be an agreement that the conventional, widely tested additive force fields currently in use will still remain an integral part of MD simulations in the years to come.[135,369,373] Polarizable force fields have a much higher computational demand than additive ones, increasing calculation times by a factor of 2.[135,398] This leads to direct restrictions of the system sizes and overall simulation time spans treatable with this method. Therefore, it is expected that polarizable force fields will be primarily employed to simulate systems that are highly sensitive to depolarization effects and which cannot be described qualitatively correctly without them. For other systems conventional additive force fields will still remain in use.[135,181,367,369]

From a practical point of view one has to consider that development and testing of force fields, especially the precise parametrization for each different class of systems is a rather time consuming process.[135,181,373,377] As has already been seen in the past in the development of additive force fields, the systems most studied with MD will be treated with priority in this process. In practice this means that force fields and corresponding parameter sets will first be tested and improved for biological systems, like proteins, lipid bilayers and nucleic acids and will only later be adapted

for small organic molecules and chemical compounds.[135] This is partly due to the fact the MD is most commonly applied in the field of molecular biology, while fewer scientific groups use the method to investigate systems of small organic molecules. Secondly, many diverse structures fall in the class of "small organic compounds", which makes the accurate parametrization of a force field for this highly diverse field extremely demanding.[135,181,194]

For these reasons we propose an alternative approach to include depolarization effects into MD simulations, which is suitable for self-assembled monolayers of aliphatic and aromatic molecules on metallic substrates. It is not intended to substitute polarizable force fields, but rather offer the user another option to account for depolarization in MD simulations, with different advantages and disadvantages.

Our suggested method is based on combining molecular dynamics simulations with an electrostatic embedding procedure[399–402] to generate more realistic partial atomic charges. The calculation of atomic charges is performed in an iterative process where the charges and molecular geometries are updated self-consistently until the molecular dipole moment is converged.

The basic principle of electrostatic embedding is surrounding a central molecule of interest with a finite size cluster of neighboring molecules to account for the influence of the electric field of the surrounding SAM. One thereby makes the assumption that an infinite 2D slab can be approximated by a finite size cluster. This issue is addressed in Section 8.3. The details of the proposed computational process are discussed in Section 8.2.

One advantage of our proposed approach over the use of polarizable force fields is that the calculation of atomic charges in the electrostatic embedding process can be performed basically with any computational method of choice. This means MD simulations can be combined with any desired level of theory suitable to the problem at hand. This puts the user in a position to decide which level of accuracy is needed and make a customized compromise between detail of description and computational demand. Additionally, any available charge partitioning scheme can be used with our method. The atomic charges calculated in the embedding step can then be used in combination with very well established and tested conventional additive force fields. This is a serious advantage of the proposed method as it can be applied to systems for which no suitable polarizable force fields are available yet.

In the following section a description of the suggested methodological approach and computational details are given.

8.2. Computational method

In standard MD simulations, partial atomic charges are calculated for one isolated molecule in vacuum. We improve this step by using an electrostatic embedding approach.[399–402] In the embedding scheme the central molecule of interest is surrounded by a 2D cluster of point charges, representing the neighboring molecules, including image charges due to the metal substrate. The atomic partial charges of the central molecule of the cluster are then calculated using density functional theory, taking into account the electrostatic potential of the surrounding cluster of point charges. This has to be done in an iterative process as the current set of partial atomic charges is used to create the embedding cluster for the next step. The process is repeated until the molecular dipole moment is converged. The atomic partial charges of a single molecule in vacuum are used as a starting guess for iteration.

With this approach depolarization as caused by charge rearrangements inside the molecule can be accounted for. However, another contribution to depolarization are structural changes of the molecular geometry arrangement on the substrate. For this reason, a second iteration loop is added to our proposed method, in which the molecular structure and packing geometry is optimized using MD simulations.

The combined iterative procedure is depicted in the form of a flowchart in Figure 8.1.

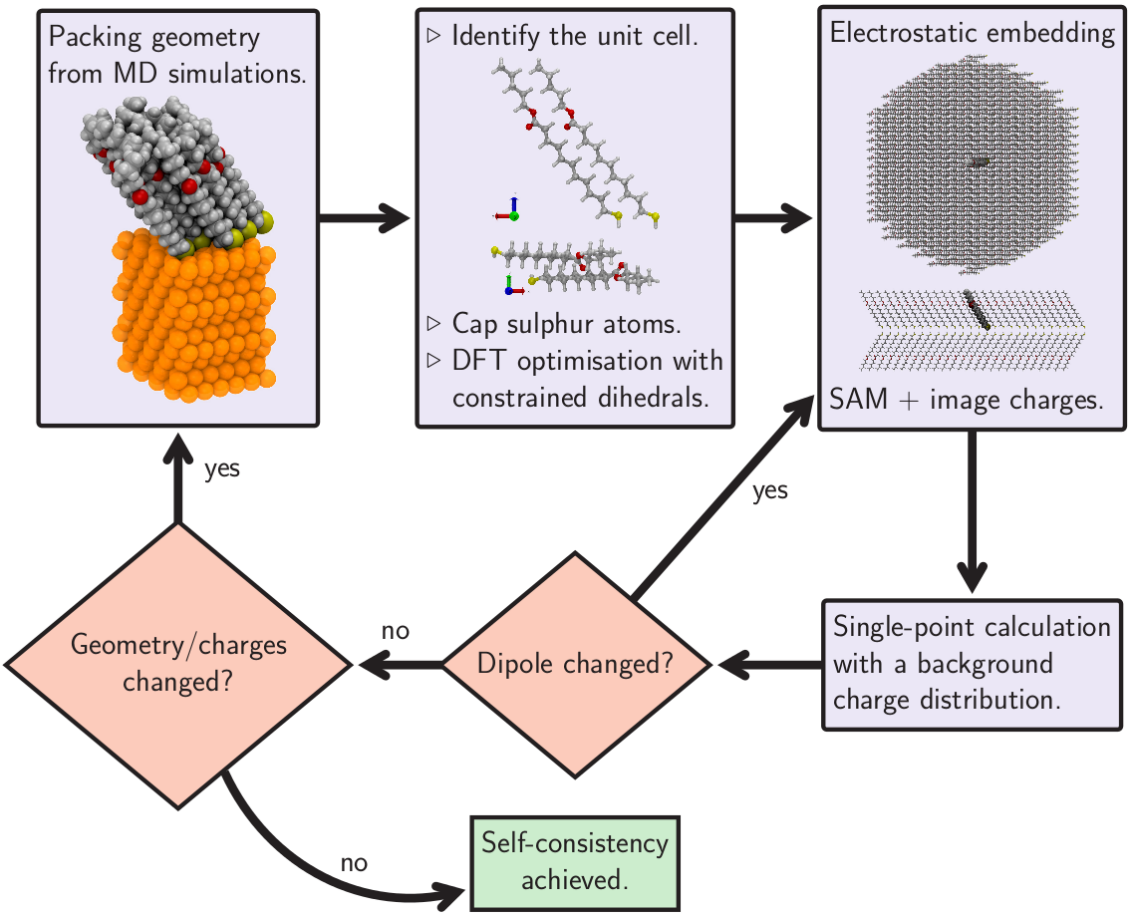

Figure 8.1.: Flowchart depicting the full procedure described above including an inner loop where the embedding iteration is performed and a connected outer loop where the molecular packing structure is adapted in MD runs. This figure was produced by Otello M. Roscioni.

In the following, a step-by-step description of the whole process, consisting of two connected iteration cycles is given. Subsections 8.2.1 and 8.2.2 add additional computational details about the inner and outer loop of the iteration cycle.

1. Calculate atomic charges for an isolated molecule in vacuum

2. Run a MD simulation of a large sample (16 or 32 molecules) in order to determine the packing structure of the SAM. Use the set of atomic charges obtained in the previous iteration run (or the initial charges determined in step 1. for the first iteration run).

3. Identify a repetitive unit and build a unit cell by selecting 2 molecules (representative of the found surface mesh; accounting for herringbone packing by using 2 molecules in the unit cell). Carry out a thermal annealing (using MD) at low temperature. This yields the unit cell for building the embedding cluster.

4. Use the geometry of the unit cell (containing 2 molecules) combined with the last set of atomic charges to build the background charge distribution for the embedding cluster according to the following steps:
   a) Transform the 2 molecules in the unit cell to a closed-shell configuration, by capping the terminal sulfur atom with a hydrogen atom. This needs to be done as the molecules extracted from MD simulations do not have a terminal hydrogen atom attached to the sulfur, due to the sulfur-gold bond in the MD run. However, as the embedding cluster contains no gold substrate this step is necessary.
   b) Optimize the geometry of both molecules in the unit cell separately at the desired quantum mechanical level, without changing the relative molecular orientation. For this optimization, the dihedral angles are constrained. This ensures that the packing geometry obtained from MD simulations is retained, but it allows the bond distances and angles to relax according to quantum mechanical interactions.
   c) Choose one molecule in the unit cell to be the central molecule.
   d) Use the unit cell (with relaxed molecular geometries) to build a circular cluster of molecules, where each molecule is represented by the atomic point charges of the central molecule (use the atomic charges calculated in the last iteration). Choose the cluster size large enough so that it sufficiently approximates the electric field of an infinite slab at the center of the cluster.
   e) Add image charges for all molecules, including the central one to the embedding cluster. The position of image plane is determined according to the method presented in ref. [403] (details see below).
   f) Compute new atomic charges for the central molecule in the presence of the embedding charge distribution constituted by the circular cluster of molecules plus the image charges.
   g) Repeat from step d) until the dipole moment of the central molecule reaches the convergence criterion.
5. Use the new set of atomic charges, which include molecular depolarization, and repeat from step 2.
6. End the procedure when the SAM structure and the molecular dipole achieve self-consistency.

8.2.1. Details on the outside loop: updating the molecular geometry

In order to avoid local minima in the MD simulations, a thermal annealing at high temperature is carried out, which melts the SAM. A new structure is obtained upon slow cooling to room temperature (T = 300 K) and further annealing at this

temperature. In order to reduce thermal disorder, the sample is then slowly cooled to T = 10 K. The unit cells of SAMs based on alkyl thiols (C10EC5 and C5EC10) contain 16 molecules (area of the unit cell: 17.3 x 20.0 Å), while they contain 32 molecules (area of the unit cell: 34.6 x 20.0 Å) for aromatic thiols (CSBPT and DPYMT, see Section 8.4 for a description of the systems). This choice ensures the melting of the sample during the annealing at high temperature, while keeping the number of molecules to a manageable level. The different number of molecules used for the two families of SAMs (linear chains or aromatic cores) arises from the fact that linear molecules are more flexible than aromatic ones and less sensitive to periodic boundary conditions.
After the annealing of the large sample, a small unit cell (containig two molecules to account for a possible herringbone structure) with a surface area of 8.7 x 5.0 Å is extracted and minimized again using the MD method. This structure is then used to build the electrostatic embedding cluster.

For these MD simulation runs the program LAMMPS[171] (version 10 Feb 2015) was used. The velocity Verlet[170] algorithm was used for time integration in time steps of 1 fs. The SHAKE[172] algorithm was used to describe hydrogen movement for the rigid aromatic molecules (CSBPT, DPYMT). The PPPM[206] solver was employed to handle electrostatic interactions. Simulations used NVT ensembles together with the Nosé-Hoover[175,176] thermostat. The CHARMM36 general force field "CGenFF"[194] (version 2b7) was used to model bonded and nonbonded atomic interactions. To describe the gold-organic interaction the GoIp[219] force field was used, whereas a special, breakable force field, developed by Jang et al.[220] was employed to describe the gold-sulfur bond. Furthermore, the gold substrate was modeled by 10 layers of fixed gold atoms, with a Au(111) surface.
The temperature profile used for MD simulations of large samples (16 or 32 molecules) was:

- 1 ns: heating from 100 K to 800 K
- 10 ns: annealing at 800 K
- 5 ns: cooling from 800 K to 300 K
- 10 ns: annealing at 300 K
- 7 ns: cooling from 300 K to 10 K

The temperature profile used for the subsequent MD simulations of small samples (2 molecules) was:

- 20 ps: heating from 10 K to 80 K
- 20 ps: annealing at 80 K
- 20 ps: cooling from 80 K to 10 K

8.2.2. Details on the inside loop: the embedding process

Figure 8.2 depicts the part of flowchart 8.1 that corresponds to the inner loop of the iterative process.

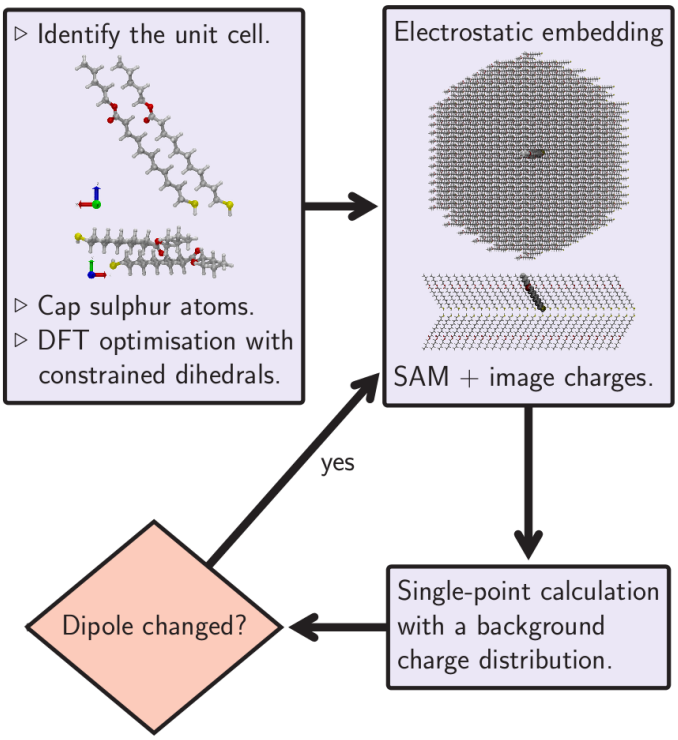

Figure 8.2.: Flowchart depicting just the inner loop of the full procedure described above, where the embedding iteration is performed (three boxes on the lower right) and the connection to the outer geometry optimization loop (top left box). This figure was produced by Otello M. Roscioni.

Figure 8.2 shows the iterative cycle of the embedding process (marked d) to g) in the step-by-step description above) as well as the connection to the outer loop, i.e. the quantum mechanical optimization of the 2 molecule MD unit cell to adjust the bond lengths and angles (top left box; points a) and b) of the step-by-step description of Section 8.2).

In this iteration process, updating the atomic charges of the embedding cluster in each run employs a mixing scheme to avoid numerical oscillations. Charges of the previous two runs are mixed in a 6:4 ratio to build the cluster of run $n+1$: $q_{cluster,(n+1)} = 0.6q_n + 0.4q_{n-1}$. This results in a smooth convergence of the molecular dipole moment without oscillations.

The circular 2D embedding cluster has to be chosen large enough so that it approximates, at its center, the electric field of an infinite 2D slab. Tests have been carried out for all four investigated systems to determine the appropriate cluster

size. The cluster size was increased until the electrostatic potential variations at the center were converged to 0.1eV. This results in cluster sizes of 1178 molecules for the C10EC5, C5EC10 and CSBPT system and 3270 molecules for the DPYMT system. Details about the studied molecules can be found in Section 8.4.

Image charges, due to the metal substrate are included into the embedding cluster, where the position of the image plane is determined according to the method presented in ref. [403]. Accordingly, the image plane is positioned at such a distance below the thiol group of the molecule as to place it 0.18 Å above the position of where the jellium edge of the gold substrate would be. The jellium edge is located d/2 above the top gold layer according to ref [403], where d=2.308 Å is the distance between individual Au(111) layers in the substrate. The adsorption distance between sulfur and gold is determined from the last MD run.

For optimizing the molecular geometry of the two-molecule unit cell on a quantum mechanical level as well as calculating the atomic charges of the central molecule in the embedding cluster, density functional theory (DFT) is used. More specifically, we make use of the program Gaussian09[210] combined with the B3LYP[211–214] functional for exchange-correlation effects. Carbon and hydrogen atoms are described with a cc-pVTZ[215–218] basis set, whereas an aug-cc-pVTZ[215–218] basis set is used for sulfur, nitrogen and oxygen atoms. Partial atomic charges are assigned according to the ESP method following the Merz-Singh-Kollman scheme.[208,209]

8.3. Comparison between 2D electrostatic embedding and the Topping model

It has been stated in a number of publications that the Madelung potential of an infinite 3D crystal cannot be approximated by a simple cluster calculation[400,404–407] and that more advanced methods have to be employed.[401,408] Our approach to include depolarization effects in MD simulations, however, is based on using electrostatic embedding to approximate the electric field of the infinite slab. We rely on the concept that the field of an infinite 2D slab can be represented by a finite cluster with reasonable accuracy.

To make sure the embedding approach is valid in two dimensions we compare the potential energy calculated for a finite 2D cluster of point dipoles with the analytical solution for an infinite 2D slab given by the Topping model.[124,409]

The analytical expression describing the mutual potential energy per dipole for an infinite 2D array of point dipoles is given by[409]

$$w_{topping} = \frac{\frac{1}{2}\mu^2}{a^3} K \ , \tag{8.1}$$

where μ is the z-component of each dipole, a is the nearest neighbor distance to the next dipole and K is a numeric factor calculated by Topping. It is given by $K_r = 9.0336$ for a rectangular arrangement of point dipoles and by $K_h = 11.0342$ for hexagonal packing.[409]

The mutual potential energy per point dipole of a finite size cluster ($w_{cluster}$) is obtained by summing up individual Coulombic contributions of dipoles up to a certain cluster size. These values are then compared to the analytical value given of the Topping model $w_{topping}$ (see Equation 8.1). Tests were performed for rectangular and hexagonal packing of dipoles, both yielding the same qualitative results. In the following we only show the results for hexagonal packing as the real SAMs we want to study with our proposed method also have hexagonal packing.

The z-dipole moment is chosen as $\mu = 5\,\text{Debye}$ and the nearest neighbor distance is $a = 5\,\text{Å}$, which has to be inserted into Equation 8.1 in units of cm. The resulting mutual potential energy per point dipole has units of ergs. The exact choice of dipole moment and lattice spacing is not essential, however, for verifying the convergence of the finite sum to the analytical value. The two parameters are included in both evaluations (finite cluster and Topping formula) and cancel each other in the ratio $w_{cluster}/w_{topping}$.

In Figures 8.3 and 8.4 the ratio of the mutual potential energy per point dipole of a finite size cluster and the analytical value of the Topping model ($w_{cluster}/w_{topping}$) is depicted as a function of cluster size.

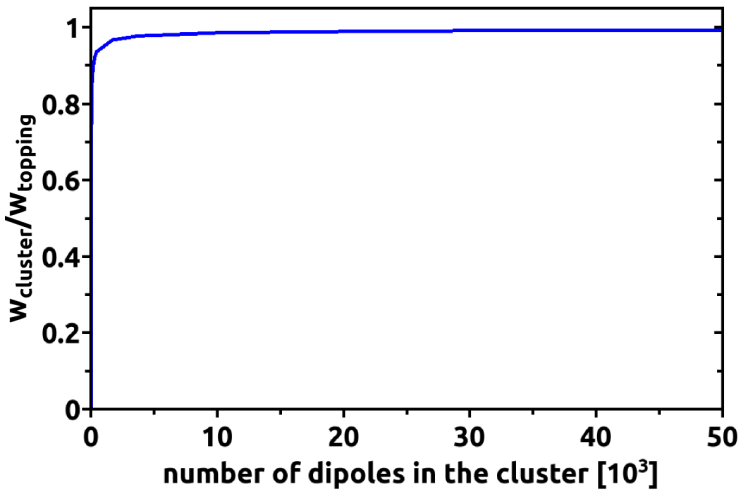

Figure 8.3.: Convergence of the electrostatic potential energy of a 2D finite cluster of point dipoles in hexagonal arrangement to the analytical value of an infinite 2D array according to the Topping model.[409]. The ratio $w_{cluster}/w_{topping}$ is plotted as a function of cluster size. The same convergence was found for a rectangular arrangement of dipoles.

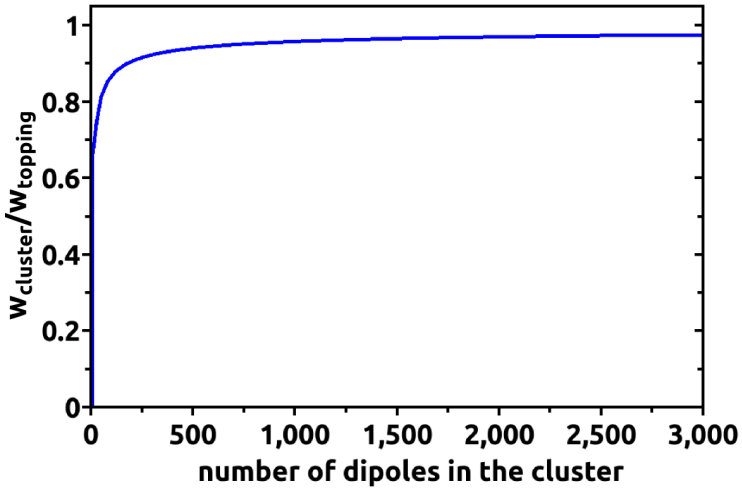

Figure 8.4.: Convergence of the mutual electrostatic potential energy of a 2D finite cluster of point dipoles in hexagonal arrangement to the analytical value of an infinite 2D array according to the Topping model.[409] The ratio $w_{cluster}/w_{topping}$ is plotted as a function of cluster size. This is a zoom of Figure 8.3 for smaller cluster sizes. At cluster sizes of around 1000 to 1500 dipoles the electrostatic potential energy of the finite cluster is already converged to 95% of the analytical value given by the Topping model.[409]

In Figure 8.3 one can clearly see that the potential energy of a finite cluster converges to the analytical value for an infinite 2D slab. This is the most important result as it shows that indeed the electrostatic effect of an infinite monolayer of dipoles can be approximated correctly by a finite size cluster in two dimensions.

Secondly, Figures 8.3 and 8.4 show that convergence is quite fast at the beginning and then slows down for huge cluster sizes. For the embedding step in the entire procedure, as described in Section 8.2, cluster sizes in the range of 1500 to 3500 molecules are used. The potential of a cluster of point dipoles of this size is already converged to $\approx$ 96% to 98% of the value given by the analytical Topping model (see Figure 8.4). Despite the fact that real extended molecules cannot be seen as perfect point dipoles, this adequate convergence in a simple point dipole model additionally supports our choice of cluster size for the embedding step of the final procedure.

8.4. Investigated systems

In Section 8.6 the full procedure as described in Section 8.2 is applied to four different SAMs. For these test cases we chose the four molecules depicted in Figure 8.5. An Au(111) substrate is used for all four systems in MD runs and all SAMs are studied at full coverage.

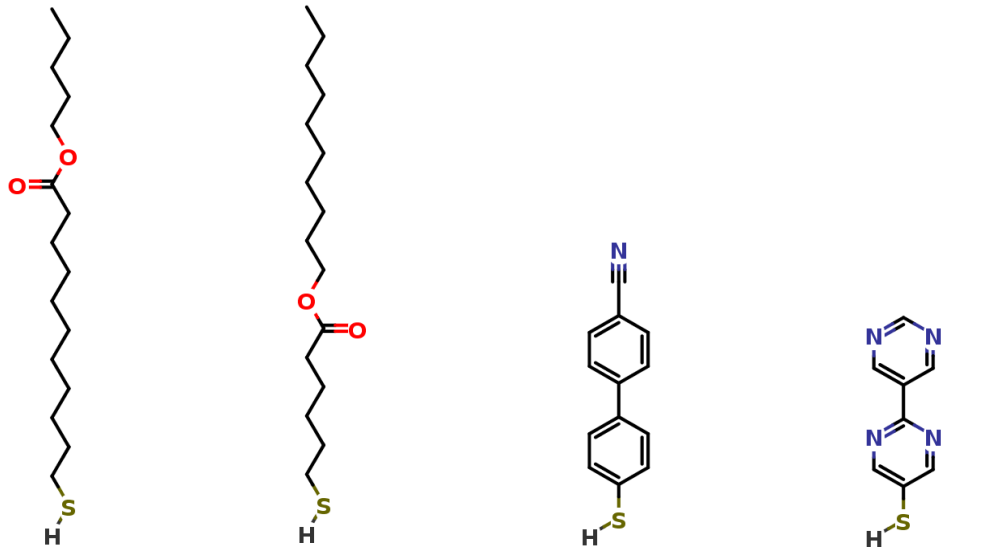

(a) C10EC5 **(b)** C5EC10 **(c)** CSBPT **(d)** DPYMT

Figure 8.5.: Chemical structures of the four test systems we chose for this study: **(a)** pentyl 11-sulfanylundecanoate (named C10EC5) and **(b)** decyl 6-sulfanylhexanoate (named C5EC10) are alkylthiolates with embedded dipolar ester groups. Molecules **(c)** 4-(4-sulfanylphenyl)benzonitrile or cyano-substituted biphenylthiol (called CSBPT) and **(d)** 2-(pyrimidin-5-yl)pyrimidine-5-thiol, dipyrimidinethiol (called DPYMT) are the test cases for SAMs of dipolar aromatic molecules.

C10EC5 and C5EC10 (Figures 8.5a and 8.5b) are alkylthiolates with embedded ester groups as already described in Section 1.2.1 and studied in Chapters 5 and 6. They have a large, off axis dipole moment associated with the embedded ester group, which makes them good candidates to study depolarization effects. From a structural point of view, these molecules are characterized by their long and highly flexible alkyl backbones. Additionally, they are quite loosely packed on a Au(111) surface even at full coverage. These structural properties allow the molecules to move and reorient rather freely even in a densely packed SAM. Consequently, it is quite a challenge to correctly determine and optimize the molecular geometry and packing structure of SAMs of these molecules, making them excellent test cases especially for the MD part of the proposed method. We chose C10EC5 and C5EC10 as representatives of this type of molecules to study the impact of odd-even effects. The former molecule has ten carbon atoms in the lower segment and five above the ester group. The situation is reversed for the C5EC10 molecule. This affects not only the vertical position of the ester group in the SAM, but also its orientation due to the odd and even number of CH_2 units in the lower segment.

CSBPT and DPYMT (Figures 8.5c and 8.5d) belong to the class of aromatic molecules which is an equally important group for SAM formation and is, therefore, included in this study. SAMs of aromatic molecules have rather different structural

properties than alkyl-based SAMs and are, therefore, a good second test case for the proposed method. Both molecules, CSBPT and DPYMT are characterized by their rigid backbone comprised of two phenylene / pyrimidine rings. Thus they have less molecular flexibility than the aliphatic molecules C10EC5 and C5EC10. The spacious aromatic rings also lead to a denser packing of CSBPT and DPYMT compared to C10EC5 and C5EC10 for the same molecular arrangment on the Au(111) surface. The rigidity of their backbone and the close packing make aromatic SAMs a quite different challenge and a good additional test case for the geometry optimization part of our procedure. Simulating SAMs of these larger molecules poses quite different requirements to the method than alkylthiolates. Aromatic molecules have less space to move individually in their close-packed SAM structure. Therefore, they tend to reorient collectively, which has to be taken into account for MD simulations. The chosen unit cell is larger for these systems (32 molecules) than for the above described C10EC5 and C5EC10 cases (16 molecules in the MD unit cell). This adaptation facilitates the reorientation of the molecules in the unit cell. When the unit cell is chosen too small, all molecules would need to reorient collectively due to the periodic boundary conditions. Individual molecular movement would be restricted. However, the energy barrier for such collective movement is too high and would not be overcome in the MD run, resulting in an erroneous final structure still influenced by the starting geometry.

When the unit cell is chosen large enough, however, SAMs of these aromatic molecules are usually easier to simulate in MD and generally yield nicely ordered structures due to the restricted possibility of molecular movement.

From an electrostatic point of view, CSBPT and DPYMT are highly interesting as both of them have a large dipole moment which, in contrast to C10EC5 and C5EC10, is oriented along the molecular axis. Furthermore, both the molecular dipoles of CSBPT and DPYMT have z-components pointing towards the docking group and the substrate not away from it like C10EC5 and C5EC10. For CSBPT the dipole mainly stems from the polar cyano group. DPYMT has no special polar terminal group, instead the two pyrimidine rings are responsible for the molecular dipole.

8.5. Testing the electrostatic embedding on a monolayer of CSBPT molecules

As a first tryout of the method on real molecules we perform a standalone test of just the electrostatic embedding iteration without the outer geometry optimization loop. The aim here is to see whether the system is described correctly and whether depolarization effects are accounted for in a correct manner. To this end we define as our test system a free standing monolayer of CSBPT molecules in a specifically chosen rectangular arrangement. The lattice spacing between the molecules is 4 Å and 8 Å in x- and y- direction respectively. The molecules are all oriented upright (z-

direction); their phenylene rings are aligned parallel to the yz-plane. We try out two cases. The first one with the arrangement described above, meaning 0° tilt angle. In the second case we tilt all molecules by 45° in x-direction to introduce a horizontal dipole component into the system and see how our embedding procedure handles it. These artificial test systems are very well defined and we exactly know the orientation of the molecular dipoles in both configurations, namely along the molecular axis.

On these systems we perform the embedding iteration, as described in Section 8.2, by building circular clusters with a cutoff radius of 150 Å , (containing 2203 molecules) from small unit cells (4 x 8 Å) containing just one molecule. The calculation parameters are slightly different from the ones described in Section 8.2 to be consistent with the VASP[238–241] calculations we use as a benchmark for the test (described in the paragraph below). We therefore use the PBE[235,236] functional together with the 6-311++G(d,p)[410–419] basis set. Also it should be noted that no image charges are included in the embedding cluster, as we investigate a free standing molecular layer without metallic substrate here.

To benchmark the results obtained with Gaussian09[210] and the embedding procedure, we perform density functional theory calculations of the same systems with the periodic boundary code VASP. This alternative calculation uses a unit cell containing one molecule combined with periodic boundary conditions, thereby mimicking an infinitely extended 2D layer of free standing CSBPT molecules. Depolarization effects are treated implicitly.

To see the influence of depolarization on the molecular dipole moments we also calculate the dipole moment of an isolated CSBPT molecule in vacuum with both different methods (Gaussian09 and VASP).
In VASP (which is a 3D periodic DFT code) an isolated molecule in vacuum is treated by placing it into a large unit cell (50 x 50 x 50 Å in this case) and including dipole corrections in all three spatial directions (details see Chapter 3).
In the end we compare the molecular dipole moments obtained with the embedding approach and the VASP code. We use the VASP results as benchmark values to see how close our embedding scheme can reproduce them.

Please note that in VASP calculations the dipole moment is only accessible indirectly through the dipole correction. For a monolayer calculation, however, only the dipole correction in z-direction is used. Therefore, the horizontal components are not calculated for a monolayer. We only get information about the z-component. This, however is no problem as the z-dipole moment is the quantity we are interested in for studying depolarization.

Table 8.1 gives the molecular dipole moments for the test system of upright standing molecules and Table 8.2 summarizes the results for the 45° tilted case.

Table 8.1.: Molecular dipole moments calculated for an isolated CSBPT molecule in vacuum and in a regular, free standing monolayer of 0° tilt angle. The results obtained with the Gaussian09[210] code for an isolated molecule and by the embedding procedure for a monolayer are compared with results obtained using the 3D periodic DFT code VASP[238–241] for the same molecular arrangements.

d_x , d_y , d_z ... x-,y-,z- components of the molecular dipole moment

$\gamma = \frac{d_{z,molecule}}{d_{z,layer}}$ ... depolarization factor

system	$\mathbf{d_x}$ [Debye]	$\mathbf{d_y}$ [Debye]	$\mathbf{d_z}$ [Debye]	γ
molecule (emb)	0.00	0.86	-5.38	
molecule (VASP)	0.00	0.68	-5.54	
layer (emb)	0.00	0.84	-2.71	1.98
layer (VASP)	-	-	-2.78	2.00

The d_y component present in the 0° tilt single molecule calculations is due to the dipole moment of the thiol group. The S-H bond is oriented along the y-axis. However, the y-component of the dipole is of minor importance for this test study, as we are primarily interested in the z-component associated with the molecular tilt angle and depolarization effects.

In table 8.1 we find a very good agreement between results obtained with the Gaussian09 code and the benchmark VASP results for the isolated molecule as well as the monolayer. Furthermore, changing the configuration from an isolated molecule to a monolayer reduces the z-component drastically by a factor of two, for both calculation methods. So we can state that depolarization indeed plays a significant role in this molecular arrangement and that our embedding strategy is able to capture this effect correctly. Table 8.2 summarizes the results obtained for the 45° tilted system.

Table 8.2.: Molecular dipole moments calculated for an isolated CSBPT molecule in vacuum and in a regular, free standing monolayer of 45° tilt angle. The results obtained with the Gaussian09[210] code for an isolated molecule and by the embedding procedure for a monolayer are compared with results obtained using the 3D periodic DFT code VASP[238–241] for the same molecular arrangements.

d_x , d_y , d_z ... x-,y-,z- components of the molecular dipole moment

$\gamma = \frac{d_{z,molecule}}{d_{z,layer}}$ ... depolarization factor

system	$\mathbf{d_x}$ [Debye]	$\mathbf{d_y}$ [Debye]	$\mathbf{d_z}$ [Debye]	γ
molecule (emb)	-3.80	0.86	-3.80	
molecule (VASP)	-3.92	0.68	-3.92	
layer (emb)	-2.80	0.80	-2.08	1.83
layer (VASP)	-	-	-2.20	1.78

In Table 8.2 we clearly see how the molecular tilt of 45° in x-direction also affects the orientation of the dipole moment, which now has a significant x-component. Also in this tilted test system we find very good agreement between the dipole moments calculated with Gaussian09 and VASP.

Looking at the values for the monolayer we see that depolarization significantly reduces the z-dipole component again by almost a factor of two. Additionally, there is also a reduction of the dipole moment in x-direction. This is a direct consequence of the 45° tilt angle. In this test calculation depolarization only happens by charge rearrangement in the molecule, not by a geometric reorientation of the molecule. So if charges redistribute along the molecular axis to reduce the z-component of the dipole moment, that automatically also reduces the x-component.

As a conclusion of this standalone test study of the proposed electrostatic embedding procedure we can summarize that firstly, depolarization indeed plays a significant role in the systems we want to describe and secondly, that our devised method is able to correctly describe charge rearrangements inside the molecule that lead to depolarization.

The second contribution to depolarization, namely change in the molecular conformation and packing structure is captured by the MD part of the full MD+embedding procedure. The combined influence of charge rearrangements and change in molecular structure on depolarization is investigated in the next Section, where the full procedure as described in Section 8.2 is applied to four different, realistic SAM structures.

8.6. Application of the full procedure to four different SAMs

In this Section we apply the full procedure as stated in Section 8.2 to SAMs of the four different molecules described in Section 8.4. The molecules differ in their position and orientation of the dipole moment, as well as the rigidity of the backbone, thus creating four distinct test cases representing different types of systems to characterize the applicability of our method.

The results of this investigation are summarized in Table 8.3 for the four respective systems. The evolution of the z-dipole moment, the absolute molecular dipole, the molecular tilt and the twist angle during the iteration process is presented.

Table 8.3.: Results obtained for the four investigated systems by applying the full iterative procedure described in Section 8.2. The given structural parameters (columns three and four) describe the 2-molecule unit cell of the embedding cluster used for calculating the atomic charges. The corresponding dipole moment is given in columns five and six.

step ... iteration step of the outer (MD) loop
tilt ... average molecular tilt angle of the embedding unit cell
twist ... twist angle of the two molecules in the embedding unit cell relative to each other; measured as the angle between the C=O vectors of the two molecules (C10EC5, C5EC10) or as the angle between the lower phenyl rings of the two molecules (CSBPT, DPYMT) respectively
$|\mathbf{d}|$ ... absolute value of the total molecular dipole moment
$\mathbf{d_z}$ ... z-component of the molecular dipole moment

system	**step**	**tilt** [°]	**twist** [°]	$\|\mathbf{d}\|$ [Debye]	$\mathbf{d_z}$ [Debye]
C10EC5	0 (gas phase)	36.3	-	1.80	1.49
	1	36.3	110.3	1.03	0.81
	2	36.9	107.2	1.12	0.67
	3	36.9	109.2	1.12	0.71
	4	36.9	109.6	1.03	0.80
C5EC10	0 (gas phase)	34.1	-	3.77	0.46
	1	34.1	89.9	4.80	0.19
	2	34.8	80.9	4.82	0.29
	3	35.3	76.9	4.78	0.32
	4	34.9	79.5	4.83	0.27
CSBPT	0 (gas phase)	25.7	-	5.33	-4.62
	1	25.7	119.4	2.02	-1.17
	2	27.9	120.7	2.47	-2.28
	3	25.9	120.7	2.45	-2.27
	4	26.0	119.9	2.44	-2.24
DPYMT	0 (gas phase)	27.4	-	4.31	-4.05
	1	27.4	174.5	1.69	-1.18
	2	27.3	82.1	2.01	-1.71
	3	25.3	1.6	2.10	-1.66
	4	29.5	45.3	2.07	-1.60
	5	30.1	44.7	2.11	-1.58
	6	29.9	45.0	2.06	-1.57

From the data presented in Table 8.3 we identify the following general trends: The z-dipole moment is reduced significantly for all four systems. Furthermore, the depolarization already happens mostly in the first embedding step. Subsequent iterations, which update the geometry, influence the dipole moment only slightly further. In this first embedding a slight numerical "overdepolarization" is encountered, which is then corrected in the following iteration steps.

The structural changes in the SAMs are rather minor for C10EC5, C5EC10 and CSBPT. Tilt and twist angles only vary in a small range during the iteration and the calculated packing structure, p $\left(\sqrt{3}\text{ x }\sqrt{3}\right)$ R30° with herringbone arrangement (see Figures 8.6a and 8.6b), remains the same throughout the iteration cycles. This arrangement of molecules on the substrate is in good agreement with experimental findings for these SAMs.[13,25,87,420–422] The calculated tilt angles are a few degrees higher than what is typically measured for these SAMs.[25,423,424] This is due to the fact that the SAM is artificially cooled to T=10K in the MD simulation to decrease thermal motion and associated structural defects. During this cooling process we find that the tilt angle increases by a few degrees compared to the room temperature situation in the simulation. Tilt angle measurements of SAMs are typically performed at room temperature.

The DPYMT SAM is an exception of this general outcome. It undergoes a structural change during the iteration from an initial (p $\left(\sqrt{3}\text{ x }\sqrt{3}\right)$ R30°) structure to a c (3 x 2) arrangement with iteration step four (further information see below).

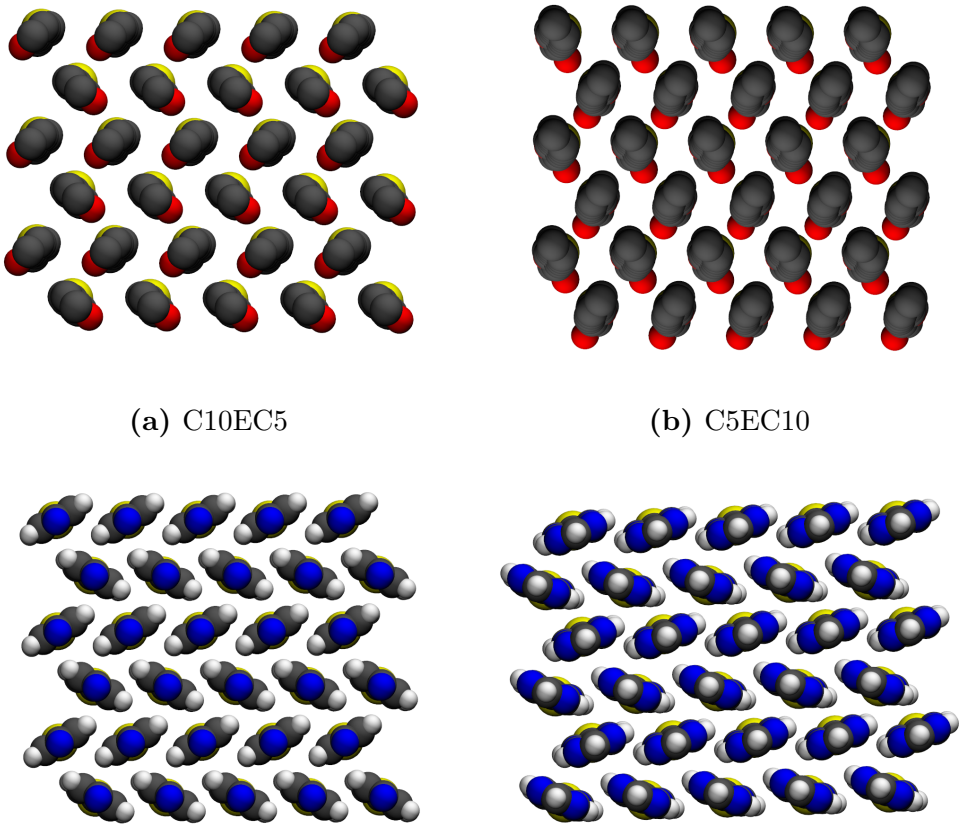

(a) C10EC5 **(b)** C5EC10

(c) CSBPT **(d)** DPYMT

Figure 8.6.: Final molecular packing structures used for the last embedding step of the four studied SAMs: (a) C10EC5, (b) C5EC10, (c) CSBPT, (d) DPYMT. For the sake of clarity, hydrogens are not depicted for (a) and (b). The viewing angle is chosen along the main molecular axis for each system. Cases (a), (b) and (c) show a herringbone p $\left(\sqrt{3}\text{ x }\sqrt{3}\right)$ R30° arrangement, whereas (d) forms a herringbone c (3 x 2) structure.

After these general findings a few system specific differences will now be addressed.

The dipole moment of the C10EC5 system has a far larger vertical component than the C5EC10 system. In the latter case the molecular dipole is oriented nearly horizontally. This phenomenon has already been addressed in Chapter 6. Thus we only give a short reminder about the origins of this difference here. Due to the $\approx 30°$ tilt angle and the zig-zag nature of the carbon backbone, combined with the odd number of carbons in the lower segment of the molecule, the ester dipole happens to be oriented fairly horizontally for the C5EC10 molecule in a SAM, whereas it is oriented at a different angle for the C10EC5 molecule which has an even number of carbons in the lower segment. This argument only holds if the molecular tilt angles and gold-sulfur bond geometries are reasonably similar in both systems, which is

the case for C10EC5 and C5EC10, as also previously stated in Chapter 6.

At first glance it seems surprising that the absolute dipole moments of the two chemically practically identical molecules C10EC5 and C5EC10 are so different, especially after depolarization. The total dipole moment of C5EC10 even increases during the procedure, which seems counterintuitive. The explanation for both effects however is fairly trivial. The embedding cluster is built from molecules in a configuration which is achieved by capping the sulfur atom with a hydrogen (as described in Section 8.2). This introduces a rather significant dipole moment oriented along the S-H bond of the thiol group which in turn is oriented nearly horizontally. Keep in mind that the odd and even number or carbons in the lower segment of C5EC10 and C10EC5 lead to a different orientation of the ester dipole moment in the two molecules. As a result the horizontal components of the ester and thiol dipole add up for C5EC10, whereas they partially compensate for C10EC5. Additionally, as mentioned above, C5EC10 has a larger horizontal ester dipole component which causes the overall larger total dipole moment of this molecule compared to the chemically very similar C10EC5 structure. During the depolarization process charges in the C5EC10 molecule redistribute in a way that decreases the z-component while increasing the x-/y- components. Thus, the total dipole moment increases during the iteration. Additionally, the horizontal dipole components of the molecules in the SAM are aligned more or less head-to-tail, which means that they even increase due to mutual polarization effects. This is basically the opposite effect to the depolarization happening in z-direction.

It should be noted, however, that the horizontal dipole component calculated in the embedding step is not directly relevant for MD simulations. The thiol dipole, causing the large horizontal contributions, is not present in MD simulations of SAMs on metal substrates, where the sulfur is bound dissociatively to the substrate.

CSBPT and DPYMT both have molecular dipole moments aligned along the molecular axes which are oriented fairly vertically in both cases (tilt angles are $\approx$ 25° and 30°). Therefore, the z-component and the absolute value of the dipole moment are nearly identical. Also in these systems a strong depolarization to about half the value (or even less for DPYMT) of a molecule in gas phase is observed.

These charge rearrangements inside the molecule might be connected to the change in packing structure found for the DPYMT SAM. In contrast to the other three systems the DPYMT SAM changes its packing from an initial p $\left(\sqrt{3}\text{ x }\sqrt{3}\right)$ R30° structure without herringbone conformation to a herringbone c (3 x 2) arrangement. Additionally the packing structure changes between herringbone (iterations 2,4,5 and 6) and non-herringbone (iterations 1 and 3) during the process. However, once the system settles in the c (3 x 2) arrangement (in iteration step 4) the packing structure does not change anymore in the following iterations 5 and 6.

The origin of this structural rearrangement might lie in the position of the nitrogen atoms inside the DPYMT molecules. Oligophenylenes usually favor herringbone

arrangement as it brings the positive hydrogens closer to the negative centers of the carbon rings. An opposing influence is the tendency to form π-π stacking, also commonly observed in aromatic molecules. This tendency seems to be the stronger one in the DPYMT SAM at the beginning of the simulation. This is presumably caused by the presence of nitrogen atoms in the DPYMT molecule, which have a quite large negative charge. In the course of the simulation procedure, the atomic charges apparently redistribute in the molecule in such a way that, starting from iteration step 4, a herringbone configuration is energetically favorable. The partial atomic charges calculated for the DPYMT molecule in gas phase and in the SAM (taken from iteration step 6) are given in Table 8.4.

Table 8.4.: Partial atomic charges of the carbon and nitrogen atoms inside the DPYMT molecule calculated for an isolated molecule in gas phase and in a densely packed SAM (atomic charges from iteration step 6) according to the ESP charge partitioning scheme.[208,209]

atom ... carbon/nitrogen atom positions:
C1-C4 and N1,N2 are part of the lower pyrimidine ring
C5-C8 and N3,N4 belong to the upper pyrimidine ring
carbons are numbered with increasing z-position in the molecule
$\mathbf{q_{i,mol}}$ ... partial atomic charges of the gas phase molecule
$\mathbf{q_{i,sam}}$ ... partial atomic charges of the molecule in a SAM

atom	$\mathbf{q_{i,mol}}$ [e]	$\mathbf{q_{i,sam}}$ [e]
C1	-0.511	-0.479
C2	0.496	0.418
C3	0.595	0.576
N1	-0.767	-0.790
N2	-0.850	-0.854
C4	1.128	1.208
C5	-0.906	-0.966
C6	0.754	0.785
C7	0.778	0.816
N3	-0.849	-0.923
N4	-0.862	-0.879
C8	0.856	0.972

Indeed we see that all atomic charges differ for a molecule in gas phase and in the SAM. All nitrogen atoms have more negative atomic charges in the SAM than in gas phase. Most carbons (but not all) show more positive charges due to depolarization. However, from this data it is not completely clear to us what exactly causes the

structural rearrangement, i.e. whether some of the atoms play a dominant role or whether the changes on all atoms combine equally to a collective, net result.

As a conclusion, we think that the DPYMT system needs to be investigated further to verify the origin of the change in packing structure. Despite the tests performed so far, the possibility remains that some computational artifacts are the source of the structural reorientation of the DPYMT SAM. The next logical steps in this investigation are quantum mechanical calculations of the same system using DFT and to compare the found structures and calculated dipole moments further with experimental data. These necessary steps have not yet been carried out, but will be tackled next in the continuation of this project.

To summarize this Section 8.6 we conclude with the following remarks:
The proposed procedure works well for all four investigated systems. Depolarization effects play a significant role in all of them with reductions of the z-dipole moment by a factor of two ore more being found. On the other hand, the studied SAMs undergo only minor structural changes during the iteration cycles, except for the DPYMT system discussed above. In this case the molecular arrangement in the SAM, determined by MD simulations, changes from non-herringbone p $\left(\sqrt{3} \text{ x } \sqrt{3}\right)$ R30° to herringbone c (3 x 2) due to depolarization effects. The impact of depolarization on the molecular packing structure seems to be highly system dependent, as the comparison between the structurally similar systems CSBPT and DPYMT and their quite different behavior in these simulations shows.

From the findings presented above it can be deduced that depolarization in the C10EC5, C5EC10 and CSBPT systems is primarily caused by charge redistribution inside the molecules, whereas geometrical and structural reorientation of the molecules plays a minor role.

With this knowledge we can justify the approach taken in Chapters 5 and 6, where MD simulations were used as a tool for preoptimizing molecular geometries and packing structures of alkyl thiolate SAMs with embedded ester groups, such as the C10EC5 and C5EC10 molecules also investigated here. In these cases, MD simulations have been performed without accounting for depolarization effects.
As we see from the results presented in this Chapter though, this is a valid approach. Including depolarization does not significantly alter the SAM structure of these systems. Therefore, returning to the less computationally demanding approach of conventional MD simulations for the purpose of preoptimization is completely justified for the systems in question. Changes in the molecular dipole due to depolarization are then implicitly accounted for in the subsequently performed DFT calculations.

9. Summary and Conclusions

In this thesis self-assembled monolayers of aliphatic and aromatic molecules with embedded dipolar groups on gold substrates have been investigated by density functional theory and molecular dynamics simulations. Structural and electronic properties related to the embedded groups, primarily atomic core level energies and work functions have been studied.

In Chapter 5 the impact of the embedded dipolar group on XP spectra has been investigated on two representative and experimentally extensively studied aliphatic SAMs on Au(111) substrate consisting of (i) partially fluorinated alkylthiols and (ii) alkylthiols with a dipolar ester group embedded in the molecular backbone. Carbon 1s core level energies were calculated using density functional theory combined with the initial state approach and XP spectra were determined from these core level energies including screening effects of the substrate and exponential damping. A good agreement was found between calculation and experiment establishing the applicability of the simulation and evaluation procedure for these systems. The partially fluorinated alkylthiolate SAM showed five distinct peaks in the experimental C 1s XP spectrum, associated to carbons in five distinct chemical neighborhoods inside the molecule. All five peaks including relative peak positions and intensities were reproduced in calculations, showing that chemical shifts in XP spectra are accurately described in calculations. The mid-chain ester functionalized aklylthiolate SAM showed four peaks in experimental XP spectra, two of which can be explained by chemical shifts as they are associated with the carbons chemically bound to oxygens. The two remaining peaks, which show a separation of 0.8 eV and are generated by the CH_2 backbone cannot be explained in the same way as the two segments below and above the ester group are chemically identical. Calculations identified electrostatic shifts, caused by the embedded ester groups as the origin of this peak splitting. The ester dipoles inside the densely packed SAM form a regular arrangement and create a potential discontinuity perpendicular to the substrate due to collective electrostatic effects. This shifts the atomic core level energies of the top segment atoms with respect to the bottom segment.

The distinction between chemical and electrostatic origins of XPS peak shifts becomes even clearer in reduced coverage SAMs. To that end calculations with artificially reduced coverage were performed. The molecular orientation was kept the same as in the full coverage case to exclude additional influences of structural reorientation. All electrostatic shifts in XP spectra gradually vanished with decreasing coverage as they rely on the collective interaction of densely packed dipoles. They completely disappeared at a coverage of 1/16 for partially fluorinated SAMs and at

a coverage of 1/32 for the embedded ester SAMs. Chemical peak shifts on the other hand were unaffected and remained present in the spectra to full extent.

As a main result of this investigation it can be stated that chemical and electrostatic shifts both occur in XP spectra simultaneously and can add up or even partially cancel. Furthermore, electrostatic shifts may not be neglected in the interpretation of XP spectra as they can be of substantial size, with values of up to 0.8 eV found in the systems investigated here. XPS could consequently be employed as a tool to probe the electrostatic situation inside a SAM.

In Chapter 5 an approach to correctly calculate core level energies within the DFT framework, based on the initial state method and including screening effects of the substrate was devised and thoroughly tested on two experimentally very well studied aliphatic SAMs. All calculations presented in Chapter 5 showed excellent agreement with experimental data. Based on these findings, the same method is applied to investigate SAMs of alkylthiolates with embedded dipolar ester groups in Chapter 6. The influence of bottom and top segment length as well as the impact of dipole orientation on work functions and core level energies were studied. Modeling results were compared to experimental data. A significant electrostatic shift of $\approx$0.8 eV between bottom and top segment core level energies was found for all systems with an ester dipole component perpendicular to the substrate, independent of chain length. The work function modification of the studied systems with respect to an unfunctionalized alkylthiolate SAM on gold substrate was also found to be around $\approx$0.8 eV, corresponding well with calculated core level shifts. Experimental results were found to qualitatively correspond well with calculations for most systems. Quantitatively, the experimentally observed XPS shifts and work function modifications were slightly smaller (about 0.1 to 0.2 eV) than the calculated values.

Calculations showed that rotating the molecule around its main axis by 180° results in horizontal orientation of the ester dipole moment. The dipole component perpendicular to the substrate vanishes. For such SAMs the core level energies of the bottom and top segment were found to be identical as no electrostatic shift occurs. The work function modification is reduced accordingly, as the contribution of the ester dipole is absent. Such a rotation around the main axis can easily happen in these systems as the highly flexible molecules are relatively loosely packed even at full coverage and have room to move. Molecular dynamics simulations of larger unit cells indicated that this rotated orientation occurs in SAMs for a certain percentage of molecules and seems to be the preferred one for molecules with an odd number of carbon atoms in the bottom segment.

A system with an embedded reverse ester group, meaning the ester group was inserted into the molecular backbone "upside down" was also studied. In this chemically different molecule the ester dipole z-component points toward the substrate instead of away from it. Consistent with expectations, all electrostatic effects were found to be reversed for this SAM. The core level energies of the top segment carbon atoms were found to be shifted to less negative values and the work function was increased instead of decreased compared to a non-functionalized akylthiolate SAM

of similar molecular length. Measurements of this system equally showed this substantial increase in work function. Experimental XP spectra, however, only showed one major peak instead of two, as would be expected from calculation results and simple electrostatics. This one main peak (associated with the top segment) is, however, shifted to lower binding energies compared to a non-functionalized alkylthiolate SAM. This observation is in good quantitative agreement with calculations. A conclusive reason for the absence of a clear signal of the reverse ester bottom segment in XP spectra has not yet been found.

The bond dipole was identified as a second important electrostatic influence in the investigated SAMs. It also forms a regular arrangement in the SAM and, therefore, creates an electrostatic shift qualitatively analogous to the ester dipole shift, but affecting the whole molecule instead of just the top segment. Therefore, electrostatic influences of the bond dipole and the ester dipole add up (or partially cancel) in the top segment of the molecule. The magnitude of the relevant bond dipole component (perpendicular to the substrate) was found to be quite sensitive to the molecular twist angle. To estimate the extent of this influence test calculations on non-functionalized alkylthiolate SAMs on gold substrate were performed. A maximum variation of 0.4 eV in work function and core level energies was found for a change in twist angle of 90°. The influence of the bond dipole raises the question of which reference to use for calculating core level shifts. Comparing top and bottom segments of the same SAM ensures that the bond dipole contribution is identical in both cases. However, screening effects influence the bottom segment more strongly than the top segment due to proximity to the substrate and therefore the calculated bot-top shift will be slightly increased. Non-functionalized alkylthiolate SAMs on gold substrate of the same total molecular length can also be used as a reference system. In this case screening effects are analogous in the compared top segments, but the bond dipole contribution in both systems may be quite different, possibly affecting the results by up to 0.4 eV. Due to the flexibility and relatively loose packing of alkylthiols on gold substrate a certain variation in twist angles and the associated change in bond dipole between different systems seems plausible. For comparing core level shifts to work function modifications using an unfunctionalized aklylthiol reference for both quantities was deemed preferential in this work to ensure consistency and better comparability of both quantities. This approach was equally employed in the evaluation of experimental data, where one is faced with the same dilemma. Analogous to calculations, the use of the bottom segment vs. a Cn SAM as a reference system produced quite different results.

The influence of the orientation of the terminal CH_3 unit on work functions was found to be negligible. Calculations of unfunctionalized alkylthiolate SAMs with odd and even numbers of carbons in the backbone showed work function modifications (compared to a pristine Au(111) surface) differing by only 0.05 eV between odd and even, independent of total chain length. This slight variation, caused by the alternating orientation of the CH_3 group in odd and even cases is deemed to be of minor importance compared to the significantly larger chemical and electrostatic shifts present in the ester-functionalized systems discussed above.

In Chapters 5 and 6 the effects of embedded dipolar groups in pure SAMs were studied. Electrostatic influences on the work function and atomic core level energies were found. Naturally, the question arises, how embedded dipolar groups influence the behavior of mixed SAMs. This topic is of special interest, as in Chapter 6, the possibility of "electrostatically inactive" molecules (due to a horizontal orientation of the ester dipole) was introduced. It is quite plausible that in real SAMs such a mixture of molecules with "regular" and "horizontal" dipole moments occurs. We, therefore, investigated how the behavior of such mixed SAMs differs from pure ones and how the homogeneity of the film influences electrostatic properties of the SAM. These questions were addressed in Chapter 7. However, ester-functionalized alkylthiols do not pose an ideal test system, due to their structural variations, their off-axis dipole moments and their sensitivity to twist angle related changes in the bond dipole. Structurally reliable, dipolar, aromatic molecules are a much better choice. Consequently, pyrimide-substituted terphenyls, which exhibit a dipole moment oriented along the molecular axis were chosen as a test system for this investigation. The central pyrimidine unit was inserted into the molecule in two possible orientations determining the direction of the electric dipole moment, towards (TP1-down) or away (TP1-up) from the substrate. A non-functionalized terphenyl (TP1) SAM, which lacks the dipolar contribution of the pyrimidine group but otherwise has identical structural properties to the functionalized SAMs was used as a reference system.

Pure SAMs of TP1-up and TP1-down show a behavior analogous to the ester-functionalized alkylthiols described in Chapters 5 and 6. The core level energies of the top phenylene ring are symmetrically shifted downward and upward with respect to the vacuum side ring according to the dipole orientation, TP1-up shifting by -0.74 eV and TP1-down by +0.77eV. The work function of the system is equally affected. Compared to a pure TP1 SAM, TP1-up decreases the work function by -0.71 eV while TP1-down increases it by +0.74 eV. These calculated values were found to qualitatively agree well with experiments, where work function modifications of -0.42 eV (TP1-up) and +0.56 eV (TP1-down) were observed. Measured shifts in binding energies, ΔBE = -0.42 eV (TP1-down) and ΔBE = 0.65 eV (TP1-up), qualitatively reproduced the trend found in calculations. Note that calculated core level energies have a negative sign, while measured binding energies have a positive sign by convention. Therefore, the XPS shifts have different signs for calculated and measured values. A calculated shift to more negative core level energies corresponds to a measured shift to higher binding energies. From a quantitative point of view, calculations slightly overestimate the core level shifts and the work function modifications compared to experiments.

After the behavior of these pure systems was established several different mixed SAMs were investigated. Firstly, mixtures of TP1 with either of the functionalized molecules TP1-up or TP1-down were treated, which result in a reduced dipole density inside the SAM while avoiding structural changes. Secondly, mixtures of TP1-up and TP1-down were investigated. Both types of mixed SAMs showed a clear cor-

relation between the mixing ratio and core level energies as well as work function modifications. The main peak in XP spectra, associated with the top phenylene ring was found to gradually shift to lower binding energies with decreasing TP1-up and increasing TP1-down content. The work function modification (relative to a pristine Au(111) substrate) follows the same trend, decreasing gradually with decreasing TP1-up and increasing TP1-down content. In the 50:50 mixture of TP1-up:TP1-down the electrostatic effects of both dipolar components effectively cancel, resulting in identical core level energies for the substrate and vacuum side phenylene ring. As a result this mixed system shows a similar work function and XP spectrum as the pure TP1 reference SAM.

To study the impact of phase separation into domains of opposite dipolar orientation, an inhomogeneously mixed 50:50 TP1-up:TP1-down SAM was simulated. A qualitatively different behavior was observed for this SAM than for the homogeneous mixture of the same mixing ratio. Molecules in the TP1-up domains experience a core level shift of -0.35 eV in the top phenylene ring, whereas molecules in the TP1-down domains shift by +0.38 eV. This observation is reminiscent of the behavior of pure SAMs albeit with a reduced energetic shift and is directly linked to the domain structure of the SAM. As molecules inside one domain all have the same dipolar orientation the resulting collective electrostatic effect leads to a potential discontinuity inside the domain at the position of the central pyrimidine unit, shifting core level energies in the top phenylene ring. The electrostatic field inside a domain was found to be effectively shielded from neighboring domains. Therefore, core level energies are shifted differently in TP1-up and TP1-down domains, which can be clearly seen as a double peak structure in XP spectra.

The work function on the other hand was found to be no clear indicator of the homogeneity of the film. The average electrostatic potential above the SAM was identified as the relevant factor influencing a system's work function. In calculations it was revealed that although the electrostatic potential directly above the SAM differs substantially for TP1-up and TP1-down domains it quickly assimilates to an average value with increasing distance from the top of the SAM reaching a homogeneous distribution at a distance of $\approx 8\,\text{Å}$.

On the basis of this insight, measured XP spectra and work functions of mixed SAMs of TP1 with TP1-up and TP1-down as well as mixtures of TP1-up and TP1-down of varying mixing ratio were interpreted. In all cases, a continuous peak shift with mixing ratio was observed in XP spectra. No double peak features were found. The work function also showed a smooth correlation with concentration. Measured spectra and work function modifications were found to be in excellent accordance with calculations of homogeneous mixtures.

However, one observed difference in the TP1-up:TP1-down mixed SAMs was that, whereas the XPS peak shifts and the work function modifications showed a clearly linear correlation with mixing ratio in calculations, this was not exactly the case in experiments. There, the shifts between pure SAMs and mixtures of 75:25 ratio were distinctly larger than the shifts between 75:25 and 50:50 mixtures. This behavior was attributed to a difference in mixing ratio between the solution used to prepare

the SAM and the actual adsorbed SAM itself. In mixed SAMs of TP1-up:TP1-down the exact mixing ratio in the adsorbed SAM cannot be determined experimentally, as both molecules contain two nitrogens each. The molecular concentrations in the solutions only provide a rough estimate of the situation in the SAM. It was concluded that solutions of a 75:25 ratio actually generate SAMs with a ratio much closer to 50:50. This is quite plausible as dipoles favor antiparallel over parallel orientation as the energetically favorable arrangement. This explanation was substantiated by calculations, which showed that the 50:50 mixed SAM had a lower total system energy than the 75:25 mixed SAMs ($\Delta E \approx 72$ meV per molecule).

Due to the absence of any double peak features in measured XP spectra and the near linear correlation of peak position with mixing ratio it was concluded that all experimentally prepared SAMs of this study were homogeneous mixtures.

As a conclusion of this investigation, it is suggested that XPS could be used as a tool to probe the homogeneity of ordered mixed monolayers of dipolar molecular constituents. Peak splitting in XP spectra could be an indication of phase separation in the SAM. The work function, however, cannot be used as a reliable indicator of the homogeneity of a SAM.

In Chapters 5 to 7 the main method of theoretical investigation was density functional theory. Molecular dynamics (MD) was only used as a tool, albeit an essential one, for geometry optimization. However, MD offers some serious advantages over density functional theory. Much larger unit cells can be studied including temporal development of the system at a variable sample temperature. This makes MD a powerful tool to investigate systems, where disorder or phase separation, like the ones addressed in Chapters 6 and 7, play a role. In Chapter 7 a SAM consisting of different dipolar domains was investigated using DFT. However, this calculation was actually only a representative description of a small scale phase separation. The unit cell needed to describe a more realistic SAM with larger domains would be completely out of the range of what is currently possible with DFT due to the high computational demand of this method. Molecular dynamics on the other hand, is an ideal technique to investigate the structural properties of such large scale systems.

One of the main setbacks of molecular dynamics simulations, however, is the omission of depolarization effects which can be substantial in densely packed SAMs. Therefore, a method to account for polarization phenomena in MD simulations of aliphatic and aromatic SAMs on metal substrates was developed and tested in Chapter 8. The proposed approach combines electrostatic embedding with MD simulations in a self-consistent iterative procedure. Depolarized atomic partial charges are calculated in the embedding step on a quantum mechanical level using density functional theory. The molecular structure of the SAM is then updated according to the new set of charges in the MD part of the procedure. Application of this method to four different SAMs, two aliphatic and two aromatic, showed that the dipole moments of molecules in SAMs were reduced to approximately half the value found for individual, isolated molecules in vacuum condition. Comparison of the values obtained with this embedding method to molecular dipole moments calculated with a

periodic boundary density functional theory code and showed excellent quantitative agreement.

Additionally, the influence of depolarization on the structural properties of SAMs was studied. In three of the four test cases (two aliphatic and one aromatic) the SAM structure was only slightly affected by depolarization. The packing structure remained the same. Tilt and twist angles showed no significant change. The fourth system (dipyrimidine-thiol), on the other hand, showed a structural reorientation during the procedure going from a non-herringbone p $\left(\sqrt{3}\text{ x }\sqrt{3}\right)$ R30° to a herringbone c (3 x 2) packing structure. In the course of the simulation, partial atomic charges in the molecules changed in such a way that, apparently, a herringbone structure became favorable compared to the tendency to form π-π stacking.

The results obtained for these four test systems show that depolarization has a significant impact on molecular dipoles and thus on any related electronic properties. Furthermore, it was found that structural properties of a SAM can indeed be affected by depolarization phenomena. However, no general rule or trend can be given as the particular behavior was found to be highly system dependent.

In conclusion it can be stated that the work function of a surface is strongly influenced by the adsorption of a dipolar SAM. This effect can be used to effectively tune substrate work functions according to the requirements of the intended application. It was further shown that homogeneously mixed SAMs of dipolar components can be used to continuously tune the work function over a sizable range. Making use of embedded dipolar groups as investigated in this thesis opens up the possibility to adapt electronic properties without changing the interface to an adjoining layer, leaving the terminal group as a second handle to modify this interface separately. Furthermore, the importance of XPS as a tool for the investigation of self-assembled monolayers was shown. It was demonstrated that, additionally to providing information about the precise chemical nature of the film, XPS can be employed to probe the local electrostatic situation inside a SAM with high accuracy. This enables a local insight into the potential landscape of the monolayer and even allows to distinguish homogeneously mixed dipolar SAMs from films exhibiting phase separation. Thus, XPS can be employed as a valuable tool to verify the homogeneity of dipolar, mixed SAMs.

For all these reasons, it is believed that pure and mixed SAMs containing embedded dipolar elements will play a significant role in the field of organic electronics, especially in the area of contact work function tuning. XP spectroscopy is expected to be of even increased relevance in the investigation of chemical, electrostatic and even structural properties of dipolar SAMs in the future.

Bibliography

(1) J. C. Love, L. A. Estroff, J. K. Kriebel, R. G. Nuzzo, G. M. Whitesides *Chemical Reviews* **2005**, *105*, 1103, DOI: 10.1021/cr0300789.

(2) C. Vericat, M. E. Vela, R. C. Salvarezza *Physical Chemistry Chemical Physics* **2005**, *7*, 3258, DOI: 10.1039/b505903h.

(3) G. E. Poirier, E. D. Pylant *Science* **24, 1996**, *272*, 1145, DOI: 10.1126/science.272.5265.1145.

(4) R. G. Nuzzo, D. L. Allara *Journal of the American Chemical Society* **1983**, *105*, 4481, DOI: 10.1021/ja00351a063.

(5) M. D. Porter, T. B. Bright, D. L. Allara, C. E. D. Chidsey *Journal of the American Chemical Society* **1987**, *109*, 3559, DOI: 10.1021/ja00246a011.

(6) L. H. Dubois, R. G. Nuzzo *Annual Review of Physical Chemistry* **1992**, *43*, 437, DOI: 10.1146/annurev.pc.43.100192.002253.

(7) C. D. Bain, J. Evall, G. M. Whitesides *Journal of the American Chemical Society* **1989**, *111*, 7155, DOI: 10.1021/ja00200a039.

(8) C. D. Bain, G. M. Whitesides *Science* **1, 1988**, *240*, 62, DOI: 10.1126/science.240.4848.62.

(9) H. A. Biebuyck, C. D. Bain, G. M. Whitesides *Langmuir* **1994**, *10*, 1825, DOI: 10.1021/la00018a034.

(10) P. E. Laibinis, G. M. Whitesides, D. L. Allara, Y. T. Tao, A. N. Parikh, R. G. Nuzzo *Journal of the American Chemical Society* **1991**, *113*, 7152.

(11) L. H. Dubois, B. R. Zegarski, R. G. Nuzzo *The Journal of Chemical Physics* **1993**, *98*, 678, DOI: 10.1063/1.464613.

(12) C. Vericat, M. E. Vela, G. Benitez, P. Carro, R. C. Salvarezza *Chemical Society Reviews* **2010**, *39*, 1805, DOI: 10.1039/b907301a.

(13) F. Schreiber *Journal of Physics: Condensed Matter* **21, 2004**, *16*, R881, DOI: 10.1088/0953-8984/16/28/R01.

(14) D. M. Alloway, A. L. Graham, X. Yang, A. Mudalige, R. Colorado, V. H. Wysocki, J. E. Pemberton, T. Randall Lee, R. J. Wysocki, N. R. Armstrong *The Journal of Physical Chemistry C* **26, 2009**, *113*, 20328, DOI: 10.1021/jp909494r.

(15) N. Ballav, A. Terfort, M. Zharnikov *The Journal of Physical Chemistry C* **5, 2009**, *113*, 3697, DOI: 10.1021/jp808303z.

(16) K. Heister, L. S. Johansson, M. Grunze, M. Zharnikov *Surface Science* **2003**, *529*, 36, DOI: 10.1016/S0039-6028(03)00299-1.

(17) D. M. Alloway, M. Hofmann, D. L. Smith, N. E. Gruhn, A. L. Graham, R. Colorado, V. H. Wysocki, T. R. Lee, P. A. Lee, N. R. Armstrong *The Journal of Physical Chemistry B* **2003**, *107*, 11690.

(18) F. Li, L. Tang, W. Zhou, Q. Guo *Physical Chemistry Chemical Physics* **2011**, *13*, 11958, DOI: 10.1039/c1cp00037c.

(19) N. Ballav, B. Schüpbach, O. Dethloff, P. Feulner, A. Terfort, M. Zharnikov *Journal of the American Chemical Society* **2007**, *129*, 15416, DOI: 10.1021/ja0751882.

(20) K. Heister, H.-T. Rong, M. Buck, M. Zharnikov, M. Grunze, L. S. O. Johansson *The Journal of Physical Chemistry B* **2001**, *105*, 6888, DOI: 10.1021/jp010180e.

(21) A. Kovalchuk, T. Abu-Husein, D. Fracasso, D. A. Egger, E. Zojer, M. Zharnikov, A. Terfort, R. C. Chiechi *Chem. Sci.* **2016**, DOI: 10.1039/C5SC03097H.

(22) B. Kretz, D. A. Egger, E. Zojer *Advanced Science* **2015**, *2*, 1400016, DOI: 10.1002/advs.201400016.

(23) F. Rissner, D. A. Egger, L. Romaner, G. Heimel, E. Zojer *ACS Nano* **23, 2010**, *4*, 6735, DOI: 10.1021/nn102360d.

(24) J. Kim, Y. S. Rim, Y. Liu, A. C. Serino, J. C. Thomas, H. Chen, Y. Yang, P. S. Weiss *Nano Letters* **14, 2014**, *14*, 2946, DOI: 10.1021/nl501081q.

(25) O. M. Cabarcos, A. Shaporenko, T. Weidner, S. Uppili, L. S. Dake, M. Zharnikov, D. L. Allara *The Journal of Physical Chemistry C* **2008**, *112*, 10842, DOI: 10.1021/jp801618j.

(26) T. Abu-Husein, S. Schuster, D. A. Egger, M. Kind, T. Santowski, A. Wiesner, R. Chiechi, E. Zojer, A. Terfort, M. Zharnikov *Advanced Functional Materials* **2015**, *25*, 3943, DOI: 10.1002/adfm.201500899.

(27) B. H. Hamadani, D. A. Corley, J. W. Ciszek, J. M. Tour, D. Natelson *Nano Letters* **2006**, *6*, 1303, DOI: 10.1021/nl060731i.

(28) G. Heimel, L. Romaner, J.-L. Brédas, E. Zojer *Physical Review Letters* **2006**, *96*, 196806, DOI: 10.1103/PhysRevLett.96.196806.

(29) E. Biemmi, C. Scherb, T. Bein *Journal of the American Chemical Society* **2007**, *129*, 8054, DOI: 10.1021/ja0701208.

(30) J. Aizenberg, A. J. Black, G. M. Whitesides *Journal of the American Chemical Society* **1999**, *121*, 4500, DOI: 10.1021/ja984254k.

(31) C. D. Tidwell, S. I. Ertel, B. D. Ratner, B. J. Tarasevich, S. Atre, D. L. Allara *Langmuir* **1997**, *13*, 3404, DOI: 10.1021/la9604341.

(32) J. P. Folkers, P. E. Laibinis, G. M. Whitesides *Langmuir* **1992**, *8*, 1330, DOI: 10.1021/la00041a015.

(33) B. T. Houseman, E. S. Gawalt, M. Mrksich *Langmuir* **2003**, *19*, 1522, DOI: 10.1021/la0262304.

(34) A. Kumar, H. A. Biebuyck, G. M. Whitesides *Langmuir* **1994**, *10*, 1498, DOI: 10.1021/la00017a030.

(35) K. Prime, G. Whitesides *Science* **24, 1991**, *252*, 1164, DOI: 10.1126/science.252.5009.1164.

(36) C. E. D. Chidsey, D. N. Loiacono *Langmuir* **1990**, *6*, 682, DOI: 10.1021/la00093a026.

(37) G. M. Whitesides, P. E. Laibinis *Langmuir* **1990**, *6*, 87, DOI: 10.1021/la00091a013.

(38) J. B. Schlenoff, M. Li, H. Ly *Journal of the American Chemical Society* **1995**, *117*, 12528, DOI: 10.1021/ja00155a016.

(39) Y. Xia, X.-M. Zhao, G. M. Whitesides *Microelectronic Engineering* **1996**, *32*, 255, DOI: 10.1016/0167-9317(95)00174-3.

(40) O. Azzaroni, M. Cipollone, M. E. Vela, R. C. Salvarezza *Langmuir* **2001**, *17*, 1483, DOI: 10.1021/la000852c.

(41) J. L. Tan, J. Tien, C. S. Chen *Langmuir* **2002**, *18*, 519.

(42) S. Tosatti, R. Michel, M. Textor, N. D. Spencer *Langmuir* **2002**, *18*, 3537, DOI: 10.1021/la011459p.

(43) M. Mrksich, J. R. Grunwell, G. M. Whitesides *Journal of the American Chemical Society* **1995**, *117*, 12009, DOI: 10.1021/ja00153a029.

(44) E. Ostuni, B. A. Grzybowski, M. Mrksich, C. S. Roberts, G. M. Whitesides *Langmuir* **2003**, *19*, 1861, DOI: 10.1021/la020649c.

(45) F. Frederix, K. Bonroy, W. Laureyn, G. Reekmans, A. Campitelli, W. Dehaen, G. Maes *Langmuir* **2003**, *19*, 4351, DOI: 10.1021/la026908f.

(46) S. J. Metallo, R. S. Kane, R. E. Holmlin, G. M. Whitesides *Journal of the American Chemical Society* **2003**, *125*, 4534, DOI: 10.1021/ja030045a.

(47) G. Ashkenasy, D. Cahen, R. Cohen, A. Shanzer, A. Vilan *Accounts of Chemical Research* **2002**, *35*, 121, DOI: 10.1021/ar990047t.

(48) D. G. Wu, D. Cahen, P. Graf, R. Naaman, A. Nitzan, D. Shvarts *Chemistry-A European Journal* **2001**, *7*, 1743.

(49) H. Sugimura, T. Hanji, K. Hayashi, O. Takai *Advanced Materials* **2002**, *14*, 524.

(50) S. Krämer, R. R. Fuierer, C. B. Gorman *Chemical Reviews* **2003**, *103*, 4367, DOI: 10.1021/cr020704m.

(51) N. Ballav, H. Thomas, T. Winkler, A. Terfort, M. Zharnikov *Angewandte Chemie International Edition* **27, 2009**, *48*, 5833, DOI: 10.1002/anie.200900950.

(52) U. Drechsler, B. Erdogan, V. M. Rotello *Chemistry - A European Journal* **19, 2004**, *10*, 5570, DOI: 10.1002/chem.200306076.

(53) X. Crispin *Solar Energy Materials and Solar Cells* **2004**, *83*, 147, DOI: 10.1016/j.solmat.2004.02.022.

(54) H.-L. Yip, S. K. Hau, N. S. Baek, H. Ma, A. K.-Y. Jen *Advanced Materials* **18, 2008**, *20*, 2376, DOI: 10.1002/adma.200703050.

(55) S. K. Hau, H.-L. Yip, H. Ma, A. K.-Y. Jen *Applied Physics Letters* **2008**, *93*, 233304, DOI: 10.1063/1.3028094.

(56) M. Campoy-Quiles, T. Ferenczi, T. Agostinelli, P. G. Etchegoin, Y. Kim, T. D. Anthopoulos, P. N. Stavrinou, D. D. C. Bradley, J. Nelson *Nature Materials* **2008**, *7*, 158, DOI: 10.1038/nmat2102.

(57) H. Bedis *Journal of Surface Engineered Materials and Advanced Technology* **2011**, *01*, 42, DOI: 10.4236/jsemat.2011.12007.

(58) M. Halik, H. Klauk, U. Zschieschang, G. Schmid, C. Dehm, M. Schütz, S. Maisch, F. Effenberger, M. Brunnbauer, F. Stellacci *Nature* **21, 2004**, *431*, 963, DOI: 10.1038/nature02987.

(59) H. Klauk, U. Zschieschang, J. Pflaum, M. Halik *Nature* **15, 2007**, *445*, 745, DOI: 10.1038/nature05533.

(60) E. C. P. Smits, S. G. J. Mathijssen, P. A. van Hal, S. Setayesh, T. C. T. Geuns, K. A. H. A. Mutsaers, E. Cantatore, H. J. Wondergem, O. Werzer, R. Resel, M. Kemerink, S. Kirchmeyer, A. M. Muzafarov, S. A. Ponomarenko, B. de Boer, P. W. M. Blom, D. M. de Leeuw *Nature* **16, 2008**, *455*, 956, DOI: 10.1038/nature07320.

(61) I. H. Campbell, S. Rubin, T. A. Zawodzinski, J. D. Kress, R. L. Martin, D. L. Smith, N. N. Barashkov, J. P. Ferraris *Physical Review B* **15, 1996**, *54*, R14321, DOI: 10.1103/PhysRevB.54.R14321.

(62) I. H. Campbell, J. D. Kress, R. L. Martin, D. L. Smith, N. N. Barashkov, J. P. Ferraris *Applied Physics Letters* **1997**, *71*, 3528, DOI: 10.1063/1.120381.

(63) S. Kobayashi, T. Nishikawa, T. Takenobu, S. Mori, T. Shimoda, T. Mitani, H. Shimotani, N. Yoshimoto, S. Ogawa, Y. Iwasa *Nature Materials* **2004**, *3*, 317, DOI: 10.1038/nmat1105.

(64) C. Bock, D. V. Pham, U. Kunze, D. Käfer, G. Witte, C. Wöll *Journal of Applied Physics* **2006**, *100*, 114517, DOI: 10.1063/1.2400507.

(65) K. Asadi, Y. Wu, F. Gholamrezaie, P. Rudolf, P. W. M. Blom *Advanced Materials* **6, 2009**, *21*, 4109, DOI: 10.1002/adma.200803455.

(66) M. Salinas, C. M. Jäger, A. Y. Amin, P. O. Dral, T. Meyer-Friedrichsen, A. Hirsch, T. Clark, M. Halik *Journal of the American Chemical Society* **2012**, *134*, 12648, DOI: 10.1021/ja303807u.

(67) C. D. Zangmeister, S. W. Robey, R. D. van Zee, Y. Yao, J. M. Tour *The Journal of Physical Chemistry B* **2004**, *108*, 16187, DOI: 10.1021/jp048134c.

(68) C. D. Zangmeister, L. B. Picraux, R. D. van Zee, Y. Yao, J. M. Tour *Chemical Physics Letters* **2007**, *442*, 390, DOI: 10.1016/j.cplett.2007.06.012.

(69) G. Heimel, L. Romaner, E. Zojer, J.-L. Brédas *Nano Letters* **2007**, *7*, 932, DOI: 10.1021/nl0629106.

(70) K. Demirkan, A. Mathew, C. Weiland, Y. Yao, A. M. Rawlett, J. M. Tour, R. L. Opila *The Journal of Chemical Physics* **2008**, *128*, 074705, DOI: 10.1063/1.2832306.

(71) G. Heimel, L. Romaner, E. Zojer, J.-L. Bredas *Accounts of Chemical Research* **2008**, *41*, 721, DOI: 10.1021/ar700284q.

(72) B. de Boer, A. Hadipour, M. M. Mandoc, T. van Woudenbergh, P. W. M. Blom *Advanced Materials* **8, 2005**, *17*, 621, DOI: 10.1002/adma.200401216.

(73) V. De Renzi, R. Rousseau, D. Marchetto, R. Biagi, S. Scandolo, U. del Pennino *Physical Review Letters* **22, 2005**, *95*, DOI: 10.1103/PhysRevLett.95.046804.

(74) I. Lange, S. Reiter, M. Pätzel, A. Zykov, A. Nefedov, J. Hildebrandt, S. Hecht, S. Kowarik, C. Wöll, G. Heimel, D. Neher *Advanced Functional Materials* **2014**, *24*, 7014, DOI: 10.1002/adfm.201401493.

(75) P. Fenter, P. Eisenberger, J. Li, N. Camillone, S. Bernasek, G. Scoles, T. A. Ramanarayanan, K. S. Liang *Langmuir* **1991**, *7*, 2013, DOI: 10.1021/la00058a008.

(76) A. Ulman, *An introduction to ultrathin organic films: from Langmuir-Blodgett to self-assembly*; Academic Press: Boston, 1991.

(77) J. Stettner, P. Frank, T. Griesser, G. Trimmel, R. Schennach, E. Gilli, A. Winkler *Langmuir* **3, 2009**, *25*, 1427, DOI: 10.1021/la802534q.

(78) J. Stettner, A. Winkler *Langmuir* **15, 2010**, *26*, 9659, DOI: 10.1021/la100245a.

(79) F. Schreiber, A. Eberhardt, T. Y. B. Leung, P. Schwartz, S. M. Wetterer, D. J. Lavrich, L. Berman, P. Fenter, P. Eisenberger, G. Scoles *Physical Review B* **15, 1998**, *57*, 12476, DOI: 10.1103/PhysRevB.57.12476.

(80) A. Eberhardt, P. Fenter, P. Eisenberger *Surface Science* **1998**, *397*, L285, DOI: 10.1016/S0039-6028(97)00873-X.

(81) P. Schwartz, F. Schreiber, P. Eisenberger, G. Scoles *Surface Science* **1999**, *423*, 208, DOI: 10.1016/S0039-6028(98)00907-8.

(82) H. Kondoh, C. Kodama, H. Sumida, H. Nozoye *The Journal of Chemical Physics* **1999**, *111*, 1175, DOI: 10.1063/1.479302.

(83) J. Zasadzinski, R. Viswanathan, L. Madsen, J. Garnaes, D. Schwartz *Science* **25, 1994**, *263*, 1726, DOI: 10.1126/science.8134836.

(84) I. R. Peterson *Journal of Physics D: Applied Physics* **14, 1990**, *23*, 379, DOI: 10.1088/0022-3727/23/4/001.

(85) T. Baumgart, A. Offenhäusser *Langmuir* **2003**, *19*, 1730, DOI: 10.1021/la0261489.

(86) A. Bhaumik, M. Ramakanth, L. K. Brar, A. K. Raychaudhuri, F. Rondelez, D. Chatterji *Langmuir* **2004**, *20*, 5891, DOI: 10.1021/la049400g.

(87) F. Schreiber *Progress in Surface Science* **2000**, *65*, 151, DOI: 10.1016/S0079-6816(00)00024-1.

(88) *Self-assembled monolayers of thiols*; Ulman, A., Ed.; Thin films 24; Acad. Press: San Diego, 1998.

(89) H. Lüth, *Surfaces and interfaces of solids*, 1993.

(90) G. Yang, G.-y. Liu *The Journal of Physical Chemistry B* **2003**, *107*, 8746, DOI: 10.1021/jp0219810.

(91) G. E. Poirier *Chemical Reviews* **1997**, *97*, 1117, DOI: 10.1021/cr960074m.

(92) J. D. E. McIntyre, D. E. Aspnes *Surface Science* **1971**, *24*, 417.

(93) A. Navarro-Quezada, M. Aiglinger, E. Ghanbari, T. Wagner, P. Zeppenfeld *Review of Scientific Instruments* **2015**, *86*, 113108, DOI: 10.1063/1.4936352.

(94) D. E. Aspnes, A. A. Studna *Physical Review Letters* **29, 1985**, *54*, 1956, DOI: 10.1103/PhysRevLett.54.1956.

(95) J. Feng, A. Scholl In *Science of Microscopy*, Hawkes, P. W., Spence, J. C. H., Eds.; Springer New York: New York, NY, 2007, 657.

(96) T. Wagner, E. Ghanbari, D. Huber, P. Zeppenfeld *Ultramicroscopy* **2015**, *159*, 464, DOI: 10.1016/j.ultramic.2015.06.013.

(97) E. Bauer In *Nanosources and Manipulation of Atoms Under High Fields and Temperatures: Applications*, Binh, V. T., Garcia, N., Dransfeld, K., Eds.; Springer Netherlands: Dordrecht, 1993, 13.

(98) E. Bauer *Reports on Progress in Physics* **1, 1994**, *57*, 895, DOI: 10.1088/0034-4885/57/9/002.

(99) J. Zegenhagen *Surface Science Reports* **1993**, *18*, 202, DOI: 10.1016/0167-5729(93)90025-K.

(100) H. Rieley, G. K. Kendall, R. G. Jones, D. P. Woodruff *Langmuir* **1999**, *15*, 8856, DOI: 10.1021/la9904253.

(101) R. G. Nuzzo, L. H. Dubois, D. L. Allara *Journal of the American Chemical Society* **1990**, *112*, 558.

(102) A. N. Parikh, D. L. Allara *The Journal of Chemical Physics* **1992**, *96*, 927, DOI: 10.1063/1.462847.

(103) J. Stöhr, *NEXAFS Spectroscopy*; Springer Berlin Heidelberg: Berlin, Heidelberg, 1992.

(104) M. Zharnikov, S. Frey, H. Rong, Y.-J. Yang, K. Heister, M. Buck, M. Grunze *Physical Chemistry Chemical Physics* **2000**, *2*, 3359, DOI: 10.1039/b004232n.

(105) D. Wegkamp, M. Meyer, C. Richter, M. Wolf, J. Stähler *Applied Physics Letters* **2013**, *103*, 151603, DOI: 10.1063/1.4823591.

(106) N. Koch, A. Kahn, J. Ghijsen, J.-J. Pireaux, J. Schwartz, R. L. Johnson, A. Elschner *Applied Physics Letters* **2003**, *82*, 70, DOI: 10.1063/1.1532102.

(107) J. Kim, B. Lägel, E. Moons, N. Johansson, I. Baikie, W. Salaneck, R. Friend, F. Cacialli *Synthetic Metals* **2000**, *111-112*, 311, DOI: 10.1016/S0379-6779(99)00354-9.

(108) J.-P. Hong, A.-Y. Park, S. Lee, J. Kang, N. Shin, D. Y. Yoon *Applied Physics Letters* **2008**, *92*, 143311, DOI: 10.1063/1.2907691.

(109) T. Nagahiro, H. Akiyama, M. Hara, K. Tamada *Journal of Electron Spectroscopy and Related Phenomena* **2009**, *172*, 128, DOI: 10.1016/j.elspec.2009.02.009.

(110) M. Zharnikov *Journal of Electron Spectroscopy and Related Phenomena* **2010**, *178-179*, 380, DOI: 10.1016/j.elspec.2009.05.008.

(111) K. Oura, M. Katayama, A. V. Zotov, V. G. Lifshits, A. A. Saranin, *Surface Science an Introduction*; Springer Berlin Heidelberg: Berlin, Heidelberg, 2003.

(112) N. D. Lang, W. Kohn *Physical Review B* **15, 1971**, *3*, 1215, DOI: 10.1103/PhysRevB.3.1215.

(113) N. D. Lang, W. Kohn *Physical Review B* **15, 1970**, *1*, 4555, DOI: 10.1103/PhysRevB.1.4555.

(114) H. Ishii, K. Sugiyama, E. Ito, K. Seki *Advanced Materials* **1999**, *11*, 605, DOI: 10.1002/(SICI)1521-4095(199906)11:8<605::AID-ADMA605>3.0.CO;2-Q.

(115) D. Cahen, A. Kahn *Advanced Materials* **17, 2003**, *15*, 271, DOI: 10.1002/adma.200390065.

(116) S. Hüfner, *Photoelectron Spectroscopy Principles and Applications*; Springer Berlin Heidelberg: Berlin, Heidelberg, 2003.

(117) R. Strayer, W. Mackie, L. Swanson *Surface Science* **1973**, *34*, 225, DOI: 10.1016/0039-6028(73)90117-9.

(118) M. Helander, M. Greiner, Z. Wang, Z. Lu *Applied Surface Science* **2010**, *256*, 2602, DOI: 10.1016/j.apsusc.2009.11.002.

(119) G. Heimel, F. Rissner, E. Zojer *Advanced Materials* **22, 2010**, *22*, 2494, DOI: 10.1002/adma.200903855.

(120) Z. Vager, R. Naaman *Chemical Physics* **2002**, *281*, 305, DOI: 10.1016/S0301-0104(02)00374-9.

(121) D. Cahen, R. Naaman, Z. Vager *Advanced Functional Materials* **2005**, *15*, 1571, DOI: 10.1002/adfm.200500187.

(122) A. Natan, L. Kronik, H. Haick, R. T. Tung *Advanced Materials* **3, 2007**, *19*, 4103, DOI: 10.1002/adma.200701681.

(123) O. L. A. Monti *The Journal of Physical Chemistry Letters* **6, 2012**, *3*, 2342, DOI: 10.1021/jz300850x.

(124) L. Romaner, G. Heimel, C. Ambrosch-Draxl, E. Zojer *Advanced Functional Materials* **22, 2008**, *18*, 3999, DOI: 10.1002/adfm.200800876.

(125) N. Koch *physica status solidi (RRL) - Rapid Research Letters* **2012**, *6*, 277, DOI: 10.1002/pssr.201206208.

(126) H. Fukagawa, H. Yamane, S. Kera, K. K. Okudaira, N. Ueno *Physical Review B* **4, 2006**, *73*, DOI: 10.1103/PhysRevB.73.041302.

(127) A. Natan, N. Kuritz, L. Kronik *Advanced Functional Materials* **25, 2010**, *20*, 2077, DOI: 10.1002/adfm.200902162.

(128) H. Weiler-Feilchenfeld, E. Bergmann *Israel Journal of Chemistry* **1968**, *6*, 823, DOI: 10.1002/ijch.196800101.

(129) G. Blackman, R. Brown, F. Burden *Journal of Molecular Spectroscopy* **1970**, *35*, 444, DOI: 10.1016/0022-2852(70)90185-2.

(130) D. W. Heermann, *Computer Simulation Methods in Theoretical Physics*; Springer Berlin Heidelberg: Berlin, Heidelberg, 1990.

(131) D. Frenkel, B. Smit, *Understanding molecular simulation: from algorithms to applications*, 2nd ed; Computational science series 1; Academic Press: San Diego, 2002.

(132) D. C. Rapaport, *The art of molecular dynamics simulation*, 2nd ed; Cambridge University Press: Cambridge, UK ; New York, NY, 2004.

(133) M. Griebel, S. Knapek, G. W. Zumbusch, *Numerical simulation in molecular dynamics: numerics, algorithms, parallelization, applications*; Texts in computational science and engineering 5; Springer: Berlin, 2007.

(134) A. D. Mackerell *Journal of Computational Chemistry* **2004**, *25*, 1584, DOI: 10.1002/jcc.20082.

(135) K. Vanommeslaeghe, A. MacKerell *Biochimica et Biophysica Acta (BBA) - General Subjects* **2014**, DOI: 10.1016/j.bbagen.2014.08.004.

(136) M. Levitt *Journal of Molecular Biology* **1983**, *170*, 723, DOI: 10.1016/S0022-2836(83)80129-6.

(137) M. Karplus, J. A. McCammon *Nature Structural Biology* **2002**, *9*, 646, DOI: 10.1038/nsb0902-646.

(138) J. L. Klepeis, K. Lindorff-Larsen, R. O. Dror, D. E. Shaw *Current Opinion in Structural Biology* **2009**, *19*, 120, DOI: 10.1016/j.sbi.2009.03.004.

(139) E. Lindahl, O. Edholm *Biophysical Journal* **2000**, *79*, 426, DOI: 10.1016/S0006-3495(00)76304-1.

(140) M. Patra, M. Karttunen, M. Hyvönen, E. Falck, P. Lindqvist, I. Vattulainen *Biophysical Journal* **2003**, *84*, 3636, DOI: 10.1016/S0006-3495(03)75094-2.

(141) J. Y. Xie, G. H. Ding, M. Karttunen *Biochimica et Biophysica Acta (BBA) - Biomembranes* **2014**, *1838*, 994, DOI: 10.1016/j.bbamem.2013.12.011.

(142) *The Structure of biological membranes*, 2nd ed; Yeagle, P., Ed.; CRC Press: Boca Raton, Fla, 2005.

(143) *Computational modeling of membrane bilayers*; Feller, S. E., Ed.; Current topics in membranes 60; Elsevier, Academic Press: Amsterdam, 2008.

(144) M. Tarek *Biophysical Journal* **2005**, *88*, 4045, DOI: 10.1529/biophysj.104.050617.

(145) Y. Andoh, S. Okazaki, R. Ueoka *Biochimica et Biophysica Acta (BBA) - Biomembranes* **2013**, *1828*, 1259, DOI: 10.1016/j.bbamem.2013.01.005.

(146) S. Bernèche, B. Roux *Biophysical Journal* **2000**, *78*, 2900, DOI: 10.1016/S0006-3495(00)76831-7.

(147) I. H. Shrivastava, M. S. Sansom *Biophysical Journal* **2000**, *78*, 557, DOI: 10.1016/S0006-3495(00)76616-1.

(148) W. Im, B. Roux *Journal of Molecular Biology* **2002**, *319*, 1177, DOI: 10.1016/S0022-2836(02)00380-7.

(149) P. L. Freddolino, A. S. Arkhipov, S. B. Larson, A. McPherson, K. Schulten *Structure* **2006**, *14*, 437, DOI: 10.1016/j.str.2005.11.014.

(150) H. Ode, M. Nakashima, S. Kitamura, W. Sugiura, H. Sato *Frontiers in Microbiology* **2012**, *3*, DOI: 10.3389/fmicb.2012.00258.

(151) D. S. D. Larsson, L. Liljas, D. van der Spoel *PLoS Computational Biology* **10, 2012**, *8*, ed. by M. Nilges, e1002502, DOI: 10.1371/journal.pcbi.1002502.

(152) C. A. Laughton, S. A. Harris *Wiley Interdisciplinary Reviews: Computational Molecular Science* **2011**, *1*, 590, DOI: 10.1002/wcms.46.

(153) T. E. Cheatham, D. A. Case *Biopolymers* **2013**, 969, DOI: 10.1002/bip.22331.

(154) N. A. Macleod, P. Butz, J. P. Simons, G. H. Grant, C. M. Baker, G. E. Tranter *Israel Journal of Chemistry* **2004**, *44*, 27, DOI: 10.1560/LM77-UMAV-80EF-VYWC.

(155) C. M. Baker, G. H. Grant *Chemical Communications* **2006**, 1387, DOI: 10.1039/b517868a.

(156) C. M. Baker, G. H. Grant *The Journal of Physical Chemistry B* **2007**, *111*, 9940, DOI: 10.1021/jp071059w.

(157) D. W. Borhani, D. E. Shaw *Journal of Computer-Aided Molecular Design* **2012**, *26*, 15, DOI: 10.1007/s10822-011-9517-y.

(158) A. T. Brünger, J. Kuriyan, M. Karplus *Science* **23, 1987**, *235*, 458, DOI: 10.1126/science.235.4787.458.

(159) N. C. Miller, E. Cho, M. J. N. Junk, R. Gysel, C. Risko, D. Kim, S. Sweetnam, C. E. Miller, L. J. Richter, R. J. Kline, M. Heeney, I. McCulloch, A. Amassian, D. Acevedo-Feliz, C. Knox, M. R. Hansen, D. Dudenko, B. F. Chmelka, M. F. Toney, J.-L. Brédas, M. D. McGehee *Advanced Materials* **27, 2012**, *24*, 6071, DOI: 10.1002/adma.201202293.

(160) L. Chen, J. P. S. Mowat, D. Fairen-Jimenez, C. A. Morrison, S. P. Thompson, P. A. Wright, T. Düren *Journal of the American Chemical Society* **23, 2013**, *135*, 15763, DOI: 10.1021/ja403453g.

(161) E. Egberts, H. J. C. Berendsen *The Journal of Chemical Physics* **1988**, *89*, 3718, DOI: 10.1063/1.454893.

(162) R. Busselez, C. V. Cerclier, M. Ndao, A. Ghoufi, R. Lefort, D. Morineau *The Journal of Chemical Physics* **7, 2014**, *141*, 134902, DOI: 10.1063/1.4896052.

(163) J. Hautman, J. P. Bareman, W. Mar, M. L. Klein *Journal of the Chemical Society, Faraday Transactions* **1991**, *87*, 2031, DOI: 10.1039/ft9918702031.

(164) W. Mar, M. L. Klein *Langmuir* **1994**, *10*, 188, DOI: 10.1021/la00013a028.

(165) K. J. Tupper, D. W. Brenner *Thin Solid Films* **1994**, *253*, 185, DOI: 10.1016/0040-6090(94)90317-4.

(166) B. Rai, S. P., C. P. Malhotra, Pradip, K. G. Ayappa *Langmuir* **2004**, *20*, 3138, DOI: 10.1021/la0357256.

(167) P. Ghorai, S. Glotzer *Journal of Physical Chemistry C* **1, 2007**, *111*, 15857, DOI: 10.1021/jp0746289.

(168) V. Vasumathi, M. N. D. Cordeiro *Chemical Physics Letters* **2014**, *600*, 79, DOI: 10.1016/j.cplett.2014.03.064.

(169) H. Yan, S. Yuan, S. Zeng, M. Niu *Applied Surface Science* **2015**, *349*, 163, DOI: 10.1016/j.apsusc.2015.04.211.

(170) L. Verlet *Physical Review* **5, 1967**, *159*, 98, DOI: 10.1103/PhysRev.159.98.

(171) S. Plimpton *Journal of Computational Physics* **1995**, *117*, 1, DOI: 10.1006/jcph.1995.1039.

(172) J.-P. Ryckaert, G. Ciccotti, H. J. Berendsen *Journal of Computational Physics* **1977**, *23*, 327, DOI: 10.1016/0021-9991(77)90098-5.

(173) J. R. Ray *Computer Physics Reports* **1988**, *8*, 109, DOI: 10.1016/0167-7977(88)90009-3.

(174) H. J. C. Berendsen, J. P. M. Postma, W. F. van Gunsteren, A. DiNola, J. R. Haak *The Journal of Chemical Physics* **1984**, *81*, 3684, DOI: 10.1063/1.448118.

(175) S. Nosé *The Journal of Chemical Physics* **1984**, *81*, 511, DOI: 10.1063/1.447334.

(176) W. G. Hoover *Physical Review A* **1, 1985**, *31*, 1695, DOI: 10.1103/PhysRevA.31.1695.

(177) H. C. Andersen *The Journal of Chemical Physics* **1980**, *72*, 2384, DOI: 10.1063/1.439486.

(178) M. Parrinello, A. Rahman *Physical Review Letters* **6, 1980**, *45*, 1196, DOI: 10.1103/PhysRevLett.45.1196.

(179) L. Monticelli, D. P. Tieleman In *Biomolecular Simulations*, Monticelli, L., Salonen, E., Eds.; Humana Press: Totowa, NJ, 2013; Vol. 924, 197.

(180) P. E. M. Lopes, O. Guvench, A. D. MacKerell In *Molecular Modeling of Proteins*, Kukol, A., Ed.; Springer New York: New York, NY, 2015, 47.

(181) C. M. Baker *Wiley Interdisciplinary Reviews: Computational Molecular Science* **2015**, *5*, 241, DOI: 10.1002/wcms.1215.

(182) N. L. Allinger *Journal of the American Chemical Society* **1977**, *99*, 8127, DOI: 10.1021/ja00467a001.

(183) N. L. Allinger, Y. H. Yuh, J. H. Lii *Journal of the American Chemical Society* **1989**, *111*, 8551, DOI: 10.1021/ja00205a001.

(184) J. H. Lii, N. L. Allinger *Journal of the American Chemical Society* **1989**, *111*, 8566, DOI: 10.1021/ja00205a002.

(185) J. H. Lii, N. L. Allinger *Journal of the American Chemical Society* **1989**, *111*, 8576, DOI: 10.1021/ja00205a003.

(186) N. L. Allinger, K.-H. Chen, J.-H. Lii, K. A. Durkin *Journal of Computational Chemistry* **2003**, *24*, 1447, DOI: 10.1002/jcc.10268.

(187) M. J. Hwang, T. P. Stockfisch, A. T. Hagler *Journal of the American Chemical Society* **1994**, *116*, 2515, DOI: 10.1021/ja00085a036.

(188) T. A. Halgren *Journal of Computational Chemistry* **1996**, *17*, 490, DOI: 10.1002/(SICI)1096-987X(199604)17:5/6<490::AID-JCC1>3.0.CO;2-P.

(189) J.-H. Lii, N. L. Allinger *Journal of Computational Chemistry* **1991**, *12*, 186, DOI: 10.1002/jcc.540120208.

(190) P. Derreumaux, G. Vergoten *The Journal of Chemical Physics* **1995**, *102*, 8586, DOI: 10.1063/1.468848.

(191) H. Sun *The Journal of Physical Chemistry B* **1998**, *102*, 7338, DOI: 10.1021/jp980939v.

(192) C. S. Ewig, R. Berry, U. Dinur, J.-R. Hill, M.-J. Hwang, H. Li, C. Liang, J. Maple, Z. Peng, T. P. Stockfisch, T. S. Thacher, L. Yan, X. Ni, A. T. Hagler *Journal of Computational Chemistry* **30, 2001**, *22*, 1782, DOI: 10.1002/jcc.1131.

(193) K. Palmo, B. Mannfors, N. G. Mirkin, S. Krimm *Biopolymers* **2003**, *68*, 383, DOI: 10.1002/bip.10254.

(194) K. Vanommeslaeghe, E. Hatcher, C. Acharya, S. Kundu, S. Zhong, J. Shim, E. Darian, O. Guvench, P. Lopes, I. Vorobyov, A. D. Mackerell *Journal of Computational Chemistry* **2009**, 671, DOI: 10.1002/jcc.21367.

(195) R. B. Best, X. Zhu, J. Shim, P. E. M. Lopes, J. Mittal, M. Feig, A. D. MacKerell *Journal of Chemical Theory and Computation* **11, 2012**, *8*, 3257, DOI: 10.1021/ct300400x.

(196) E. J. Denning, U. D. Priyakumar, L. Nilsson, A. D. Mackerell *Journal of Computational Chemistry* **15, 2011**, *32*, 1929, DOI: 10.1002/jcc.21777.

(197) K. Hart, N. Foloppe, C. M. Baker, E. J. Denning, L. Nilsson, A. D. MacKerell *Journal of Chemical Theory and Computation* **10, 2012**, *8*, 348, DOI: 10.1021/ct200723y.

(198) J. B. Klauda, R. M. Venable, J. A. Freites, J. W. O'Connor, D. J. Tobias, C. Mondragon-Ramirez, I. Vorobyov, A. D. MacKerell, R. W. Pastor *The Journal of Physical Chemistry B* **17, 2010**, *114*, 7830, DOI: 10.1021/jp101759q.

(199) P. M. Morse *Physical Review* **1, 1929**, *34*, 57, DOI: 10.1103/PhysRev.34.57.

(200) F. Jensen, *Introduction to computational chemistry*, 2nd ed; John Wiley & Sons: Chichester, England, 2007.

(201) F. London *Zeitschrift für Physik* **1930**, *63*, 245, DOI: 10.1007/BF01421741.

(202) R. Eisenschitz, F. London *Zeitschrift für Physik* **1930**, *60*, 491, DOI: 10.1007/BF01341258.

(203) F. London *Transactions of the Faraday Society* **1937**, *33*, 8b, DOI: 10.1039/TF937330008B.

(204) A. J. Stone, *The theory of intermolecular forces*; International series of monographs on chemistry 32; Clarendon Press ; Oxford University Press: Oxford : Oxford ; New York, 1996.

(205) A. D. Buckingham *Canadian Journal of Chemistry* **1960**, *38*, 300, DOI: 10.1139/v60-040.

(206) R. W. Hockney, J. W. Eastwood, *Computer simulation using particles*; McGraw-Hill International Book Co: New York, 1981.

(207) J. Eastwood, R. Hockney, D. Lawrence *Computer Physics Communications* **1980**, *19*, 215, DOI: 10.1016/0010-4655(80)90052-1.

(208) U. C. Singh, P. A. Kollman *Journal of Computational Chemistry* **1984**, *5*, 129, DOI: 10.1002/jcc.540050204.

(209) B. H. Besler, K. M. Merz, P. A. Kollman *Journal of Computational Chemistry* **1990**, *11*, 431, DOI: 10.1002/jcc.540110404.

(210) M. J. Frisch, G. W. Trucks, H. B. Schlegel, G. E. Scuseria, M. A. Robb, J. R. Cheeseman, G. Scalmani, V. Barone, B. Mennucci, G. A. Petersson, H. Nakatsuji, M. Caricato, X. Li, H. P. Hratchian, A. F. Izmaylov, J. Bloino, G. Zheng, J. L. Sonnenberg, M. Hada, M. Ehara, K. Toyota, R. Fukuda, J. Hasegawa, M. Ishida, T. Nakajima, Y. Honda, O. Kitao, H. Nakai, T. Vreven, J. A. Montgomery Jr., J. E. Peralta, F. Ogliaro, M. Bearpark, J. J. Heyd, E. Brothers, K. N. Kudin, V. N. Staroverov, R. Kobayashi, J. Normand, K. Raghavachari, A. Rendell, J. C. Burant, S. S. Iyengar, J. Tomasi, M. Cossi, N. Rega, J. M. Millam, M. Klene, J. E. Knox, J. B. Cross, V. Bakken, C. Adamo, J. Jaramillo, R. Gomperts, R. E. Stratmann, O. Yazyev, A. J. Austin, R. Cammi, C. Pomelli, J. W. Ochterski, R. L. Martin, K. Morokuma, V. G. Zakrzewski, G. A. Voth, P. Salvador, J. J. Dannenberg, S. Dapprich, A. D. Daniels, Ö. Farkas, J. B. Foresman, J. V. Ortiz, J. Cioslowski, D. J. Fox Gaussian09, Revision A.01., Gaussian Inc. Wallingford CT 2009.

(211) A. D. Becke *The Journal of Chemical Physics* **1993**, *98*, 5648, DOI: 10.1063/1.464913.

(212) W. W. Lee, S.-i. Choi *The Journal of Chemical Physics* **1980**, *72*, 6164, DOI: 10.1063/1.439074.

(213) S. H. Vosko, L. Wilk, M. Nusair *Canadian Journal of physics* **1980**, *58*, 1200.

(214) P. J. Stephens, F. J. Devlin, C. F. Chabalowski, M. J. Frisch *The Journal of Physical Chemistry* **1994**, *98*, 11623, DOI: 10.1021/j100096a001.

(215) T. H. Dunning *The Journal of Chemical Physics* **1989**, *90*, 1007, DOI: 10.1063/1.456153.

(216) R. A. Kendall, T. H. Dunning, R. J. Harrison *The Journal of Chemical Physics* **1992**, *96*, 6796, DOI: 10.1063/1.462569.

(217) E. R. Davidson *Chemical Physics Letters* **1996**, *260*, 514, DOI: 10.1016/0009-2614(96)00917-7.

(218) D. E. Woon, T. H. Dunning *The Journal of Chemical Physics* **1993**, *98*, 1358, DOI: 10.1063/1.464303.

(219) F. Iori, R. Di Felice, E. Molinari, S. Corni *Journal of Computational Chemistry* **15, 2009**, *30*, 1465, DOI: 10.1002/jcc.21165.

(220) S. S. Jang, Y. H. Jang, Y.-H. Kim, W. A. Goddard, A. H. Flood, B. W. Laursen, H.-R. Tseng, J. F. Stoddart, J. O. Jeppesen, J. W. Choi, D. W. Steuerman, E. DeIonno, J. R. Heath *Journal of the American Chemical Society* **2005**, *127*, 1563, DOI: 10.1021/ja044530x.

(221) R. M. Martin, *Electronic structure: basic theory and practical methods*, 1st pbk. ed. with corrections; Cambridge University Press: Cambridge, UK ; New York, 2008.

(222) D. S. Sholl, J. A. Steckel, *Density functional theory a practical introduction*; Wiley: Hoboken, N.J., 2009.

(223) J. P. Perdew, S. Kurth In *A primer in density functional theory*; Springer: 2003, 1.

(224) K. Burke, *The ABC of DFT*; Department of Chemistry, University of California: Irvine, CA 92697, 2007.

(225) K. Burke, L. O. Wagner *International Journal of Quantum Chemistry* **15, 2013**, *113*, 96, DOI: 10.1002/qua.24259.

(226) P. Hohenberg, W. Kohn *Physical Review* **9, 1964**, *136*, B864, DOI: 10.1103/PhysRev.136.B864.

(227) W. Kohn, L. J. Sham *Physical Review* **15, 1965**, *140*, A1133, DOI: 10.1103/PhysRev.140.A1133.

(228) W. Kohn *Reviews of Modern Physics* **1999**, *71*, 1253.

(229) M. Born, R. Oppenheimer *Annalen der Physik* **1927**, *389*, 457, DOI: 10.1002/andp.19273892002.

(230) M. Levy *Proceedings of the National Academy of Sciences* **1979**, *76*, 6062.

(231) M. Levy *Physical Review A* **1, 1982**, *26*, 1200, DOI: 10.1103/PhysRevA.26.1200.

(232) M. Levy, J. P. Perdew In *Density Functional Methods In Physics*, Dreizler, R. M., Providência, J., Eds.; Springer US: Boston, MA, 1985, 11.

(233) E. Lieb In *Physics as Natural Philosophy*, Shimony, A., Feshbach, H., Eds.; MIT Press: Cambridge, 1982.

(234) E. H. Lieb *International Journal of Quantum Chemistry* **1983**, *24*, 243, DOI: 10.1002/qua.560240302.

(235) J. P. Perdew, K. Burke, M. Ernzerhof *Physical Review Letters* **28, 1996**, *77*, 3865, DOI: 10.1103/PhysRevLett.77.3865.

(236) J. P. Perdew, K. Burke, M. Ernzerhof *Physical Review Letters* **17, 1997**, *78*, 1396, DOI: 10.1103/PhysRevLett.78.1396.

(237) L. Kronik, T. Stein, S. Refaely-Abramson, R. Baer *Journal of Chemical Theory and Computation* **8, 2012**, *8*, 1515, DOI: 10.1021/ct2009363.

(238) G. Kresse, J. Hafner *Physical Review B* **1, 1993**, *47*, 558, DOI: 10.1103/PhysRevB.47.558.

(239) G. Kresse, J. Hafner *Physical Review B* **15, 1994**, *49*, 14251, DOI: 10.1103/PhysRevB.49.14251.

(240) G. Kresse, J. Furthmüller *Computational Materials Science* **1996**, *6*, 15, DOI: 10.1016/0927-0256(96)00008-0.

(241) G. Kresse, J. Furthmüller *Physical Review B* **15, 1996**, *54*, 11169, DOI: 10.1103/PhysRevB.54.11169.

(242) P. E. Blöchl *Physical Review B* **15, 1994**, *50*, 17953, DOI: 10.1103/PhysRevB.50.17953.

(243) P. E. Blöchl, J. Kästner, C. J. Först In *Handbook of Materials Modeling*; Springer: 2005, 93.

(244) V. G. Ruiz, W. Liu, E. Zojer, M. Scheffler, A. Tkatchenko *Physical Review Letters* **6, 2012**, *108*, 146103, DOI: 10.1103/PhysRevLett.108.146103.

(245) W. A. Al-Saidi, V. K. Voora, K. D. Jordan *Journal of Chemical Theory and Computation* **10, 2012**, *8*, 1503, DOI: 10.1021/ct200618b.

(246) H. J. Monkhorst, J. D. Pack *Physical Review B* **15, 1976**, *13*, 5188, DOI: 10.1103/PhysRevB.13.5188.

(247) L. Köhler, G. Kresse *Physical Review B* **11, 2004**, *70*, 165405, DOI: 10.1103/PhysRevB.70.165405.

(248) J. L. Cabellos, D. J. Mowbray, E. Goiri, A. El-Sayed, L. Floreano, D. G. de Oteyza, C. Rogero, J. E. Ortega, A. Rubio *The Journal of Physical Chemistry C* **30, 2012**, *116*, 17991, DOI: 10.1021/jp3004213.

(249) W. Olovsson, C. Göransson, T. Marten, I. A. Abrikosov *physica status solidi (b)* **2006**, *243*, 2447, DOI: 10.1002/pssb.200642165.

(250) C. Freysoldt, P. Rinke, M. Scheffler *Physical Review Letters* **31, 2009**, *103*, 056803, DOI: 10.1103/PhysRevLett.103.056803.

(251) A. Biller, I. Tamblyn, J. B. Neaton, L. Kronik *The Journal of Chemical Physics* **2011**, *135*, 164706, DOI: 10.1063/1.3655357.

(252) G. Heimel, L. Romaner, J.-L. Brédas, E. Zojer *Surface Science* **2006**, *600*, 4548, DOI: 10.1016/j.susc.2006.07.023.

(253) E. Pehlke, M. Scheffler *Physical Review Letters* **4, 1993**, *71*, 2338, DOI: 10.1103/PhysRevLett.71.2338.

(254) S. Lizzit, A. Baraldi, A. Groso, K. Reuter, M. V. Ganduglia-Pirovano, C. Stampfl, M. Scheffler, M. Stichler, C. Keller, W. Wurth, D. Menzel *Physical Review B* **3, 2001**, *63*, DOI: 10.1103/PhysRevB.63.205419.

(255) S. García-Gil, A. García, P. Ordejón *The European Physical Journal B* **2012**, *85*, DOI: 10.1140/epjb/e2012-30334-5.

(256) E. J. Baerends, O. V. Gritsenko, R. van Meer *Physical Chemistry Chemical Physics* **2013**, *15*, 16408, DOI: 10.1039/c3cp52547c.

(257) N. Pueyo Bellafont, P. S. Bagus, F. Illas *The Journal of Chemical Physics* **7, 2015**, *142*, 214102, DOI: 10.1063/1.4921823.

(258) N. Pueyo Bellafont, F. Illas, P. S. Bagus *Phys. Chem. Chem. Phys.* **2015**, *17*, 4015, DOI: 10.1039/C4CP05434B.

(259) M. Methfessel, D. Hennig, M. Scheffler *Surface Science* **1993**, *287-288*, 785, DOI: 10.1016/0039-6028(93)91072-W.

(260) C. L. Lamont, J. Wilkes *Langmuir* **1999**, *15*, 2037.

(261) J. D. Jackson, *Classical electrodynamics*, 3rd ed; Wiley: New York, 1999.

(262) J. Neaton, M. Hybertsen, S. Louie *Physical Review Letters* **2006**, *97*, 216405, DOI: 10.1103/PhysRevLett.97.216405.

(263) M. Hestenes, E. Stiefel *Journal of Research of the National Bureau of Standards* **1952**, *49*, 409, DOI: 10.6028/jres.049.044.

(264) K. E. Atkinson, *An introduction to numerical analysis*; Wiley: New York, 1989.

(265) M. J. Hostetler, J. J. Stokes, R. W. Murray *Langmuir* **1996**, *12*, 3604, DOI: 10.1021/la960249n.

(266) R. Bhatia, B. J. Garrison *Langmuir* **1997**, *13*, 765, DOI: 10.1021/la960955o.

(267) T. Bučko, J. Hafner, J. G. Ángyán *The Journal of Chemical Physics* **2005**, *122*, 124508, DOI: 10.1063/1.1864932.

(268) T. H. Fischer, J. Almlof *The Journal of Physical Chemistry* **1992**, *96*, 9768.

(269) T. C. Taucher, I. Hehn, O. T. Hofmann, M. Zharnikov, E. Zojer *The Journal of Physical Chemistry C* **18, 2016**, *120*, 3428, DOI: 10.1021/acs.jpcc.5b12387.

(270) X. J. Feng, L. Jiang *Advanced Materials* **4, 2006**, *18*, 3063, DOI: 10.1002/adma.200501961.

(271) S. L. Gras, T. Mahmud, G. Rosengarten, A. Mitchell, K. Kalantar-zadeh *ChemPhysChem* **8, 2007**, *8*, 2036, DOI: 10.1002/cphc.200700222.

(272) N. Ballav, A. Shaporenko, A. Terfort, M. Zharnikov *Advanced Materials* **6, 2007**, *19*, 998, DOI: 10.1002/adma.200602168.

(273) L. Srisombat, A. C. Jamison, T. R. Lee *Colloids and Surfaces A: Physicochemical and Engineering Aspects* **2011**, *390*, 1, DOI: 10.1016/j.colsurfa.2011.09.020.

(274) J. Landoulsi, K. Cooksey, V. Dupres *Biofouling* **16, 2011**, *27*, 1105, DOI: 10.1080/08927014.2011.629043.

(275) P. M. Mendes *Chemical Society Reviews* **2008**, *37*, 2512, DOI: 10.1039/b714635n.

(276) N. Ballav, S. Schilp, M. Zharnikov *Angewandte Chemie International Edition* **8, 2008**, *47*, 1421, DOI: 10.1002/anie.200704105.

(277) J. Adams, G. Tizazu, S. Janusz, S. R. J. Brueck, G. P. Lopez, G. J. Leggett *Langmuir* **17, 2010**, *26*, 13600, DOI: 10.1021/la101876j.

(278) O. El Zubir, I. Barlow, G. J. Leggett, N. H. Williams *Nanoscale* **2013**, *5*, 11125, DOI: 10.1039/c3nr04701f.

(279) C. Schmidt, A. Witt, G. Witte *The Journal of Physical Chemistry A* **30, 2011**, *115*, 7234, DOI: 10.1021/jp200328r.

(280) N. Crivillers, S. Osella, C. Van Dyck, G. M. Lazzerini, D. Cornil, A. Liscio, F. Di Stasio, S. Mian, O. Fenwick, F. Reinders, M. Neuburger, E. Treossi, M. Mayor, V. Palermo, F. Cacialli, J. Cornil, P. Samorì *Advanced Materials* **18, 2013**, *25*, 432, DOI: 10.1002/adma.201201737.

(281) D. A. Egger, F. Rissner, G. M. Rangger, O. T. Hofmann, L. Wittwer, G. Heimel, E. Zojer *Physical Chemistry Chemical Physics* **2010**, *12*, 4291, DOI: 10.1039/b924238b.

(282) B. D. Ratner, D. G. Castner, *Surface analysis: the principal techniques*; Vickerman, J. C., Ed.; John Wiley: Chichester [England] ; New York, 1997.

(283) H. Ahn, M. Zharnikov, J. E. Whitten *Chemical Physics Letters* **2006**, *428*, 283, DOI: 10.1016/j.cplett.2006.07.053.

(284) Y. Ge, T. Weidner, H. Ahn, J. E. Whitten, M. Zharnikov *The Journal of Physical Chemistry C* **19, 2009**, *113*, 4575, DOI: 10.1021/jp809975x.

(285) N. V. Venkataraman, S. Zürcher, A. Rossi, S. Lee, N. Naujoks, N. D. Spencer *The Journal of Physical Chemistry C* **9, 2009**, *113*, 5620, DOI: 10.1021/jp809156a.

(286) P. S. Bagus, G. Pacchioni, C. Sousa, T. Minerva, F. Parmigiani *Chemical physics letters* **1992**, *196*, 641.

(287) A. Natan, Y. Zidon, Y. Shapira, L. Kronik *Physical Review B* **18, 2006**, *73*, 193310, DOI: 10.1103/PhysRevB.73.193310.

(288) H. Lu, D. Zeysing, M. Kind, A. Terfort, M. Zharnikov *The Journal of Physical Chemistry C* **19, 2013**, *117*, 18967, DOI: 10.1021/jp405475h.

(289) C. A. Alves, M. D. Porter *Langmuir* **1993**, *9*, 3507, DOI: 10.1021/la00036a027.

(290) G.-y. Liu, P. Fenter, C. E. D. Chidsey, D. F. Ogletree, P. Eisenberger, M. Salmeron *The Journal of Chemical Physics* **1994**, *101*, 4301, DOI: 10.1063/1.467479.

(291) K. Tamada, T. Ishida, W. Knoll, H. Fukushima, R. Colorado, M. Graupe, O. E. Shmakova, T. R. Lee *Langmuir* **2001**, *17*, 1913, DOI: 10.1021/la001212c.

(292) K. Tamada, J. Nagasawa, F. Nakanishi, K. Abe, M. Hara, W. Knoll, T. Ishida, H. Fukushima, S. Miyashita, T. Usui, T. Koini, T. R. Lee *Thin Solid Films* **1998**, *327-329*, 150, DOI: 10.1016/S0040-6090(98)00618-X.

(293) C. W. Bunn, E. R. Howells *Nature* **18, 1954**, *174*, 549, DOI: 10.1038/174549a0.

(294) P. Fenter, A. Eberhardt, K. S. Liang, P. Eisenberger *The Journal of Chemical Physics* **1997**, *106*, 1600, DOI: 10.1063/1.473281.

(295) N. Camillone, C. E. D. Chidsey, G.-y. Liu, G. Scoles *The Journal of Chemical Physics* **1993**, *98*, 3503, DOI: 10.1063/1.464071.

(296) G. E. Poirier, M. J. Tarlov *Langmuir* **1994**, *10*, 2853, DOI: 10.1021/la00021a001.

(297) E. Delamarche, B. Michel, C. Gerber, D. Anselmetti, H.-J. Guentherodt, H. Wolf, H. Ringsdorf *Langmuir* **1994**, *10*, 2869, DOI: 10.1021/la00021a006.

(298) J. P. Bucher, L. Santesson, K. Kern *Applied Physics A Solids and Surfaces* **1994**, *59*, 135, DOI: 10.1007/BF00332205.

(299) G. Kresse, D. Joubert *Physical Review B* **15, 1999**, *59*, 1758, DOI: 10.1103/PhysRevB.59.1758.

(300) *CRC handbook of chemistry and physics: a ready-reference book of chemical and physical data*, 93. ed., 2012 - 2013; Haynes, W. M., Lide, D. R., Eds.; CRC Press: Boca Raton, Fla., 2012.

(301) P. Haas, F. Tran, P. Blaha *Physical Review B* **10, 2009**, *79*, DOI: 10.1103/PhysRevB.79.085104.

(302) J. Neugebauer, M. Scheffler *Physical Review B* **15, 1992**, *46*, 16067, DOI: 10.1103/PhysRevB.46.16067.

(303) J. Vackář, M. Hyt'ha, A. Šimůnek *Physical Review B* **15, 1998**, *58*, 12712, DOI: 10.1103/PhysRevB.58.12712.

(304) M. Methfessel, V. Fiorentini, S. Oppo *Physical Review B* **15, 2000**, *61*, 5229, DOI: 10.1103/PhysRevB.61.5229.

(305) Y. Morikawa, T. Hayashi, C. C. Liew, H. Nozoye *Surface science* **2002**, *507*, 46.

(306) V. Blum, R. Gehrke, F. Hanke, P. Havu, V. Havu, X. Ren, K. Reuter, M. Scheffler *Computer Physics Communications* **2009**, *180*, 2175, DOI: 10.1016/j.cpc.2009.06.022.

(307) J. C. Slater, *Quantum Theory of Molecules and Solids. Vol. 4*; McGraw-Hill: New York, 1974.

(308) Y. Li, D. Lu, G. Galli *Journal of Chemical Theory and Computation* **14, 2009**, *5*, 881, DOI: 10.1021/ct800465f.

(309) D. A. Egger, Z.-F. Liu, J. B. Neaton, L. Kronik *Nano Letters* **8, 2015**, *15*, 2448, DOI: 10.1021/nl504863r.

(310) P. S. Bagus, E. S. Ilton, C. J. Nelin *Surface Science Reports* **2013**, *68*, 273, DOI: 10.1016/j.surfrep.2013.03.001.

(311) J. Hwang, E.-G. Kim, J. Liu, J.-L. Brédas, A. Duggal, A. Kahn *The Journal of Physical Chemistry C* **2007**, *111*, 1378, DOI: 10.1021/jp067004w.

(312) C. Lee, W. Yang, R. G. Parr *Physical Review B* **15, 1988**, *37*, 785, DOI: 10.1103/PhysRevB.37.785.

(313) A. Ulman *Chemical reviews* **1996**, *96*, 1533.

(314) L. A. Bumm, J. J. Arnold, T. D. Dunbar, D. L. Allara, P. S. Weiss *The Journal of Physical Chemistry B* **1999**, *103*, 8122, DOI: 10.1021/jp9921699.

(315) A. Vilan, A. Shanzer, D. Cahen *Nature* **2000**, *404*, 166.

(316) A. L. Briseno, J. Aizenberg, Y.-J. Han, R. A. Penkala, H. Moon, A. J. Lovinger, C. Kloc, Z. Bao *Journal of the American Chemical Society* **2005**, *127*, 12164, DOI: 10.1021/ja052919u.

(317) A. L. Briseno, S. C. B. Mannsfeld, M. M. Ling, S. Liu, R. J. Tseng, C. Reese, M. E. Roberts, Y. Yang, F. Wudl, Z. Bao *Nature* **14, 2006**, *444*, 913, DOI: 10.1038/nature05427.

(318) S. Bastide, R. Butruille, D. Cahen, A. Dutta, J. Libman, A. Shanzer, L. Sun, A. Vilan *The Journal of Physical Chemistry B* **1997**, *101*, 2678, DOI: 10.1021/jp9626935.

(319) K. Gartsman, D. Cahen, A. Kadyshevitch, J. Libman, T. Moav, R. Naaman, A. Shanzer, V. Umansky, A. Vilan *Chemical Physics Letters* **1998**, *283*, 301, DOI: 10.1016/S0009-2614(97)01387-0.

(320) R. Cohen, L. Kronik, A. Shanzer, D. Cahen, A. Liu, Y. Rosenwaks, J. K. Lorenz, A. B. Ellis *Journal of the American Chemical Society* **1999**, *121*, 10545, DOI: 10.1021/ja9906150.

(321) R. W. Zehner, B. F. Parsons, R. P. Hsung, L. R. Sita *Langmuir* **1999**, *15*, 1121, DOI: 10.1021/la981114f.

(322) J. Krüger, U. Bach, M. Grätzel *Advanced Materials* **2000**, *12*, 447, DOI: 10.1002/(SICI)1521-4095(200003)12:6<447::AID-ADMA447>3.0.CO;2-8.

(323) M. Fahlman, W. Salaneck *Surface Science* **2002**, *500*, 904, DOI: 10.1016/S0039-6028(01)01554-0.

(324) X. Crispin, V. Geskin, A. Crispin, J. Cornil, R. Lazzaroni, W. R. Salaneck, J.-L. Brédas *Journal of the American Chemical Society* **2002**, *124*, 8131, DOI: 10.1021/ja025673r.

(325) E. Margapoti, J. Li, Ö. Ceylan, M. Seifert, F. Nisic, T. L. Anh, F. Meggendorfer, C. Dragonetti, C.-A. Palma, J. V. Barth, J. J. Finley *Advanced Materials* **2015**, *27*, 1426, DOI: 10.1002/adma.201405110.

(326) J. Takeya, T. Nishikawa, T. Takenobu, S. Kobayashi, Y. Iwasa, T. Mitani, C. Goldmann, C. Krellner, B. Batlogg *Applied Physics Letters* **2004**, *85*, 5078, DOI: 10.1063/1.1826239.

(327) V. Palermo, M. Palma, P. Samorì *Advanced Materials* **19, 2006**, *18*, 145, DOI: 10.1002/adma.200501394.

(328) D. Cornil, J. Cornil *Journal of Electron Spectroscopy and Related Phenomena* **2013**, *189*, 32, DOI: 10.1016/j.elspec.2013.06.004.

(329) S. D. Evans, A. Ulman *Chemical Physics Letters* **1990**, *170*, 462, DOI: 10.1016/S0009-2614(90)87085-6.

(330) L. Wang, G. M. Rangger, L. Romaner, G. Heimel, T. BucÌko, Z. Ma, Q. Li, Z. Shuai, E. Zojer *Advanced Functional Materials* **9, 2009**, *19*, 3766, DOI: 10.1002/adfm.200901152.

(331) H. J. Yoon, C. M. Bowers, M. Baghbanzadeh, G. M. Whitesides *Journal of the American Chemical Society* **8, 2014**, *136*, 16, DOI: 10.1021/ja409771u.

(332) *Noncontact Atomic Force Microscopy*; Morita, S., Wiesendanger, R., Meyer, E., Eds.; NanoScience and Technology; Springer Berlin Heidelberg: Berlin, Heidelberg, 2002.

(333) *Scanning Probe Microscopy*; Kalinin, S., Gruverman, A., Eds.; Springer New York: New York, NY, 2007.

(334) *Surface chemical analysis - X-ray photoelectron spectrometers - Calibration of energy scales: ISO 15472:2001.*

(335) P. Fenter, P. Eisenberger, K. S. Liang *Physical Review Letters* **19, 1993**, *70*, 2447, DOI: 10.1103/PhysRevLett.70.2447.

(336) F. Chesneau, J. Zhao, C. Shen, M. Buck, M. Zharnikov *The Journal of Physical Chemistry C* **22, 2010**, *114*, 7112, DOI: 10.1021/jp100522n.

(337) P. C. Rusu, G. Giovannetti, C. Weijtens, R. Coehoorn, G. Brocks *The Journal of Physical Chemistry C* **11, 2009**, *113*, 9974, DOI: 10.1021/jp902905y.

(338) A. Rosenhahn, S. Schilp, H. J. Kreuzer, M. Grunze *Physical Chemistry Chemical Physics* **2010**, *12*, 4275, DOI: 10.1039/c001968m.

(339) F. Hamelmann, U. Heinzmann, U. Siemeling, F. Bretthauer, J. Vor der Brüggen *Applied Surface Science* **2004**, *222*, 1, DOI: 10.1016/j.apsusc.2003.08.006.

(340) G. Pace, V. Ferri, C. Grave, M. Elbing, C. von Hänisch, M. Zharnikov, M. Mayor, M. A. Rampi, P. Samorì *Proceedings of the National Academy of Sciences* **2007**, *104*, 9937.

(341) R. Schmidt, E. McNellis, W. Freyer, D. Brete, T. Gießel, C. Gahl, K. Reuter, M. Weinelt *Applied Physics A* **2008**, *93*, 267, DOI: 10.1007/s00339-008-4829-z.

(342) M. Han, D. Ishikawa, T. Honda, E. Ito, M. Hara *Chemical Communications* **2010**, *46*, 3598, DOI: 10.1039/b921801g.

(343) D. Brete, D. Przyrembel, C. Eickhoff, R. Carley, W. Freyer, K. Reuter, C. Gahl, M. Weinelt *Journal of Physics: Condensed Matter* **3, 2012**, *24*, 394015, DOI: 10.1088/0953-8984/24/39/394015.

(344) R. Hatton *Thin Solid Films* **15, 2001**, *394*, 291, DOI: 10.1016/S0040-6090(01)01191-9.

(345) L. Zhu, H. Tang, Y. Harima, K. Yamashita, Y. Aso, T. Otsubo *J. Mater. Chem.* **2002**, *12*, 2250, DOI: 10.1039/B201391F.

(346) S. Besbes, A. Ltaief, K. Reybier, L. Ponsonnet, N. Jaffrezic, J. Davenas, H. Ben Ouada *Synthetic Metals* **2003**, *138*, 197, DOI: 10.1016/S0379-6779(02)01270-5.

(347) M. McDowell, I. G. Hill, J. E. McDermott, S. L. Bernasek, J. Schwartz *Applied Physics Letters* **2006**, *88*, 073505, DOI: 10.1063/1.2173711.

(348) V. Chechik, R. M. Crooks, C. J. M. Stirling *Advanced Materials* **2000**, *12*, 1161, DOI: 10.1002/1521-4095(200008)12:16<1161::AID-ADMA1161>3.0.CO;2-C.

(349) C. Haensch, S. Hoeppener, U. S. Schubert *Chemical Society Reviews* **2010**, *39*, 2323, DOI: 10.1039/b920491a.

(350) K. Heister, S. Frey, A. Ulman, M. Grunze, M. Zharnikov *Langmuir* **2004**, *20*, 1222, DOI: 10.1021/la030352u.

(351) R. M. Petoral, K. Uvdal *The Journal of Physical Chemistry B* **2005**, *109*, 16040, DOI: 10.1021/jp0526445.

(352) S. Krakert, N. Ballav, M. Zharnikov, A. Terfort *Phys. Chem. Chem. Phys.* **2010**, *12*, 507, DOI: 10.1039/B915036F.

(353) P. A. Lewis, C. E. Inman, F. Maya, J. M. Tour, J. E. Hutchison, P. S. Weiss *Journal of the American Chemical Society* **2005**, *127*, 17421, DOI: 10.1021/ja055787d.

(354) *Handbook of X-ray photoelectron spectroscopy: a reference book of standard spectra for identification and interpretation of XPS data*, Update; Moulder, J. F., Chastain, J., Eds.; Perkin-Elmer Corporation: Eden Prairie, Minn, 1992.

(355) T. Ishida, W. Mizutani, U. Akiba, K. Umemura, A. Inoue, N. Choi, M. Fujihira, H. Tokumoto *The Journal of Physical Chemistry B* **1999**, *103*, 1686, DOI: 10.1021/jp983547x.

(356) T. Ishida, W. Mizutani, N. Choi, U. Akiba, M. Fujihira, H. Tokumoto *The Journal of Physical Chemistry B* **2000**, *104*, 11680, DOI: 10.1021/jp0018450.

(357) C. Fuxen, W. Azzam, R. Arnold, G. Witte, A. Terfort, C. Wöll *Langmuir* **2001**, *17*, 3689, DOI: 10.1021/la0018033.

(358) W. Azzam, A. Bashir, A. Terfort, T. Strunskus, C. Wöll *Langmuir* **2006**, *22*, 3647, DOI: 10.1021/la053065u.

(359) J. N. Hohman, P. Zhang, E. I. Morin, P. Han, M. Kim, A. R. Kurland, P. D. McClanahan, V. P. Balema, P. S. Weiss *ACS Nano* **24, 2009**, *3*, 527, DOI: 10.1021/nn800673d.

(360) R. K. Smith, S. M. Reed, P. A. Lewis, J. D. Monnell, R. S. Clegg, K. F. Kelly, L. A. Bumm, J. E. Hutchison, P. S. Weiss *The Journal of Physical Chemistry B* **2001**, *105*, 1119, DOI: 10.1021/jp0035129.

(361) F. L. Hirshfeld *Theoretica Chimica Acta* **1977**, *44*, 129, DOI: 10.1007/BF00549096.

(362) J. P. Ritchie *Journal of the American Chemical Society* **1985**, *107*, 1829, DOI: 10.1021/ja00293a005.

(363) J. P. Ritchie, S. M. Bachrach *Journal of Computational Chemistry* **1987**, *8*, 499, DOI: 10.1002/jcc.540080430.

(364) R. S. Mulliken *The Journal of Chemical Physics* **1955**, *23*, 1833, DOI: 10.1063/1.1740588.

(365) F. Iori, S. Corni *Journal of Computational Chemistry* **30, 2008**, *29*, 1656, DOI: 10.1002/jcc.20928.

(366) C. J. Illingworth, C. Domene *Proceedings of the Royal Society A: Mathematical, Physical and Engineering Sciences* **8, 2009**, *465*, 1701, DOI: 10.1098/rspa.2009.0014.

(367) T. A. Halgren, W. Damm *Current opinion in structural biology* **2001**, *11*, 236.

(368) S. W. Rick, S. J. Stuart In *Reviews in Computational Chemistry*, Lipkowitz, K. B., Boyd, D. B., Eds.; John Wiley & Sons, Inc.: 2002, 89.

(369) A. Warshel, M. Kato, A. V. Pisliakov *Journal of Chemical Theory and Computation* **2007**, *3*, 2034, DOI: 10.1021/ct700127w.

(370) R. I. Ainsworth, D. D. Tommaso, J. K. Christie, N. H. de Leeuw *The Journal of Chemical Physics* **2012**, *137*, 234502, DOI: 10.1063/1.4770295.

(371) P. E. Lopes, E. Harder, B. Roux, A. D. Mackerell In *Multi-scale Quantum Models for Biocatalysis: Modern Techniques and Applications*, York, D. M., Lee, T.-S., Eds.; Springer Netherlands: Dordrecht, 2009, 219.

(372) H. Yu, W. F. van Gunsteren *Computer Physics Communications* **2005**, *172*, 69, DOI: 10.1016/j.cpc.2005.01.022.

(373) P. Cieplak, F.-Y. Dupradeau, Y. Duan, J. Wang *Journal of Physics: Condensed Matter* **19, 2009**, *21*, 333102, DOI: 10.1088/0953-8984/21/33/333102.

(374) P. E. M. Lopes, B. Roux, A. D. MacKerell *Theoretical Chemistry Accounts* **2009**, *124*, 11, DOI: 10.1007/s00214-009-0617-x.

(375) H. S. Antila, E. Salonen In *Biomolecular Simulations: Methods and Protocols*, Monticelli, L., Salonen, E., Eds.; Humana Press: Totowa, NJ, 2013, 215.

(376) W. Xie, J. Gao *Journal of Chemical Theory and Computation* **2007**, *3*, 1890, DOI: 10.1021/ct700167b.

(377) L.-P. Wang, T. Head-Gordon, J. W. Ponder, P. Ren, J. D. Chodera, P. K. Eastman, T. J. Martinez, V. S. Pande *The Journal of Physical Chemistry B* **29, 2013**, *117*, 9956, DOI: 10.1021/jp403802c.

(378) G. Lamoureux, B. Roux *The Journal of Chemical Physics* **2003**, *119*, 3025, DOI: 10.1063/1.1589749.

(379) G. Lamoureux, E. Harder, I. V. Vorobyov, B. Roux, A. D. MacKerell *Chemical Physics Letters* **2006**, *418*, 245, DOI: 10.1016/j.cplett.2005.10.135.

(380) R. Kumar, F.-F. Wang, G. R. Jenness, K. D. Jordan *The Journal of Chemical Physics* **2010**, *132*, 014309, DOI: 10.1063/1.3276460.

(381) R. Kumar, F.-F. Wang, G. R. Jenness, K. D. Jordan *The Journal of Chemical Physics* **2010**, *132*, 139902, DOI: 10.1063/1.3371871.

(382) P. T. Kiss, P. Bertsyk, A. Baranyai *The Journal of Chemical Physics* **2012**, *137*, 194102, DOI: 10.1063/1.4767063.

(383) T. R. Lucas, B. A. Bauer, S. Patel *Biochimica et Biophysica Acta (BBA) - Biomembranes* **2012**, *1818*, 318, DOI: 10.1016/j.bbamem.2011.09.016.

(384) J. W. Ponder, C. Wu, P. Ren, V. S. Pande, J. D. Chodera, M. J. Schnieders, I. Haque, D. L. Mobley, D. S. Lambrecht, R. A. DiStasio, M. Head-Gordon, G. N. I. Clark, M. E. Johnson, T. Head-Gordon *The Journal of Physical Chemistry B* **4, 2010**, *114*, 2549, DOI: 10.1021/jp910674d.

(385) P. Ren, J. W. Ponder *The Journal of Physical Chemistry B* **2003**, *107*, 5933.

(386) M. Souaille, H. Loirat, D. Borgis, M. Gaigeot *Computer Physics Communications* **2009**, *180*, 276, DOI: 10.1016/j.cpc.2008.08.008.

(387) D. Jiao, P. A. Golubkov, T. A. Darden, P. Ren *Proceedings of the National Academy of Sciences* **29, 2008**, *105*, 6290, DOI: 10.1073/pnas.0711686105.

(388) D. Jiao, J. Zhang, R. E. Duke, G. Li, M. J. Schnieders, P. Ren *Journal of Computational Chemistry* **2009**, *30*, 1701, DOI: 10.1002/jcc.21268.

(389) E. Harder, A. D. MacKerell, B. Roux *Journal of the American Chemical Society* **4, 2009**, *131*, 2760, DOI: 10.1021/ja806825g.

(390) Z. Zuo, N. S. Gandhi, R. L. Mancera *Journal of Chemical Information and Modeling* **27, 2010**, *50*, 2201, DOI: 10.1021/ci100321h.

(391) Y. Shi, Z. Xia, J. Zhang, R. Best, C. Wu, J. W. Ponder, P. Ren *Journal of Chemical Theory and Computation* **10, 2013**, *9*, 4046, DOI: 10.1021/ct4003702.

(392) J. Huang, P. E. M. Lopes, B. Roux, A. D. MacKerell *The Journal of Physical Chemistry Letters* **18, 2014**, *5*, 3144, DOI: 10.1021/jz501315h.

(393) J. Huang, A. D. MacKerell *Biophysical Journal* **2014**, *107*, 991, DOI: 10.1016/j.bpj.2014.06.038.

(394) H. Li, V. Ngo, M. C. Da Silva, D. R. Salahub, K. Callahan, B. Roux, S. Y. Noskov *The Journal of Physical Chemistry B* **23, 2015**, *119*, 9401, DOI: 10.1021/jp510560k.

(395) T. G. Kucukkal, S. J. Stuart *The Journal of Physical Chemistry B* **2, 2012**, *116*, 8733, DOI: 10.1021/jp300528m.

(396) M. Doemer, M. Guglielmi, P. Athri, N. S. Nagornova, T. R. Rizzo, O. V. Boyarkin, I. Tavernelli, U. Rothlisberger *International Journal of Quantum Chemistry* **15, 2013**, *113*, 808, DOI: 10.1002/qua.24085.

(397) A. Savelyev, A. D. MacKerell *Journal of Computational Chemistry* **15, 2014**, *35*, 1219, DOI: 10.1002/jcc.23611.

(398) W. Jiang, D. J. Hardy, J. C. Phillips, A. D. MacKerell, K. Schulten, B. Roux *The Journal of Physical Chemistry Letters* **20, 2011**, *2*, 87, DOI: 10.1021/jz101461d.

(399) J. Kästner, S. Thiel, H. M. Senn, P. Sherwood, W. Thiel *Journal of Chemical Theory and Computation* **2007**, *3*, 1064, DOI: 10.1021/ct600346p.

(400) A. M. Burow, M. Sierka, J. Döbler, J. Sauer *The Journal of Chemical Physics* **2009**, *130*, 174710, DOI: 10.1063/1.3123527.

(401) P. V. Sushko, I. V. Abarenkov *Journal of Chemical Theory and Computation* **13, 2010**, *6*, 1323, DOI: 10.1021/ct900480p.

(402) S. J. Fox, C. Pittock, T. Fox, C. S. Tautermann, N. Malcolm, C.-K. Skylaris *The Journal of Chemical Physics* **2011**, *135*, 224107, DOI: 10.1063/1.3665893.

(403) H. Heinz, K. C. Jha, J. Luettmer-Strathmann, B. L. Farmer, R. R. Naik *Journal of The Royal Society Interface* **6, 2011**, *8*, 220, DOI: 10.1098/rsif.2010.0318.

(404) H. M. Evjen *Physical Review* **1932**, *39*, 675.

(405) I. D. C. Gurney *Physical Review* **1953**, *90*, 317.

(406) R. Euwema, G. Surratt *Journal of Physics and Chemistry of Solids* **1975**, *36*, 67, DOI: 10.1016/0022-3697(75)90115-8.

(407) A. Redlack, J. Grindlay *Journal of Physics and Chemistry of Solids* **1975**, *36*, 73.

(408) B. Herschend, M. Baudin, K. Hermansson *The Journal of Chemical Physics* **2004**, *120*, 4939, DOI: 10.1063/1.1635802.

(409) J. Topping *Proceedings of the Royal Society A: Mathematical, Physical and Engineering Sciences* **1, 1927**, *114*, 67, DOI: 10.1098/rspa.1927.0025.

(410) T. Clark, J. Chandrasekhar, G. W. Spitznagel, P. V. R. Schleyer *Journal of Computational Chemistry* **1983**, *4*, 294, DOI: 10.1002/jcc.540040303.

(411) A. D. McLean, G. S. Chandler *The Journal of Chemical Physics* **1980**, *72*, 5639, DOI: 10.1063/1.438980.

(412) R. Krishnan, J. S. Binkley, R. Seeger, J. A. Pople *The Journal of Chemical Physics* **1980**, *72*, 650, DOI: 10.1063/1.438955.

(413) J.-P. Blaudeau, M. P. McGrath, L. A. Curtiss, L. Radom *The Journal of Chemical Physics* **1997**, *107*, 5016, DOI: 10.1063/1.474865.

(414) A. J. H. Wachters *The Journal of Chemical Physics* **1970**, *52*, 1033, DOI: 10.1063/1.1673095.

(415) P. J. Hay *The Journal of Chemical Physics* **1977**, *66*, 4377, DOI: 10.1063/1.433731.

(416) R. C. Binning, L. A. Curtiss *Journal of Computational Chemistry* **1990**, *11*, 1206, DOI: 10.1002/jcc.540111013.

(417) M. P. McGrath, L. Radom *The Journal of Chemical Physics* **1991**, *94*, 511, DOI: 10.1063/1.460367.

(418) L. A. Curtiss, M. P. McGrath, J.-P. Blaudeau, N. E. Davis, R. C. Binning, L. Radom *The Journal of Chemical Physics* **1995**, *103*, 6104, DOI: 10.1063/1.470438.

(419) M. J. Frisch, J. A. Pople, J. S. Binkley *The Journal of Chemical Physics* **1984**, *80*, 3265, DOI: 10.1063/1.447079.

(420) Y.-T. Tao, C.-C. Wu, J.-Y. Eu, W.-L. Lin, K.-C. Wu, C.-h. Chen *Langmuir* **1997**, *13*, 4018, DOI: 10.1021/la9700984.

(421) T. Leung, P. Schwartz, G. Scoles, F. Schreiber, A. Ulman *Surface Science* **2000**, *458*, 34, DOI: 10.1016/S0039-6028(00)00385-X.

(422) W. Azzam, C. Fuxen, A. Birkner, H.-T. Rong, M. Buck, C. Wöll *Langmuir* **2003**, *19*, 4958, DOI: 10.1021/la020868y.

(423) S. Frey, V. Stadler, K. Heister, W. Eck, M. Zharnikov, M. Grunze, B. Zeysing, A. Terfort *Langmuir* **2001**, *17*, 2408, DOI: 10.1021/la001540c.

(424) J. F. Kang, A. Ulman, S. Liao, R. Jordan, G. Yang, G.-y. Liu *Langmuir* **1, 2001**, *17*, 95, DOI: 10.1021/la001217+.